SOIL MOISTURE REMOTE SENSING USING ACTIVE MICROWAVES AND LAND SURFACE MODELING

Rogier van der Velde

Examining Committee:

Prof.dr. F.D. van der Meer	University of Twente
Prof.dr.ing. W. Verhoef	University of Twente
Prof. Y. Ma	Chinese Academy of Sciences
Prof.dr.ir. N. Verhoest	Ghent University
Prof.dr.ir. N. van de Giesen	Delft University of Technology
Dr. M. Rodell	NASA

UNIVERSITY OF TWENTE.

FACULTY OF GEO-INFORMATION SCIENCE AND EARTH OBSERVATION

ITC dissertation number 176
ITC, P.O. Box 6, 7500 AA Enschede, The Netherlands

ISBN 978-90-6164-296-1
Cover designed by Benno Masselink
Printed by ITC Printing Department

SOIL MOISTURE REMOTE SENSING USING ACTIVE MICROWAVES AND LAND SURFACE MODELING

DISSERTATION

To obtain
the doctor's degree at the University of Twente,
on the authority of the Rector Magnificus,
prof.dr. H. Brinksma,
on account of the decision of the graduation committee,
to be publicly defended
on Friday 5 November 2010 at 15:00 hrs

by

Rogier van der Velde

born on 11 June 1980

in Rotterdam

This thesis is approved by
Prof. Dr. Ir. Z. Su, promotor
Dr. Ir. P.J. van Oevelen, assistant promotor

Preface

This thesis probably began at one of the fields in the western part of Netherlands on 11 November 2001. On that day I broke my leg in the most dramatic way; playing soccer with my brother, Clemens, against the first team of the rival club from the neighboring town. I could not play soccer for a long time and a life till then focused on sports needed some remodelling. Being not a very social person, I turned to studying, which later became sitting behind a computer and at least for most of time pretending to do research.

After about two years, I got from Peter van Oevelen, also the co-promotor here, the opportunity to do an internship with Dr. Tom Jackson in the United States at the Hydrology and Remote Sensing Laboratory. Not knowing that this group is one of the soil moisture remote sensing centers in the world, I participated as an MSc student in large scale field campaigns and met internationally recognized scientists. This led to a PhD position at ITC several months after my return to the Netherlands.

Bob Su, my promoter at ITC, offered me the PhD position, gave me responsibilities in several research projects and, as such, created the boundary conditions for the start of a scientific carreer, for which I am all very grateful. Nevertheless, for several reasons the first years were not that succesfull. This changed after Bob Su hired in 2006 a female PhD student named Harmke van Aken, whom earlier this year became my wife. As ITC is originally an institute with a strong focus on education and less on research, it lacked the expertise in our research fields. Hence, we became effectively each other's advisor. Although Harmke is on none of the papers from this thesis a co-author, she easily could have been on each single one. Harmke, you decided to end your scientific career, but this thesis is also a bit yours. Thank you for all the discussions and allowing me the peacefull worktime during the evenings and weekends.

The other person whom deserves my sincere gratitude is Alicia Joseph from NASA's Goddard Space Flight Center (GSFC). She gave me not only friendship, but also access to the extraordinary active microwave data sets collected by her and her colleques Peggy O'Neill from NASA GSFC and Prof. Roger Lang from George Washington University (GWU). Without these data sets, half of this thesis could not have been written.

Further, Prof. Yaoming Ma from the Institute of Tibetan Plateau Research (ITP/CAS) is acknowledged for facilitating the field campaigns on the Tibetan Plateau and providing data. I also would like to thank the co-authors on the papers for their constructive criticisms and suggestions, Matt Rodell (NASA/GSFC), Mike Ek (EMC/NCEP), Fred Bosveld (KMNI) and Peter van Oevelen (GEWEX).

Then at ITC, there were early morning coffees with Wim and Suhyb, especially over the past two years. From sharing our complaints, successes and frustrations related to work as well as the normal struggles of life evolved a strong friendship. I hope that we still have many years of working and coffee (or beer) drinking together ahead of us.

For the right boundary conditions in my personal life, apart from Harmke, also Clemens is acknowledged. He took care of our parents and the bussiness after in January 2009 my father got ill and thereby relieved me from a great number of worries at the moment it was needed most. My parents, I would like to thank for the childhood in your protective care and encouraging me to aim for the highest possible in everything you do. The Van Aken's are thanked for providing a comfortable holiday place on the island Texel anytime of the year.

Harmke, it is done then …

List of symbols

Greek

Symbol	Name	Units
α	Albedo	-
β	Bowen ratio	-
γ	Attenuation by the canopy	-
γ_d	Density of dry soil	kg m^{-3}
γ_p	Psychrometric constant	kPa K^{-1}
Δ	Slope of the saturated vapor pressure curve	kPa K^{-1}
ε	Electric permittivity	F m^{-1}
ε_0	Electric permittivity of free space	F m^{-1}
ε_r	Relative permittivity or dielectric constant	-
κ_{dry}	Thermal conductivity under dry soil moisture conditions	W m^{-1} K^{-1}
κ_e	Extinction coefficient	m^{-1}
κ_h	Thermal conductivity	W m^{-1} K^{-1}
κ_{h_2o}	Thermal conductivity of water	W m^{-1} K^{-1}
κ_{ice}	Thermal conductivity of ice	W m^{-1} K^{-1}
κ_o	Thermal conductivity of soil particles other than quartz	W m^{-1} K^{-1}
κ_{qtz}	Thermal conductivity of quartz	W m^{-1} K^{-1}
κ_{sat}	Thermal conductivity under saturated soil moisture conditions	W m^{-1} K^{-1}
λ	Wavelength	m
λ_v	heat of vaporization	J kg^{-1}
μ	Magnetic permeability	N A^{-2}
μ_0	Magnetic permeability of free space	N A^{-2}
θ	Soil moisture content	m^3 m^{-3}
θ_c	Critical soil moisture content below which transpiration is reduced due to soil moisture stress	m^3 m^{-3}
$\theta_{(i)}$	Moisture content in the i^{th} soil layer	m^3 m^{-3}
θ_i	Incidence angle	degrees

θ_{ice}	Frozen soil moisture content	$m^3\ m^{-3}$
θ_{lig}	Liquid soil moisture content	$m^3\ m^{-3}$
θ_s	Saturated soil moisture content	$m^3\ m^{-3}$
θ_w	Soil moisture content at wilting point below which soil plants cannot take up soil water	$m^3\ m^{-3}$
ρ	correlation	-
ρ_{air}	Air density	$kg\ m^{-3}$
σ	scattering cross section of a target	$m^2\ m^{-2}$
σ_v	Scattering cross section of the vegetation	m^{-1}
σ_s	Stefan-Boltzmann constant	$W\ m^{-2}\ K^{-4}$
σ^o	backscattering coefficient	$m^2\ m^{-2}$ or dB
σ^o_{surf}	Surface scattering	$m^2\ m^{-2}$ or dB
σ^o_s	Soil surface scattering contribution	$m^2\ m^{-2}$ or dB
$\sigma^o_{s\leftrightarrow v}$	Scattering contribution from the soil-vegetation pathways	$m^2\ m^{-2}$ or dB
σ^o_v	Vegetation scattering contribution	$m^2\ m^{-2}$ or dB
σ^2_b	Mean squared difference between two samples caused by an inherent bias due to differences in the climatology of the two samples	-
σ^2_s	Mean squared difference between two samples caused by difference in the spatial resolution of the two samples	-
σ^2_t	Mean total squared difference between two samples	-
σ^2_u	Mean squared difference between two samples caused by uncertainties in the two samples	-
ψ	Soil water potential	m
ψ_s	Saturated soil water potential	m

Roman

Symbol	Name	Units
a_0	Soil texture dependent parameters for converting the dielectric constant measured by an impedance probe (Delta-T theta probe) into sol moisture	-
a_1		-
A	Empirical crop parameter for the cloud model	-
A_0	Area illuminated by a radar beam	m^2
A_e	Effective area of the antenna	m^2
b_c	Empirical parameter of the Campbell soil hydraulic model	-
b_{clim}	Systematic bias in soil moisture data sets due to a difference in climatology between the two samples	$m^3\ m^{-3}$
B	Empirical crop parameter for the cloud model	-
c_p	Specific heat capacity of moist air	$kJ\ kg^{-1}\ K^1$
C	Differential water capacity	m^{-1}
C_h	Surface exchange coefficient for heat	-
C_q	Surface exchange coefficient for moisture	-
C_s	Soil thermal heat capacity	$J\ m^{-3}\ K^{-1}$
C_{soil}	Thermal heat capacity of air	$J\ m^{-3}\ K^{-1}$
C_w	Thermal heat capacity of water	$J\ m^{-3}\ K^{-1}$
cmc	Moisture content on the leaves of the canopy	$kg\ m^{-2}$
cmc_{max}	Maximum moisture content on the leaves of the canopy	$kg\ m^{-2}$
D	Soil water diffusivity	$m^2\ s^{-1}$
D_b	Soil moisture deficit in the soil column	$m^3\ m^{-3}$
D_s	Saturated soil water diffusivity	$m^2\ s^{-1}$
e	Vapor pressure	kPa
e_s	Surface emissivity	-
E_c	Evaporation of rain intercepted by vegetation	$W\ m^{-2}$
E_{dir}	Soil evaporation	$W\ m^{-2}$
E_t	Evaporation through the stomata of vegetation	$W\ m^{-2}$
E_p	Potential evaporation	$W\ m^{-2}$
$\mathbf{E}$	Electric field vector	$V\ m^{-1}$
f_{air}	Volume fraction air within the soil matrix	-
f_c	Fractional vegetation cover	-

f_{soil}	Volume fraction soil within the soil matrix	-
f_w	Volume fraction water within the soil matrix	-
f_{pq}	Kirchhoff field coefficients utilized with the IEM model	-
F_{pq}	Complementary field coefficients utilized with the IEM model	-
fx	Empirical parameter affecting the soil evaporation reduction under soil moisture stress conditions	-
f_{root}	Fraction of the root zone represented by the i^{th} layer	-
G_0	Soil heat flux at the surface	W m^{-2}
G_{10}	Soil heat flux at a 0.10 m soil depth	W m^{-2}
G_t	Power gain of the transmitting antenna	-
h	Canopy height	m
h_s	Empirical parameter describing the optimal transpiration conditions with respect to the air humidity	-
H	Sensible heat flux	W m^{-2}
H	Magnetic field vector	A m^{-1}
I_{max}	Maximum infiltration capacity	m s^{-1}
k	Wave number	m^{-1}
K	Hydraulic conductivity	m s^{-1}
K_e	Kersten number	-
K_{ref}	Empirical parameter for Noah runoff simulations	m s^{-1}
K_s	Saturated hydraulic conductivity	m s^{-1}
kdt	Empirical parameter for Noah runoff simulations	-
kdt_{ref}	Empirical parameter for Noah runoff simulations	-
l	Correlation length	m
$L^{\downarrow}$	Longwave incoming radiation	W m^{-2}
LAI	Leaf Area Index	m^2 m^{-2}
λE	Latent heat flux	W m^{-2}
n	Number of samples	#
nroot	Number of root zone layer within the Noah model	#
P	Rain intensity	m s^{-1}
P_a	Air pressure	kPa
P_t	Power transmitted by an antenna	W
P_r	Power received by an antenna	W
q	Actual specific humidity	kg kg^{-1}

q_s	Saturated specific humidity	kg kg^{-1}
qtz	Volume fraction quartz	-
R	Distance between the target and antenna	m
$R_{c,min}$	Minimum stomatal resistance	s m^{-1}
$R_{c,hum}$	Factor increasing the stomatal resistance in case of a sub-optimal air humidity for transpiration	-
$R_{c,rad}$	Factor increasing the stomatal resistance in case of a sub-optimal radiative conditions for transpiration	-
$R_{c,soil}$	Factor increasing the stomatal resistance in case of soil moisture stress on transpiration	-
$R_{c,temp}$	Factor increasing the stomatal resistance in case of a sub-optimal air temperature for transpiration	-
R_{gl}	Parameter characterized the light-use efficiency of a canopy	W m^{-2}
R_n	Net radiation	W m^{-2}
R_p	*p*-polarized Fresnel reflectivity	-
R_{surf}	Surface runoff	m s^{-1}
s	Root mean square of surface height variations	m
S	Water sinks and source to the soil column	m s^{-1}
$S^{\downarrow}$	Shortwave incoming radiation	W m^{-2}
t	Time step	s
T_{air}	Air temperature	K
T_{opt}	Optimum temperature for transpiration	K
$T_{p\ air}$	Potential air temperature	K
$T_{s(i)}$	Soil temperature in the ith soil layer	K
T_{skin}	Skin temperature	K
u	Wind speed	m s^{-1}
V_1	vegetation descriptor 1 used within the cloud model	-
V_2	vegetation descriptor 2 used within the cloud model	-
W	Vegetation water content	kg m^{-2}
x	Horizontal displacement	m
z	Surface height	m
z_{0m}	Aerodynamic roughness length for momentum transport	m
z_{0h}	Aerodynamic roughness length for heat transport	m

List of abbreviations

ACF	Autocorrelation length Function
ACM	Atmospheric Circulation Models
ALSIS	Atmospheric and Land-Surface Interaction Scheme
ASCAT	Advanced Scatterometer
ARS	Agricultural Research Service
ASAR	Advanced Synthetic Aperture Radar
BARC	Beltsville Agriculture Research Center
BREB	Bowen Ratio Energy Balance
BST	Beijing Standard Time
CAMP	CEOP Asia-Australia Monsoon Project
CAS	Chinese Academy of Sciences
CDF	Cumulative Distribution Function
CEOP	Coordinated Enhanced Observing Period
EC	Eddy Correlation
ENVISAT	Environmental Satellite
ERS	European Remote Sensing satellite
ESA	European Space Agency
GAME	GEWEX Asian Monsoon Experiment
GEWEX	Global Energy and Water cycle Experiment
GM	Global Monitoring mode
GMES	Global Monitoring for Environment and Security
GSFC	Goddard Space Flight Center
GWU	George Washington University
ITP	Institute for Tibetan Plateau Research
JAXA	Japan Aerospace Exploration Agency
KNMI	Koninklijk Nederlands Meteorologisch Instituut
LSM	Land Surface Model
LAI	Leaf Area Index
MM5	Meso-scale Model version 5
MOST	Ministry of Science and Technology
NASA	National Aeronautics and Space Administration
NCAR	National Center for Atmospheric Research
NCEP	National Centers for Environmental Prediction
NDVI	Normalized Difference Vegetation Index
OPE^3	Optimizing Production Inputs for Economic and Environmental Enhancements
OSU	Oregon State University
PALSAR	Phased Array type L-band SAR
PDF	Probability Density Function
PSU	Penn State University
PTF	PedoTransfer Function
RMSD	Root Mean Squared Differences
SAR	Synthetic Aperture Radar

SHF	Soil Hydraulic Function
SHM	Soil Hydraulic Model
SHP	Soil Hydraulic Parameters
SMAP	Soil Moisture Active/Passive mission
SMOS	Soil Moisture and Ocean Salinity mission
SSD	Sum of Squared Differences
STL	Soil Thermal Layer
STP	Soil Thermal Properties
SWB	Simple Water Balance model
TM	Thematic Mapper
USA	United States of America
USDA	United States Department of Agriculture
VIC	Variable Infiltration Capacity model
WS	Wide Swath mode

Table of Contents

1 Introduction

1.1 Background

The partitioning of solar radiation into energy for warming the atmosphere and for evaporation is constrained by the availability of water in the soil. Below critical soil moisture levels evaporation is suboptimal and the radiation excess is converted into heat. Hence, more water vapour is brought into the atmosphere under wet than under dry soil conditions, which positively influences the formation of clouds that leads eventually to precipitation. There is evidence that this feedback mechanism can result in persistent wet and dry patterns (e.g. Koster et al. 2004, Shukla and Mintz 1982) causing extreme events, such as floods and droughts. Several studies (e.g. Bosilovich and Sun 1999, Ferranti and Viterbo 2006) have shown that the skill of atmospheric circulation models (ACM's) in predicting the timing and severity of such extreme events on a seasonal scale would increase when the simulation of soil moisture is improved.

In the coupling of land surface models (LSM's) to ACM's progress has been made towards an improved soil moisture simulation. As quantification of land-atmosphere interactions is its main task, a LSM focuses on characterizing physical processes related to the surface hydrology and the surface energy budget. ACM's are, however, computationally demanding and, thus, the numerical complexity of the LSM has to be limited. Traditionally, the LSM structure includes a detailed description of the 'above-ground' processes, whereas parsimonious parameterizations are used for the surface hydrology component (e.g. De Rosnay et al. 2000, Yang et al. 2005, Gulden et al. 2007). Merely based on this fact, soil moisture simulations by a LSM are expected to be uncertain. However, as any model, the reliability of LSM simulations is also affected by uncertainties in applied parameterizations (i.e. Gutmann and Small 2007), the initial and boundary conditions (i.e. Rodell et al. 2005) and, if operated separately from an ACM, the atmospheric forcings (i.e. Kato et al. 2007, Sheffield et al. 2006, Berg et al. 2003).

Thorough evaluation against a 'ground truth' can identify the impact of these different sources of uncertainty and improve the overall performance. In general, a comprehensive set of *in-situ* measurements is regarded as the foundation for assessing the performance of LSM's. The scientific community has, therefore, set up various intensive measurement programs (e.g. Henderson-Sellers et al. 1996, Wood et al. 1998, Lawford et al. 2007). Nevertheless, the distribution of *in-situ* measurements throughout the globe remains sparse. Moreover, a challenge lies also in comparing measurements

to model outputs. The spatial and temporal representation and, most of all, the reliability of measurements cannot be taken for granted.

An alternative approach towards reducing model uncertainties forms data assimilation (e.g. Evensen 2006). Over the past decade, its potential application to global LSM simulations increased with the availability of remote sensing observations capable of monitoring relevant states. Large-scale soil moisture monitoring is, for example, possible by interpreting microwave measurements (e.g. Jackson 1993, Owe et al. 2001, Dubois et al. 1995, Wagner and Scipal 2000). Favorable for soil moisture monitoring purposes are the lower microwave frequencies (<6.6 GHz) because they are less affected by clouds and vegetation.

Various low frequency passive as well as active sensors are in orbit or scheduled for launch. However, the first mission, Soil moisture and Ocean Salinity (SMOS), dedicated to soil moisture has only recently been launched by the European Space Agency (ESA) and another one, Soil Moisture Active/Passive (SMAP), by National Aeronautics and Space Administration (NASA) is in preparation (expected launch: 2015). Both missions (will) collect L-band (~ 1.4 GHz) microwave measurements at temporal resolutions of 2-3 days. Similar specifications are expected for NASA's Aquarius mission (expected launch: 2011), but its main objective is monitoring the ocean salinity.

Although it is expected that these missions will have unprecedented contributions to global soil moisture monitoring, the employed sensing techniques limit the spatial resolution of their measurements to several tens of kilometers. Soil moisture observed at this resolution is important for explaining variations on a seasonal scale (e.g. Vinnikov et al. 1996), but is unable to capture the dynamics at smaller time scales. At present, spatial resolutions up to several meters can only be achieved from space when active microwave measurements are collected using the Synthetic Aperture Radar (SAR) technique. However, the temporal resolution of SAR observations is either coarse (> 30 days) due to limitations in the sensing configuration or cannot be guarantied in case of multi-mode systems. Moreover, the reliability of SAR based soil moisture products is considered to be inferior to the coarser resolution products.

Retrieval of soil moisture using active microwaves is, in general, complicated by the scattering from rough surfaces and vegetation whose geometry is unknown. Therefore, large-scale soil moisture mapping relies often on semi-empirical radiative transfer models (e.g. Attema and Ulaby 1978, Bindlish and Barros 2000) or on empirical change detection approaches (e.g. Wagner and Scipal 2000, Njoku et al. 2002). Semi-empirical radiative transfer models provide only a partial description of the scattering from vegetation covered surfaces

and, using a change detection method, the surface roughness and vegetation effects on scattering are assumed to be time-invariant. This shows that active microwave soil moisture retrieval algorithms have not been fully developed yet. Moreover, the uncertainties imposed on the retrievals by the simplifying assumptions have not been quantified.

1.2 Thesis outline

This thesis contributes to the reliability of active microwave soil moisture retrieval algorithms and discusses uncertain LSM simulations. Via data integration techniques, such as data assimilation, the availability of more accurate soil moisture retrievals can assist in reducing model uncertainties. Much progress can, however, also be obtained by evaluating LSM uncertainties caused by the parameterizations and/or the model structure.

Soil moisture retrieval using active microwaves is studied using two data sets. First, C- and L-band backscatter (σ^o) measured throughout the corn growth cycle at a field near Beltsville (Maryland, USA) by a truck-mounted scatterometer is discussed. Based on these measurements, vegetation effects on active microwaves are identified and a new concept to correct for these effects is presented (**Chapter 5**). Then, **Chapter 6** discusses the influence of assumptions regarding the surface roughness on the soil moisture retrieved from the vegetation corrected radar measurements.

A 2.5 years series of C-band SAR images acquired by the Advanced SAR (ASAR) over the central part of the Tibetan Plateau forms the second set. In **Chapter 7**, the impact of changes in land surface states (e.g. soil moisture, temperature and biomass) on those σ^o signatures is analyzed. Based on this knowledge, a method is developed for retrieving soil moisture from the ASAR data sets (**Chapter 8)**.

The Noah LSM is adopted for the modelling part of this thesis. Using atmospheric forcings measured at the Cabauw meteorological station (The Netherlands) its operational soil water flow scheme is evaluated (**Chapter 9**). Noah's application to measurements collected at a Tibetan site addresses the implications of parameter uncertainties (**Chapter 10)**. **Chapter 11** presents a comparison of the soil moisture retrievals from Chapter 8 against simulations by Noah coupled to the MM5 (Meso-scale Model version 5, Grell et al.1994) regional climate model.

Further, **Chapters 2 – 4** describe the principle of soil moisture retrieval from active microwaves, the Noah model structure and the utilized data sets.

2 Active microwave remote sensing

2.1 Introduction

Backscattering coefficient

Remote sensing radars transmit electromagnetic waves to the earth' surface and measure the amount of radiation scattered back at the same position as where the waves were originally transmitted. Then, the power received by a radar antenna is a function of the transmitted power corrected for the two-way spreading loss and losses caused by the target, which can be expressed by (e.g. Ulaby 1982),

$$P_r = \frac{P_t G_t A_e}{\left(4\pi R^2\right)^2}\sigma \qquad (2.1)$$

where, P_t is the transmitted power [W], P_r is the received power [W], G_t is the transmitter power gain [-], A_e is the effective area of the antenna [m^2], R is the distance from the radar to the target [m] and σ is the scattering cross section [m^2].

Eq. 2.1 is known as the *radar equation*. Via the radar theory (e.g. Ulaby et al. 1981) it can be shown that the effective area of a radar antenna and the power gain are related to each other as,

$$A_e = \frac{\lambda^2 G_t}{4\pi} \qquad (2.2)$$

where, λ is the wavelength [m].

Substitution of Eq. 2.2 into 2.1 yields a more commonly used form of the radar equation, in which the received power is expressed in terms of the effective antenna area according to,

$$P_r = \frac{P_t A_e^{\,2}}{4\pi\lambda^2 R^4}\sigma \qquad (2.3)$$

Intrinsically Eq. 2.1 and 2.3 are the same, both allowing the calculation of the received power from a single target. The scattering cross section (σ) is only representative for a single target. However, remote sensing radars illuminate an area and observe the σ as a collection of scatterers, written as,

$$\sigma^o = \frac{\langle\sigma\rangle}{A_0} \qquad (2.4)$$

where, A_0 is the illuminated area [m^2] and σ^o is referred to as the backscattering coefficient [$m^2\ m^{-2}$ or decibels, dB].

In this context, the *backscattering coefficient* (σ^o) is defined as the ratio of the power received by a radar antenna over the power that the antenna would have received if target area would be a perfectly isotropic (Lambertian) scatterer. As such, the σ^o represents the power losses caused by the target area due to the scattering of

radiation away from the sensor and, to lesser extent, the absorption of radiation. A flat and lossless surface scatters most radiation away from the antenna and produces a low σ^o response. This type of scattering is referred to as *specular reflection*. Rougher surfaces redirect also radiation back towards the antenna and generate a larger σ^o response. Typically, as a surface appears rougher its scattering behaviour become more isotropic as is illustrated in Figure 2-1. The material, shape and size of scatterers with respect to the wave properties (e.g. wavelength, polarization, and incidence angle) determine whether a target area appears rough.

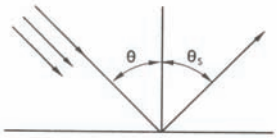

Smooth surface: only coherent scattering (specular reflectance).

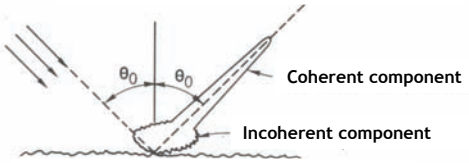

Slightly rough surface: scattering consists of a coherent and incoherent component

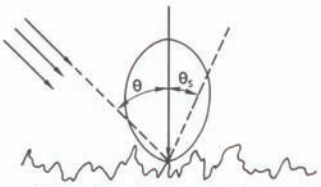

Rough surface: scattering consists of largely of incoherent component and approach an isotropic scatterer

Figure 2-1 illustration of scattering patterns under varying surface roughness conditions (adopted from Ulaby et al 1982).

Dielectric constant

The electric permittivity (ε) is a measure for the ability of a medium to store an electric charge (*capacitance*), after which the stored energy is reradiated. A medium with a large ε behaves, therefore, more as an isotropic scatterer and produces a larger σ^o

response. In electromagnetism, it is common to express the ε relative to the electric permittivity of free space (ε_0), which is also referred to as the relative permittivity or *dielectric constant* (ε_r).

Because the molecular structure of liquid water consists of strong dipole bonds, the ε_r of media with a high moisture content is in the microwave portion of the electromagnetic spectrum significantly larger than for low moisture contents. Hence, microwave observations are sensitive to changes in the water content of both soils and vegetation.

The ε_r depends, however, also on the strength of the bonds between the water and the other molecules in the medium. In soils these intermolecular forces are strongly affected by its texture and mineral composition. The relationships between the soil texture, moisture content and ε_r have been experimentally determined in laboratories, which led to various empirical models referred to as *dielectric mixing* models. The models by Topp et al. (1980), Wang and Schmugge (1980) and Dobson et al. (1985) are most commonly used in microwave remote sensing. In this thesis conversions from the ε_r into soil moisture have been performed using Dobson's model.

Similarly, Mätzler (1994) and El-Rayes and Ulaby (1987) used laboratory measurements to establish the relationship between the ε_r and the water content in vegetation. Such information is, however, only needed as input for physically based vegetation scattering models, which have not been applied for this thesis.

Surface and vegetation geometry

The surface and vegetation geometry (or vegetation morphology) have an important effect on the returned amount of scattering. Both the surface and vegetation geometry are extremely irregular under natural conditions and difficult to describe mathematically. Physically based scattering models need a rigorous description of vegetation morphology including the sizes and shapes of the main constituents of the canopy (e.g. Lang and Sidhu 1983, Chauhan et al. 1994, Ferrazzoli and Guerriero 1995), which is typically not available at a large-scale. Within the semi-empirical models applied for the retrieval of soil moisture over large domains, the effects of the vegetation morphology are embedded within empirical parameters. In this thesis, vegetation morphological measurements have not been used. Examples of scattering model applications that do use the canopy structure as input can be found in Della Vecchia (2007).

The surface geometry represents surface height variations in the horizontal plane induced by components with different spatial scales (e.g. Verhoest et al 2008). These surface height variations are hereafter referred to as the *surface roughness*. A full field characterization of the surface roughness requires a 2-dimensional

mapping of the soil surface. It is, however, more common to record only a transect of surface heights and assume that the roughness is isotropic in the horizontal plane. Different methods are available for measuring the 1-dimensional surface height profile ranging from fairly simple grid (or needle) boards to the more sophisticated laser profilers (e.g Davidson et al. 2000, Callens et al. 2006).

A stochastic representation of the surface roughness can be derived from the field measured surface height profiles. This characterization consists of three parameters: the root mean square height (*s*), autocorrelation length (*l*) and autocorrelation function (ACF).

The *s* is defined as the standard deviation of the surface height variations represented by,

$$s = \sqrt{\frac{1}{n-1}\sum_{i=1}^{n}\left(z_i - \overline{z}\right)^2} \tag{2.5}$$

where, *z* is the surface height [m], $\overline{z}$ is the mean surface height within the profile [m] and *n* is the number of samples [#].

The *l* is defined as the distance (*x*') over which the normalized autocorrelation (ρ) becomes less than 1/*e* (≈0.3678...), whereby the normalized autocorrelation is formulated as,

$$\rho\left(x'\right) = \frac{\sum_{i=1}^{n} z\left(x\right) z\left(x + x'\right)}{\sum_{i=1}^{n} z\left(x\right)^2} \tag{2.6}$$

where, z(*x*) is the surface height at point *x* [m].

Further, the ACF characterizes the surface roughness spectrum, which is often defined as a Gaussian or an Exponential function. The expression for the ACF can be found in textbooks, such as Ulaby et al. (1982) and Fung (1994).

Intuitively, soil surfaces whose horizontal dimensions are large compared to wavelength may appear smooth to a radar. Conversely, large vertical dimensions with respect to the wavelength are indicative for a rough surface. Hence, the scattering is more isotropic for surfaces with a small autocorrelation length (*l*) and a large root mean square height (*s*).

Even though the stochastic analysis of the surface height profiles provides a objective means for evaluating the roughness of a surface, the direct use of these parameters in surface scattering models is often cumbersome. One complicating factor is the scale dependency of the surface roughness (e.g. Verhoest et al. 2008). Surface height variations much smaller than the wavelength contribute very little to the amount of scattering, but they do affect the calculation of the roughness parameters. Depending on the wavelength an appropriate horizontal resolution should, therefore, be selected for characterizing

the surface height profile. Ulaby et al. (1982) propose a horizontal resolution smaller than one tenth of the wavelength as a rule of thumb, but no exact quantitative criterion exists. Further, studies (e.g. Oh and Kay 1998, Callens et al. 2006, Bryant et al. 2007) report that the determination of the *l* and ACF from field measurements is affected by the length of the surface height profile.

As such, it will be difficult to use field measured surface roughness parameters as input for a surface scattering model and obtain a good agreement with the observed σ^o. A practical approach to the roughness parameterization problem is to fit the roughness parameters by matching the observed and simulated σ^o (e.g. Su et al. 1997, Mattia et al. 2006). Similar approaches for estimating the roughness parameters have been adopted for this thesis, which are described in Chapters 5, 6 and 8.

2.2 Backscatter modeling

Soil surface scattering

The soil surface scattering (σ^o_{surf}) depends on the soil dielectric constant, the surface roughness and the wave properties (e.g incidence angle, polarization and wavelength). The basis for all scattering problems follows from the Maxwell equations, which resemble the conservation of electromagnetic energy in a volume. A complete derivation of these equations can be found in textbooks such as Ulaby et al. (1982) and Hecht (1998).

Solving the Maxwell equations requires certain boundary conditions. In the special case of a perfectly flat surface Snell's law applies, which states that the angle of the incoming wave equals the angle of the outgoing wave. When assuming a lossless, perfectly conducting medium and that the magnetic permeability (μ) is equal to that of free space (μ_0), the reflection coefficients for the horizontal and vertical polarization may be calculated as,

$$R_h = \left| \frac{\cos\theta_i - \sqrt{\varepsilon - \sin^2\theta_i}}{\cos\theta_i + \sqrt{\varepsilon - \sin^2\theta_i}} \right|^2 \quad (2.7)$$

$$R_v = \left| \frac{\varepsilon\cos\theta_i - \sqrt{\varepsilon - \sin^2\theta_i}}{\varepsilon\cos\theta_i + \sqrt{\varepsilon - \sin^2\theta_i}} \right|^2 \quad (2.8)$$

where, θ_i is the incidence angle [degrees], R_p is the *p*-polarized reflectivity [-] and subscripts *h* and *v* indicate the horizontal and vertical polarization, respectively.

The equations 2.7 and 2.8 are commonly known as the *Fresnel reflection* coefficients and describe the reflection of a specular surface. Over natural land covers, however, the complex surface geometry needs be taken into consideration for simulating the σ^o.

Approximations regarding the surface geometry are necessary for remote sensing applications. The two most frequently used methods are the *Kirchhoff approaches* and the *Small Perturbation Method* (SPM).

Within the Kirchhoff approaches, the surface geometry is represented by a series of tangent planes (or facets). Then, for the scattering from each plane the specular reflection coefficients apply (Eqs. 2.7 and 2.8). This assumption limits the applicability of the Kirchhoff approaches to surfaces whose horizontal dimensions are large compared to the length of the incoming wave (Ulaby et al. 1982). This means that the correlation length, *l*, should be large with respect to the wavelength and root mean square height, *s*.

Although the Kirchhoff concept is fairly straightforward, additional simplifications are needed to obtain an analytical solution. The two most common assumptions are the *stationary phase* and the *scalar approximations*, from which the *Geometric Optics* and *Physical Optics* models follow. The stationary phase approximation implies that scattering occurs only along directions for which there are specular points on the surface and, thus, the effects of local diffraction (or multiple scattering) are excluded. This limits the applicability of the Geometric Optics model further to surfaces with large average vertical dimensions (or a large *s*) with respect to the wavelength. Conversely, the Physical Optics model applies when the *s* is small compared to the wavelength. Under these surface conditions vector formulation of the Kirchhoff fields reduces to a scalar form (see Ulaby et al. 1982 and Beckmann and Spizzichino 1963). Hence, this approximation is referred to as the scalar approximation.

For surfaces with a small correlation length, *l*, with respect to the wavelength the Kirchhoff approximation is no longer valid. In the case that both the *l* and the *s* are small compared to the wavelength the Small Perturbation Method (SPM, Rice 1957) is applicable. Within the SPM, the surface geometry is assumed to be a superposition of the different spectral components and can be transformed in Fourier components. Application of this Fourier transformed surface geometry to the field equations yields analytical expressions for the σ^o_{surf}. Validity of the SPM ranges to surfaces with small vertical dimensions with respect to the wavelength.

From the discussion above follows that the Kirchhoff approaches and SPM can only be applied to surface with a certain roughness. The validity ranges for these three models are provided in Table 2-1. The Kirchhoff models are valid for surfaces that appear ‘rough’, the high-frequency solution, and the SPM model applies to surfaces that appear ‘smooth’, the low-frequency solution (Fung and Pan 1987). Attempts to unite the two approaches resulted in the development of so-called ‘two-scale’ models, which basically model the σ^o_{surf} as the

sum of the Kirchhoff and SPM solution (Van Oevelen 2000). A limitation of the two-scale models is that they are not valid outside validity ranges of the Kirchhoff and SPM model. To overcome this problem Fung and Pan (1987) and Pan and Fung (1987) adopted an integral approach. Later on, Fung et al. (1992) presented this method with some modifications as the Integral Equation Method (IEM) model.

Table 2-1 Roughness conditions for which the Physical Optics, Geometric Optics and Small Perturbation Method surface scattering models are considered to be valid (after Van Oevelen 2000).

	Validity*		
Physical Optics	$s/l < 0.25$	$kl>6$	$l^2>2.76s\lambda$
Geometric Optics	$(2ks\cos\theta_i)^2 > 10$	$kl>6$	$l^2>2.76s\lambda$
Small Perturbation Model	$ks < 3$, $s/l < 0.3$		

*k ~wave number ($2\pi/\lambda$)

The complete mathematical derivation of the IEM model is found in the literature (Fung et al. 1992 and Fung 1994) and starts from expressing the integral equation for the tangential surface electric (**E**) and magnetic (**H**) field by a Kirchhoff ($\mathbf{E}^k$ and $\mathbf{H}^k$) and a complementary ($\mathbf{E}^c$ and $\mathbf{H}^c$) term. Then, in accordance with the Stratton-Chu (Ulaby et al. 1982) integral the far zone scattered fields can be expressed in terms of these Kirchhoff and complementary tangential surface fields. This yields the coherent Kirchhoff and complementary **E** scattered fields. In the backscattering case, however, the power measured mostly consists of incoherent scattering, at least at larger off-nadir angles. By subtracting the average coherent **E** field from the average total power the incoherent scattering is obtained within the IEM model. Substitution of this incoherent power into the radar equation yields analytical expressions for the like- and cross-polarization. Fung et al. (1992) show that for rough surfaces the IEM model reduces to standard Kirchhoff approach, while under smooth conditions the IEM model reduces to the SPM solution.

Intrinsically, this IEM approach poses no restrictions to the applicability of the resulting model with respect to the surface roughness conditions and frequency (Fung 1994). In the original derivation, however, phase differences in the scattered fields were assumed to be negligible. As such, the effects of multiple scattering are excluded. Multiple scattering occurs when an incident wave is scattered to another point on the surface, which is typical for surfaces that are rough with respect to wavelength. Hence, the original IEM version is also referred to *small to moderate ks approximation* and its validity is defined as $ks < 3.0$.

The original form of the analytical σ^o expressions for the like polarization reads,

$$\sigma_{pq}^{o} = \frac{k^2}{2}\exp\left(-2k_z^2 s^2\right)\sum_{n=1}^{\infty} s^{2n}\left|I_{pq}^{n}\right|^2 \frac{W^n\left(-2k_x,0\right)}{n!} \tag{2.9}$$

with

$$I_{pq}^{n} = \left(2k_z\right)^n f_{pq}\exp\left(-s^2 k_z{}^2\right) + \frac{k_z^n\left[F_{pq}\left(-k_x,0\right)+F_{pq}\left(-k_x,0\right)\right]}{2} \tag{2.10}$$

where, k is the wave number ($=2\pi/\lambda$), $k_z = k\cos\theta_i$, $k_x = k\sin\theta_i$, $W^n(-2k_x,0)$ is the n^{th} power Fourier transform of the surface correlation function, and f_{pq} and F_{pq} are the Kirchhoff and complementary field coefficients depending on the incidence angle and electromagnetic properties of the medium; its mathematical formulations can be found in Fung (1994).

A good agreement between the IEM simulations and laboratory measurements was obtained for surface conditions falling within its validity ranges (e.g. Mancini et al. 1999 and Macelloni et al. 2000). Mancini et al. (1999) found, however, that the simulations underestimate the measured σ^o for surface conditions outside the validity range of the IEM (e.g. rough surface, high frequency, large incidence angle). This result showed the limitation of the ignoring multiple scattering effects. Subsequently improvements to the original IEM were made to include these effects (Hsieh et al. 1997, Hsieh and Fung 1999, Fung et al. 2002, Chen et al. 2003). The IEM model version by Chen et al. (2003) has been applied in this thesis for simulating the σ^o_{surf}, which has been named the Advanced IEM (AIEM) model.

Despite the IEM is valid for a wide range of surface roughness conditions, model validations against σ^o measurements acquired over natural surface have not always been successful (e.g. Altese et al. 1996). Most difficulties follow from formulating a representative set of surface roughness parameters because the surface roughness effect on σ^o is scale dependent. As a result, the use of surface roughness measured at a local scale as input for the IEM model can lead to large discrepancies between the measured and simulated σ^o (Bryant et al. 2007). A derivation of the roughness parameterization from the radar measurements itself is, therefore, preferred. For example, multi-channel σ^o data sets have been employed for the simultaneous retrieval of the surface roughness and soil moisture (e.g. Su et al. 1997, Van Oevelen and Hoekman 1999, Bindlish et al. 2000, Rahman et al. 2007). Also, time series of σ^o measurements have been utilized to identify the roughness effects (e.g. Wagner and Scipal 2000, Wen

and Su 2003b). For the soil moisture retrieval applications presented in this thesis both approaches have been applied.

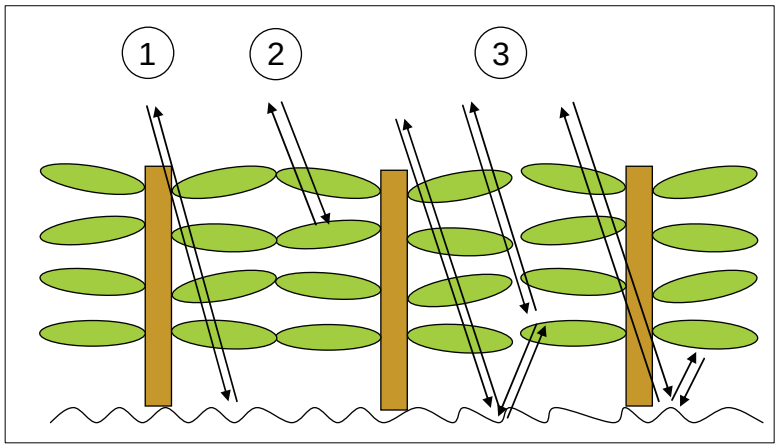

Figure 2-2 Scattering contributions observed over a vegetated surface, 1) the surface scattering attenuated by the vegetation cover, 2) the direct scattering from the canopy, 3) the scattering along the soil-vegetation pathways.

Vegetation effects on surface scattering

The amount of scattering observed over vegetation covered surfaces consists of three scattering contributions as schematized in Figure 2-2. The first scattering component characterizes the soil surface contribution (σ^o_s), which is the surface scattering attenuated by the vegetation cover. Direct scattering from the canopy is represented by the second term (σ^o_v) and the third scattering component resembles the scattering along the soil-vegetation pathways ($\sigma^o_{s\leftrightarrow v}$). Both physical and semi-empirical models simulate the scattering from vegetation covered surfaces as the sum of these individual components according to,

$$\sigma^o = \sigma^o_s + \sigma^o_v + \sigma^o_{s\leftrightarrow v} \qquad (2.11)$$

In physically-based vegetation scattering (emission) models, the scattering and absorption characteristics of the canopy are determined based on the dimensions and dielectric properties of individual elements (e.g. stems, leafs and cobs) in the canopy. This approach is referred to as the *discrete medium approach*. The complex morphological structure of a canopy is represented in models by defining the electric field of individual plants components using specific approximations regarding the shape. For example, stems can be modelled as cylinders using the infinite length approximation (Seker and Schneider 1988) and leaves may be represented as discs or ellipses using the Rayleigh-Gans (Eom and Fung 1984) or the Physical Optics (Le Vine et al. 1983) approximations in case the dimensions of the leaves small or large with respect to the

wavelength, respectively. The computation of the backscatter coefficient (or emissivity) by a discrete medium model can be based on the *wave theory* (e.g. Lang and Sidhu 1983, Chauhan et al. 1991, Chauhan et al. 1994) or on the *radiative transfer theory* (e.g. Ulaby et al. 1990, Karam et al. 1992, Ferrazzoli and Guerriero 1995 and Karam, 1997).

Simulations by these discrete medium models require an extensive parameterization of the vegetation morphology. Such detailed information is not available for large spatial domains, which limits their applicability for large-scale soil moisture retrieval. A more practical approach is to describe the effects of vegetation in terms of 'bulk' variables. The most widely used method for describing the vegetation scattering effects is the semi-empirical Cloud model (Attema and Ulaby 1978).

The main assumption of the Cloud model is that the absorption and scattering characteristics of the canopy are represented as the sum of individual particles. Hence, the vegetation layer is considered as a volume of identical uniformly distributed scatterers, for which the effects of multiple scattering within the canopy are negligible. Using these simplifications the direct scattering from vegetation is approximated by (e.g. Ulaby et al. 1982, Woodhouse 2006),

$$\sigma_v^o = \left(1-\gamma^2\right)\frac{\sigma_v \cos\theta_i}{2\kappa_e} \tag{2.12}$$

where, σ_v is the vegetation scattering cross section [m^{-1}], κ_e is the extinction coefficient [m^{-1}] and γ^2 is the two-way attenuation represented by,

$$\gamma^2 = \exp\left[-\frac{2\kappa_e h}{\cos\theta_i}\right] \tag{2.13}$$

with h as the canopy height [m].

The soil surface scattering contribution is calculated as,

$$\sigma_s^o = \gamma^2 \sigma_{surf}^o \tag{2.14}$$

Most applications of the Cloud model assume that the higher order scattering terms are negligible, which reduces the calculation of the total backscatter to,

$$\sigma_t^o = \gamma^2 \sigma_{surf}^o + \left(1-\gamma^2\right)\frac{\sigma_v \cos\theta_i}{2\kappa_e} \tag{2.15}$$

This form of the Cloud model has been widely used for the soil moisture retrieval (e.g. Prevot et al. 1993, Bindlish and Barros 2001, Wen and Su 2003a) and vegetation properties (e.g. Prevot et al. 1993, Durden et al. 1995, Maity et al. 2004). For retrieval applications, however, estimates for the σ_v and κ_e should be obtained. Originally, Attema and Ulaby (1978) used the definition of the single scattering albedo, being equal to σ_v/κ_e, for justifying the

representation of the σ^o_v as a function of an empirical crop dependent parameter. Further, they defined the κ_e as the product of the volumetric vegetation water content (expressed in kg m^{-3}) and an empirical parameter. In a later study, however, Ulaby et al. (1984) concluded that the single scattering albedo may also be proportional to the volumetric water content and found that for frequencies larger than 8.6 GHz the vegetation scattering and extinction properties can also be described as a function of the Leaf Area Index (LAI). A more generalized form of the volume scattering and two-way attenuation can, thus, be formulated as,

$$\sigma_v^o = \left(1-\gamma^2\right) A \cdot V_1 \cos\theta_i \tag{2.16}$$

with

$$\gamma^2 = \exp\left[-\frac{B \cdot V_2}{\cos\theta_i}\right] \tag{2.17}$$

where A and B are crop dependent parameters that should be fitted using field measurements, and V_1 and V_2 are so-called vegetation descriptors.

In the literature V_1 is often taken equal to V_2 and a variety of bulk variables have been used as the vegetation descriptors (e.g. the vegetation water content (W), LAI and Normalized Difference Vegetation Index (NDVI)). Moreover, the canopy height is typically omitted from equation 2.13 assuming that its effect on the attenuation will be included within the calibrated parameter B.

The selection of the vegetation descriptor used for retrieval applications depends strongly on the application. For example, for studying the potential of radar for retrieving vegetation biomass, physical quantities (e.g. W and LAI) are adopted (e.g. Ulaby et al. 1984, Durden et al. 1995, Inoue et al. 2002). For soil moisture retrieval over large spatial domains, however, it is accustomed to use a readily available proxy variable, such as the NDVI (e.g. Bindlish and Barros 2001, Wen and Su 2003a).

Further, also a large variety exists among the complexity of the surface scattering model adopted for describing the soil scattering contribution within the Cloud model. For example, Ulaby et al. (1984) and Prevot et al. (1993) utilize a simple linear relationship between the σ^o_{surf} and soil moisture content. De Roo et al. (2001) and Wen and Su (2003a) use semi-empirical scattering approaches and the IEM model has been included within the Cloud model by Bindlish and Barros (2001). Again, the choice of the method used depends on the retrieval application. For the retrieval of vegetation characteristics a simple linear relationship will probably be sufficiently accurate. In case of soil moisture retrieval, however, it is beneficial to use a semi-empirical and physically based scattering model.

In this thesis, the Cloud concept is used to correct the σ^o observation for the vegetation effects in Chapter 5 and the utilized implementation is described therein.

3 The Noah land model

3.1 Introduction

The importance of land surface hydrology on the development of weather systems has been widely acknowledged (e.g. Shukla and Mintz 1982, Garatt 1993, Koster et al. 2004). *Land Surface Models* (LSM's) are, therefore, coupled to Atmospheric Circulation Models (ACM's) to characterize the exchange of heat and moisture between the land surface and atmosphere (e.g. Chen and Dudhia 2001, Ek et al. 2003, Dickinson et al. 2006). Development of the first LSM for an ACM dates back to the early 1970's, which resulted in the 'bucket' models (Manabe 1969). The structure of those bucket models was quite simple and considered only the most basic water balance components, such as water storage, rainfall, runoff and evaporation. Implementation of more sophisticated physical processes was in those days restricted by the available computer power. As the computing capacity increased the model structures became gradually more sophisticated.

In the early 1980s, for example, multiple layers and thermodynamic components were introduced in the representation of the soil column (e.g. McCumber and Pielke 1981, Mahrt and Pan 1984). Further, throughout the 1980s and in the early 1990's, the land models underwent extensive 'greening' leading in a comprehensive description of 'above-ground' processes (e.g. Sellers et al. 1986, Noilhan and Planton 1989, Dickinson et al. 1993). Within the development of the Variable Infiltration Capacity (VIC, Liang et al. 1994), Simple Water Balance (SWB, Koren et al. 1996) and Mosaic (Koster and Suarez 1992), the spatial variability within the coarse modelling grids of LSM's (> 50x50 km^2) was explicitly addressed. More recent developments have focused on introducing explicit groundwater reservoirs (e.g. Dai et al. 2003, Koster et al. 2000).

The Noah LSM coupled to the AGCM systems of National Centers for Environmental Prediction (NCEP) has gone through a similar evolution and has been used for this thesis. The Noah LSM originates from the Oregon State University (OSU) LSM, which includes a diurnally dependent Penman approach for the calculation of the latent heat flux under non-restrictive soil moisture conditions (Marht and Ek 1984), a simple canopy model (Pan and Marht 1987), a four-layer soil model (Marht and Pan 1984, Schaake et al. 1996) and a Reynolds number based approach for determining the ratio of the roughness lengths for momentum and heat transport (Zilintinkevich 1995, Chen et al. 1997). As a result of a good performance in intercomparison projects (e.g. Chen et al. 1996, Chen et al. 1997), the modestly parameterized OSU LSM was incorporated in the ACM of the National

Centers for Environmental Prediction (NCEP). Being implemented in an operational weather forecasting system, the OSU LSM experienced continuous developments and was gradually extended to be representative for a broad range of land surface conditions, after which it was renamed Noah. An overview of the latest changes to Noah is documented in Ek et al. (2003), which affect the cold-season processes most notably (e.g. frozen soil moisture, snow pack process). A schematization of the model structure is shown in Figure 3-1 and the model physics relevant for this thesis is briefly described below.

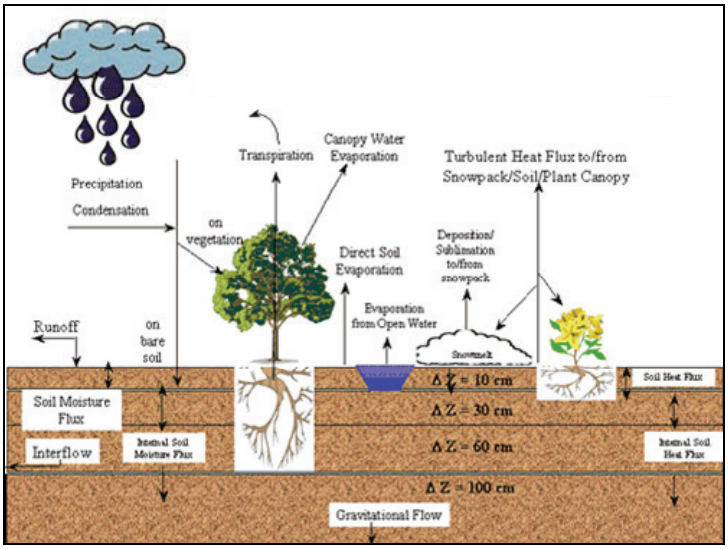

Figure 3-1 Schematization of the Noah model structure taken from http://www.ral.ucar.edu/research/land/technology/lsm.php.

3.2 Soil Water Movement

Noah simulates soil water flow through application of Richards' equation, which is derived by substituting Darcy's Law into the mass balance equation and reads,

$$\frac{\partial \theta}{\partial t} = \frac{\partial}{\partial z}\left(K(\theta)\frac{\partial \psi}{\partial z}\right) + \frac{\partial K(\theta)}{\partial z} + S(\theta) \qquad (3.1)$$

where, θ is the soil moisture content [$m^3\ m^{-3}$], K is the hydraulic conductivity [$m\ s^{-1}$], ψ is the soil water potential [m], S represents the sinks and sources (i.e. rainfall, dew, evaporation and transpiration) [$m\ s^{-1}$], and t and z represent the time and the vertical height [s and m, resp.].

Due to the non-linearity of the soil hydraulic functions describing the relationship between K, θ and ψ is the numerical solution to Eq. 3.1 expensive. Noah and various other LSM's employ, therefore, the diffusivity form of Richards' equation, which allows soil water flow

simulations using the soil moisture content as the only prognostic variable. The soil water diffusivity is defined as the ratio of the hydraulic conductivity over the differential water capacity according to,

$$D(\theta) = \frac{K(\theta)}{C(\theta)} = K(\theta)\frac{\partial \psi}{\partial \theta} \tag{3.2}$$

where, C is the differential water capacity [m^{-1}], D is the soil water diffusivity [$m^2\ s^{-1}$]

Substitution of Eq. 3.2 into Eq. 3.1 yields the Richards' diffusivity form,

$$\frac{\partial \theta}{\partial t} = \frac{\partial}{\partial z}\left(D(\theta)\frac{\partial \theta}{\partial z}\right) + \frac{\partial K(\theta)}{\partial z} + S(\theta) \tag{3.3}$$

The first term on the right-hand side of Eq. 3.3 characterizes the diffusive flow component driven by the vertical ψ gradient. The second term describes the convective flow mechanism forced by gravity. Through the gravity induced convective flow, water is transported downwards. The ψ gradient can be pointing downwards or upwards depending on the soil moisture profile and, thus, the diffusive flow mechanism may also transport water upwards. This represents the Noah's ability to simulate capillary rise. Time-integration of Eq. 3.3 is obtained by using the numerical scheme presented in Kalnay and Kanamitsu (1988), which employs an explicit solution when no rain is registered and implicit one for time steps with rain.

Both convective and diffusive flow mechanisms are parameterized by the transport coefficients, K and D, which depend on both the soil texture and soil moisture content. The empirical soil hydraulic model by Campbell (1974) is utilized to parameterize the K-θ and D-θ relationships as function of soil texture,

$$K(\theta) = K_s\left(\frac{\theta}{\theta_s}\right)^{2b_c+3} \tag{3.4}$$

$$D(\theta) = D_s\left(\frac{\theta}{\theta_s}\right)^{b_c+2} \tag{3.5}$$

where, b_c is an empirical parameter [-], K_s is the saturated hydraulic conductivity [$m\ d^{-1}$] and θ_s is the saturated soil moisture content [$m^3\ m^{-3}$], and D_s is the saturated soil water diffusivity [$m^2\ d^{-1}$], defined by,

$$D_s = b_c \cdot K_s\left(\frac{\psi_s}{\theta_s}\right) \tag{3.6}$$

where, ψ_s is the soil water potential at air-entry [m].

Standard in Noah is a soil column of 2 m depth divided over four layers of 0.1, 0.3, 0.6 and 1.0 m with increasing thicknesses towards

the bottom. Nine soil classes are defined for large-scale applications, for which the soil specific hydraulic parameters (e.g. θ_s, K_s, b_c and ψ_s) are obtained from Cosby et al. (1984). These parameter sets are listed in Table 3-1.

Table 3-1 Soil parameter sets defined for the 9 soil texture classes used within large-scale Noah applications (after Cosby et al. 1984).

Soil texture class	θ_s [$m^3\ m^{-3}$]	ψ_s [m^{-1}]	K_s [$m\ d^{-1}$]	b_c [-]	Qtz [-]
Loamy sand	0.421	0.04	1.22	4.26	0.82
Silty clay loam	0.464	0.62	0.17	8.72	0.10
Light clay	0.468	0.47	0.09	11.55	0.25
Sandy loam	0.434	0.14	0.45	4.74	0.60
Sandy clay	0.406	0.10	0.62	10.73	0.52
Clay loam	0.465	0.26	0.22	8.17	0.35
Sandy clay loam	0.404	0.14	0.39	6.77	0.60
Organic	0.439	0.36	0.29	5.25	0.40
Glacial/land ice	0.421	0.04	1.22	4.26	0.82

Qtz ~ quartz content.

3.3 Drainage and surface runoff

Noah calculates drainage at the bottom of the soil column using a free-drainage condition and proportional to the $K(\theta)$ of the bottom layer. Further, surface runoff is generated when the rain intensity exceeds the infiltration capacity and is calculated as,

$$R_{surf} = P - I_{max} \tag{3.7}$$

where, R_{surf} is the surface runoff [$m\ s^{-1}$], P is the rain intensity [$m\ s^{-1}$] and I_{max} is the maximum infiltration capacity [$m\ s^{-1}$].

The Simple Water Balance model (Schaake et al. 1996) concept is used to determine I_{max}. By assuming exponential spatial distributions for infiltration and rainfall, they arrived at the following expression for the I_{max},

$$I_{max} = P\frac{D_b\left[1-\exp(kdt)\right]}{P + D_b\left[1-\exp(kdt)\right]} \tag{3.8}$$

where, D_b is the total soil moisture deficit in the soil column [$m^3\ m^{-3}$] and kdt is a constant [-] defined by,

$$kdt = kdt_{ref}\frac{K_s}{K_{ref}} \tag{3.9}$$

where, kdt_{ref} and K_{ref} are experimentally determined parameters set to 3.0 [-] and 2.0 10^{-6} [$m\ s^{-1}$] (or 0.17 [$m\ d^{-1}$]) for large-scale simulations, respectively.

3.4 Surface Energy Balance

In general, the surface energy budget can be formulated as,

$$F - e_s \sigma_s T_{skin}^4 = H + \lambda E + G_0$$

with (3.10)

$$F = (1-\alpha) S^{\downarrow} + L^{\downarrow}$$

where, H is the sensible heat flux [W m^{-2}], λE is the latent heat flux [W m^{-2}], G_0 is soil heat flux [W m^{-2}], T_{skin} is the skin temperature [K], α is the albedo [-], e_s is the surface emissivity [-], σ_s is the Stefan-Boltzmann constant [=5.67 10^{-8} W m^{-2} K^{-4}], $S^{\downarrow}$ and $L^{\downarrow}$ are the incoming short- and longwave radiation [W m^{-2}], respectively.

The soil heat flux, G_0, is calculated following Fourier's Law using the temperature gradient between the surface and the mid-point of the first soil-layer,

$$G_0 = \kappa_h(\theta) \frac{\partial T}{\partial z} = \kappa_h(\theta) \frac{T_{skin} - T_{s1}}{dz} \quad (3.11)$$

where, T_{s1} is the temperature at the mid-point of the first soil-layer [K] and κ_h is the thermal conductivity [W m^{-1} K^{-1}] specified in the following section.

The sensible heat flux, H, is calculated through application of the bulk transfer relationships (i.e. Garratt 1993), written as,

$$H = \rho_{air} c_p C_h u \left[T_{skin} - T_{p\_air} \right] \quad (3.12)$$

where, ρ_{air} is the air density [kg m^{-3}], c_p is specific heat capacity of dry air [= 1005 J kg^{-1} K^{-1}], C_h is the surface exchange coefficient for heat [-], u is the wind speed [m s^{-1}] and T_{p_air} is the potential air temperature [K].

The surface exchange coefficient for heat is obtained through application of the Monin-Obukhov similarity theory, whereby the ratio of the roughness length for momentum and heat transport (kB^{-1} = $\ln[z_{0m}/z_{0h}]$) is determined by the Reynolds number dependent formulation of Zilintinkevich (1995).

Simulation of the latent heat flux, λE, is performed using a Penman-based diurnally dependent potential evaporation (E_p) approach (Mahrt and Ek 1984), and applying a Jarvis (1976)-type surface resistance parameterization similar to the one of Jacquemin and Noilhan (1990) to impose soil and atmosphere constraints to obtain the actual λE. Assuming equal surface exchange coefficient for heat (C_h) and moisture (C_q), the diurnally dependent potential evaporation can be written as,

$$\lambda E_p = \frac{\Delta (R_n - G_0) + \rho \lambda C_q u (q_s - q)}{1 + \Delta} \quad (3.13)$$

where, R_n is the net radiation [W m^{-2}], Δ is the slope of the saturated vapour pressure curve [kPa K^{-1}], q_s and q are the saturated and actual specific humidity [kg kg^{-1}].

The actual λE is calculated as the sum of three components: 1) soil evaporation (E_{dir}), 2) evaporation of intercepted precipitation by the canopy (E_c) and 3) transpiration through the stomata of the vegetation (E_t). The linear method by Mahfouf and Noilhan (1991) is used to compute the soil evaporation extracted from the top soil layer, according to,

$$E_{dir} = (1 - f_c)\left(\frac{\theta_1 - \theta_w}{\theta_s - \theta_w}\right)^{fx} E_p \tag{3.14}$$

where, f_c is the fractional vegetation cover, *fx* is an empirical constant taken equal to 2.0; θ_s is the saturated soil moisture content, θ_w is the soil moisture content at wilting point and θ_1 is the soil moisture content in the first soil layer [all in m^3 m^{-3}].

The direct evaporation of rain intercepted by the canopy is calculated as,

$$E_c = f_c E_p \left(\frac{cmc}{cmc_{\max}}\right)^{0.5} \tag{3.15}$$

where, *cmc* and cmc_{max} are the actual and maximum canopy moisture contents [kg m^{-2}].

Further, the evaporation from the root zone through the stomata, often referred to as transpiration, is determined following,

$$E_t = f_c P_c E_p \left(1 - \left(\frac{cmc}{cmc_{\max}}\right)^{0.5}\right) \tag{3.16}$$

where, P_c is the plant coefficient defined as,

$$P_c = \frac{1 + \frac{\Delta C_h u P_a}{6.48 \cdot 10^{-8} T_{air}^4}}{1 + R_c C_h + \frac{\Delta C_h u P_a}{6.48 \cdot 10^{-8} T_{air}^4}} \tag{3.17}$$

where, P_a is the air pressure [kPa], and,

$$R_c = \frac{R_{c,\min}}{LAI\, R_{c,rad} R_{c,temp} R_{c,hum} R_{c,soil}} \tag{3.18}$$

where, *LAI* is the leaf area index [m^2 m^2], $R_{c,min}$ is the minimum stomatal resistance [s m^{-1}], and $R_{c,rad}$, $R_{c,temp}$, $R_{c,hum}$, $R_{c,soil}$ represent sub-optimal conditions for transpiration in terms of incoming solar radiation, temperature, humidity and soil moisture, respectively, which are formulated as,

$$\begin{aligned} R_{c,rad} &= \frac{R_{c,\min}/R_{c,\max} + ff}{1 + ff} \text{ where } ff = 1.10 \frac{S^{\downarrow}}{LAI \cdot R_{gl}} \\ R_{c,temp} &= 1 - 0.0016\left(T_{opt} - T_{air}\right)^2 \end{aligned} \tag{3.19}$$

$$R_{c,hum} = \frac{1}{1 + h_s \left(q_{sat} - q \right)}$$

$$R_{c,soil} = \sum_{i=1}^{nroot} \frac{\theta(i) - \theta_w}{\theta_c - \theta_w} f_{root}(i)$$

where, $\theta_{(i)}$ is the soil moisture content in the ith soil layer [m^3 m^{-3}], θ_c is the critical soil moisture content below which the simulated root water uptake and transpiration are reduced [m^3 m^{-3}], *nroot* is the number of root zone layers [-], $f_{root}(i)$ is the fraction of the total root zone the ith layer represents [-], $R_{c,min}$ and $R_{c,max}$ are the minimum and maximum stomatal resistance [s m^{-1}], R_{gl} characterizes the light-use efficiency of a canopy [W m^{-2}], T_{opt} represents the optimum temperature for transpiration [K] and h_s is an empirical parameter describing the optimal transpiration conditions with respect to the air humidity.

Table 3-2 Vegetation parameter sets defined for the 13 land cover types used within large-scale Noah applications.

Land cover type	***nroot*** [#]	$R_{c,min}$ [s m^{-1}]	R_{gl} [W m^{-2}]	H_s [kg kg^{-1}]	z_0 [m]
Tropical Forest	4	150	30	41.69	2.653
Deciduous Trees	4	100	30	54.53	0.826
Mixed Forest	4	125	30	51.91	0.563
Needleleaf-evergreen forest	4	150	30	47.35	1.089
Needleleaf-deciduous forest	4	100	30	47.35	0.854
Savanna	4	70	65	54.53	0.856
Only Ground cover	3	40	100	36.35	0.035
Shrubs w. perennial	3	300	100	42	0.238
Shrubs w. bare soil	3	400	100	42	0.065
Tundra	2	150	100	42	0.076
Bare soil	3	400	100	42	0.011
Cultivations	3	40	100	36.36	0.035
Glacial	2	150	100	42	0.011

In Noah, the parameters, *nroot*, $R_{c,min}$, R_{gl}, h_s and the roughness length for momentum transport (z_{0m}) depend explicitly on the vegetation type. Thirteen vegetation classes are defined for the entire globe, which are given in Table 3-2 along with their predefined parameterizations. The other parameters are typically assumed to be constant, for which the reader is referred to the references cited above.

Further, the θ_c and θ_w are crucial parameters defining the transpiration and soil evaporation reduction under soil moisture stress. The θ_c is often taken equivalent to field capacity, which occurs when the water in the soil profile is in a hydrostatic equilibrium. In soil physics textbooks (e.g. Koorevaar et al. 1983, Hillel 1998) field capacity is defined at specific soil water potentials varying from -1.0

to -3.3 m depending on the circumstances such as the presence of groundwater tables. In hydrology, however, it is also common to define field capacity as the soil moisture content at which the flux density becomes negligible. In standard Noah applications, θ_c is defined at a drainage flux of 0.5 mm day^{-1} and wilting point, θ_w, is taken at ψ = -200 m.

3.5 Soil Heat Flow

The transfer of heat through the soil column is governed by the thermal diffusion equation,

$$C_s(\theta)\frac{\partial T}{\partial t} = \frac{\partial}{\partial z}\left(k_h(\theta)\frac{\partial T}{\partial z}\right) \tag{3.20}$$

where, κ_h is the thermal heat conductivity [W m^{-1} K^{-1}] and C_s is the soil thermal heat capacity [J m^{-3} K^{-1}].

The layer integrated form of Eq. 3.20 is solved using a Crank-Nicholson scheme and the temperature at the bottom boundary is defined as the mean annual 2 m air temperature, which is specified at a depth of 8 m. The top boundary condition is confined by skin temperature, which is computed using the surface energy balance. For this calculation of the surface temperature the following linearization is employed,

$$T_{skin}^4 \approx T_{air}^4\left[1+4\left(\frac{T_{skin}-T_{air}}{T_{air}}\right)\right] \tag{3.21}$$

Substitution of Eq. 3.21 into the energy balance equation (Eq. 3.10) yields the following expression for the surface temperature,

$$T_{skin} = T_{air} + \frac{F-H-\lambda E-G_0}{4T_{air}^3} - \tfrac{1}{4}\varepsilon_s\sigma T_{air} \tag{3.22}$$

The heat flow through the soil column is parameterized by the thermal heat conductivity, κ_h, and capacity, C_s, which depend both on the soil texture and soil moisture content. The thermal heat capacity is calculated as follows (e.g. McCumber and Pielke 1981),

$$C_s = f_{soil}C_{soil} + f_w C_w + f_{air}c_p \tag{3.23}$$

where, f is the volume fraction of the soil matrix, and subscripts 'soil', 'w', 'air' refer to the solid soil, water and air media. In Noah, C_{soil}, c_p and C_w are defined as $2.0\cdot10^6$, 1005 and $4.2\cdot10^6$ J m^{-3} K^{-1}, respectively. In reality, C_{soil} depends also on the soil textural properties, but differences in the heat capacity of the soil constituents are typically assumed negligible (Hillel 1998) and are, therefore, not accounted for in Noah.

The thermal heat conductivity is calculated (e.g. Johansen 1975, Peters-Lidard et al. 1998) as a weighted combination of the saturated

(κ_{sat}) and dry thermal conductivity (κ_{dry}) depending on the degree of saturation,

$$\kappa_h = K_e \left(\kappa_{sat} - \kappa_{dry} \right) + \kappa_{dry} \tag{3.24}$$

where, K_e is the Kersten (1949) number representing the degree of saturation,

$$\begin{aligned} &\text{for } \theta / \theta_s > 0.1 \qquad K_e = \log 10 \left(\theta / \theta_s \right) + 1.0 \\ &\text{for } \theta / \theta_s \le 0.1 \qquad K_e = 0.0 \end{aligned} \tag{3.25}$$

The κ_{dry} is calculated using a semi-empirical equation,

$$\kappa_{dry} = \frac{0.135 \gamma_d + 64.7}{2700 - 0.947 \gamma_d} \tag{3.26}$$

where, γ_d is the density of dry soil approximated by $\gamma_d = (1 - \theta_s) 2700$ [kg m^{-3}] and κ_{sat} depends on the volume fractions of the solid particles, frozen and unfrozen soil water in the matrix,

$$\kappa_{sat} = \kappa_{soil}^{(1-\theta_s)} \kappa_{ice}^{(1-\theta_{ice})} \kappa_{h2o}^{(\theta_{liq})} \tag{3.27}$$

where, κ_{ice} and κ_{h20} are the thermal conductivities for ice and liquid water [= 2.2 and 0.57 W m^{-1} K^{-1}, respectively], θ_{ice} and θ_{liq} are the frozen and liquid soil moisture contents [m^3 m^{-3}] and κ_{soil} is the thermal conductivity of the dry soil matrix calculated as a function of the volume fraction quartz (*qtz*),

$$\kappa_{soil} = \kappa_{qtz}^{(qtz)} \kappa_o^{(1-qtz)} \tag{3.28}$$

where, κ_{qtz} and κ_o are the thermal conductivity of quartz and others soil particles, which are set to 7.7 and 2.0 [W m^{-1} K^{-1}], respectively. For standard Noah simulations, the sand fraction is taken equivalent to the volume fraction quartz, which is defined for each of the nine soil classes and given in Table 3-1.

4 Data sets

Three data sets have been used for the research presented in this Thesis.

One of the data sets for studying the retrieval of soil moisture consists of backscatter measured by a truck-mounted scatterometer. These measurements were collected during a field campaign covering the 2002 corn growth cycle and were performed by NASA's Goddard Space Flight Center (GSFC), George Washington University (GWU) and the United States Department of Agriculture Agricultural Research Service (USDA-ARS). This data set is hereafter referred to as the '*OPE^3 campaign*[*]'.

The data set used solely for Noah LSM applications has been collected at the meteorological station operated by the Royal Netherlands Meteorological Institute (KNMI) about two kilometres east of Cabauw; hereafter referred to as the '*Cabauw data set*'.

The third data set has been collected over the central part of the Tibetan Plateau, and is used for both soil moisture retrieval and land surface modelling. Synthetic Aperture Radar (SAR) acquisitions collected by the Advanced SAR (ASAR) onboard the European Space Agency's (ESA's) Environmental Satellite (EnviSat) is utilized for soil moisture retrieval. The validation of Noah LSM simulations is performed using the meteorological measurements by the Institute for Tibetan Plateau Research Chinese Academy of Science (ITP/CAS). This data set will be referred to as the *'Tibetan data set'.*

These three data sets are described in the text below.

[*] OPE^3 ~ optimizing production inputs for Economic and Environmental Enhancements.

4.1 OPE^3 campaign

Site description

OPE^3 is a multi-disciplinary research project of the United States Department of Agriculture - Agricultural Research Service (USDA-ARS) focusing on issues related to agriculture (Gish et al. 2003). The research carried out within this project takes place on a field on the grounds of the Beltsville Agriculture Research Center (BARC) near Beltsville (Maryland, USA); hereafter referred to as the *OPE^3 site*. The climate of this region can be characterized as humid with mild winters and hot (and humid) summers. Annual amount of rainfall is about 990 mm evenly distributed throughout the year. At this field, experiments have been conducted focusing on studying the transport of chemicals in the vadose zone, the exchange of water and energy between the land surface and atmosphere, and remote sensing techniques for retrieving biophysical variables. For more information

on the OPE^3 project readers are referred to http://hydrolab.arsusda.gov/ope3 (verified on: 16 September 2010).

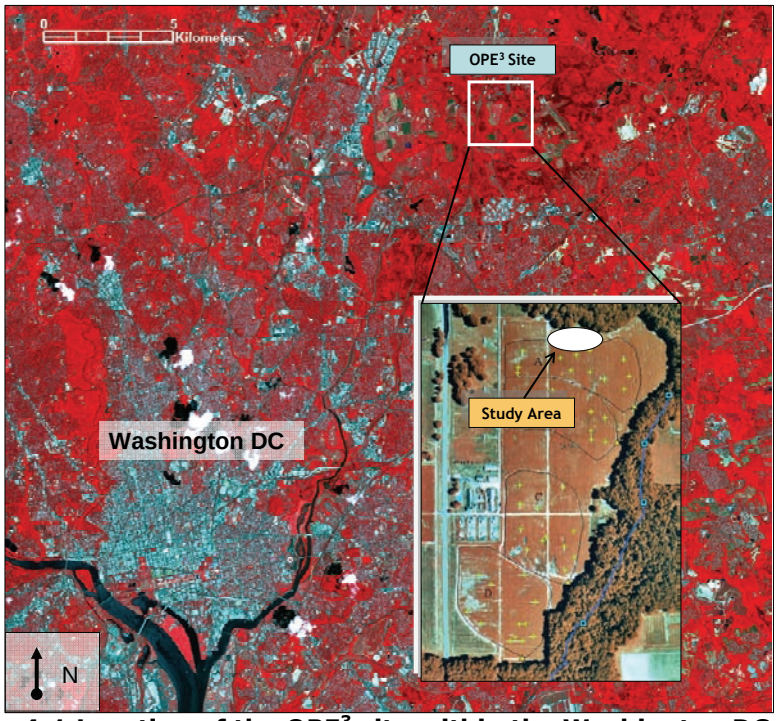

Figure 4-1 Location of the OPE^3 site within the Washington DC area with as background is an ASTER (Advanced Spaceborne Thermal Emission and Reflection Radiometer) false color composite collected June 2002.

The OPE^3 site comprises four adjacent watersheds located at an elevation of approximately 40 meters above sea level with slopes varying from 1 to 4%. During the summers all fields are grown with corn, which typically emerges in the beginning of May and is harvested in October. The 2002 field campaign took place at the northern edge of the test site (see Figure 4-1) as this area is the flattest part. In this area, soil texture is classified as sandy loam with on average 23.5% silt, 60.3% sand, 16.1% clay and a bulk density of 1.25 g cm^{-3}.

Scatterometer measurements

The σ^o measurements were collected by the NASA/George Washington University (GWU) truck-mounted scatterometer starting from the emergence of the corn plants on May 10th and ending at the harvest on October 2nd. This scatterometer system is capable of measuring both the amplitude and phase of backscattered signals at

X-, C- and L-band (10.0, 4.75 and 1.6 GHz) and at four linear polarizations (HH, HV, VV, VH). For each band, a single transmiting-receiving antenna with a 3 dB beam width of 12 degrees is mounted on a 20 m boom. The deployed system has provided reliably calibrated measurements across the United States since the early 1990s (i.e. O'Neill et al. 1996, Chauhan and Lang 1999, Laymon et al. 1999). More details on the system itself can be found in O'Neill and Chauhan (1992).

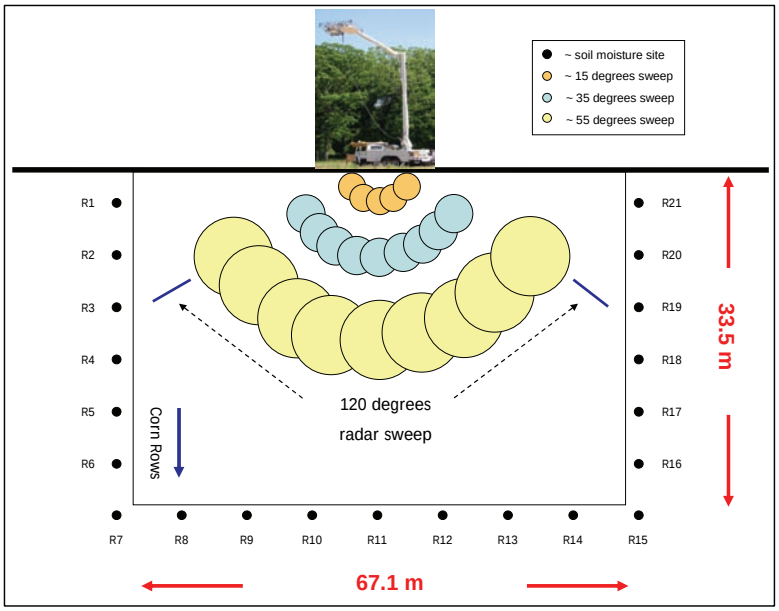

Figure 4-2 Schematization of the experimental setup during the 2002 OPE^3 field campaign.

During the 2002 field operations, quad-polarized C- and L-band σ^o measurements were collected from a boom height of 12.2 m whereby the truck was aligned perpendicular towards the corn row orientation. Data acquisitions took place once a week (rainy days excluded) resulting in a total of 21 days distributed over the corn growth cycle. On each acquisition day, σ^o data was acquired at four nominal times (8:00h, 10:00h and 12:00h and 14:00h) and at three incidence angles (15, 35 and 55 degrees). The footprints of a single sample are estimated to be 2.75, 3.83 and 7.98 m for incidence angles of 15, 35 and 55 degrees, respectively. Prior to data collection, the measurement of the C- and L-band amplitudes was calibrated against external targets whose cross sections are known such as a disk and a dihedral corner reflector at different angles. An absolute calibration of the C- and L-band σ^o measurements are obtained following the same procedure as described in Nesti and Hohmann (1990).

The system was programmed to scan the field 120 degrees in the azimuth direction and collect sixty independent samples for each data run. These independent calibrated samples are averaged to one σ^o value for the study site at each time, for each incidence angle and polarization, which is necessary to reduce the effects of Rayleigh signal fading caused by the interference of coherent scattering from individual objects (e.g. Hoekman 1991, Monakov et al. 1994). The effects of the periodic structures imposed by both tillage and corn rows are assumed to be smoothed out. The absolute calibration accuracy of the averaged σ^o values is estimated to be lower than 1.0 dB (O'Neill et al. 1996). Figure 4-2 presents a diagram of this experimental setup.

Ground measurements

Around the periphery of the radar footprints a detailed characterization of the land surface conditions took place, which included surface roughness, vegetation biomass, and soil moisture measurements. The vegetation biomass was quantified once on each radar acquisition day via a destructive sampling technique applied to a 1 m^2 area (about 12 corn plants). By oven drying the plants, the water content, fresh and dry biomasses were determined. In 2002, the corn was planted on April 17, the crops emerged around May 4, reached peak biomass at July 24 and were harvested on October 2. At peak biomass, vegetation water content (W) of 5.1 kg m^{-2} and a crop height of 2.2 meters were measured. After the planting the crops, no other tillage operations were undertaken until the harvest on October 2.

Table 4-1 Surface roughness parameters derived from the measured surface profiles.

	Along row		Across row	
	s **[cm]**	***l*** **[cm]**	***s*** **[cm]**	***l*** **[cm]**
Profile 1	1.11	5.18	2.35	8.95
Profile 2	0.81	6.35	2.46	12.20
Profile 3	0.95	6.39	1.95	10.75
Profile 4	0.75	3.22	1.91	8.16
Profile 5	0.74	4.52	1.68	6.84

Profiles of the surface height variations were characterized at the beginning of the campaign (May 2) via photos of the soil surface in front of a 2 m long gridded board (see Figure 4-3). A total of ten pictures were taken, of which five were collected with the board placed along the row direction and the other five with the board in the across row direction. These ten surface photos were digitized at an approximate horizontal interval of 0.5 cm. From the digitized surface height profiles the surface roughness parameters were

calculated using Eqs. 2.5 and 2.6, which are listed in Table 4-1. The spectral density of surface height variations was found to be best represented by an Exponential distribution function for the along row direction, while a Gaussian function was found more appropriate for the across row direction.

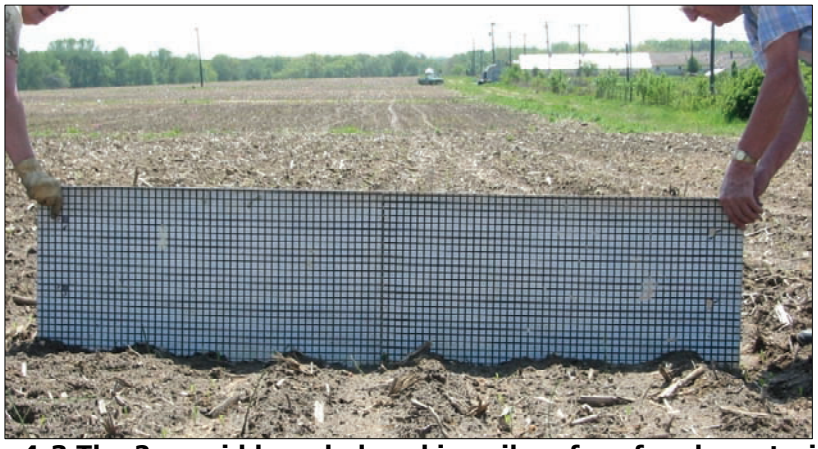

Figure 4-3 The 2 m grid board placed in soil surface for characterizing the surface roughness.

The top 6-cm soil moisture was measured using a gravimetric sampling technique and a portable impedance probe (Delta-T theta probe) at twenty-one sites located at the edge of a 67.0 x 33.5 m rectangular area situated around the radar footprints indicated in Figure 4-2. Two impedance probe readings were taken per site each time the radar collected observations, while the gravimetric sampling took place along with the first radar acquisitions of the day. From the gravimetric measurements the volumetric soil moisture (θ) is determined using the bulk density measured at each site. The voltages recorded by the impedance probe are converted to the dielectric constant (ε_r) according to the manufacturer's instructions (Miller and Gaskin, 1999), from which the θ can be determined using,

$$\theta = \frac{\sqrt{\varepsilon} - a_0}{a_1} \tag{4.1}$$

where, a_0 and a_1 are calibration parameters depending on the soil texture.

A generalized calibration provided by the manufacturer yields an estimated accuracy of 0.05 $m^3\ m^{-3}$. A more reliable impedance probe θ can be obtained when the a_0 and a_1 are fitted against a reference. Here, the pair of the gravimetric θ and the mean of the two simultaneously collected impedance probe readings have been used to fit for each site a specific a_0 and a_1. This led to a Root Mean

Squared Difference (RMSD) of 0.024 $m^3 m^{-3}$ between the gravimetric and the impedance probe θ. The site-specific calibration parameters have been applied to the mean of two impedance probe readings collected each time step.

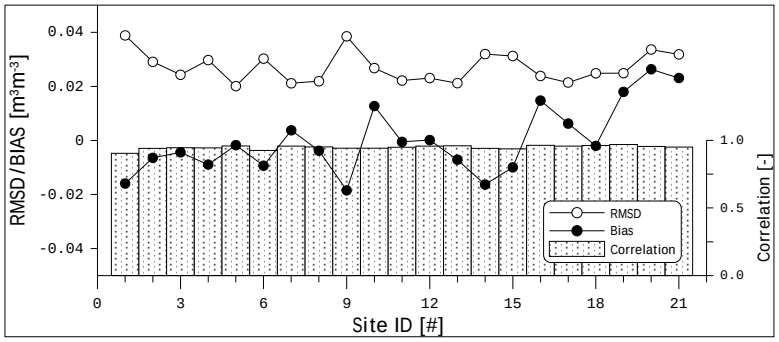

Figure 4-4 RMSD, bias and correlation coefficients calculated between the mean impedance probe θ of the twenty-one sites and the θ measured at each site separately.

As the θ is known to be spatially variable (e.g. Famiglietti et al. 1999, Cosh et al. 2004) also variations can be expected among the measurements taken at the different sites. For further analysis of this variability, the RMSD, bias and correlation coefficient (ρ) are calculated between the mean impedance probe θ of the twenty-one sites and the θ measured at a single site, which are plotted in Figure 4-4. The biases show that on average the θ at the western (sites R1-R6) and eastern (sites R16-R21) edges are respectively wetter and dryer than the mean, while the θ measured along the southern edge (sites R7-R15) may over- or underestimate the mean. The obtained biases (-0.018 – 0.026 m^3m^{-3}) as well as RMSD's (0.020 – 0.038 m^3m^{-3}) are, however, on the same order of magnitude as the calibration accuracy of the impedance probe. The mean θ is, therefore, considered to be representative for the radar footprints, which is also supported by the high ρ's (0.90-0.97). The mean θ of the twenty-one impedance probe θ values will be used for further analysis of the radar measurements.

Figure 4-5 show the temporal evolution of the mean θ, W and rain events measured throughout the campaign. During the campaign rain events are temporally well-distributed up to August 2nd resulting in a total of 187.9 mm rain. After that, a period of relative drought occurred during which the soil dried down to values of 0.016 $m^3 m^{-3}$ measured on August 21th. A 50.2 mm rain event on August 27th ended this drought leading to a θ of 0.262 $m^3 m^{-3}$ on August 30th, which was also the maximum θ measured during the campaign. Given reports of saturated θ (θ_s) of 0.41- 0.44 $m^3 m^{-3}$ for sandy loam

soils in the United States (Clapp and Hornberger 1978, Cosby et al. 1984, Carsel and Parrish 1988), the dynamic range observed during campaign covers about 60% of the maximum θ range. This in combination with the coverage of the complete corn growth forms a solid basis for the evaluation of soil moisture retrieval algorithms, which will be further discussed in Chapters 5 and 6.

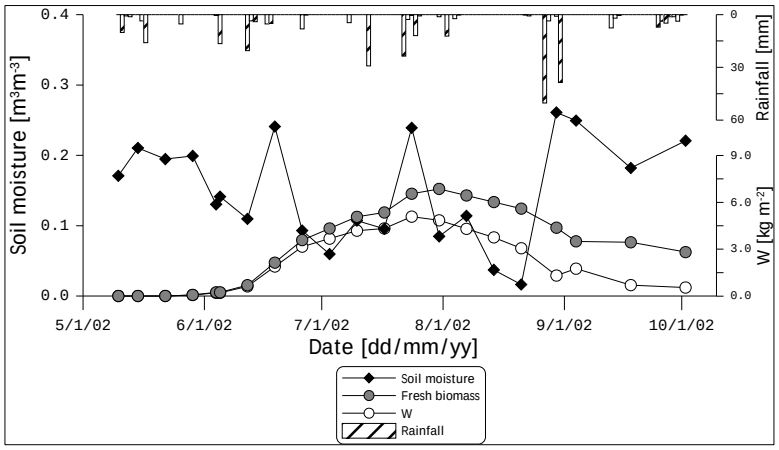

Figure 4-5 Rainfall, soil moisture, fresh biomass and vegetation water content (*W*) measured throughout the OPE^3 field campaign.

4.2 Cabauw data set

Site description

Since 1973, the Royal Netherlands Meteorological Institute (KNMI) operates a comprehensive atmosphere research program at a site about two kilometers east of Cabauw (The Netherlands). This meteorological site is well-known for its 213 m high mast (see Figure 4-6) and the resulting boundary layer research (e.g. Beljaars and Holtslag 1991, Ek and Holtslag 2004, Ek and Holtslag 2005). For an extensive site description readers are referred to Van Ulden and Wieringa (1996) and www.knmi.nl/~bosveld/ (verified on: 16 September 2010). Specific details relevant for this thesis are briefly described below.

The land cover in the Cabauw area is dominated by dense grasses fully covering the soil surface throughout the entire year, which may reach typical heights of 0.15-0.20 m during summers. At the measuring field, however, the grass is kept at a height of about 0.08 m. The local scale aerodynamic roughness length for momentum transport (z_{0m}) is estimated to be on the order 0.01 m, typical for short grasslands (Beljaars et al. 1983).

Figure 4-6 The Cabauw meteorological mast (photograph taken on December 2008).

A description of the soil properties is provided in Beljaars and Bosveld (1997) using field and laboratory analyses reported by Jager et al. (1976). The soil profile is characterized as follows; the top 0.03 m consists of a turf layer; fairly heavy clay is found up to a depth of 0.60 m; a transition zone from heavy clay to peat characterizes the 0.60 – 0.75 m layer and below 0.75 m only peat is found. Following the Dutch soil classification (Wösten et al. 2001), the upper 0.18 m corresponds to the fairly heavy clay class for top-soils (class: B11), the 0.18 – 0.75 m layer can be classified as the fairly heavy clay for sub-soils (class: O12) and the layer below 0.75 m complies with the peat class (class: O16). The soil textural properties of these classes are presented in Table 4-2.

In the Cabauw region, parallel ditches cut the grassland with typical distances of 20 to 40 m, in which the water table is kept constant at a winter (low) level and a summer (high) level. This results in groundwater tables at inland points in the middle of two ditches varying from -0.1 m during wet episodes in winters to -1.0 m during dry summers.

The Cabauw data set is used, here, to study the soil water flow under dry conditions simulated by Noah. For those simulations, the meteorological measurements collected from 1 January through 5 September 2003 are used to force the model. This period includes the 2003 European heat wave and consists of a range from wet to dry conditions. During the 2003 heat wave, the groundwater table

reached levels of -1.8 m in the period from 22 August to 2 September.

Table 4-2 Soil texture classes and their properties at Cabauw after the Dutch soil classification (Wösten et al. 2001).

Description	*Class*[*]	*Clay* [%]	*Silt* [%]	*Organic* [%]	*M50*[**] [µm]	*Density* [kg m^{-3}]
Fairly heavy clay	B11	35 – 50	-	3 – 15	-	0.9 – 1.7
Fairly heavy clay	O12	35 - 48	-	0 - 3	-	1.0 – 1.5
Peat	O16	-	-	40 – 96		0.1 – 0.7

[*] Soil type assigned in the Staring Series;
[**] M50 ~ median of the particle size of the sand faction.

Atmospheric forcings

Atmospheric forcings required for Noah simulations are rainfall, wind speed, specific humidity, surface pressure, air temperature, shortwave and longwave downward radiation. At Cabauw, all these forcing variables are measured at a 10 minute interval.

Precipitation, shortwave and longwave downward radiation are measured at a separate field 100 m south of the main mast. Wind speed, air and dew temperature observations are obtained by instrumentation installed at 10 m height on the mast. Further, surface pressure measurements are taken from an automated weather station situated 200 m south-west of the main mast. Specific details about the instrumentation are provided in Table 4-3.

Table 4-3 Instrumentation used for measuring the atmospheric forcings at the Cabauw meteorological station.

Variables	Instrument	Accuracy
Precipitation	KNMI rain gauge	0.2 mm
Shortwave downward radiation	Kipp&Zn CM11 pyranometer	Several W/m^2
Longwave downward radiation	Eppley pyrgeometers	Several W/m^2
Wind speed	KNMI cup-anemometer	0.5 m/s
Air temperature	KNMI Pt500-element	0.1^oC
Dewpoint temperature	Vaisala HMP243	0.1^oC
Surface pressure	Paroscientific 1016B-01	0.1 hPa

4.3 The Tibetan data set

Description of the study area

The Tibetan study area is a part of the Naqu basin and its location is depicted within the Landsat TM false color composite shown in Figure 4-7. Elevation in this region is 4500 m above mean sea level and the hilltops may reach heights just above 5000 m. Despite the

high overall altitude and significant relief in some parts, the terrain in the selected study area is fairly smooth with rolling hills. Characteristic for the study area are soils with a high saturated hydraulic conductivity (K_s = 1.2 m d^{-1}) positioned on top of an impermeable rock formation (or permafrost layer). Rain falling on the surface runs off rapidly and accumulates in local depressions forming lakes and the biotopes for wetland vegetation indicated by the bright red colors in Figure 4-7. The land cover in the higher parts of the study area can be characterized as grasslands consisting of prairie grasses and mosses represented by the gray colors in Figure 4-7.

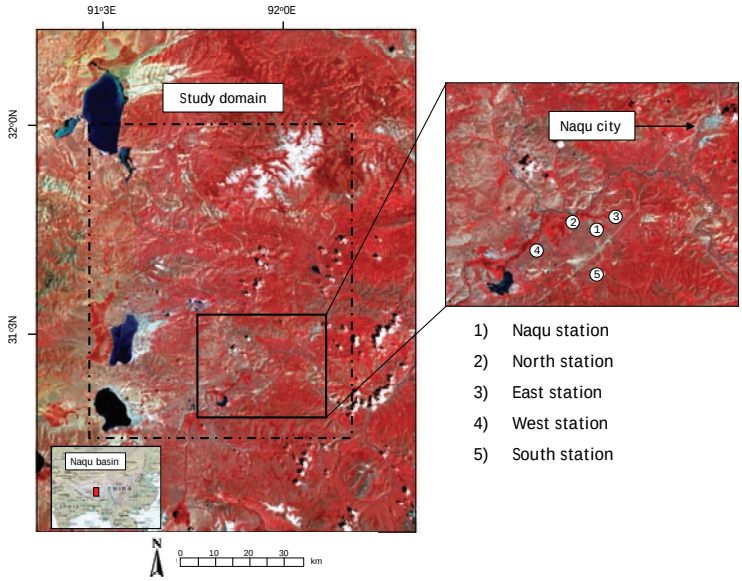

Figure 4-7 A Landsat TM false color image (from September 2004) indicating the study area and the location of soil moisture stations.

In the winter period from November to April, temperatures in this region are generally below freezing point and soil water is predominantly frozen. During this period, very little precipitation occurs either in liquid or frozen state as snow resulting in soil moisture dynamics that are both spatially and temporally stable. From April till October, the Asian Monsoon influences the weather, which reaches its peak intensity in the months June, July and August. In this three-month period, often more than 300 mm of a total annual amount of 400 mm rain is measured. The runoff produced by the thawing of frozen soil water in upstream areas accumulates in the wetlands and increases the soil moisture conditions towards saturation. During the monsoon, soil moisture conditions in the wetland areas remain relatively stable near saturation due to the water supply from upstream areas. In the grasslands, soil moisture

conditions depend on antecedent rainfall and may vary between saturated and residual soil moisture contents. As grasslands and wetlands coexist in the landscape within spatial scales of several kilometers, the differences in their soil moisture dynamics impose a large spatial variability across the study area.

Table 4-4 List of atmospheric variables measured at Naqu station that have been used for this thesis.

Variables	Instrument	Height	Measurement uncertainty
Air pressure	PTB220C, Vaisala	+ 1.5 m	±1hPa
Incoming and outgoing, longwave and shortwave radiation	CM21, Kipp & Zonen	+ 2.0 m	±0.5% at 20^0C
Wind speed	WS-D32, Komatsu	+ 1.0 m, +5.0 m, + 8.2 m	±0.8m/s *u*<10m/s ±5% *u*>10m/s
Humidity	HMP-45D, Vaisala	+ 1.0 m, + 8.2 m	±3%
Air temperature	TS-801(Pt100), Okazaki	+ 1.0 m, + 8.2 m	±3%
Soil heat flux	MF-81,EKO	-0.10 m	±5%
Soil temperature	Pt100, Vaisala	Surface, -0.05 m, -0.10 m, -0.20 m, -0.40 m	± 0.5 ^{0}C
Soil moisture	10 cm ECH2O probe, decagon devices	-0.05 m, -0.20 m	0.029 cm^3cm^{-3}

Ground measurements

Located about 20 km southwest of Naqu city is one of the key meteorological stations within a meso-scale network installed as a part of Global Energy and Water cycle Experiment (GEWEX) supported field campaigns; hereafter referred to as *Naqu station*. At Naqu station, a comprehensive set of instruments measures water and energy exchanges between the land surface and atmosphere (e.g. Ma et al. 2006, Van der Velde et al. 2009). This set consists of instrumentation capable of measuring atmospheric variables at different levels (e.g. wind speed, humidity and temperature), incoming and outgoing (shortwave and longwave) radiation, turbulent heat fluxes, soil moisture at depths of 0.05 and 0.20 m, and temperatures in the soil profile up to a depth of 0.40 m. All variables are recorded at a 10 minute interval and Table 4-4 lists the variables used for evaluating the performance of the Noah land model.

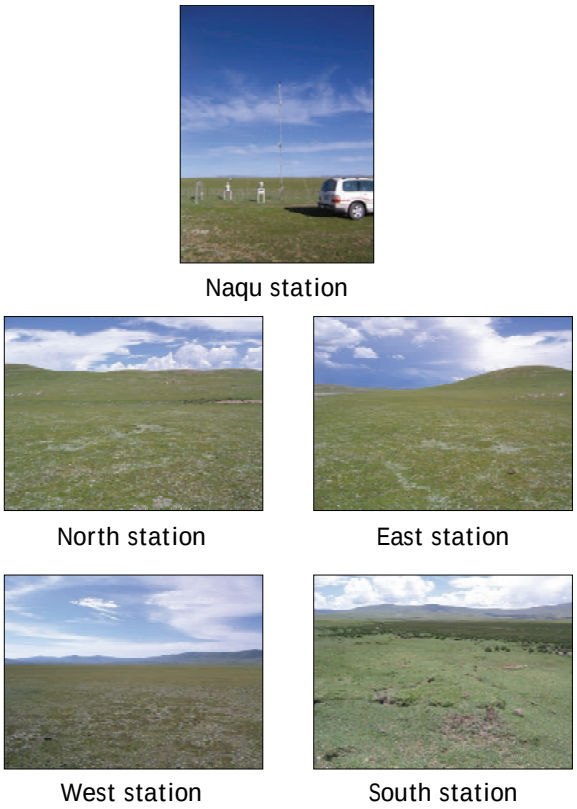

Figure 4-8 Photographs of the landscape within proximity of the soil moisture stations taken on 18 July 2006.

To further complement this surface energy and water budget characterization, four additional soil moisture stations were installed within 10 km from Naqu station during the 2006 summer (16 – 27 July, 2006). The soil moisture stations have been placed north, south, west and east of Naqu station as is shown in Figure 4-7. Besides additional soil moisture instrumentation was also installed at Naqu station itself. Grasslands dominate the land cover at the north, west, east and Naqu stations and south station is located at the edge of a wetland. An impression of the local conditions is given by the photographs presented in Figure 4-8.

The instrumentation used for these stations consists of EM5b data loggers and 10-cm long ECH_2O (type: EC-10) impedance probes both manufactured by Decagon Devices. At each station, probes have been installed horizontally at depths of 2.5, 7.5, 15.0, 30.0 and 60.0 cm. The EM5b loggers take a measurement every minute, which are averaged to values at preset intervals. Due to limitations in the loggers' storage capacity and accessibility of the study area, soil moisture values were recorded at noon and nighttime.

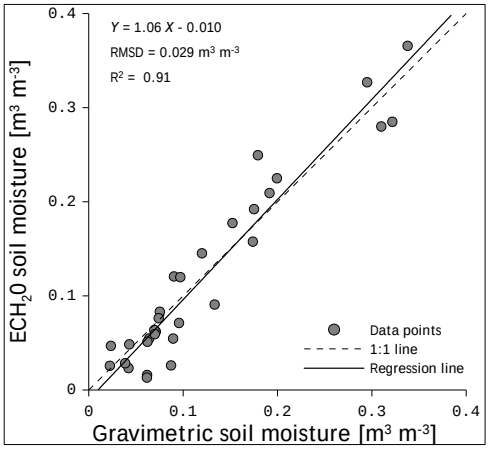

Figure 4-9 Comparison of soil moisture determined gravimetrically against in ECH_2O probe readings.

During the period 16-27 July 2006, however, the loggers were set to record readings every 30 minutes. On eight days within this episode, soil samples were taken near each station to determine the soil moisture content gravimetrically. This gravimetric soil moisture is plotted in Figure 4-9 against to the ECH_2O readings for the mineral soils. A well-defined linear relationship is noted between gravimetrically determined and impedance probe soil moisture resulting in a RMSD of 0.029 m^3 m^{-3}. This relationship has been utilized to calibrate ECH_2O readings at a 2.5 cm soil depth, which are used for the analyses of the ASAR measurements presented in Chapters 7 and 8.

Unfortunately, the measurements at the 2.5 cm were not recorded at west and south stations over the period July 2006 till September 2007. West station had been completely destroyed. Further, the logger at south station was severely affected by corrosion resulting in an unreliably fluctuating soil moisture values at 2.5 cm. The data from probe installed at a 7.5 cm soil depth was, however, reliably retrieved.

Calibrated soil moisture values from 2.5 cm probes at naqu, north and east stations and from the 7.5 cm probe of south station are plotted in Figure 4-10 for period 2005 through 2007. This figure shows that the soil moisture time series at the grassland locations has a clear relationship with the precipitation amounts. For example, an episode with lower rainfall amounts in 2006 coincides with a decrease in the soil moisture. Similar relationship between the soil moisture and precipitation can also be observed in 2005 and 2007. As expected, however, the soil moisture dynamics recorded at the wetland location is different, which is characterized by wet and relatively stable conditions during monsoon, and abrupt

increase/decrease of the liquid moisture content at the onset of spring/winter.

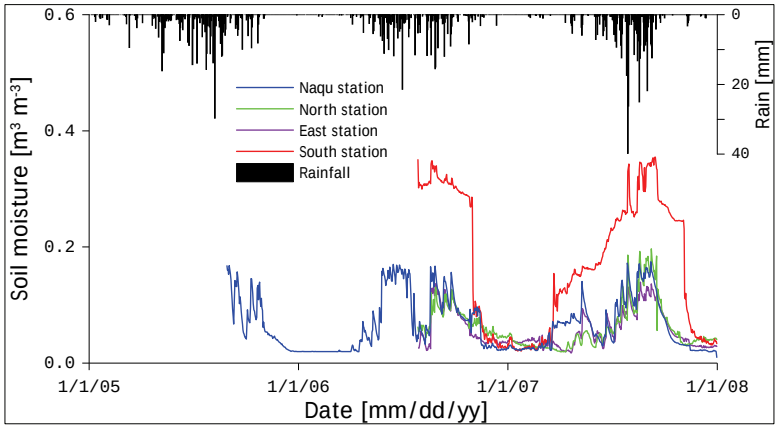

Figure 4-10 Soil moisture measured at a 2.5 cm soil depth at Naqu, east and north stations and at a 7.5 cm soil depth at south station over period 2005 through 2007 and rainfall amounts collected at Naqu station.

Calculation of heat fluxes

From the measurements collected at Naqu station the surface energy budget components can be derived.

Fourier's Law (Eq. 3.11) has been used to reconstruct the soil heat flux (G_0) from the temperature gradient between the soil surface (skin temperature) and the soil layer at 0.05 m depth (the first temperature measurement). Application of this approach requires formulation of the thermal heat conductivity, κ_h, which depends on the soil constituents, such as quartz and organic matter contents. Although generic formulations for the κ_h has been developed (e.g. Eqs. 3.24-3.28), Hillel (1998) points out that the κ_h depends also on the spatial arrangement of soil particles.

Given the rather specific conditions on the Tibetan Plateau, κ_h under the initial soil moisture conditions of a specific period is derived from the measured soil heat flux at a 0.10 m soil depth (G_{10}) and the soil temperature gradient. For the following time steps, the κ_h is extrapolated using the measured soil moisture and this initial κ_h following,

$$\kappa_h(\theta) = \kappa_h^i + (\theta_i - \theta)\kappa_{h_2o} \qquad (4.2)$$

where, sub- and superscript *i* refer to the initial conditions of the selected period.

The availability of the turbulent heat fluxes measured by the eddy correlation (EC) instrumentation at Naqu station is unfortunately limited. The sensible (H) and latent heat (λE) fluxes have, therefore, been computed using the Bowen Ratio Energy Balance (BREB)–

method (i.e. Perez et al 1999, Pauwels and Samson 2006), whereby the Bowen Ratio (β) is defined as,

$$\beta = \frac{H}{\lambda E} = \gamma \frac{T_{air1} - T_{air2}}{e_{air1} - e_{air2}} \quad (4.3)$$

where, e is vapor pressure [kPa], subscripts *air*1 and *air*2 indicate the first and second atmospheric level, respectively, and γ_p is psychrometric constant [kPa K^{-1}] defined as,

$$\gamma_p = \frac{c_p P_a}{0.622 \cdot \lambda_v} \quad (4.4)$$

where, P_a is the air pressure [kPa] and λ_v is the latent heat of vaporization [= $2.5 \cdot 10^6$ J kg^{-1}].

Once the β has been determined from the air temperature and vapor pressure profiles measurements, the λE and H can be calculated using,

$$\lambda E = \frac{R_n - G_0}{1 + \beta} \quad (4.5)$$

$$H = \frac{\beta}{1 + \beta}\left(R_n - G_0\right) \quad (4.6)$$

The β has been computed using the air temperature and vapor pressure measurements at levels of 1.0 m and 8.2 m. As BREB-method has a limited validity when β approaches -1.0, latent and sensible heat fluxes derived from β values between -1.3 and -0.7 have been omitted from the data analysis (e.g. Perez et al. 1999, Pauwels et al. 2008).

ASAR observations

The Advanced SAR (ASAR) onboard the ENVISAT is able to collect C-band (5.331 GHz) σ^o measurements in different imaging modes. Depending on the selected mode, either single polarized (HH or VV) can be obtained at resolutions of 1000, 150 and 25 m or dual polarized (HH/HV, VV/VH or HH/VV) observations can be acquired at a 25 m resolution. In the Wide Swath (WS) mode, single polarized σ^o's are measured at a 150 m spatial resolution over a swath width of 400 km covering a 16-43 degrees view angle range. The analyzed ASAR WS images have been requested in the VV polarization and delivered as ellipsoid geocoded level 1b products with a grid spacing of 75 m. The Tibetan data set includes 150 scenes acquired from April 2005 through September 2007, of which 101 and 49 scenes have been obtained in an ascending and a descending orbit, respectively. In the ascending and descending orbits, ASAR acquires measurements at 22:00 p.m. and 10:00 a.m. Beijing Standard Time (BST), respectively.

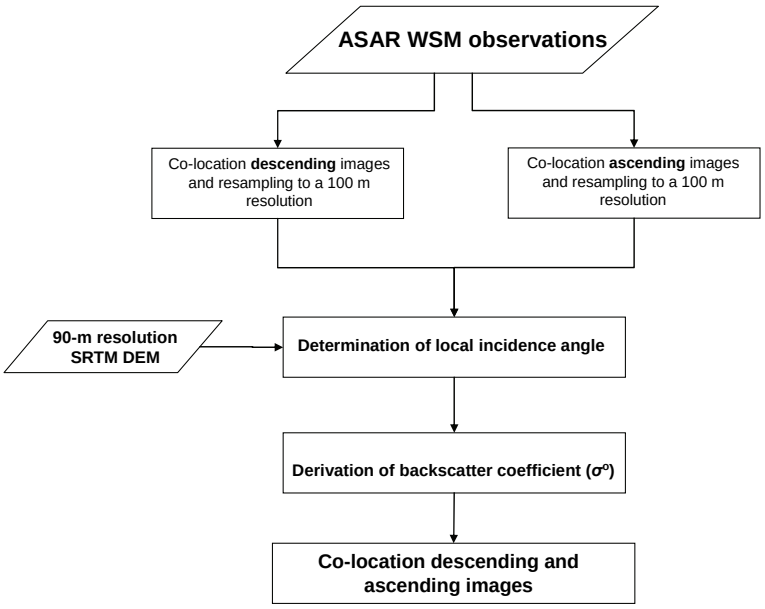

Figure 4-11 Schematization of the processing steps for deriving radiometrically terrain corrected σ^o observations from the ASAR WS images.

Prior to derivation of the σ^o observations, the ascending and descending scenes have been geo-registered separately and resampled to a 100 m spatial resolution using a nearest neighbour algorithm. Based on the 90 m resolution Digital Elevation Model (DEM) from Shuttle Radar Topography Mission (SRTM), the terrain elevation angle has been computed for the ascending and descending view geometries. Radiometrically terrain corrected σ^o observations have, then, been derived following ASAR product handbook (available at: http://envisat.esa.int/handbooks/asar) by using the local incidence angle. A schematization of these processing steps is presented in Figure 4-11 and Figure 4-12 shows subsets of several processed ASAR WS images.

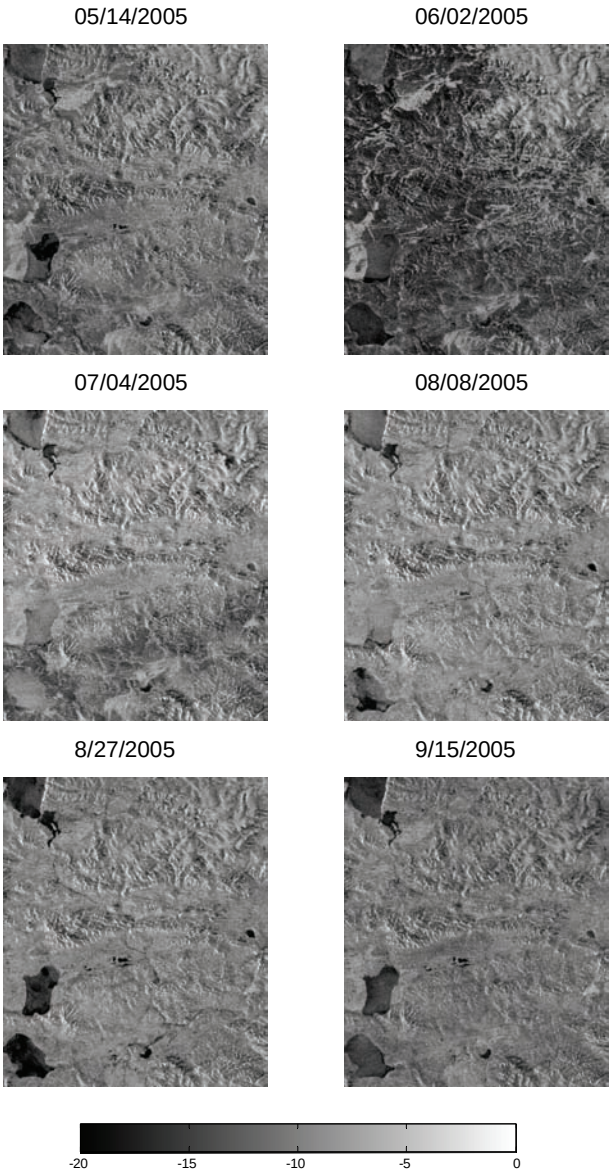

Figure 4-12 A selection of processed ASAR WS image subsets acquired over the study area in the period between May and September 2005.

The requested WS products have been processed to multi-look images with an equivalent number looks (ENL) of 12 (Zink et al. 2002). Based on comprehensive internal and external calibration

loops, the absolute calibration accuracy is estimated to be less than 1.72 dB with a temporal stability of less than 0.42 dB (Buck et al. 2000). Because of the multi-look processing chain no additional speckle filter has been applied to the processed WS products.

5 Effects of a corn canopy on C- and L-band backscatter

This chapter is based on:

Joseph, A.T., van der Velde, R., O'Neill, P.E., Lang, R.H., Gish, T., 2008, "Soil moisture retrieval during a corn growth cycle using L-band (1.6 GHz) radar observations", *IEEE Transactions on Geoscience and Remote Sensing*, **46**, pp. 2365-2374.

Joseph, A.T., van der Velde, R., O'Neill, P.E., Lang, R.H., Gish, T., 2010, "Effects of a corn canopy on C- and L-band radar backscatter: a correction method for soil moisture retrieval", *Remote Sensing of Environment*, **114**, pp. 2417-2430.

5.1 Introduction

The semi-empirical Cloud (Attema and Ulaby 1978, Ulaby et al. 1984, Prevot et al. 1993, Taconet et al. 1994, Bindlish et al. 2001) and empirical change detection approaches (Moran et al. 2002, Oldak et al. 2003, Njoku et al. 2002, Narayan et al. 2006) are often used within active microwave soil moisture retrieval applications. With the application of empirical change detection approaches, scattering induced by vegetation is assumed to be time-invariant, which restricts its application to observations acquired over time intervals with limited vegetation growth. The Cloud model assumes that a canopy can be represented by a Cloud of water droplets and higher order scattering contributions are negligible. Changes in biomass are taken into account by changing the density of the water droplets. The vegetation effects on the observed backscatter coefficient (σ^o) are described via two mechanisms: 1) attenuation of the soil surface scattering component and 2) scattering of elements (e.g. leaves, stalks and branches) within the vegetation layer. Implementations of the Cloud approach parameterize both mechanisms as a function of (an) empirical parameter(s) and (a) 'bulk' vegetation variable(s), such as the Leaf Area Index (LAI, e.g. Prevot et al. 1993), and/or vegetation water content (W, e.g. Ulaby et al. 1984 and De Roo et al. 2001).

A consequence of this modeling concept is that in the limit of dense vegetation the modeled σ^o is only a function of the vegetation scattering component and the contribution of soil surface scattering becomes negligible. The soil moisture sensitivity of the Cloud approach becomes under dense vegetation very small. In reality, however, radar observations display a much higher soil moisture sensitivity over dense vegetation because of microwave scattering along the soil-vegetation pathways (e.g. Chiu and Sarabandi 2000,

Stiles et al 2000, Cookmartin et al. 2000 and Macelloni et al. 2001). These higher order scattering terms are not included in the Cloud approach. De Roo et al. (2001) extended the Cloud concept by including first and second order scattering components, but found for soybeans that the contribution of these modeled scattering components to the total modeled σ^o is negligible.

In this chapter, the effects of corn on C- and L- band radar measurements are analyzed for the growth cycle monitored during the OPE^3 field campaign, which has been described in Section 4.1. An alterative method is presented to correct radar measurements for the effects of a corn canopy, which is subsequently applied for the retrieval of soil moisture. The resulting retrievals are compared to soil moisture retrieved with the Cloud approach and validated against *in-situ* measurements. Further, the potential application of this method to larger scales is discussed.

5.2 Surface scattering

Before the vegetation effects on the radar measurements can be analyzed the surface scattering component must be known. For this purpose, the AIEM scattering model described in Chen et al. (2003) is employed. Similar to its original version, the AIEM simulates the σ^o from bare soil surfaces based on the input of soil dielectric properties and surface roughness parameters. Here, the surface roughness parameters, *s* and *l*, are inverted from the four radar measurements acquired on May 10th, while assuming an 'exponential' correlation length function. On this day, the land surface was almost a bare soil with a vegetation water content (*W*) of 0.006 kg m^{-2} and the soil moisture was on average 0.18 m^3 m^{-3}. Using the soil texture and soil moisture measured during the four radar acquisitions, the complex dielectric constant is calculated with the Dobson et al. (1985) mixing model.

As shown in Figure 4-2, the footprints of the three incidence angles are different and, thus, the surface roughness in these footprints can be expected to be different. Moreover, the impact of the periodic structure of the tillage rows on σ^o measurements may be different for HH and VV polarization (e.g. Beaudion et al. 1990, Zribi et al. 2002). Champion and Faivre (1996) conclude, however, that backscattering from eroded rows as shown in Figure 4-3 behaves similarly as isotropic surfaces. An *effective* roughness parameterization may, therefore, be used to estimate the surface scattering component, which has been done for many previous applications (i.e. Zribi and Dechambre 2002, Baghdadi et al. 2004, Zribi et al. 2006). For these reasons, different roughness parameterizations are derived for each of the three incidence angles and two polarizations. The resulting *s* and *l* parameters are given in

Table 5-1 along with the RMSD computed between the AIEM simulated and measured σ^o.

Table 5-1 Surface roughness parameters inverted from backscatter measured over bare soil conditions and assuming an Exponential ACF.

Band	Pol.	*Angle* [degrees]	*s* [cm]	*l* [cm]	*RMSD* [dB]
C-band	HH	15	0.65	9.54	0.93
		35	0.73	9.79	0.83
		55	0.82	11.05	1.04
	VV	15	0.42	10.96	0.08
		35	0.45	10.65	0.75
		55	0.35	10.18	0.95
L-band	HH	15	0.42	9.85	0.84
		35	0.61	9.60	0.47
		55	0.46	10.05	0.39
	VV	15	0.46	9.92	0.87
		35	0.68	12.84	0.51
		55	0.38	10.16	0.09

The obtained RMSD's are on the same order of magnitude as the radar measurement uncertainty. Compared to roughness measurements in Table 4-1, however, the retrieved roughness values are somewhat small. As is indicated above, the surface roughness is treated in this case as an effective parameterization and, also, its influence on the radar measurements is affected by the view angle and the wavelength (Ulaby et al. 1986). It is, therefore, difficult to interpret the validity of the retrieved roughness based on the values derived from measurements.

In this chapter, the surface roughness parameters inverted from the σ^o measured at the start of the campaign are used to evaluate the surface scattering component and retrieve soil moisture for the entire campaign. This implicates that the surface roughness is assumed to be temporally stable; an assumption frequently adopted for soil moisture retrieval applications (i.e. Verhoest et al. 1998, Narayan et al. 2006, Moran et al. 2002, Thoma et al. 2006, Alvarez-Mozos et al. 2006). However, it is well understood that due to environmental conditions (e.g. rainfall and wind) and agricultural practices the surface roughness may change.

Zobeck and Onstad (1987) and Jackson et al. (1997) conclude that rainfall has a considerable impact on the surface roughness, while the surface roughness measurements reported in Callens et al. (2006) show that the change in surface roughness due to rainfall is only significant when the field has recently (within a few days) been tilled. During the OPE^3 campaign, the field was not tilled after the corn crops were planted on April 17th, which was almost four weeks before the first radar observation on May 10th. In the period from

April 17th to May 10th, 87 mm of rain was measured at the OPE3 site, which smoothed the ploughed soil surface. Thus, based on the conclusions drawn by Callens et al. (2006), the use of a time-invariant roughness parameterization can be justified. Impact of this assumption on the soil moisture retrievals will be further discussed in Chapter 6.

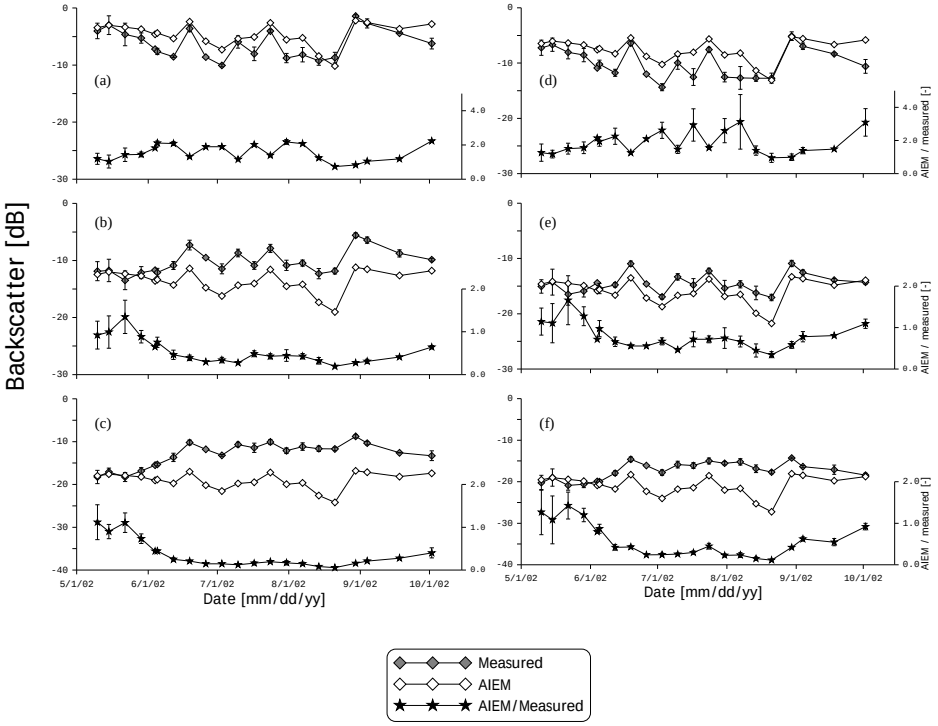

Figure 5-1 Daily averaged C-band σ^o measurements and AIEM forward simulations over the corn growth cycle. Subplots a), b), c) show the result for the HH polarization and incidence angle of 15, 35 and 55 degrees, respectively. Subplots d), e), f) show the results for the VV polarization and the same incidence angles.

5.3 σ^o measurements vs. AIEM simulations

The AIEM surface scattering model has been used to simulate the bare soil σ^o for the complete field campaign with input of the roughness parameters in Table 5-1 and the measured soil moisture. These simulated AIEM σ^o values are averaged for each radar acquisition day and are plotted against time along with the daily averaged σ^o measurements. Figures 5-1 and 5-2 show the results for C- and L-band, respectively. Further, the ratio of the AIEM simulated and measured σ^o is presented in each plot to indicate how differences between the simulations and measurements, and the effects of vegetation evolve over time.

The two figures show that the AIEM σ^o matches the measurements at the beginning of the campaign. This is expected because the land surface is virtually a bare soil surface. For the 35 and 55 degrees incidence angles, the AIEM σ^o remains in close agreement with the measured C- and L-band σ^o up to June 5th (W = 0.2 kg m^{-2}). The C- and L-band σ^o measured at a later date and larger biomass is, however, systematically larger than the AIEM σ^o. The measured σ^o increase can be ascribed to an increased amount of scattering from the canopy directly and from the soil-vegetation pathways, while the overlaying vegetation cover attenuates the surface scattering component (e.g. Chauhan et al. 1994, Stiles and Sarabandi 2000, Macelloni et al. 2001). This indicates that, at incidence angles of 35 and 55 degrees, the C- and L-band scattering induced by the corn canopy (with W > 0.2 kg m^{-2}) is dominant over the attenuated soil return.

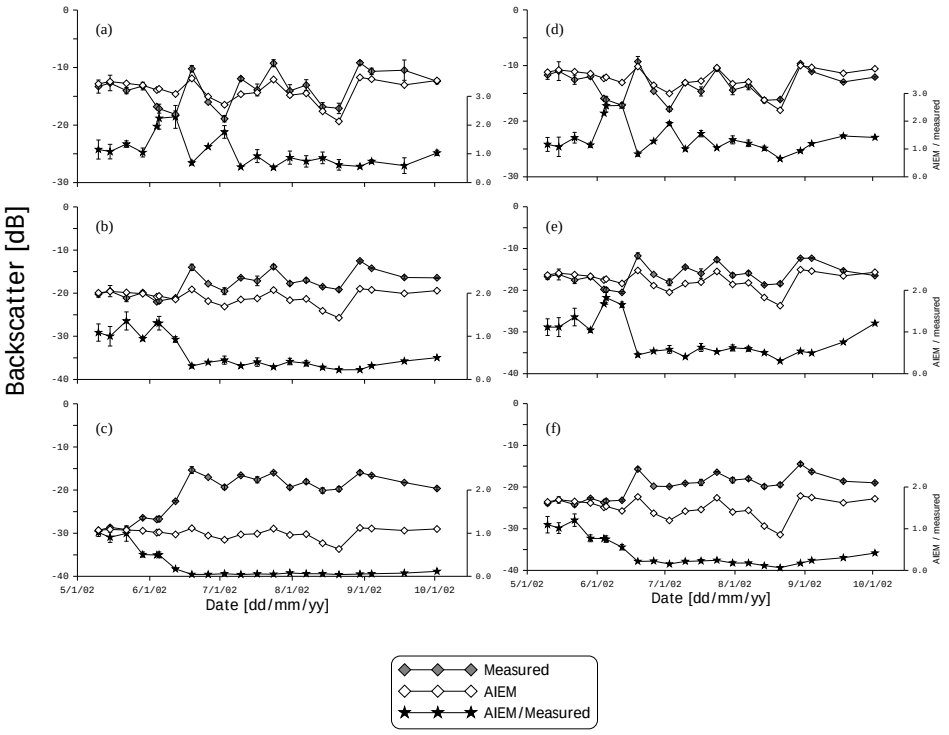

Figure 5-2 Same as Figure 5-1 except that the results for L-band are shown.

At both C- and L-band, the largest differences between the measured and AIEM σ^o are obtained for the HH polarization and the 55 degrees incidence angle, while the smallest differences are noted for the VV polarization and 35 degrees incidence. These differences

appear overall to be smaller for C- than for L-band. A full analysis of the individual scattering contributions by means of a physically based scattering model reaches beyond the scope here. It is, however, commonly understood that the attenuation of the soil return by vegetation is larger for VV polarization and at smaller wavelengths (e.g. Mattia et al. 2003a, Brown et al. 2003). This explains the smaller σ^o differences between the measurements and simulations when comparing VV versus HH polarization, and C- versus L-band. In addition, Stiles et al. (2000) have reported on a larger amount of direct vegetation scattering simulated by a physically based vegetation scattering model at larger incidence angles. This supports the larger differences noted between the measured and AIEM σ^o at 55 degrees than at 35 degrees, which can also be explained by the larger vegetation volume observed from larger incidence angles.

Despite the attenuation of the soil return and scattering by vegetation, the measured σ^o response to soil moisture is notable even when the canopy is at peak biomass (compare Figure 4-5 with Figures 5-1 and 5-2). Previous investigations (e.g. Lang and Sidhu 1983, Chauhan et al. 1994, Macelloni et al. 2001) have shown that under densely vegetated conditions the scattering along soil-vegetation pathway may become significant. This higher order scattering term includes also soil (moisture) information (e.g. Stiles et al. 2000, Chiu and Sarabandi 2000) and explains the observed σ^o sensitivity to soil moisture. As a result, the ratio of the AIEM σ^o over measured σ^o has a slight increasing trend for W values larger than 3.0 kg m^{-2}.

At the 15 degrees incidence angle, the temporal evolution of σ^o measurements with respect to the AIEM simulations follows a different pattern. The C-band σ^o measurements drop below the AIEM simulations just after the corn plants have emerged and remain lower for almost the entire duration of the campaign. These deviations between the measured and AIEM σ^o are larger for the VV than for the HH polarization. Mattia et al. (2003a) and Brown et al. (2003) made similar observations over wheat canopies. They concluded that the measured σ^o mainly consists of an attenuated soil return. This is supported by a model investigation of Cookmartin et al. (2000). Their simulations showed that a canopy may attenuate the soil scattering component, while the contribution of the direct vegetation scattering component is small. It can, thus, be concluded based on these previous reports that the C-band σ^o measured at a 15 degrees incidence over corn is dominated by an attenuated soil return and the VV attenuation by vegetation is larger than for the HH polarization.

The L-band σ^o at a 15 degrees incidence behaves similarly, but to a lesser extent. The AIEM σ^o is only significantly larger than the measured σ^o on June 5th and 12th (W = 0.2 and 0.6 kg m^{-2},

respectively). This is explained by the fact that the longer L-band microwaves are less attenuated by vegetation.

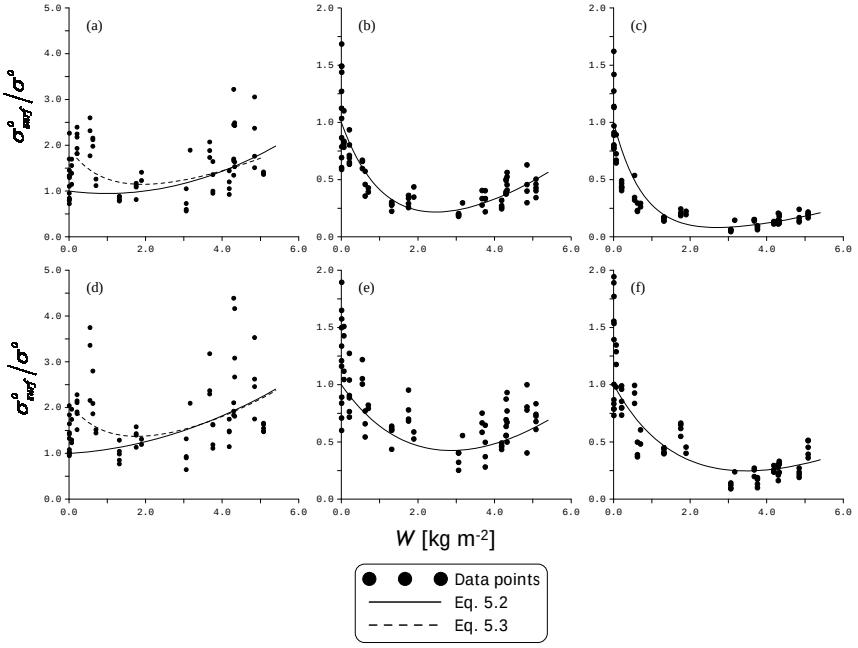

Figure 5-3 The σ^o_{surf}/σ^o for C-band plotted against the vegetation water content (W). a), b), c) show the result for the HH polarization at incidence angles of 15, 35 and 55 degrees, respectively. d), e), f) show the results for the VV polarization at the same incidence angles.

5.4 Vegetation correction

The previous discussion has shown that throughout the corn growth cycle both an attenuated soil return and vegetation scattering can dominate the measured σ^o. The latter scattering mechanism is more important at 35 and 55 degrees incidence angles and vegetated conditions (W > 0.2 kg m^{-2}), while attenuation is more pronounced in C-band VV σ^o measured at a 15 degrees incidence angle and over sparse vegetation (W < 0.2 kg m^{-2}). Somewhat surprising is, however, that even at peak biomass (W > 3.0 kg m^{-2}) the σ^o measured in each antenna configuration displays some sensitivity to soil moisture. This σ^o response to soil moisture under densely vegetated conditions can be ascribed to scattering along the soil-vegetation pathway. Ideally, a soil moisture retrieval algorithm takes these higher order scattering mechanisms into account. Physically based vegetation scattering models (e.g. Lang and Sidhu 1983, Karam et al. 1992, Ferrazzoli and Guerriero 1996) are able to simulate the soil-vegetation scattering contributions. This type of

modeling requires, however, a rigorous description of the vegetation morphology, which is typically not available at regional (or larger) scales.

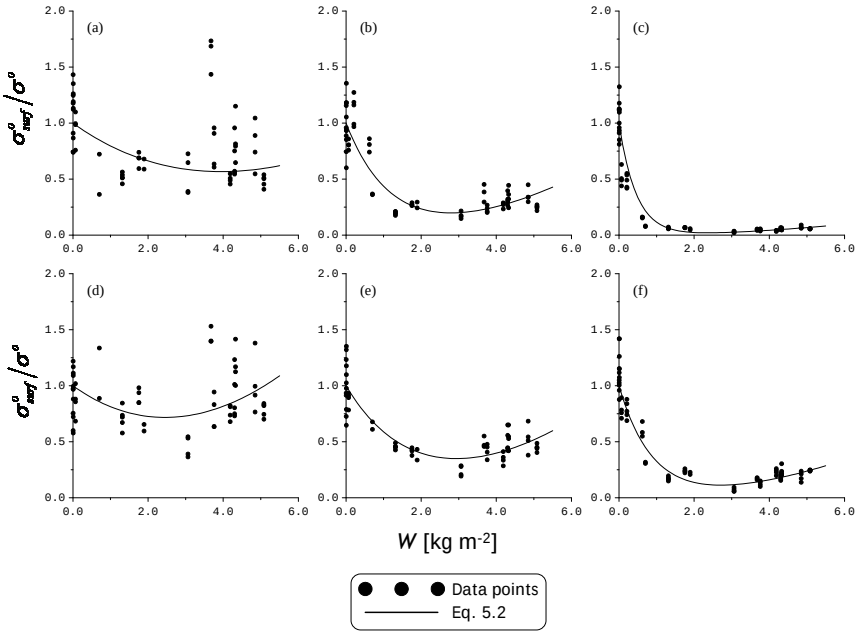

Figure 5-4 Same as Figure 5-3 except that the results for L-band are shown.

Therefore, soil moisture retrieval over vegetation covered surfaces is often based on the semi-empirical Cloud model (e.g. Attema and Ulaby 1978, Bindlish and Barros 2001, Alvarez-Mozos et al. 2006), which assumes a negligible scattering contribution from the soil-vegetation pathways as shown in,

$$\sigma^o = \gamma^2 \sigma_s^o + \sigma_v^o \tag{5.1}$$

where, σ^o_s is the soil surface scattering, σ^o_v is the vegetation scattering contribution and γ^2 is the two-way attenuation.

As described in Section 2.2, the Cloud model represents the canopy as a slab of identical uniformly distributed scatterers and approximates the σ^o_v and γ^2 as (e.g. Ulaby et al. 1982),

$$\sigma_v^o = \left(1-\gamma^2\right) A \cdot V_1 \cos\theta_i \tag{2.16}$$

with

$$\gamma^2 = \exp\left[-\frac{B \cdot V_2}{\cos\theta_i}\right] \tag{2.17}$$

where, A and B are crop dependent parameters specific for each antenna configuration, and V_1 and V_2 are so-called "vegetation descriptors".

Based on the observations in the previous section, an alternative method is proposed for correcting σ^o for the effects of vegetation. This method is based on the concept that for a specific antenna configuration the ratio of the soil surface scattering over the measured σ^o (σ^o_{surf}/σ^o) is primarily influenced by vegetation biomass; hereafter referred to as the *ratio method*. Relationships between the ratio and biomass are described, here, as a function of the *W*. Figures 5-3 and 5-4 present these relationships for C- and L-band, whereby the σ^o_{surf} is represented by AIEM simulations with the measured soil moisture and surface roughness parameters of Table 5-1 as input.

Then, the following equation is used to describe the σ^o_{surf}/σ^o in terms of the *W*,

$$\frac{\sigma^o_{surf}}{\sigma^o} = \left[a\, W^2 + \exp(-b\, W) \right] \quad (5.2)$$

where, *a* and *b* are crop dependent parameters specific for each antenna configuration [$m^2\ kg^{-1}$].

The first term on the right-hand side of Eq. 5.2 assures an σ^o_{surf}/σ^o increase under densely vegetated conditions. As such, this term can account for the increasing trend of σ^o_{surf}/σ^o at *W* values larger than 3.0 kg m^{-2} observed in Figures 5-1 and 5-2. The second term accounts for the σ^o_{surf}/σ^o decrease from sparse vegetation to densely vegetated conditions when vegetation scattering is the dominant mechanism.

At C-band, however, the σ^o measured at 15 degrees is dominated by an attenuated soil return. As a result, the ratio is systematically larger than 1.0. At low *W* values, this cannot be reproduced by Eq. 5.2, which is, therefore, modified for the 15 degrees incidence angle as follows,

$$\frac{\sigma^o_{surf}}{\sigma^o} = \left[a\, W^2 + \exp(-b\, W) + c \right] \quad (5.3)$$

where, *c* is crop dependent parameter specific for each antenna configuration.

Eq. 5.2 has been fitted through the data points of Figures 5-3 and 5-4 obtained for 35 and 55 degrees using a least squares optimization algorithm for minimizing the RMSD between the simulated and measured σ^o. Similarly, both Eqs. 5.2 and 5.3 have been applied to the C-band 15 degrees σ^o_{surf}/σ^o. The resulting fits are shown in Figures 5-3 and 5-4, and Table 5-2 presents the parameters as well as the RMSD's between the simulated and measured σ^o. The RMSD's in Table 5-2 are smaller than 1.71 dB. Given an estimated absolute calibration accuracy of < 1.0 dB, the ratio method provides reasonable estimates of the measured σ^o. The obtained differences between the simulated and measured σ^o follow from the scatter noted among the points in Figures 5-3 and 5-4. This scatter can be attributed to the different sources of uncertainty inherent to the

σ^o_{surf}/σ^o estimation. For example, the surface roughness is assumed to be constant; the measured soil moisture and *W* are assumed to be representative for the footprint; and the radar measurements include calibration uncertainties. In an absolute sense, the impact of these uncertainties on σ^o_{surf}/σ^o will be higher when its value is larger. Therefore, the largest scatter in Figures 5-3 and 5-4 is noted for 15 degrees because at this angle the σ^o_{surf} is largest as compared to the measured σ^o.

Table 5-2 Vegetation parameters for σ^o simulation and soil moisture retrievals with the ratio method obtained through calibration, and RMSD's computed between the simulated and measured σ^o. In parenthesis are the vegetation parameters, RMSD's obtained by the ratio method using Eq. 5.2.

Band	Pol.	*Angle* [degrees]	*a* [m^4 kg^{-2}]	*b* [m^2 kg^{-1}]	*c* [-]	*RMSD* [dB]
C-band	HH	15	0.047 (0.049)	0.446 (0.106)	0.503	1.59 (1.91)
		35	0.0191	0.9309	-	1.18
		55	0.0072	1.3012	-	1.53
	VV	15	0.057 (0.038)	0.329 (0.049)	0.610	1.71 (2.09)
		35	0.0225	0.3770	-	1.36
		55	0.0105	0.6096	-	1.62
L-band	HH	15	0.0115	0.1332	-	1.57
		35	0.0173	0.8980	-	1.20
		55	0.0033	2.2624	-	1.77
	VV	15	0.0028	-0.0318	-	1.26
		35	0.0211	0.4812	-	0.96
		55	0.0096	1.2902	-	1.27

Although the σ^o calculations using the ratio method are reasonable, a true appreciation of its performance is difficult solely based on Table 5-2. A comparison is, therefore, made against σ^o simulations by the Cloud model. Here, the Cloud model is applied using AIEM simulations for describing the σ^o_{surf} and the *W* for representing V_1 and V_2. Then, its vegetation parameters, *A* and *B*, are estimated using a least squares optimization algorithm. The parameter values and RMSD's are presented in Table 5-3. Further, Figures 5-5 and 5-6 show respectively C- and L-band the daily averaged σ^o measurements and σ^o simulated by the Cloud model and the ratio method against time. At 15 degrees, it is noted that the σ^o computed by the ratio method and the Cloud model are comparable to each other. Only at the start of the growth cycle the ratio σ^o computed using Eq. 5.3 matches the measured σ^o better lowering the RMSD by about 0.28 dB on average.

Table 5-3 Calibrated vegetation parameters of the semi-empirical Cloud model and the resulting RMSD's.

Band	Pol.	*Angle* [degrees]	*A* [cm]	*B* [cm]	*RMSD* [dB]
C-band	HH	15	0.019	0.068	1.52
		35	15.965	0.000	2.35
		55	5.569	0.000	3.06
	VV	15	0.006	0.098	1.69
		35	3.048	0.000	1.47
		55	2.961	0.000	1.66
L-band	HH	15	0.796	0.000	1.69
		35	3.418	0.000	2.35
		55	0.011	1.668	2.99
	VV	15	0.007	0.048	1.21
		35	0.576	0.001	1.42
		55	0.519	0.001	2.66

Clear differences between the ratio method and Cloud model are, however, observed at incidence angles of 35 and 55 degrees. Most notable are the differences at the early growth stage and at senescence (W < 1.0 kg m^{-2}). At those biomass levels, vegetation scattering becomes increasingly dominant resulting in a sharp σ^o increase with the W. Such increment in the measured σ^o cannot be reproduced by the Cloud model without compromising the σ^o simulation for other parts of the growth cycle; because a strong σ^o increase can only be obtained by the Cloud model as a result of vegetation growth when also the γ^2 decreases. The difference between the measured and Cloud σ^o is largest for the HH polarization. This is explained by a larger measured σ^o increase because the stronger VV attenuation compensates for a part of the increase in vegetation scattering. At the HH polarization, RMSD's calculated for the Cloud simulations are, therefore, twice as large as computed for the ratio method; on average 2.7 versus 1.3 dB, respectively.

Further, interesting from a soil moisture retrieval perspective is that the ratio method is able to reproduce the σ^o variations correlated to soil moisture changes also at peak biomass. The σ^o computed by the ratio method is, thus, somewhat sensitive to soil moisture, which allows its retrieval. The Cloud σ^o is, however, dominated by the vegetation scattering term at peak biomass, and is, thus, primarily determined by the W and insensitive to soil moisture. This difference between the two methods is stronger at 55 than at 35 degrees.

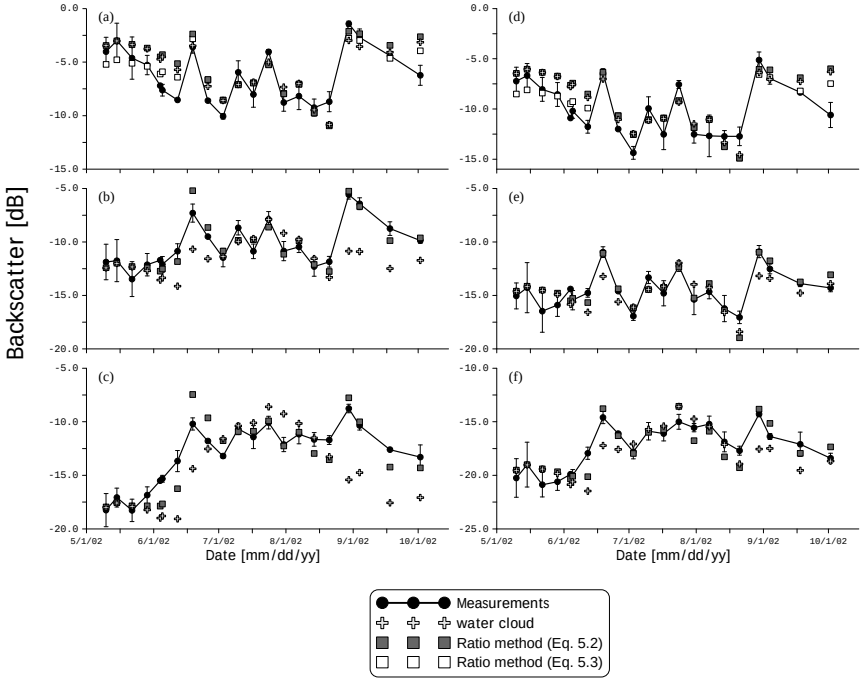

Figure 5-5 Daily averaged C-band σ^o measurements and simulation by the ratio method and the Cloud model. Subplots a), b), c) show the result for the HH polarization and incidence angle of 15, 35 and 55 degrees, respectively. Subplots d), e), f) show the results for the VV polarization and the same incidence angles.

5.5 Soil moisture retrieval

Rather than simulating the σ^o, the Cloud model and, specifically, the ratio method have primarily been developed for retrieval purposes. The text below discusses, therefore, the soil moisture retrieved from C-band σ^o using the Cloud model and ratio method. The required surface roughness and vegetation parameters for these retrievals are adopted from Table 5-1, and from Tables 5-2 and 5-3, respectively. Soil moisture inversion from the C- and L-band measurements is based on the minimization of the difference between the measured and computed σ^o using a least squares optimization technique. The obtained soil moisture retrievals are validated against *in-situ* measurements as shown in the scatter plots of Figures 5-7 and 5-8 for C- and L-band, respectively. In addition, Table 5-4 presents RMSD's and correlation coefficients (ρ's) computed between the measured and retrieved soil moisture. It should be noted that the soil moisture retrievals in Figure 5-7 are obtained using Eq. 5-2, while the RMSD's and ρ's achieved using Eq.

5-3 for C-band and incidence of 15 degrees are also given in Table 5-4.

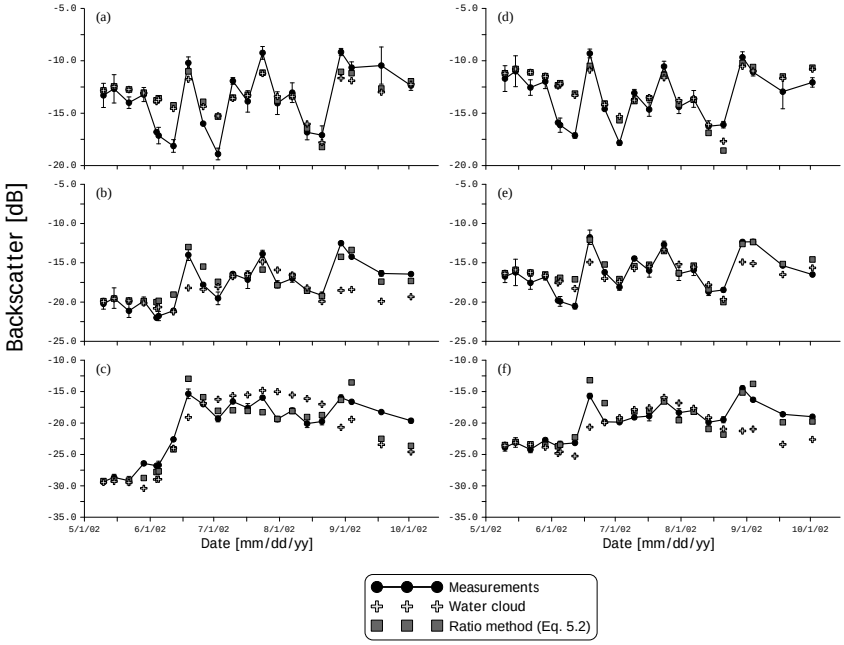

Figure 5-6 Same as Figure 5-5 except that the results for L-band are shown.

As can be observed in Figures 5-7 and 5-8, positive relationships are obtained for each sensing configuration between the measurements and the soil moisture retrieved by the Ratio method. A larger scatter is noted among the Cloud model retrievals. Retrieval uncertainties for the Cloud model tend to increase as incidence angle increases, while for the Ratio method the highest RMSD is typically found at 15 degrees. However, even at the 15 degrees, the RMSD of the Ratio method is lower than the one obtained with the Cloud model. It can, thus, be concluded that more accurate soil moisture retrievals are obtained with the Ratio method.

In general, the soil moisture retrieval errors obtained with the Ratio method model vary from 0.033 to 0.062 m^3 m^{-3}. An exception is, however, found for L-band HH polarized σ^o collected at 55 degrees. The explanation is found in the surface roughness parameterization, which will be addressed in Chapter 6. Apart from this anomaly, the obtained retrieval errors are comparable to (or better than) than the uncertainties reported in previous investigations considering that the soil moisture is retrieved over the entire corn growth cycle with a maximum W of 5.1 kg m^{-2}. For example, Taconet

et al. (1994) and Prevot et al. (1993) report on errors of 0.060 and 0.065 for winter wheat, respectively.

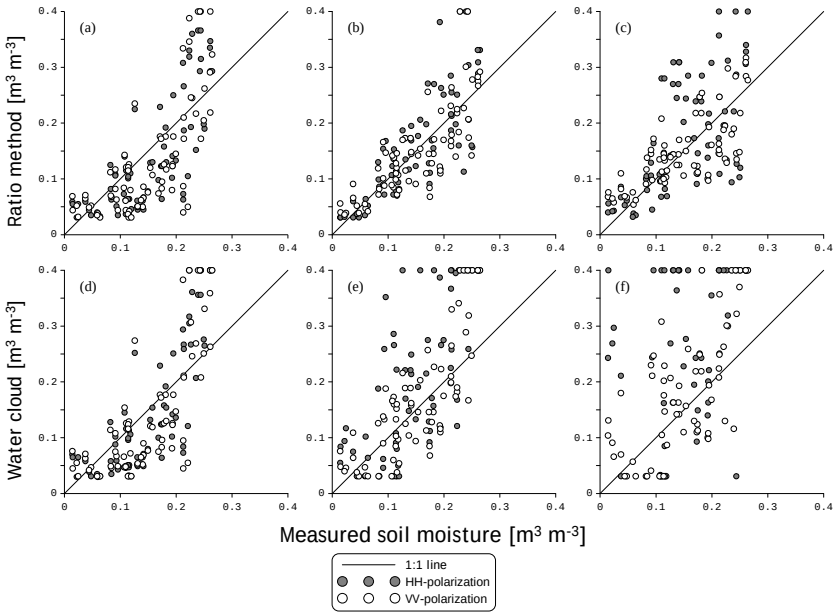

Figure 5-7 Scatter plots between the measurements and soil moisture retrieved from C-band σ^o. Subplots a), b), c) show the result for the HH polarization and incidence angle of 15, 35 and 55 degrees, respectively. Subplots d), e), f) show the results for the VV polarization and the same incidence angles.

Further, it should be noted that for C- as well as L-band considerable lower retrieval errors are obtained for the VV polarization. These RMSD's from VV polarized σ^o measured at angles of 35 and 55 degrees are comparable to errors levels obtained within passive microwave soil moisture retrieval applications (e.g. Jackson et al. 1999, Bindlish et al. 2003, Cashion et al. 2005) and fall within the requirements typically set for satellite-based soil moisture missions (e.g. Kerr et al. 2001, Entekhabi et al. 2004). It should be noted that the passive microwave observations used within these investigations were acquired at resolutions varying between several hundred meters up to tens of kilometers. Because of the highly variable spatial soil moisture dynamics, the spatial representativeness of the soil moisture measurements is a larger source of uncertainty in the validation of those retrievals than for our small scale experiment. On the other hand, the temporal soil moisture variability is typically larger at small scales.

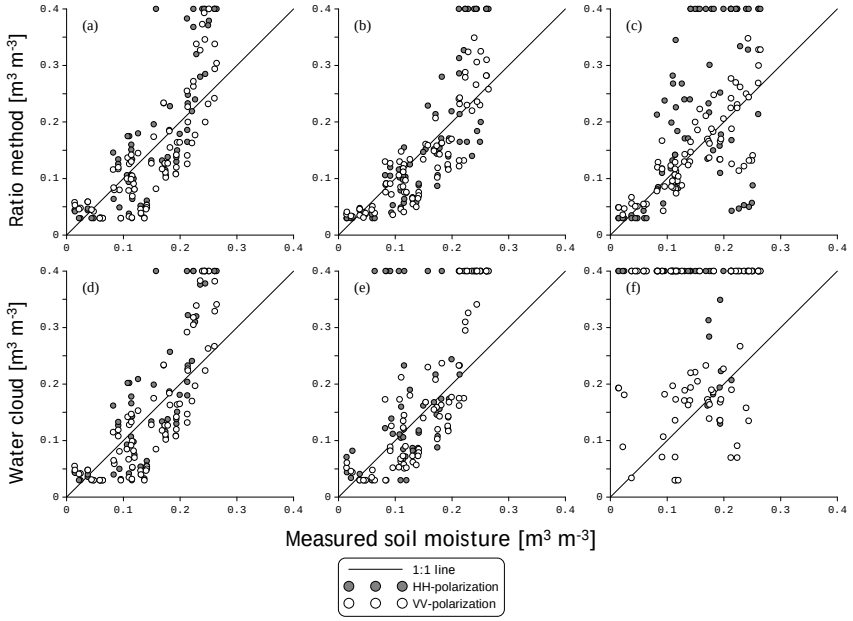

Figure 5-8 Same as Figure 5-7 except that the results for L-band are shown.

Table 5-4 Correlation coefficients and RMSD's between the measered soil moisture and retrievals obtained through application of the Ratio method and Cloud model. For C-band 15 degrees, the retrieval statistics obtained using Eq. 5.2 are in parenthesis.

Band	**Pol.**	***Angle*** [degrees]	***Cloud model*** ρ [-]	***Cloud model*** *RMSD* [$m^3\ m^{-3}$]	***Ratio Method*** ρ [-]	***Ratio Method*** *RMSD* [$m^3\ m^{-3}$]
C-band	HH	15	0.80	0.061	0.052 (0.055)	0.79 (0.76)
		35	0.73	0.095	0.79	0.044
		55	0.40	0.141	0.64	0.063
	VV	15	0.75	0.062	0.56 (0.057)	0.72 (0.72)
		35	0.79	0.057	0.78	0.037
		55	0.62	0.081	0.71	0.042
L-band	HH	15	0.83	0.070	0.82	0.062
		35	0.67	0.080	0.81	0.056
		55	0.60	0.142	0.55	0.103
	VV	15	0.83	0.053	0.81	0.048
		35	0.85	0.061	0.86	0.035
		55	0.60	0.090	0.81	0.033

The explanation for the typical difference between the VV and HH is provided in Joseph et al. (2008). They show that the soil moisture sensitivity of the AIEM simulated σ^o is at all three incidence angles larger for VV than HH. As a result, uncertainties in the retrieval

procedure have a larger impact on the HH polarization. Moreover, they note a strong decrease in the soil moisture sensitivity of the AIEM σ^o under wetter conditions, which explains the larger scatter observed above 0.20 m^3 m^{-3}. More details regarding the retrieval uncertainties are provided in the following section.

5.6 Discussion

The previous section showed that retrievals obtained with the ratio method outperform the soil moisture retrieved by the Cloud model at each antenna configuration. The ratio method is particularly effective in reducing the effects of vegetation when σ^o measurements are dominated by vegetation scattering. For the monitored corn growth cycle, this is only not the case for C-band σ^o measured at a 15 degrees incidence angle. A further analysis of other radar data sets should indicate which scattering mechanism is dominant over other vegetation types. The successful vegetation correction at larger angles, however, leads to retrieval accuracies compliant with the requirements set for satellite-based soil moisture missions (e.g. Kerr et al. 2001, Entekhabi et al. 2004) with exception of 55 degrees HH polarized channels. Of course, the success of applying the ratio method to larger scales depends on the selection of the appropriate vegetation parameters and the availability of reliable ancillary data sets, specifically the *W* and the surface roughness.

Accurate estimation of vegetation parameters, however, is a problem affecting any soil moisture retrieval algorithm accounting for the effects of vegetation explicitly. Nonetheless, before the ratio method can be applied at larger scales, an estimate of vegetation parameters is needed for a range of vegetation types. Comprehensive data sets collected in the past can be used for the development of a database of vegetation type specific parameterizations. As such, a similar retrieval method can be adopted as is often being used for passive microwave soil moisture retrieval applications (e.g. Jackson et al. 1999, Wigneron et al. 2007), in which the vegetation type specific parameters are assigned based on a land cover classification.

Apart from its parameterization, the vegetation correction applied to σ^o measurements using the ratio method depends also on the availability of reliable *W* data. Previously, various authors have investigated the potential of retrieving *W* from observations in the optical and near-infrared domain (e.g. Jackson et al. 2004, Yilmaz et al. 2008). Also, polarimetric σ^o measurements have been shown to be sensitive to changes in biomass. For example, Dente et al. (2008) employed the HH/VV σ^o ratio for retrieving LAI over wheat canopies, while Della Vecchia et al. (2008) demonstrated the sensitivity of VV/VH σ^o ratio to fresh biomass.

Despite the potential of deriving vegetation information from various data sources, the retrieval of *W* (like soil moisture retrieval) poses various challenges, which in turn will affect the reliability of the retrieved soil moisture. The impact of such *W* uncertainties on the soil moisture retrieved is investigated by perturbing the measured *W* by random values with fixed standard deviations varying from 1.0 to 200.0 % of the *W*. The random values consist of 500 realizations from a normally distributed random number generator. For each realization, the RMSD between the retrieved and measured soil moisture is calculated. All 500 RMSD's obtained for a specific *W* standard deviation are averaged. Differences between these mean values and the original RMSD are computed, which are plotted against the *W* standard deviation in Figure 5-9 for C-band. It should be noted that, here, the standard deviation is assumed to represent *W* uncertainties.

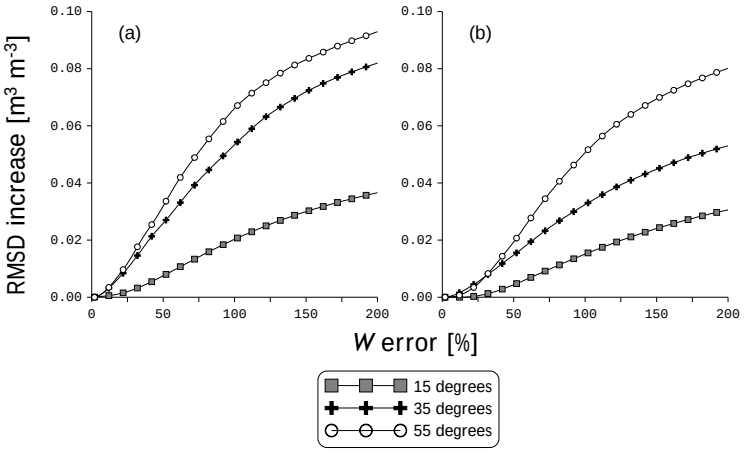

Figure 5-9 Increments in the RMSD between the measured and C-band retrieved soil moisture as a function of the *W* errors; a) HH polarization b) VV polarization.

The plots show that the obtained retrieval accuracy is least affected by the *W* uncertainties at a 15 degrees incidence. The σ^o measured at this angle consists mainly of an attenuated soil return, which alters the σ^o values less than vegetation scattering contributions at larger incidence angles. The applied vegetation correction at 15 degrees is, therefore, smaller and leads to RMSD increase at 100% *W* error of less than 0.020 and 0.015 m^3 m^{-3} for HH and VV polarization, respectively.

The influence of *W* uncertainties at the larger incidence angles is larger and more pronounced at HH polarization. At this polarization, vegetation scattering has a larger impact on σ^o measurements. The

magnitude of the vegetation correction is, therefore, larger, which increases the impact of the *W* on the retrieved soil moisture. Figure 5-9 shows that if a RMSD increase of 0.01 m^3 m^{-3} is tolerated, the *W* error should be less than 23 and 35 % for HH and VV polarization at a 55 degrees angle, respectively.

Also, important for the reliability of soil moisture retrievals is the reliability of the estimated surface roughness parameters. Tillage operations and weathering are known to affect the roughness conditions. Yet, for retrieving soil moisture over natural environments, the surface roughness is often assumed to be temporally stable. The same assumption has been adopted for this study, which has been justified based on the fact that after planting the crops no other tillage operations were performed. The validity of this assumption and uncertainties imposed on retrievals is more thouroughly evaluated in the following chapter.

5.7 Conclusions

The effects of a corn canopy on HH and VV polarized C- and L-band σ^o measured at incidence angles of 15, 35, and 55 degrees are studied for a growth cycle. This analysis is performed by comparing the measured σ^o against simulations by the AIEM surface scattering model. The comparison shows that depending on the antenna configuration and growth stage, the σ^o measurements are dominated either by an attenuated soil return or by scattering from vegetation. The first mechanism is strongest within the C-band measurements collected at 15 degrees and the early growth stage. At larger incidence angles, the latter is more notable, specifically among the σ^o measured at peak biomass and the HH polarization. Surprising is, however, that even at peak biomass and large incidence angles the measured σ^o response to soil moisture is considerable. This σ^o sensitivity to soil moisture is ascribed to scattering along the soil-vegetation pathways.

A method is proposed to correct σ^o measurements for effects of corn vegetation. This method is based on the concept that the ratio of the surface scattering contribution over the measured σ^o is affected by vegetation and can be described as a function of the *W*. Experimentally determined relationships between this ratio and *W* have been used to compute the measured σ^o and reconstruct the amount of surface scattering. Subsequently, the AIEM has been used for retrieving soil moisture from the derived surface scattering component. For comparison purposes, the semi-empirical Cloud model has also been used for σ^o simulation and soil moisture retrieval.

An evaluation of the simulated σ^o and retrieved soil moisture against measurements shows that the results obtained by the ratio

method are superior. It is noted that the differences between the two methods increase with the incidence angle. At larger angles, the vegetation scattering becomes more prominent causing a σ^o increase, which can only be reproduced by the Cloud model when the σ^o_v increases. This reduces, however, the sensitivity of the computed σ^o to soil moisture. As a result, the observed soil moisture sensitivity at peak biomass cannot be reproduced by the Cloud model. Since the HH polarization is more affected by vegetation scattering, differences between measured and Cloud simulated σ^o are particularly large at this polarization. The ratio method is able to correct for these vegetation scattering effects resulting in RMSD between the measured and simulated σ^o of 1.3 dB versus 2.7 dB obtained with the Cloud model.

The ratio method produces also more accurate soil moisture retrievals, where again the deviations with the Cloud model increase with the incidence angle. Overall, the highest retrieval accuracy obtained with the ratio method is from σ^o measured at a 35 degrees incidence angle resulting for C-band in a RMSD of 0.044 and 0.037 $m^3\ m^{-3}$ for HH and VV, respectively. The higher RMSD's found for the 15 degrees incidence angle are somewhat contradicting with past research, but are explained as a less effective vegetation correction when the attenuated soil return is the dominant scattering mechanism.

This leads to the question whether the ratio method is also applicability to other vegetation types and larges spatial scales. Therefore, before this method could become operational, additional data sets should be analyzed to establish its validity and derive the necessary parameters for other vegetation types. When proven successful, a similar retrieval approach can be adopted as is being used for passive microwave soil moisture retrieval, whereby a specific vegetation parameterization is assigned based on a land cover classification. In this context, the sensitivity of soil moisture retrievals to W uncertainties has been analyzed, which shows that W error should be smaller than 23 and 35 % for HH and VV respectively to minimize the increase in the retrieval error to less than 0.01 $m^3\ m^{-3}$.

6 Roughness parameter uncertainties on soil moisture retrievals

This chapter is based on:

Van der Velde, R., Joseph, A.T., O'Neill, P.E., Lang, R.H., Gish, T., "Surface roughness parameter uncertainties on radar based soil moisture retrievals", to be submitted to *IEEE Transactions on Geoscience and Remote Sensing*.

6.1 Introduction

Characterization of the amount of surface scattering and emission forms the basis of most soil moisture retrieval algorithms, and requires the definition of the surface roughness conditions and dielectric properties. The dielectric properties of a soil surface are affected by the soil moisture content and soil texture, and can be determined through application of a mixing model (e.g. Wang and Schmugge 1980, Dobson et al. 1985). The roughness of a surface represents its geometry and can be described by means of statistical properties of field measured surface profiles: root mean square height (s), correlation length (l) and autocorrelation length function (ACF) (see Chapter 3, Ulaby et al. 1982). Utilization of roughness parameters derived from field measurements for large scale soil moisture retrieval is, however, found to be unpractical because surface roughness is spatially variable (e.g. Bryant et al. 2007, Alvarez-Mozos et al. 2009). Obtaining a spatially representative parameterization is, thus, cumbersome. Moreover, even when roughness is reliably measured, an accurate σ^o simulation is often hindered by the simplifications used for the development of surface scattering models (e.g. Verhoest et al. 2008). For example, within most surface scattering models the complex surface geometry is represented as a single-scale stationary process (e.g. Davidson et al. 2000, Mattia et al. 2003b). Natural environments may, however, exhibit various roughness components perturbing the surface over different spatial scales (e.g. Beaudoin et al. 1990). A derivation of the surface roughness parameters from σ^o measurements itself is, therefore, preferred.

Investigations (i.e. Rahman et al. 2007, Bindlish and Barros 2001) have shown that multi-channel σ^o measurements may be availed to derive the roughness parameterization. In the case of multi-scale rough surfaces, however, the measured angular and polarimetric σ^o behavior is different from simulations by single-scale surface scattering model (e.g. Champion and Faivre 1996, Zribi et al. 2002).

Hence, the use of multiple channels σ^o measurements may not always yield the appropriate roughness parameterization, which can cause large retrievals uncertainties. Yet, effective parameterizations can usually be obtained to describe those σ^o measurements and its response to soil moisture by single-scale models (e.g. Champion and Faivre 1996, Mattia et al. 2006, Verhoest et al. 2008)

For this reason, the surface roughness is assumed to be temporally stable in many large scale soil moisture mapping applications (i.e. Wagner and Scipal 2000, Moran et al. 2002, Thoma et al. 2006, Bartalis et al. 2007). For natural vegetation covers (i.e. forest, grasslands and wetlands) changes in the surface roughness are relatively small, while in agricultural areas the roughness changes can be severe due to weathering and farming practices (Zobeck and Onstad 1987). For example, Jackson et al. (1997) and Callens et al. (2006) have reported on the impact of weathering on surface roughness through analysis of a comprehensive set of field measurements. More recently, Alvarez-Mozos et al. (2009) studied the impact of measured temporal roughness variations on the σ^o simulated by a surface scattering model. They found temporal σ^o variations up to 2.77 dB due to measured roughness changes, which cause soil moisture retrieval errors up to 0.05 m^3 m^{-3} under dry conditions. However, the impact of such roughness changes on the soil moisture retrieved from σ^o measured over vegetation covers has to be quantified.

Apart from this issue on the temporal stability, the actual parameterization needed to obtain accurate soil moisture retrievals has also been subject of discussion. For example, the Advanced Integral Equation Method (AIEM, Chen et al. 2003), the most widely applicable single-scale surface scattering model, requires the *s*, *l* and ACF as input. The ACF describes the height probability distribution function of a random rough surface and is typically assumed to have either an Exponential or Gaussian shape (e.g. Ulaby et al. 1982, Zribi et al 2000, Verhoest et al. 2008). Exponential ACF's have been mostly reported for smooth agricultural surfaces, whereas the Gaussian shape has been found more appropriate for very rough surfaces (e.g. Oh et al. 1992, Davidson et al. 2000). With the ACF fixed, the other two parameters, *s* and *l*, remain for simulating the surface scattering as a function of the soil moisture content.

Of these two parameters specifically the *l* is difficult to determine reliably from *in-situ* measurements. Oh and Kay (1998) showed that for the estimation of *l* with a 10% accuracy a surface height profile length of at least 200*l* is needed. Moreover, the separate effects of *s* and *l* on σ^o measurements and simulations can not be distinguished (Su et al. 1997). Therefore, the *l* is often treated as a calibration parameter, and described as a function of the *s* (e.g. Su et al. 1997,

Baghdadi et al. 2002a, Zribi and Dechambre 2002, Bryant et al. 2007). This raises the question on the value of estimating a unique *l* within soil moisture retrieval applications. Hence, the most widely used semi-empirical surface scattering models (e.g. Oh et al. 1992, Dubois et al. 1995, Shi et al. 1997) use only the *s* to parameterize the surface roughness.

In this chapter, the impact of assuming a temporally stable surface roughness and a specific roughness parameterization is studied within the context of soil moisture retrieval over the 2002 corn growth cycle. The C- and L-band σ^o measurements collected during the OPE^3 field campaign (see Chapter 4) are used for this investigation. These σ^o measurements are corrected for the vegetation effects through application of the Ratio method described in the previous chapter. Then, the AIEM is used to retrieve the soil moisture based on the input of soil texture information and a surface roughness parameterization.

Similar to the previous chapter, the roughness parameters are determined using the σ^o measured over bare soil conditions collected at the beginning of the campaign. In estimating the roughness, here, four types of parameterizations are derived assuming both Exponential and Gaussian ACF's, and a fixed or variable *l*. Using the inverted roughness parameterizations, soil moisture is retrieved over the complete corn growth cycle and its accuracy is evaluated. To examine the temporal stability, the assumed time-invariant roughness parameters are optimized by minimizing the Root Mean Squared Difference (RMSD) between the measured and retrieved soil moisture. The evolution of the remaining retrieval errors is investigated and its relationship to weathering (rainfall) is evaluated.

6.2 Estimated surface roughness parameters

In the previous chapter, the surface roughness parameterization was determined to quantify the surface scattering component as a function of the soil moisture through the dielectric properties. In accordance with the reported ACF's for agricultural fields, an Exponential ACF was assumed for this surface roughness inversion. Then, the *s* and *l* were inverted from the four σ^o measurements collected on May 10th, during which the land cover was bare soil. The same approach is applied, here, to determine the *s* and *l* for an assumed Gaussian ACF. In addition, for both types of ACF's, parameterizations are also derived by only calibrating the *s*, while taking the average of ten measured surface height profiles as the *l* (which is 7.25 cm).

The roughness parameters obtained for an 'Exponential' and 'Gaussian' ACF are given in Tables 6-1 (essentially the same as Table 5-1) and 6-2, and the parameters obtained by fixing *l* are presented

in Tables 6-3 and 6-4 for the 'Exponential' and 'Gaussian' ACF, respectively. Apart from the inverted roughness parameters, also the RMSD between the AIEM simulated and measured σ^o are presented. A comparison shows that the differences in the RMSD between the four parameterizations are negligible. This indicates that the σ^o measured over bare soils can be described using each of the four parameterizations by means of the so-called "effective parameters".

Table 6-1 Surface roughness parameters inverted assuming an Exponential ACF ('bare soil' parameterization').

Band	Pol.	*Angle* [degrees]	*s* [cm]	*l* [cm]	*RMSD* [dB]
C-band	HH	15	0.65	9.54	0.93
		35	0.73	9.79	0.83
		55	0.82	11.05	1.04
	VV	15	0.42	10.96	0.08
		35	0.45	10.65	0.75
		55	0.35	10.18	0.95
L-band	HH	15	0.42	9.85	0.84
		35	0.61	9.60	0.47
		55	0.46	10.05	0.39
	VV	15	0.46	9.92	0.87
		35	0.68	12.84	0.51
		55	0.38	10.16	0.09

Table 6-2 Surface roughness parameters inverted assuming a Gaussian ACF ('bare soil' parameterization').

Band	Pol.	*Angle* [degrees]	*s* [cm]	*l* [cm]	*RMSD* [dB]
C-band	HH	15	2.99	7.81	0.93
		35	1.62	9.98	0.84
		55	2.75	9.69	1.05
	VV	15	2.56	4.42	0.25
		35	1.38	10.02	0.74
		55	2.42	9.78	0.95
L-band	HH	15	0.31	9.48	0.83
		35	0.67	10.16	0.47
		55	1.06	10.07	0.41
	VV	15	0.34	9.46	0.87
		35	0.71	10.27	0.51
		55	1.19	10.10	0.10

Obviously, differences are noted among the absolute values of the inverted parameters. An evaluation of the parameters obtained via the simultaneous inversion of *s* and *l* versus the calibration of the *s* alone shows that the magnitude of *s* changed somewhat, but that the general trends observed among the parameters remained the same. This could also be expected based on the fact that within various studies the relationship between *l* and *s* is used to reduce the number of (A)IEM input parameters (e.g. Su et al. 1997, Baghdadi et al.

2002b, Zribi and Dechambre 2002, Baghdadi et al. 2004). On the other hand, significant differences are observed between the parameters obtained with the Exponential and Gaussian ACF. Most notable is the angular dependence of the parameters obtained with the Gaussian ACF, while no such dependency is found for the Exponential ACF. This suggests that the AIEM is better in describing the angular σ^o response, which is particularly important when using multi-angular σ^o data as is, for example, measured by ASAR in the Wide Swath mode.

Table 6-3 Surface roughness parameters inverted assuming an Exponential ACF and *l* of 7.25 cm ('bare soil' parameterization').

Band	Pol.	*Angle* [degrees]	*s* [cm]	*l* [cm]	*RMSD* [dB]
C-band	HH	15	0.57	7.25	0.93
		35	0.65	7.25	0.83
		55	0.70	7.25	1.05
	VV	15	0.34	7.25	0.08
		35	0.37	7.25	0.76
		55	0.30	7.25	0.91
L-band	HH	15	0.42	7.25	0.84
		35	0.55	7.25	0.47
		55	0.40	7.25	0.39
	VV	15	0.46	7.25	0.88
		35	0.54	7.25	0.50
		55	0.33	7.25	0.09

Table 6-4 Surface roughness parameters inverted assuming a Gaussian ACF and *l* of 7.25 cm ('bare soil' parameterization').

Band	Pol.	*Angle* [degrees]	*s* [cm]	*l* [cm]	*RMSD* [dB]
C-band	HH	15	2.78	7.25	0.93
		35	1.14	7.25	0.84
		55	1.98	7.25	1.05
	VV	15	0.34	7.25	0.09
		35	0.95	7.25	0.74
		55	1.69	7.25	0.95
L-band	HH	15	0.35	7.25	0.83
		35	0.40	7.25	0.47
		55	0.48	7.25	0.39
	VV	15	0.39	7.25	0.87
		35	0.39	7.25	0.51
		55	0.40	7.25	0.09

Often, the actual surface roughness is of lesser interest and the objective is usually the retrieval of soil moisture (or another biophysical parameter). The retrieval accuracy obtained with each of the four roughness parameterizations is, therefore, evaluated. The algorithm used for these retrievals employs the Ratio method discussed in the previous chapter to correct for the effects of

vegetation and uses the roughness parameters from Tables 6-1 to 6-4 as input for the AIEM. The RMSD between measured and retrieved soil moisture is calculated for each roughness parameterization to indicate its performance. Figure 6-1 shows the obtained RMSD's for each of the twelve channels (two bands, two polarizations and three incidence angles).

Figure 6-1 RMSD calculated between the measured and retrieved soil moisture obtained via application of four roughness parameterizations for twelve channels: C- and L-band, HH and VV polarization and incidence angles of 15, 35 and 55 degrees.

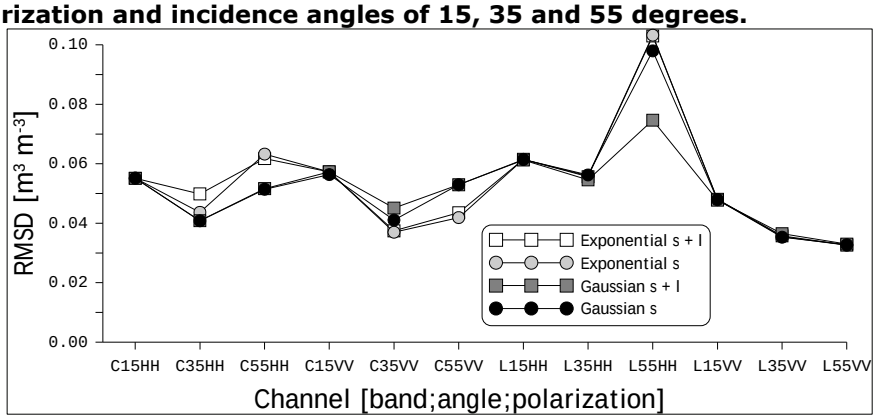

Within this plot, fairly small differences are noted between RMSD's obtained with the parameterizations inverted using both *s* and *l*, and using only *s*. Differences in the obtained RMSD by assuming either a Gaussian or an Exponential ACF's are, however, more substantial at C-band. At C-band and angles of 35 and 55 degrees, the Gaussian ACF yields the more accurate soil moisture retrievals for the HH polarization, while the Exponential ACF provides better results for the VV polarization. The typical differences observed between the two ACF's are on the order of 0.01 $m^3 m^{-3}$. An exception is, however, the L-band HH polarization 55 degrees retrievals. For this sensing configuration the AIEM simulates for all roughness parameterizations only a 5 dB σ^o range from completely dry to completely wet conditions; except when both *s* and *l* are calibrated using a Gaussian ACF. Because of the significantly larger soil moisture sensivity of the σ^o simulated using the Gaussian ACF, uncertainties affecting retrievals (e.g. reliability of σ^o and *W* measurements) have a smaller impact on the overall retrieval accuracy leading to a 0.028 $m^3 m^{-3}$ decrease of the RMSD. It should, however, be noted that in spite of the observed differences, no single parameterization type produces consistently for all channels the most accurate soil moisture retrievals.

Table 6-5 Surface roughness parameters inverted assuming an Exponential ACF by minimizing RMSD between the measured and retrieved soil moisture ('growth cycle' parameterization').

Band	Pol.	*Angle* [degrees]	*s and l inversion* *s* [cm]	*l* [cm]	*s inversion* *s* [cm]	*l* [cm]
C-band	HH	15	1.68	13.10	1.24	7.25
		35	3.46	10.80	2.85	7.25
		55	1.27	24.60	0.77	7.25
	VV	15	0.30	3.70	0.36	7.25
		35	0.30	4.50	0.37	7.25
		55	0.30	6.60	0.31	7.25
L-band	HH	15	3.46	3.70	0.47	7.25
		35	0.89	24.40	0.54	7.25
		55	0.85	24.90	0.44	7.25
	VV	15	0.51	5.80	0.49	7.25
		35	0.50	4.50	0.56	7.25
		55	0.31	6.10	0.33	7.25

Table 6-6 Surface roughness parameters inverted assuming a Gaussian ACF by minimizing RMSD between the measured and retrieved soil moisture ('growth cycle' parameterization').

Band	Pol.	*Angle* [degrees]	*s and l inversion* *s* [cm]	*l* [cm]	*s inversion* *s* [cm]	*l* [cm]
C-band	HH	15	1.01	13.60	2.56	7.25
		35	1.82	10.90	1.17	7.25
		55	3.19	10.80	2.04	7.25
	VV	15	0.30	6.70	0.34	7.25
		35	0.31	3.50	0.95	7.25
		55	0.42	3.00	1.71	7.25
L-band	HH	15	3.48	3.00	0.40	7.25
		35	2.48	22.00	0.40	7.25
		55	3.13	17.60	0.56	7.25
	VV	15	0.35	13.00	0.41	7.25
		35	0.42	3.20	0.40	7.25
		55	0.31	6.50	0.40	7.25

6.3 Temporal stability of surface roughness

The previous section showed that by using time-invariant roughness parameterizations derived from σ^o measured at the beginning of the OPE^3 campaign retrieval accuracies can be achieved varying from 0.033 to 0.063 m^3 m^{-3}. Hereafter, this parameterization is referred to as 'bare soil'. The focus of this section lies on evaluating the impact of surface roughness changes on the reliability of soil moisture retrieved throughout the growth cycle. To this aim, the parameter(s) of the four parameterization types are inverted by minimizing the RMSD between the measured and retrieved soil moisture. The resulting roughness parameters are given in Tables 6-5 and 6-6 for the two Exponential and two Gaussian ACF

parameterizations, respectively. Hereafter, these parameterizations are referred to as 'growth cycle'. Further, Figure 6-2 presents the obtained RMSD's for each of the twelve channels and four parameterization types.

The plots of Figure 6-2 show that the differences in the retrieval accuracy obtained with bare soil and growth cycle parameterizations are, in general, limited and in some cases even non-existent. Most significant improvements are noted at the largest angle of incidence: 55 degrees. The obtained differences at this incidence angle are typically on the order of 0.01 m^3 m^{-3}. The retrievals from 55 degrees HH polarized L-band σ^o form, however, an exception. The RMSD's obtained with growth cycle parameterization is typically more than 0.02 m^3 m^{-3} smaller than the ones obtained with the bare soil parameterizations.

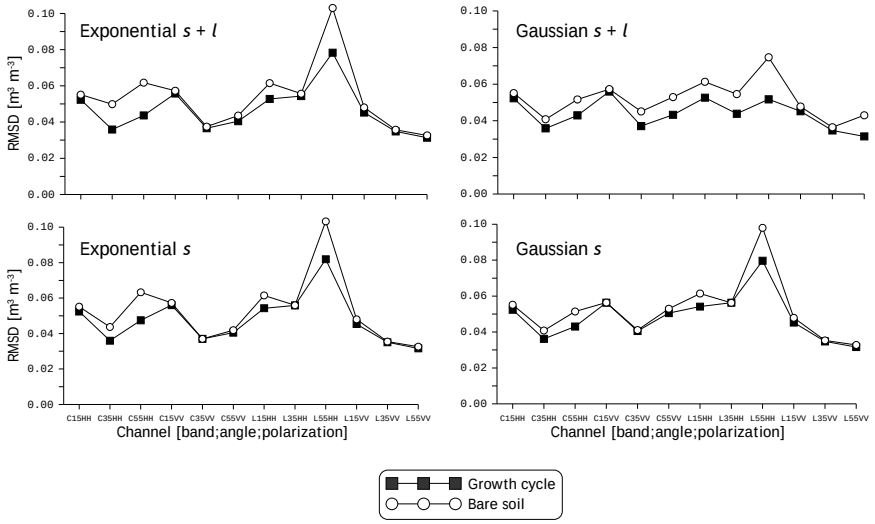

Figure 6-2 RMSD's obtained between the measured and the soil moisture retrieved through application of the bare soil and growth cycle roughness parameterizations.

Thus, the overall differences in the RMSD's obtained between the bare soil and growth cycle parameterizations are relatively small. This justifies the use of roughness parameters estimated under bare soil conditions for the retrieval of soil moisture throughout the entire corn growth cycle. Moreover, this indicates that the surface roughness changes have a fairly limited impact on the reliability of retrievals on a seasonal time scale.

A comparison of the parameterizations in Table 6-5 and 6-6 with the ones reported in the previous section (Table 6-1 to 6-4) shows, however, that differences in the parameter values can be quite large when both *s* and *l* are optimized. On the other hand, the inversion of *s* alone yields for both ACF's similar values for the growth cycle as for

the bare soil parameterization. These parameterizations can, thus, be considered as temporally stable. This discrepancy with the parameterization obtained by inverting both *s* and *l* is explained by the numerical dependency of their impact on AIEM simulations.

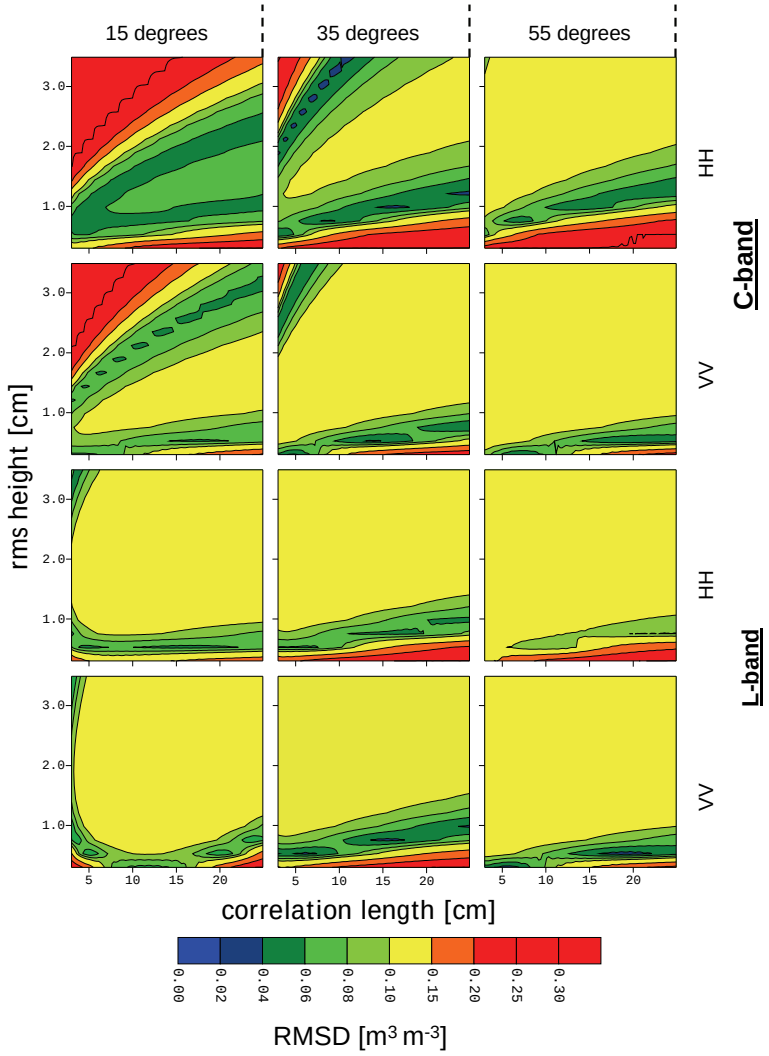

Figure 6-3 The RMSD between the measured and retrieved soil moisture computed for the complete corn growth cycle plotted for the twelve channels as a function of the *s* and *l* for an assumed Exponential ACF.

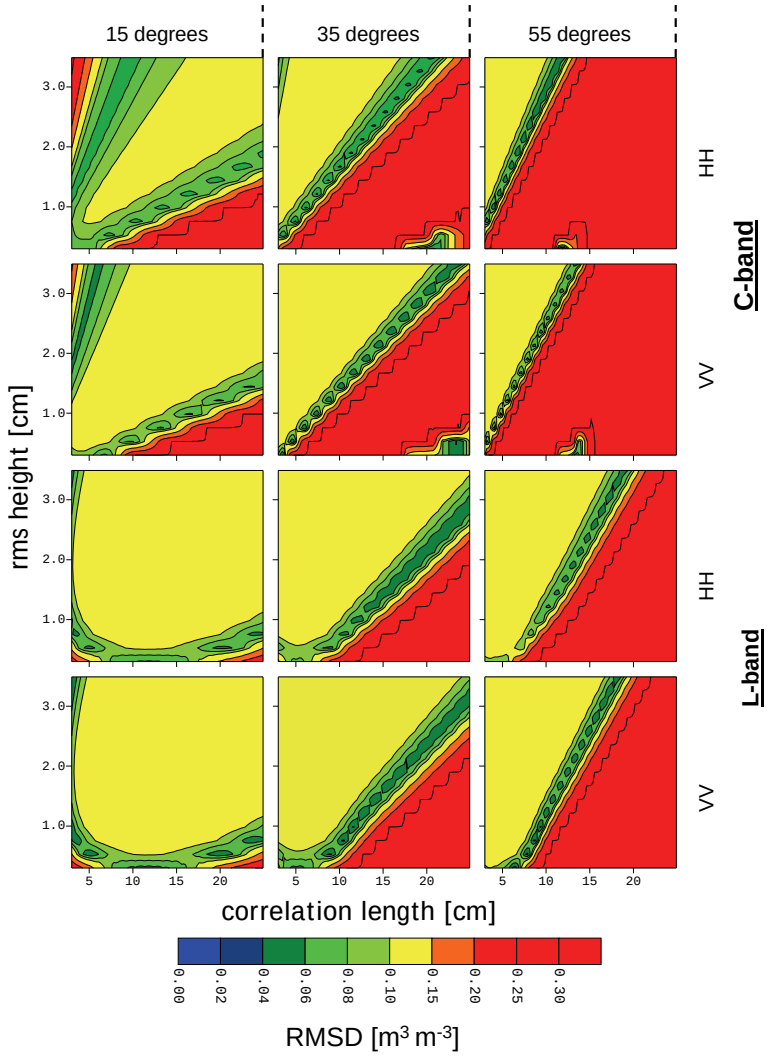

Figure 6-4 Same as Figure 6-3 only a Gaussian ACF is assumed.

To illustrate how this numerical dependency behaves, a broad range of roughness parameter sets has been used as AIEM input for the retrieval of soil moisture. The parameter range is established by varying *s* and *l* independently from 0.3 to 3.5 cm and from 3.0 to 25.0 cm with intervals of 0.01 and 0.1 cm, respectively. Then, for each parameter set the RMSD between measured and retrieved soil moisture is calculated, which is plotted as a function of the *s* and *l* for the twelve channels in Figure 6-3 for the Exponential ACF and the Figure 6-4 for the Gaussian ACF.

These plots illustrate is that using both ACF's the highest retrieval accuracy can be achieved for various combinations of *s* and *l*. The RMSD's between the measured and soil moisture retrieved with the Exponential ACF appear to be least sensitive to changes of *l*. Especially the plots for L-band and the large incidence angles show that the minimum RMSD can be obtained with most *l* values as long as the appropriate *s* is selected. A certain tolerance for *s* is also noticed in the plots for C-band and incidence angles of 15 and 35 degrees. However, even for those channels the RMSD is less sensitive for the *l* than for the *s*.

Similar relationships between roughness parameters and RMSD are found when a Gaussian ACF is used for the retrieval of soil moisture from σ^o measured from a 15 degrees incidence. At larger angles, however, the RMSD becomes more sensitive to changes in *s*. At 55 degrees, it is even not possible to obtain the minimum RMSD when the *l* is larger than 18.0 cm for L-band and larger than 13.0 cm for C-band. This angular dependency is consistent with the relationship found between the roughness parameters and incidence angle observed among the parameter values in Tables 6-4 and 6-6.

Further, it should be noted that the parameter range needed to obtain a low RMSD is smaller for a Gaussian ACF than for an Exponential ACF. This means that the RMSD can have a larger tolerance for roughness parameter uncertainties when an Exponential ACF is selected. On the other hand, from the parameter estimation perspective a larger sensitivity is often preferred, which would opt for the Gaussian ACF.

6.4 Temporal evolution of retrieval errors

A comparison of the RMSD's obtained with the bare soil and growth cycle parameterizations was utilized to study the impact of surface roughness changes on the soil moisture retrieval accuracy over the complete corn growth cycle. The improvements noted by using the growth cycle parameterization is for most channels less than 0.01 $m^3 m^{-3}$. This indicates that the surface roughness estimated at the beginning of the monitored growth cycle can be considered representative for the entire growth cycle when a time invariant roughness parameterization is assumed. Obviously, the soil surface during the OPE[3] campaign was not disturbed by farming practices after the crops were planted.

The impact of roughness changes over short time scales is, however, not evaluated by analyzing the RMSD's computed over the entire campaign. To study the impact of surface roughness changes over short time scales the differences between the measured and retrieved soil moisture are computed and averaged for each acquisition day. The roughness parameterization obtained by

calibrating both the *s* and *l* with a Gaussian ACF is used for these retrievals because with this parameterization significantly more accurate retrievals are obtained for L-band HH σ^o collected from 55 degrees incidence angle. The daily averaged values are presented in Figure 6-5 for the twelve channels. In addition, rainfall amounts are plotted on the secondary axis as it is understood that weathering induced by precipitation may have a prominent role in changing the surface roughness (e.g. Zobeck and Onstad 1987, Callens et al. 2006).

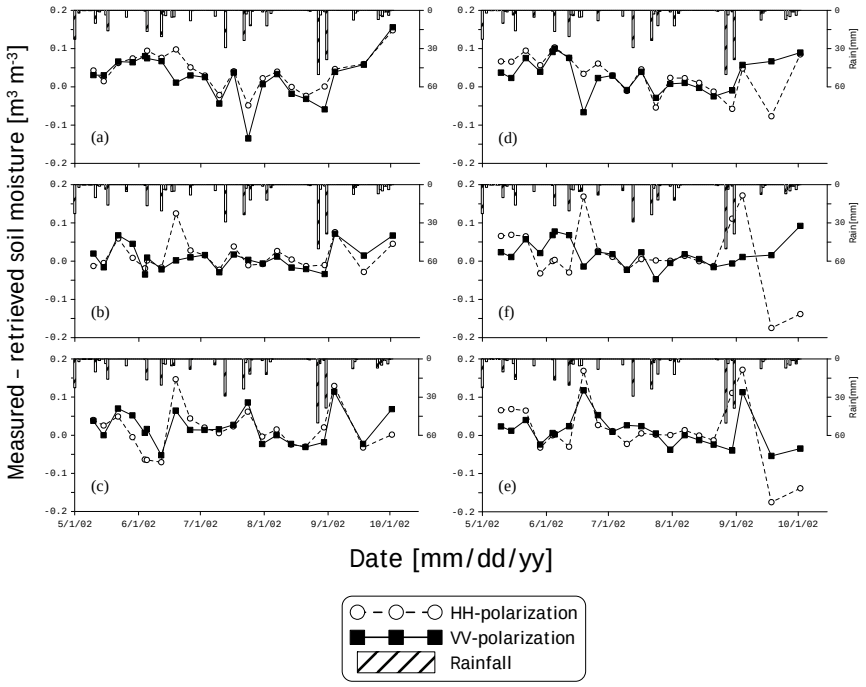

Figure 6-5 Differences between the measured and retrieved soil moisture averaged for each acquisition day and plotted against time; C-band results for incidence angles of 15, 35 and 55 degrees are shown in a), b) and c), respectively, and the L-band results are shown in d), e) and f), respectively.

Of course, the analysis of only the temporal evolution of retrieval errors is not the best approach to study its dependency to surface roughness changes. Other uncertainties could also affect the retrieval accuracy such as inconsistencies in applied vegetation correction method. A full investigation of these temporal roughness variations would, therefore, require *in-situ* measurements as has been done by Callens et al. (2006) and Alvarez-Mozos et al. (2009). Unfortunately, a time series of surface roughness measurements is not available for the OPE^3 campaign.

The plots of Figure 6-5 show, however, that the development of the soil moisture retrieval errors has some consistency with the antecedent precipitation. Especially for incidence angles of 35 and 55 degrees, the largest retrieval errors occur after intensive rainfall. For example, prior to June 19th about 40 mm of rain was measured and 93 mm of rain fell before September 4th, which result in soil moisture underestimations up to 0.15 and 0.13 m^3 m^{-3}, respectively. In addition, the variations in the retrieval errors become smaller close to peak biomass suggesting that the surface roughness remained constant. This can be argued for because fully grown corn plants shield the land surface from the direct impact of rain droplets and may, thus, suppress the effects of weathering.

The increase of the retrieval errors after intensive rain is stronger for the HH than for the VV polarization and also more pronounced at L-band and the larger incidence angles (35 and 55 degrees). This is somewhat expected based on previous investigations. For example, Holah et al. (2005) showed that HH σ^o measurements are more sensitive to the surface roughness than the VV polarization. Similarly, Beaudoin et al. (1990) and Baghadi et al. (2002b) found that at large incidence angles the influence of roughness dominates the σ^o. Further, over a range of roughness conditions, Zribi et al (1997) observed a larger σ^o variability for L-band than for C-band.

This higher σ^o sensitivity to surface roughness reported for L-band, HH polarization and large incidence angles means that those σ^o measurements are also more affected by changes in roughness due to weathering. Hence, the soil moisture retrieval errors after intensive rain events are larger for those sensing configurations. An important conclusion is that the retrieval accuracy is not only determined by σ^o sensitivity to soil moisture, but is also affected by its sensitivity to other time varying land surface parameters. Therefore, hardly any differences in RMSD's are observed between C- and L-band, and more accurate retrievals are obtained for the VV polarization. In the literature, however, there are various reports on larger σ^o sensitivities to soil moisture for the lower frequencies and the HH polarization (e.g. Ulaby and Batlivala 1976, Ulaby et al. 1996, Shi et al. 1997, Macelloni et al. 1999).

Now looking back to the results presented in the previous chapter on the impact of vegetation on σ^o measurements, the inaccuracies in the modelled σ^o may also be a consequence of assuming a constant roughness parameterization. With no surface roughness measurements, however, it is difficult to explain the exact source of these retrieval errors.

6.5 Conclusions

In this chapter, the impact of surface roughness parameter uncertainties on soil moisture retrieved from σ^o measured throughout the corn growth cycle is discussed. These σ^o measurements have been corrected for the effects of vegetation through application of the Ratio method as described in the previous chapter. Then, the AIEM is utilized to evaluate the assumptions made regarding the utilized roughness parameterization, and to analyze the validity of time-invariant parameters.

As a first step, surface roughness parameters are inverted from σ^o measured over bare soil conditions as has been done in the previous chapter resulting in a parameterization referred to as 'bare soil'. Via this approach, parameterizations are derived for an assumed Exponential and Gaussian ACF's, and a fixed (measured) or variable *l*. Thus, in total four types of parameterization are obtained. Each of those has been used as input for the AIEM for the retrieval of soil moisture over the entire growth cycle.

In general, the most significant differences in the retrieval accuracies are observed between the two ACF's, while using a variable *l* had only minor impact on the soil moisture retrieval accuracy. Overall, the differences in the retrieval accuracies are, however, smaller than 0.01 $m^3\ m^{-3}$. Given such small differences it can be concluded that, from the soil moisture retrieval perspective, effective roughness parameters can be estimated for each parameterization type.

Next to the inversion of the bare soil parameterizations, the roughness parameters have also been inverted by minimizing RMSD between the measured and retrieved soil moisture resulting to a parameterization referred to as 'growth cycle'. Compared to using bare soil parameterization, the retrieval accuracy achieved with growth cycle parameters are an improvement. However, the differences between the two parameterizations are typically smaller than 0.01 $m^3\ m^{-3}$. Thus, the roughness parameters estimated at the beginning of the OPE^3 campaign approximate the surface conditions throughout the entire campaign fairly well. This means that on average over the monitored growth season the impact of surface roughness changes on the retrieved soil moisture is limited.

An analysis of the differences between the measured and retrieved soil moisture shows that the largest errors occur specifically after precipitation events. It is found that the increase in the retrieval error after intensive rain is strongest at HH polarization, L-band, and large incidence angles, which is in agreement with previous reports on σ^o sensitivities to surface roughness. This can be considered as a reason for the more accurate soil moisture retrievals from the VV polarized σ^o measured during the OPE^3 campaign.

7 Tibetan land surface conditions observed by ASAR

This chapter is based on:

Van der Velde, R., Su, Z., Ma, Y., 2008, "Impact of soil moisture dynamics on ASAR σ^o signatures and its spatial variability observed over the Tibetan Plateau", *Sensors*, **8**, pp. 5479-5491.

Van der Velde, R., and Su, Z., 2009, "Dynamics in land-surface conditions on the Tibetan Plateau observed by Advanced Synthetic Aperture Radar (ASAR)", *Hydrological Sciences Journal*, **54**, pp. 1079-1093.

7.1 Introduction

Since the launch of the first European Remote Sensing (ERS) satellite in 1992, σ^o measurements acquired by space borne scatterometers and SAR systems have become available to a broader community. The sensors onboard this platform provided, however, measurements only at C-band, VV polarization and fixed incidence angles. At present, the constellation of satellites maintained by various space agencies includes active microwave instrumentation operational at different frequencies, in (fully) polarimetric mode and at various incidence angles. Specifically, interesting from a soil moisture retrieval perspective is the Phased Array type L-band SAR (PALSAR) by the Japan Aerospace Exploration Agency (JAXA) and the Advanced Scatterometer (ASCAT) by the ESA. Moreover, the NASA is in preparation of two missions, SMAP and Aquarius, carrying the first two L-band scatterometers.

Most of the missions mentioned above are, however, primarily focussed on the development of the science needed for establishing continuous monitoring programs. On the other hand, the need for monitoring environmental disasters (e.g. floods and droughts) has been formulated within Global Monitoring for Environment and Security (GMES) program of the European Commission. In this framework, the ESA is in preparation of a series of Sentinel missions that will bring together the satellite measurements required to meet these objectives. Although the exact antenna configuration has to be defined, the first Sentinel satellite scheduled for launch will be a SAR system comparable to the ASAR currently flown onboard ENVISAT.

Advantageous of the SAR technique is that it is able to provide high resolution microwave measurements from space. At microwave frequencies, the dielectric properties are strongly affected by the liquid water content in the surface soil layer and vegetation cover. Based on this characteristic, SAR data has been investigated for its

potential to observe changes in land surface states, such as soil moisture (i.e. Su et al. 1997, Bindlish and Barros 2001, Löw et al. 2006, Baup et al. 2007a, Thoma et al. 2008, Van der Velde et al. 2008), vegetation biomass (i.e. Rignot et al. 1994, Saatchi et al. 1997, LeToan et al. 2004) and freeze/thaw conditions (i.e. Rignot and Way 1994, Way et al. 1997, Koskinen et al. 1997, Wismann 2000).

The derivation of the biophysical variables from SAR data on an operational basis poses, however, various challenges. For example, at the high resolution of SAR spatially representative parameterizations required to describe surface roughness and vegetation effect on σ^o are difficult to define. Moreover, due to limitations in the sensing systems (e.g. ERS-1/-2) or conflicts with other users in case of multi-mode sensing systems (e.g. RADARSAT-1/-2, ASAR, PALSAR), long-term SAR data sets with a high temporal resolution are difficult to obtain. The temporal resolution of most existing SAR data sets has, therefore, been too coarse for capturing changes in highly dynamic land surface states such as soil moisture and freeze/thaw conditions.

In the framework of the ESA-Ministry of Science and Technology of China (MOST) sponsored Dragon programme, consistent data requests have resulted in a unique time series of ASAR images acquired in the WS mode over the central part of the Tibetan Plateau. This data set has been described in Section 4.3 and is referred to as the *Tibetan data set*. In this chapter, the collected ASAR WS data set is utilized to analyze the impact of changes in land surface states on σ^o. The land surface states considered are soil moisture, soil temperature and biomass, for which the NDVI is taken as a proxy.

Comparison of σ^o signatures from two different land units (of 1x1 km^2) with contrasting land surface hydrology (a grassland and a wetland) and located in each others proximity is utilized to study the impact of these land surface states on the temporal σ^o variability. In addition, the σ^o from domains of 5x5 km^2 and 30x30 km^2 selected around the two 1x1 m^2 areas is studied to evaluate the impact of the variability in the land surface states on the σ^o variability within those areas. A time series of soil moisture and temperature measurements collected at the Naqu station and Système Pour l'Observation de la Terre (SPOT) NDVI products are used to identify the impact of soil moisture, soil temperature and biomass on the σ^o response. A multivariate regression analysis of four linear models is presented to statistically evaluate the contribution of each land surface state to the observed temporal σ^o variability.

7.2 Definition of the study areas

As described in Chapter 4, the land cover in the Tibetan study area consists of grasslands and wetlands. The soil moisture in the grasslands is typically subject to a large temporal variability, while

the wetlands remain fairly wet throughout the monsoon season due to its water supply from upstream areas. Further, weather on the Plateau is dominated by a dry winter season from November till April, and wet and warm monsoon during the months July, August and September. Thus, land surface conditions in the selected study area are highly dynamic in both space and time.

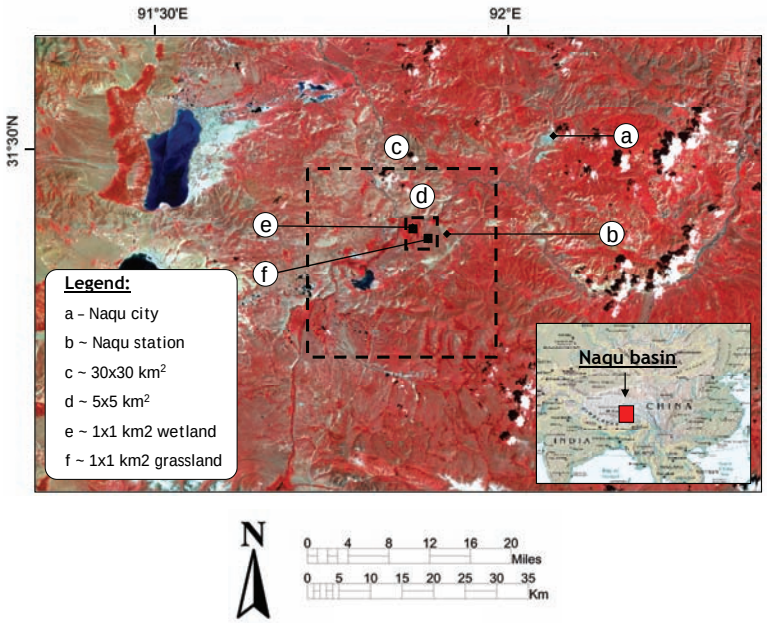

Figure 7-1 LandSat TM false color image of a part of the Naqu river basin and the location of the selected spatial domains.

The impact of these land surface dynamics on σ^o signatures and its spatial variability are investigated for four study domains. Among these four domains are areas of 30x30 km^2, 5x5 km^2 and two of 1x1 km^2. The areas are selected in such way that 5x5 km^2 domain is included in the 30x30 km^2 domain and the both 1x1 km^2 domains are included in the 5x5 km^2 domain as is shown in Figure 7-1. Land covers in the 30x30 km^2 and 5x5 km^2 consist of a mixture of wetland and grassland, while for the 1x1 km^2 domain uniform grassland and wetland areas have been selected.

7.3 Temporal σ^o variability

In the WS mode, ASAR measures σ^o over an incidence angle range of 16^o to 43^o. As the previous two chapters also showed that the σ^o depends on the incidence angle, a correction is needed before the σ^o response to changes in land surface states can be studied. The σ^o is normalized to an incidence angle of 23^o using,

$$\sigma^o\left(23^o\right)=\frac{\cos^2\left(23^o\right)}{\cos^2\theta_i}\sigma^o\left(\theta_i\right) \quad (7.1)$$

where, $\sigma^o(\theta_i)$ represents the angular dependent ASAR σ^o measurements, θ_i is the local incidence angle [degrees], and $\sigma^o(23^o)$ is the backscatter normalized to an incidence angle of 23 degrees.

This theoretical approach is based on Lambert's law for optics, which assumes that the relationship between the incidence angle and amount of scattering per unit surface area follows the cosine law. This behaviour is typical for the middle range of incidence angles, in which σ^o is measured in the WS mode (Ulaby et al. 1982).

Figure 7-2 presents the normalized σ^o and NDVI collected over the 1x1 km^2 grassland and wetland areas, and the soil moisture measured at Naqu station. The soil temperature measurements and daily precipitation amounts are shown at the top of the figure. Unfortunately, due to mechanical difficulties with the logging systems, soil moisture and temperature measurements are not available prior to 2 September 2005.

The plots illustrate the impact of the seasonal dynamics in land surface conditions on the temporal σ^o variability of the grassland and wetland areas. During winters, the σ^o over the two areas is low and remain stable around –16.0 dB. In this period, the soil temperature is primarily below freezing point and soil water is frozen, as is indicated by the soil temperatures. Under these conditions, the dielectric constant is small and comparable to values for dry soil (Wang and Schmugge 1980; Dobson et al. 1985), which results in a low σ^o response.

In spring, the frozen soil water melts due to an increase in the temperature. Hence, the dielectric properties of the soil surface become larger and, over both the grassland and wetland, higher σ^o values are recorded. The wetland σ^o increases rapidly towards the summer and remains high throughout the monsoon season, with few temporal variations. Also, the grassland σ^o response increases on average, but the temporal σ^o variability observed during the summer is much larger than that over the wetland. This contrast between the wetland and grassland is somewhat expected and can be explained by the differences in the pedosphere and hydrographic location.

Wetlands are situated in the lowest part of the watershed, and runoff produced upstream by thawing of frozen water accumulates in these areas. From the onset of thaw, the liquid soil moisture content in the wetlands increases, even in the absence of antecedent precipitation. Grasslands, however, are located at a higher elevation and lack the water supply from upstream areas. As the melted soil water drains into the deep soil profile or runs off to the lower parts of the watershed; the soil moisture in the grassland depends solely on antecedent precipitation. The soils in the grasslands are highly water conductive (K_s = 1.2 m d^{-1}), and are subject to a high evaporative demand (Ma et al. 2006). Therefore, the dry down cycles are short, which is reflected in the high temporal σ^o variability.

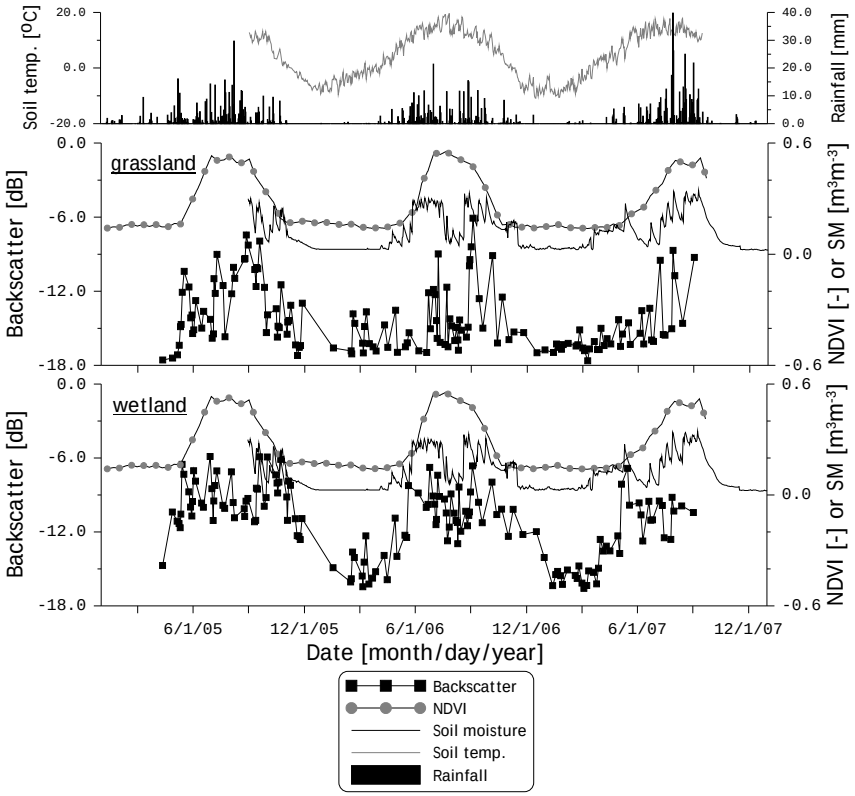

Figure 7-2 Time series of soil moisture, incidence angle normalized σ^o and NDVI over 1x1 km² grassland area and a 1x1 km² wetland area. Soil temperature and daily precipitation amounts are presented at the top.

7.4 Spatial σ^o variability

The influence of land surface conditions on the temporal σ^o variability is described above. For studying the effects of those land

surface dynamics on the spatial σ^o variability, the mean σ^o and its standard deviation (stdev) computed for the four domains (as defined in Figure 7-1) is analysed. Figure 7-3 presents for each domain the mean σ^o plotted against the σ^o stdev. Characteristic for the data point distribution in those plots is the triangular shape consistently observed for all four domains. This particular shape is explained as follows and by the diagram shown in Figure 7-4.

The lowest mean σ^o and σ^o stdev represent dry and frozen conditions. Because drought and freezing conditions have an impact on large areas, the spatial σ^o variability is small and the σ^o stdev is primarily caused by speckle and spatial surface roughness variations. Comparison of the minimum stdev's obtained from the different domains shows that the spatial σ^o variability increases with the size of the domain. This might be expected because over larger domains the spatial variability due to roughness increases.

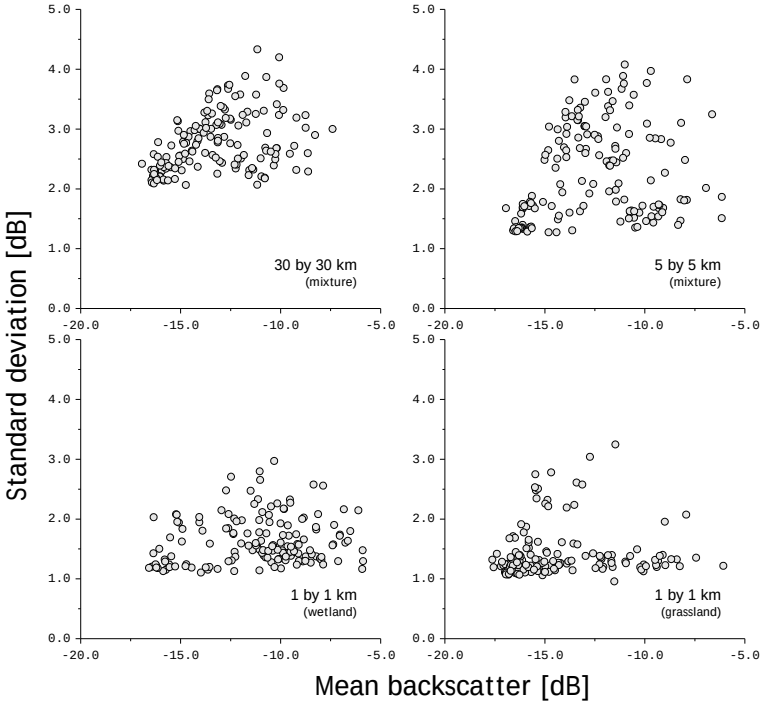

Figure 7-3 The standard deviation plotted against the mean σ^o measured by ASAR over four domains around Naqu station.

The mean σ^o value increases under conditions where liquid soil moisture is present. When freeze/thaw cycles and precipitation are spatially homogeneous, the σ^o variability remains relatively low. The σ^o variability increases due to spatial differences in soil thermal and hydraulic properties, and precipitation inputs.

For each of the four domains, a well-defined and linear relationship exists between the mean σ^o and maximum stdev at specific mean σ^o levels, and its slope could be seen as measure for the surface heterogeneity of a specific domain. Steeper slopes indicate a larger surface heterogeneity. For the 5x5 km^2 domain, the slope is steepest and its surface heterogeneity is considered to be the largest of the four domains. This is, however, also influenced by the distribution of wetlands and grasslands in the selected areas, because differences in land surface conditions between wetlands and grasslands persist, specifically during the monsoon. The similarity between the slopes in plots of the 30x30 km^2, and 1x1 km^2 wetland and grassland domains is striking and suggests a similarity in the surface heterogeneity between these areas.

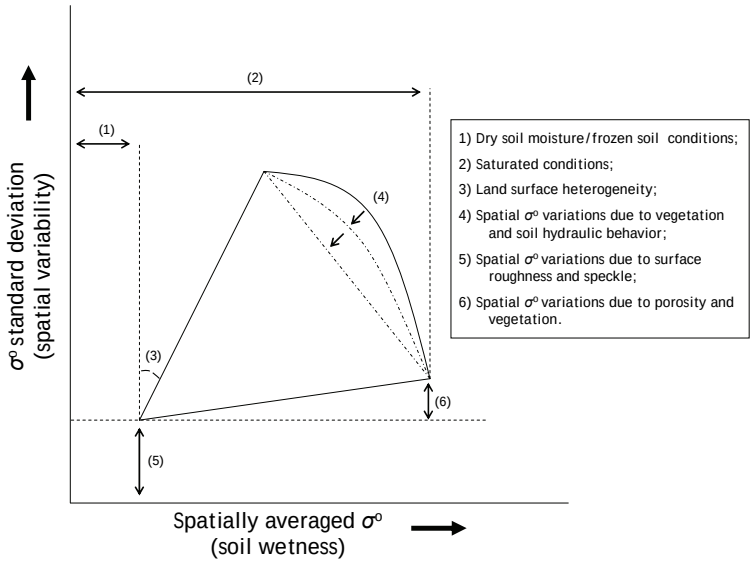

Figure 7-4 Schematization of the relationship between the mean σ^o and the standard deviation, and its coherence with specific land surface conditions and characteristics.

Additionally, it should be noticed that for the grassland domain the number of data points with a high stdev is small. Soils in the grasslands are sandy and have a high hydraulic conductivity. Over short time periods, soil moisture is transported from the top to deeper soil layers. Spatial variations due to dry-down cycle diminish, therefore, quickly and are difficult to capture at an averaged temporal resolution of 6-days.

During monsoon periods, land surfaces are wetter and vegetation grows, which both lead to an increase in the average σ^o values. Simultaneous to these higher mean σ^o values, their spatial variability

decreases for three reasons. Firstly, high σ^o values are only obtained when the entire domain is at or near saturation. Secondly, vegetation attenuates the soil surface scattering contribution and reduces the σ^o sensitivity to soil moisture changes. Thirdly, the σ^o response is less sensitive to soil moisture changes under wet than under dry conditions. This decreasing σ^o sensitivity to soil moisture due to either vegetation or soil wetness reduces the impact of spatial soil moisture variations on the σ^o variability.

Further, the plots show that the σ^o variability is higher under saturated than under dry conditions, which is caused by a combination of spatial variations in the porosity and vegetation. The increase in the spatial variability is stronger for larger domains (30x30 km^2 and 5x5 km^2) than the 1x1 km^2 domains, which is expected because the variability in the porosity and vegetation tend to increase over larger distances.

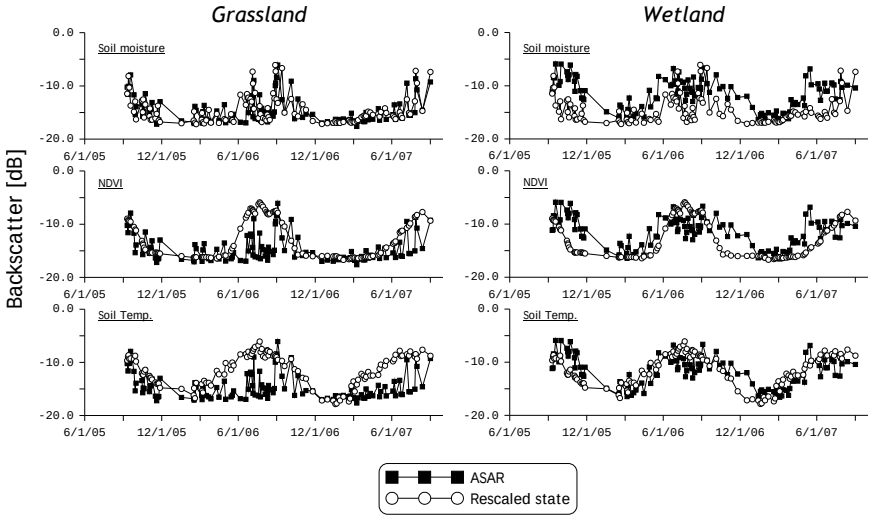

Figure 7-5 Time series of the grassland and wetland σ^o and soil moisture, NDVI and soil temperature rescaled to the dynamic grassland and wetland σ^o range, respectively.

7.5 Multivariate analysis

In addition, a multivariate analysis is performed to quantify statistically the impact of the land surface states variations (e.g. NDVI, soil moisture and temperature) on the σ^o observed over the 1x1 km^2 grassland and wetland areas. For this analysis, the dynamic ranges of the states are normalized by rescaling the NDVI, soil moisture and temperature to the dynamic σ^o range following,

$$x_{\mathrm{dB}} = x_{\min} + \left(\sigma^{o}_{\max} - \sigma^{o}_{\min}\right)\frac{x_i - x_{\min}}{x_{\max} - x_{\min}} \qquad (7.2)$$

where, x is the land surface state, subscripts $_i$, $_{\min}$ and $_{\max}$ indicate a member, and the minimum and maximum values of the data set, respectively, and subscript $_{\mathrm{dB}}$ represents the land surface state rescaled to the dynamic σ^o range. This rescaling of the land surface states has been performed for the part of the ASAR data set for which the NDVI, soil moisture and soil temperature measurements are available, which is from 10 September 2005.

Figure 7-5 presents the time series of the rescaled land surface states, and the grassland and wetland σ^o. This figure shows that the NDVI explains grassland σ^o variability only on a seasonal time scale. The σ^o variations over short periods are best described by the temporal evolution of the rescaled soil moisture measurements. Also, some correlation is observed between soil temperature changes and the σ^o variations during winter.

This correlation between the σ^o and soil temperature is, however, more pronounced for the wetland. Annual cycles of soil temperature and wetland σ^o match very well; specifically, the onset of the soil temperature and wetland σ^o increase in spring coincides for both 2006 and 2007. The rescaled soil moisture characterizes only a part of the σ^o variations over short time scales. It should, however, be noted that the soil moisture measurements have not been collected directly in the wetland, which explains the differences between the wetland σ^o and soil moisture dynamics.

Table 7-1 Variance (s^2) of backscatter measurements (σ^o) collected over a Tibetan grassland and wetland, and normalized soil moisture (sm), NDVI and soil temperature (T_{soil}) and correlations calculated between the original variables.

	σ^o	*sm*	*NDVI*	T_{soil}	s^2
Grassland					
σ^o	1.00	0.59	0.47	0.43	6.11
sm		1.00	0.66	0.66	10.77
NDVI			1.00	0.83	17.27
T_{soil}				1.00	9.11
Wetland					
σ^o	1.00	0.62	0.56	0.64	8.03
sm		1.00	0.67	0.66	9.68
NDVI			1.00	0.85	13.46
T_{soil}				1.00	8.19

Further, a clear discrepancy is noted between the wetland σ^o and NDVI annual cycles. With respect to the wetland σ^o, the NDVI

increase in spring is delayed and the NDVI decrease in the post-monsoon season starts earlier. This is caused by the runoff from upstream areas, which increases the soil moisture in the wetland and σ^o. In spring, the runoff produced by melt increases the soil wetness and, in the post-monsoon season, runoff from rain ensures a gradual drying of the wetland, while the temperatures in these two periods are too low to sustain a large biomass.

In support of this descriptive analysis, variances of the σ^o and the normalized NDVI, soil moisture and soil temperature, and correlation coefficients between the original variables were calculated and are presented in Table 7-1 for both the grassland and wetland. Here, the variance, s^2, and correlation coefficient, ρ, are defined by:

$$s^2 = \frac{\sum (x_i - \overline{x})^2}{n-1} \tag{7.3}$$

$$\rho = \frac{\sum (x_i - \overline{x})(y_i - \overline{y})}{\sqrt{\sum (x_i - \overline{x})^2 \sum (y_i - \overline{y})^2}} \tag{7.4}$$

where n is the number of observations, x and y represent the independent variables (e.g. σ^o, NDVI, soil moisture and temperature) and the overbar indicates the mean of a variable.

As expected, Table 7-1 shows that, for the grassland σ^o, the largest ρ's are obtained with the soil moisture. However, for the wetland, the statistics computed between σ^o and soil temperature, and between σ^o and soil moisture are comparable. Further, it should be noted that, although some correlation is observed between the soil temperature and grassland σ^o during winter, low statistics are obtained. An explanation is that very little correlation exists between the soil temperature and σ^o during the monsoon, which reduces the overall value of ρ.

A quantification of the relationship between land surface conditions and temporal σ^o variations requires also considering the cross-correlation between states. For example, a high ρ of 0.85 (wetland) and 0.83 (grassland) are found between the NDVI and soil temperature. Thus, the NDVI contains similar information for describing the σ^o variations as the soil temperature measurements. A more thorough evaluation of the impact of the three land surface states on the σ^o is performed through a multivariate regression of four empirical linear models, which are defined as follows:

Model 1: $$\sigma^o_{\mathrm{mod}1} = A \cdot sm_{dB} \tag{7.5}$$

Model 2: $$\sigma^o_{\mathrm{mod}2} = A \cdot sm_{dB} + B \cdot NDVI_{dB} \tag{7.6}$$

Model 3: $$\sigma^o_{\mathrm{mod}3} = A \cdot sm_{dB} + C \cdot STEMP_{dB} \tag{7.7}$$

Model 4: $$\sigma^o_{\mathrm{mod}4} = A \cdot sm_{dB} + B \cdot NDVI_{dB} + C \cdot STEMP_{dB} \tag{7.8}$$

where, sm_{dB} is the rescaled soil moisture [dB], $NDVI_{dB}$ is the rescaled NDVI [dB], $STEMP_{dB}$ is the rescaled soil temperature [dB], A, B and C are empirical regression coefficients and σ^o_{mod1}, σ^o_{mod2}, σ^o_{mod3} and σ^o_{mod4} are the simulated σ^o using model 1, 2, 3 and 4, respectively.

Table 7-2 Regression coefficients obtained for four linear models by minimizing the RMSD calculated between the modelled and measured σ^o over a Tibetan grassland and wetland for the period 10 September 2005–30 July 2005 and RMSD computed separately for calibration (56 points) and validation (61 points) periods.

	A	*B*	*C*	RMSD [dB] Calibration	RMSD [dB] Validation
Grassland					
Model 1	0.986	-	-	1.92	1.35
Model 2	0.821	0.169	-	1.84	1.32
Model 3	0.610	-	0.437	1.73	1.55
Model 4	0.604	–0.009	0.456	1.73	1.56
Wetland					
Model 1	0.792	-	-	2.26	2.24
Model 2	0.448	0.394	-	2.11	1.90
Model 3	0.368	-	0.561	2.01	1.63
Model 4	0.363	–0.041	0.612	2.01	1.64

The regression coefficients are fitted by minimizing the root mean squared difference (RMSD) between the modelled and measured σ^o for the period 10 September 2005 to 30 July 2006 (56 points). The optimized regression coefficients for the grassland and wetland are presented in Table 7-2. The RMSD values obtained for the calibration and validation (61 points) periods are also given in Table 7-2. A comparison of these RMSD's shows, somewhat surprisingly, a better agreement of modelled and measured σ^o for the validation set. This can explained by the larger σ^o and soil moisture variations measured over short time scales included in the calibration set.

Further, Figures 7-6 and 7-7 present plots of the modelled and measured σ^o against time for the grassland and wetland, respectively. In these plots, absolute differences between the modelled and measured σ^o ($\Delta\sigma^o$) and the standard deviation of the σ^o within the defined areas (stdev σ^o) are given on the secondary y-axis. The stdev σ^o is used, here, to represent the various sources of uncertainty within the mean σ^o values, such as the applied incidence angle normalization, spatial representation, speckle and calibration of the ASAR instrument. On average, this stdev σ^o is 1.38 and 1.65 dB for the grassland and wetland, respectively.

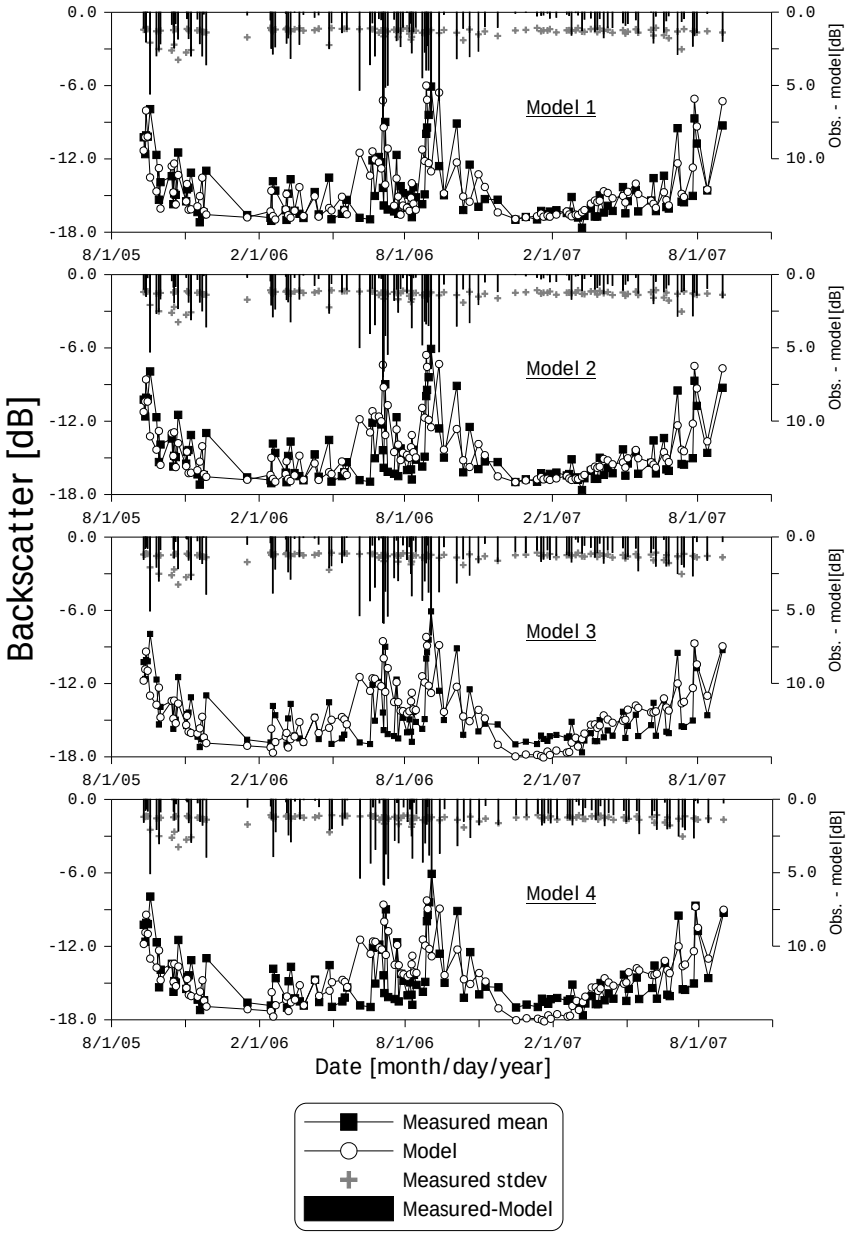

Figure 7-6 Modelled and measured grassland σ^o plotted against time, whereby the modelled σ^o is obtained through a multivariate regression of four linear models. On the secondary y-axis the stdev σ^o and the $\Delta\sigma^o$ are plotted.

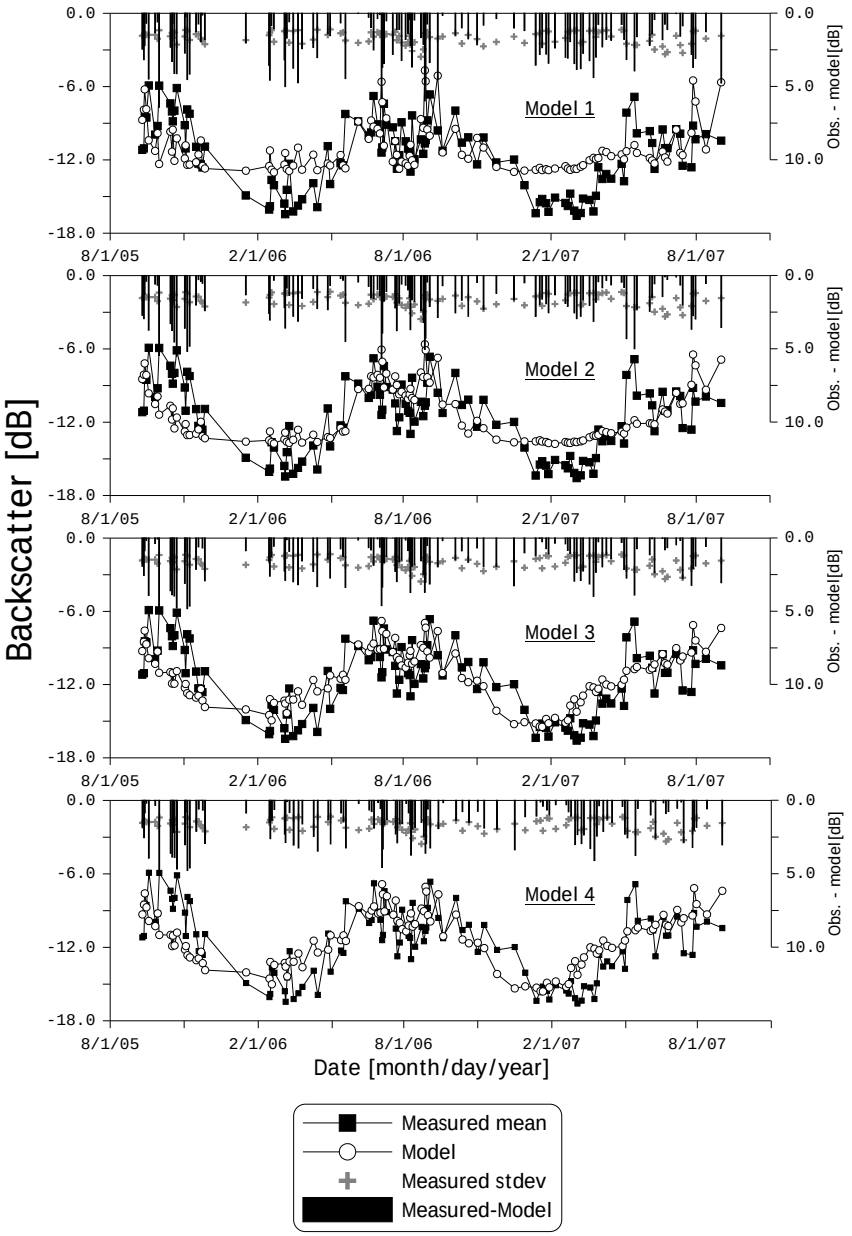

Figure 7-7 Same as Figure 7-6 except the multivariate regression results of the wetland are shown.

Figure 7-6 shows that soil moisture is the dominant land surface state affecting the grassland σ^o, which is also supported by the large values of A (0.986–0.604). Including the NDVI in the empirical model reduces the RMSD obtained for both the calibration and validation periods, but only by 0.08 and 0.03 dB, respectively. Adding the soil

temperature to the linear models leads to a more significant reduction of the RMSD (on averaged 0.20 dB), but results in an equally large RMSD increase for the validation period. In the calibration set, soil temperature and σ^o increments are partially correlated during the winter, which was previously attributed to the melting of frozen soil water. These freeze/thaw effects are less marked in the winter season included in the validation set. This causes a bias in the winter period of the validation set and explains the difference between the calibration and validation RMSD values. Further, it should be noted that relatively large $\Delta\sigma^o$ values (up to 7.0 dB) are obtained in summer when the soil moisture conditions are wetter. Since the regression models with NDVI do not yield significantly better results, it is assumed that differences in the spatial representation of the soil moisture and grassland σ^o cause this larger $\Delta\sigma^o$.

As is indicated by the lower A values (0.792 for Model 1 to 0.363 for Model 4), the impact of soil moisture on σ^o is less pronounced for the wetland. With Model 1, a systematic underestimation of the σ^o is obtained during the winters because of the different dynamics of the soil moisture measurements and the wetland conditions. The largest discrepancies between measured and actual wetland soil moisture are expected to occur when the temporal soil moisture variability is high, which is during the monsoon. To compensate for these differences, the regression of Model 1 results in a bias towards the summer σ^o values. This bias is somewhat reduced by including NDVI in the regression (Model 2). The largest improvement is, however, obtained through incorporation of the soil temperature (Model 3), while adding the NDVI into the linear model (Model 4) does not further improve the results.

This multivariate regression illustrates that, within linear models, the NDVI contributes only a little to explaining the temporal σ^o variability observed over Tibetan grassland and wetland areas. Over the grassland, σ^o is mostly affected by the soil moisture and the wetland σ^o is best described by the annual soil temperature cycle, while the soil moisture impact is less dominant. Comparison of RMSD with stdev σ^o shows that the regression results are acceptable, but could be better when using a more physically-based modelling concept such as the ones applied in Chapters 5 and 6. Besides, differences in the spatial representation of the point-scale soil moisture measurements and the spatially-averaged σ^o values also explain part of the somewhat large RMSD values.

7.6 Conclusions

The impact of land surface states on spatial and temporal σ^o variability measured by ASAR has been analysed for four spatial domains on the Tibetan Plateau. The selected spatial domains have

areas of 30x30, 5x5 km^2 and 1x1 km^2 (two domains). The 30x30 km^2 and 5x5 km^2 domains are covered by a mixture of grasslands and wetlands, while for the 1x1 km^2 domain a grassland and wetland have been selected.

The temporal evolution of σ^o observed over the 1x1 km^2 grassland and wetland areas is studied to identify its relation to land surface states. Over the grassland as well as wetland, the lowest σ^o values are obtained during winters, because, in this season, the soil water is predominantly frozen resulting in dielectric properties that are comparable to dry soil conditions. Towards the summer, the wetland σ^o increases gradually and reaches its maximum extent when the monsoon is at peak intensity, while the grassland σ^o in the summer is characterized by large temporal variations. This contrast in the grassland and wetland temporal σ^o variability is attributed to the accumulation of runoff in wetlands and the short dry-down cycles of the grasslands.

The relation between the spatial σ^o variability and the land surface conditions is evaluated by comparing the mean σ^o with the stdev measured in the four domains. This results in very specific triangular data point distributions for all domains. The decrease of σ^o stdev as the mean σ^o decreases is observed because dry and freezing conditions have an impact on large areas and are typically spatially homogeneous. During the monsoon, however, intensive rain showers may saturate large areas. A decrease in the σ^o stdev is, therefore, observed as the mean σ^o approaches its maximum value. This impact of the land surface dynamics during monsoon and winter periods on the σ^o variability is consistently observed for all four domains.

When these σ^o dynamics are considered to be representative for the soil moisture conditions, a consequence of the reported results is that the relationship between mean soil moisture and the spatial variability is not always uniquely defined. In downscaling coarse resolution soil moisture products changes in the relationship between the mean soil moisture and spatial variability should be considered, and should ideally be obtained on additional near real time data sources. In this context, SAR data could be utilized to provide soil moisture information within the coarse passive microwave and scatterometer footprints.

Moreover, a multivariate regression analysis is presented to statistically quantify to contribution of specific land surface states (e.g. biomass, soil moisture and temperature) in describing the temporal σ^o variations observed over the 1x1 km^2 grassland and wetland areas. Here, the biomass is represented by the NDVI as a proxy. This analysis shows that the NDVI explains only a small portion of the σ^o variations over both the Tibetan grassland and wetland. Further, a discrepancy is noted between the annual cycle of

the NDVI and the wetland σ^o. The NDVI increase starts later than the wetland σ^o and the decrease is observed earlier than that for wetland σ^o. This supports the hypothesis that the land surface conditions in the wetland are strongly affected by runoff from upstream areas produced by melt in spring and by rainfall in the post-monsoon season. The temporal σ^o variability observed over the grassland σ^o is best described by the soil moisture, while a small correlation is found with the soil temperature.

8 Soil moisture mapping over the Central Tibet

This chapter is based on:

Van der Velde, R., Su, Z., Van Oevelen, P.J., Wen, J., Ma, Y., "Soil moisture mapping over the central Tibet using a time series of ASAR WS images", to be submitted to *Remote Sensing of Environment*.

8.1 Introduction

The influence of land surface state on the time series of ASAR WS data was discussed in the previous chapter for a typical grassland and wetland on the Tibetan Plateau. This analysis showed that for both land covers the temporal σ^o variability is best described by soil moisture, while the effects of vegetation has only a minor impact. Here, this soil moisture information included in the ASAR data set is used for soil moisture mapping.

Considerable success in retrieving soil moisture from both active and passive microwave observations has previously been obtained at continental and global scales (e.g. Jackson et al. 1999, Woodhouse and Hoekman 2000, Owe et al. 2001, Le Hegerat 2002, Wen et al. 2003). As a result, space borne microwave instruments capable of monitoring soil moisture globally have either become recently operational (e.g. ASCAT and SMOS) or are approved for launch (e.g. Aquarius, SMAP). This will open up new opportunities for monitoring soil moisture globally. However, a fairly low spatial resolution is characteristic for the measurements gathered by these sensors, which is on the order of tens of kilometers.

An alternative is provided by active microwave measurements obtained via the SAR technique, which can be processed to resolutions of several meters. A large number of studies have demonstrated the potential of retrieving soil moisture at a resolution in the order of tens of meters (e.g. Quesney et al. 2000, Le Hegerat et al. 2002, Oldak et al. 2003). This high resolution poses, however, restrictions on the revisit times, which were 35 days and longer for the first generation SAR systems (e.g. RadarSat-1, ERS-1/2, JERS). Soil moisture retrieved at those temporal resolutions has only a limited hydrological applicability (e.g. Hoeben and Troch 2000, Walker and Houser 2004).

In the design of the following generation of space borne SAR systems this issue was addressed by incorporating imaging modes for measuring σ^o at various spatial resolutions, swath widths and revisit times. The high resolution, multi-angular σ^o measurements collected

by RadarSat-1/-2 and ASAR have already been used extensively for soil moisture retrieval purposes (e.g Mattia et al. 2006, Alvarez-Mozos et al. 2006, Baghdadi et al. 2006, Zribi et al. 2007, Rahman et al. 2008). The combination of different image swaths offers the possibility for obtaining a higher temporal resolution over a specific study area. These high spatial resolution imaging modes are, however, less suited for monitoring purposes over large spatial domains because its spatial coverage is restricted to swath widths of about 100 km.

In this context, wide swath (WS) and global monitoring (GM) modes provide a good compromise between the spatial coverage (400 km), resolution (150 m for WS and 1000 m for GM) and revisit time (3-4 days). A consequence of operating at a wider swath is, however, the rather large view angle range (about 16-43 degrees). In most studies, SAR observations collected over a wide range of view angles are normalized to a specific angle. In the previous chapter, a theoretical approach was adopted for this normalization. In other studies (Baup et al. 2007b, Löw et al. 2006, Pathe et al. 2009) regression functions between the σ^o and incidence angle are used. A drawback of such normalizations is that a specific angular response has to be assumed. This angular response is, however, also represented within physically based scattering models. Zribi and Dechambre (2002) and Rahman et al. (2008) use this property of models to derive a parameter for estimating the surface roughness, which is used for the retrieval of soil moisture from high resolution multi-angular σ^o measurements.

In this chapter, a similar approach is adopted for estimating the roughness parameterization of the AIEM surface scattering model and the retrieval of soil moisture. Three ASAR WS images collected at different view angles under assumed constant land surface conditions is used to invert the roughness parameters of the AIEM model. Then, assuming the surface roughness to be temporally stable and the effects of vegetation to be negligible, soil moisture is retrieved from the ASAR data set by inverting the AIEM model. Validation of the retrievals is performed quantitatively against measurements collected at four different stations within a 10x10-km^2 domain and, for the study area described in Chapter 4, qualitatively by evaluating the spatial distributions of the retrievals.

8.2 Retrieval algorithm

The applied retrieval method is based on the AIEM model, which requires, apart from dielectric properties, a surface roughness parameterization and the sensing configuration as input, including the incidence angle. Minimization of the absolute difference between the ASAR and AIEM simulated σ^o is used to invert the dielectric constant.

This dielectric constant is, then, converted into soil moisture using the mixing model by Dobson et al. (1985) and soil texture information obtained from 1 km resolution global maps (Reynolds et al. 2000). Figure 8-1 presents a diagram of this retrieval algorithm. The algorithm is, thus, solely based on the AIEM surface scattering model. This implicates that the vegetation effects on ASAR WS σ^o measurements are assumed negligible, which is justifiable based on the results presented in the previous chapter.

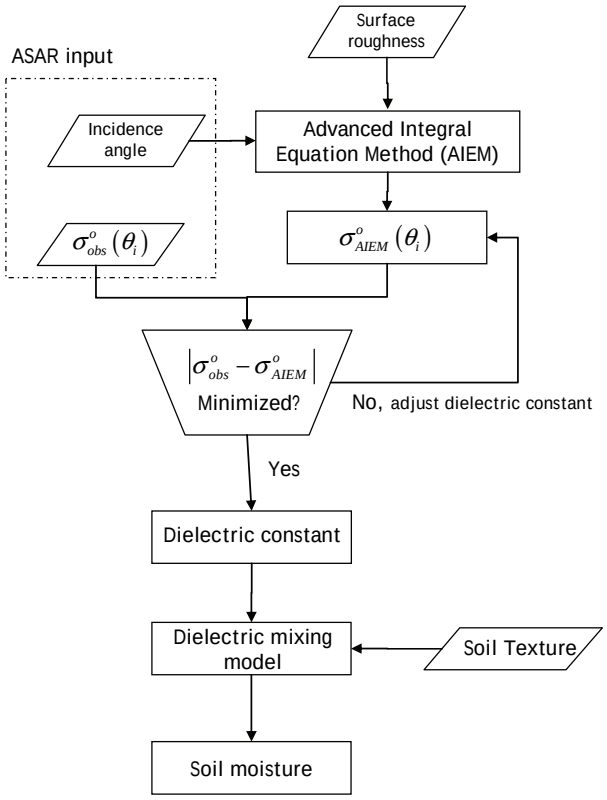

Figure 8-1 Outline of the soil moisture retrieval algorithm.

8.3 Surface roughness estimation

Crucial for the performance of the described retrieval algorithm is a proper estimation of the surface roughness parameters needed for the AIEM. As explained in Chapters 2 and 6, the AIEM roughness parameterization consists of the rms height (*s*), autocorrelation length (*l*) and autocorrelation length function (ACF). It is shown in Chapter 6 (and other investigations cited therein) that simulations with the Exponential ACF characterize the angular response over bare soil surfaces best. An Exponential ACF is, therefore, assumed as input

for the AIEM. This leaves the roughness parameters, *s* and *l*, as the two remaining unknowns for retrieving the dielectric constant (or soil moisture).

For an agricultural setting, the effect of temporal roughness variations on soil moisture retrievals was discussed in Chapter 6. This showed that the roughness parameters estimated at the beginning of the growth cycle are representative for the roughness conditions during the entire growth cycle. Surface roughness conditions in natural environments are typically less variable than the ones in agricultural fields. This justifies the use of time-invariant parameterizations for the Tibetan wetlands and grasslands.

Even with assuming an Exponential ACF the estimation of a time-invariant parameterization remains a challenge. The dielectric constant (or soil moisture) has to be known for the σ^o simulation and the angular σ^o response included in the Tibetan ASAR WS data set needs to be properly simulated. Also, view geometry in azimuth direction should be taken into consideration for the roughness estimation, which is different for the ascending and descending orbit.

Table 8-1 Dates of ASAR WS acquisition used for surface roughness estimation and the view angle range at which the study area was covered.

Ascending		Descending	
Date	**View angle range** [degrees]	**Date**	**View angle range** [degrees]
02/15/2006	17.7 – 21.2	01/13/07	25.7 – 29.0
02/18/2006	26.6 – 30.1	01/26/07	38.2 – 42.5
02/21/2006	35.0 – 38.6	01/29/07	28.7 – 33.4

Information on the angular σ^o response is embedded within the series of ASAR WS images, which are collected at different view angles over the selected study area. Then, a period should be selected during which ASAR collected data at different view angles and the soil dielectric constant can be estimated with a reasonable accuracy. Such episode is most likely to be found during winters because in this season weather on the plateau is cold and dry. The water content present in the soil surface is, thus, very low and/or in frozen state. Under these conditions the soil dielectric constant is comparable to a dry soil. As these winter conditions often affect large spatial domains, it can be assumed that these dry soil dielectric properties are valid for the entire study area.

A sequence of ASAR WS acquisitions collected during the winter period can in potential be used for estimating the roughness parameters. This sequence of ASAR WS images should, however, be selected with care because an thawed soil surface has a significantly larger dielectric constant than a frozen soil. Moreover, the vast

amount of water present in the wetlands takes a long period of subzero temperatures to become completely frozen. This restricts the months suitable for roughness estimation to January and February, because before January water in the wetlands might not yet be frozen and after February the surface layer may melt.

Taking these restrictions into account, a set of three images collected in February 2006 and in January 2007 has been selected for estimating the roughness parameters, *s* and *l*, for the ascending and descending passes, respectively. Table 8-1 shows the date and view angle range, at which the study area was covered by ASAR. These two specific ASAR data sets have been selected because the images were acquired within a short period from each other and their view angle ranges cover a large portion of the total range.

From these two series of ASAR images, independent roughness parameterizations are estimated for the ascending and descending passes by minimizing the averaged absolute differences between the ASAR and AIEM simulated σ^0 collected at three view angles. For these AIEM simulations, the dielectric constant is assumed to be equivalent to that of a dry soil with a soil moisture content of 0.03 m^3 m^{-3}. A schematization of this method for estimating the surface roughness is presented in Figure 8-2.

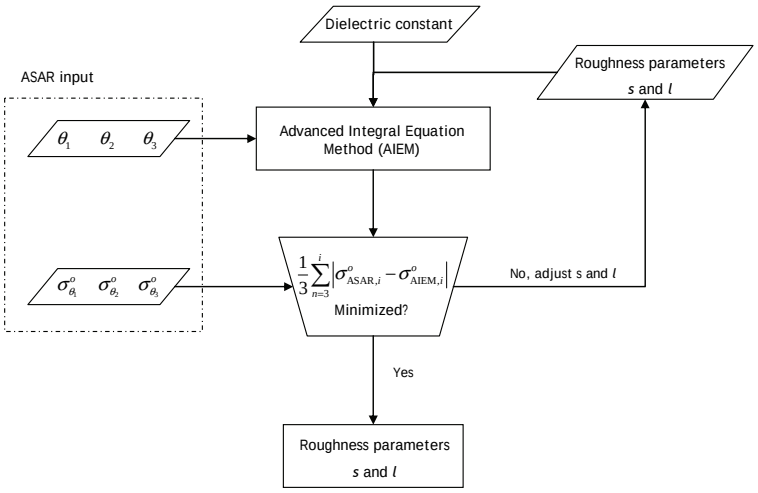

Figure 8-2 Schematization of the method used for the estimation of surface roughness parameters.

Validation of the inverted roughness parameterizations is not possible due to the absence of *in-situ* measurements. An indication of the range and distribution of the derived parameterizations is, however, given in the form of probability density function (PDF's) for the *s* and *l* in Figure 8-3. In addition, the cumulative probability of the

averaged absolute differences between the measured and the simulated σ^o is provided in Figure 8-3. The PDF's obtained for the roughness parameters show that the majority of the *s* values are centred on 0.38 and 0.30 cm for ascending and descending passes and peak of *l* values is located at about 1.7 and 0.8 cm, respectively. Further, the distribution of the parameters indicates a higher occurrence of larger values for both parameters, which is best represented by an exponential distribution function. This could, however, also be a consequence of assuming an exponential ACF.

The retrieved *s* values are of the same order of magnitude as the parameterizations presented in Chapter 6. However, the presented *l* parameters are significantly lower than the ones reported in Chapter 6. The soil surface of the corn field, for which the surface roughness was estimated in Chapter 6, has a distinctive periodic structure. The autocorrelation between surface height variations in the corn manifests itself, therefore, at a larger spatial scale for this agricultural field than for more randomly distributed roughness of natural environment. Therefore, lower *l* values are obtained for the Tibetan surface.

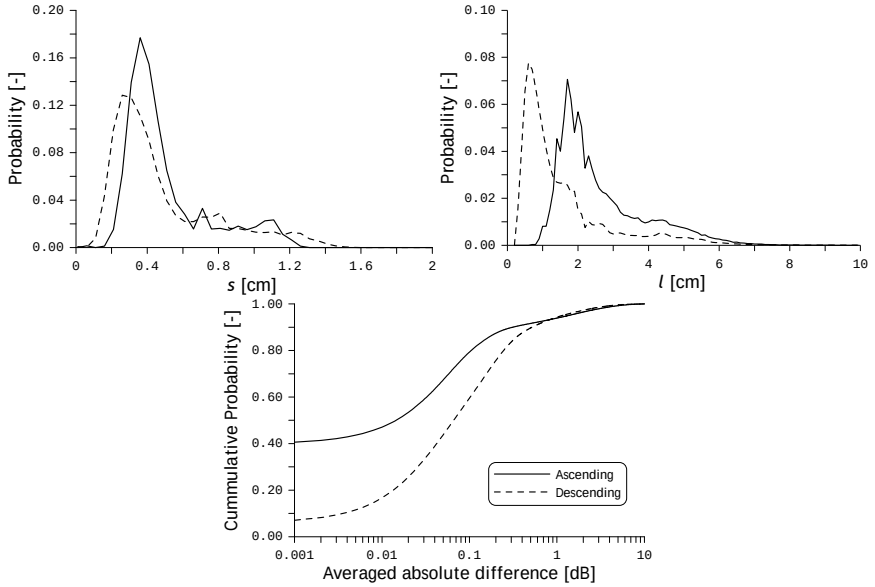

Figure 8-3 Probability density functions for the retrieved roughness parameters (*s* and *l*) and cumulative probability for the averaged absolute differences between the measured and simulated σ^o.

The cumulative probability shows that the averaged absolute σ^o differences for the ascending as well as descending passes is less than 0.5 dB for more than 90% of the parameterizations. This error level is similar to the radiometric stability of ASAR σ^o in the WS. The

combination of reasonable parameter values and small differences between the measured and simulated σ^o suggests that roughness parameters are reliably estimated.

8.4 Soil moisture mapping and validation

With the roughness parameters, *s* and *l*, as the main input for the algorithm described in Section 8.2, soil moisture is retrieved from the time series of ASAR WS images. Firstly, the reliability of the resulting soil moisture products is assessed by evaluating the time series of retrieved and measured soil moisture. Figure 8-4 presents the time series of soil moisture measured and retrieved at four stations. As described in Section 4.3, South station is located in a wetland and did not record any soil moisture measurements at the 2.5 cm soil depth. For this station, the soil moisture measured at 7.5 cm is, therefore, used for validation. For the stations (e.g. East, North and Naqu) situated within a grassland environment the soil moisture measured at 2.5 cm are presented.

Figure 8-4 shows that the soil moisture retrieved over the wetland site (south station) increases rapidly during spring 2005 and 2006, and remains wet (> 0.3 m^3 m^{-3}) throughout a large portion of the monsoon. In August 2005, however, the wetland soil moisture retrievals are close to 0.1 m^3 m^{-3}, while the retrievals over the grassland sites reach their peak values of about 0.2 m^3 m^{-3}. It is likely that during this period the soil surface in the wetland was flooded. A water surface reflects microwave specularly causing lower σ^o from the wetland and as a result the retrieved soil moisture is low. Similarly, there is a drop in wetland soil moisture in the beginning of July 2006. In this case, however, the retrievals from the grassland sites are also low. A prolonged period with less rain is most likely the cause for those low soil moisture values retrieved from the wetland site.

Unfortunately, the soil moisture measurement at South station started on 27 July 2006 and are, thus, not available for validation. For the second part of 2006, however, the measurements confirm that surface conditions in the wetland remain wet throughout the monsoon season. Also, the gradual soil moisture increase of the retrievals during 2007 spring agrees well with the coinciding measurements.

The weather during the monsoon affects the soil moisture dynamics of the grassland sites differently. As explained before, dry-down cycles on the Plateau are short due to a high evaporative demand and a large hydraulic conductivity of the soils. Both the retrieved and measured soil moisture at the grassland sites has, therefore, a larger temporally variability. On a seasonal time scale, the temporal evolution of the retrievals is in agreement with the

measurements. During extreme wet episodes, such as August 2005, the retrieved soil moisture is high on average and during prolonged dry periods, such as July 2006, the retrieved soil moisture is low. On smaller time scale, however, large discrepancies are noted between the measured and retrieved soil moisture. The measurements are collected at single location, while soil moisture is retrieved from σ^o with a 75 m spatial resolution. Because spatial soil moisture variability is large, the difference in scales of the measurements and retrievals contributes to the somewhat larger deviations observed for the grassland sites.

For quantification of the differences between the retrieved and measured soil moisture, separate scatter plots for the wetland and grassland sites are presented in Figure 8-5. The basic statistics related to this comparison, such as the RMSD, bias and R^2, are given in Table 8-2. These statistics are also shown for the individual stations.

Table 8-2 Statistics computed between the retrieved and measured soil moisture.

`		**Land cover**		**Soil moisture station**			
		wetland	*grassland*	*South*	*East*	*North*	*Naqu*
Number of pairs	[#]	63	236	63	58	60	118
RMSD	[m^3 m^{-3}]	0.060	0.032	0.060	0.027	0.026	0.034
Bias	[m^3 m^{-3}]	-0.018	0.005	-0.013	-0.008	0.003	0.012
R^2	[-]	0.667	0.544	0.667	0.668	0.642	0.503

The scatter plots illustrate that positive relationships exist between the soil moisture measured and retrieved from both the wetland and grassland site(s). This is supported by the R^2 that varies from 0.667 for South station to 0.503 for Naqu station, which is of a similar level as has been previously reported (e.g. Löw et al. 2006, Baup et al. 2007b, Pathe et al. 2009). Comparable to the retrievals presented in Chapter 5, the retrievals overestimate the measurements in the wetland as well as the grassland under wet conditions. As explained before, this is due to the fact that the AIEM σ^o is less sensitive to soil moisture under wet conditions. In the scatter plot of the grassland sites also a significant underestimation of the measured soil moisture is noted under dry conditions. A large vertical soil moisture gradient could be an explanation. It is very common that a shallow topsoil layer may become very dry, while deeper in the profile the soil remains somewhat wet. A particular volume of the topsoil is observed by the incident microwave radiation, while the sensor is place at a soil depth of 2.5 cm.

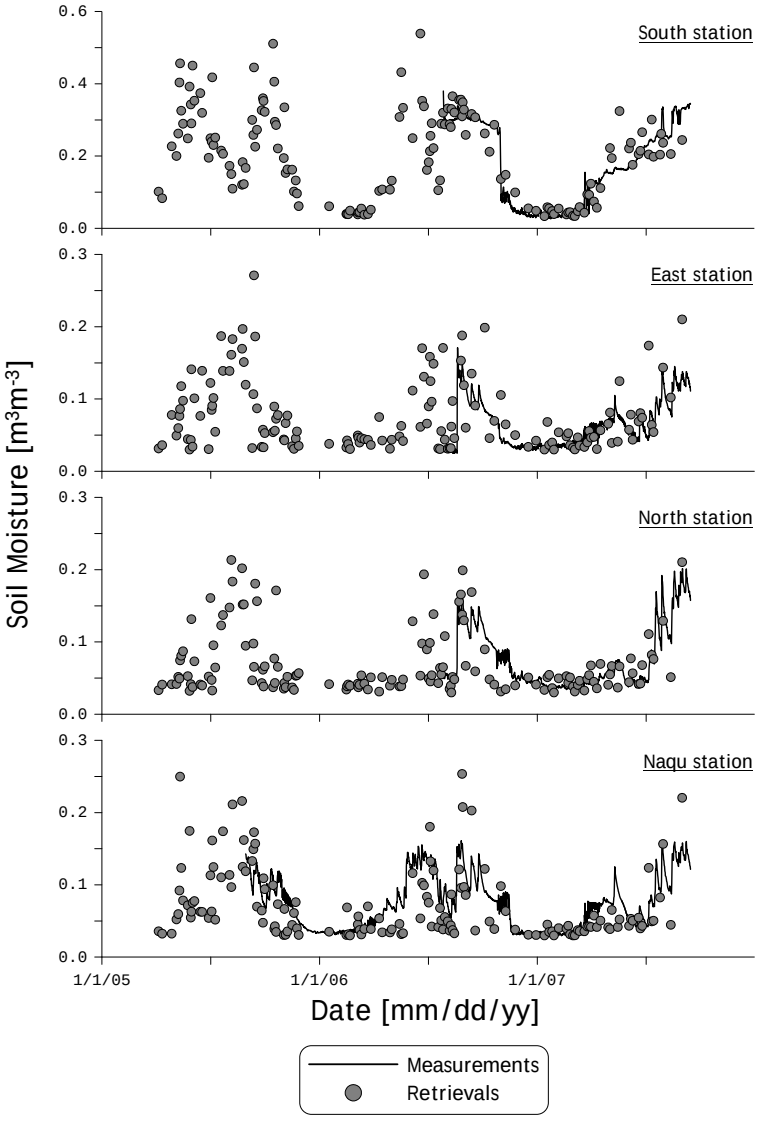

Figure 8-4 Time series of soil moisture measurements and retrievals from one wetland site (South station) and three grassland sites (East, North and Naqu station).

In spite of these differences between the retrievals and measurements, the obtained uncertainty levels are comparable to the results of previous SAR based soil moisture retrieval studies (e.g. Dubois et al. 1995, Shi et al. 1997, Bindlish and Barros 2000, Thoma et al. 2006, Rahman et al. 2008). RMSD's of 0.060 and 0.032 $m^3 m^{-3}$ are computed for the wetland and grassland sites, respectively, and the biases are smaller than 0.02 $m^3 m^{-3}$. The wetland RMSD is, thus,

almost two times larger than grassland RMSD. The measured soil moisture ranges in these two land covers are, however, also different and varies from 0.027 to 0.38 $m^3 m^{-3}$ for the wetland site and from 0.026 to 0.210 $m^3 m^{-3}$ for the grassland sites. When this is taken into account through the division of the RMSD by the dynamic soil moisture range, the retrieval uncertainties obtained over the wetland and grassland sites are quite similar, 16.9 and 17.3 % respectively

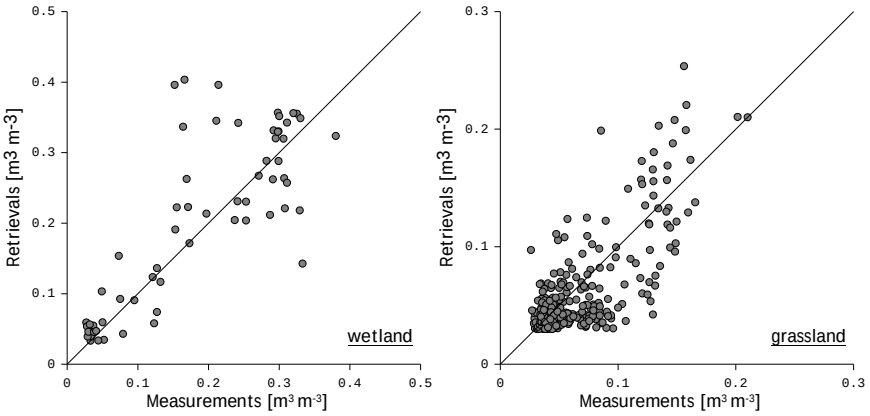

Figure 8-5 Scatter plots between the retrieval and measured soil moisture; on the left results of the wetland site and on the right results of the grassland sites.

So far the time series of soil moisture retrievals was only discussed for the sites at which soil moisture measurements are available. These stations are located in a 10x10 km^2 area about 25 kilometers southwest of Naqu city and, thus, do not give a good representation of the spatial distribution in the entire study area. As an illustration of the retrieved spatial distributions, a selection of the soil moisture maps obtained during the 2005 and 2006 monsoon seasons are presented in Figure 8-6 and 8-7, respectively. The maps are selected in such way that for about every 30 days three images are shown starting from the beginning of May till the end of October.

The series of soil moisture images for both 2005 and 2006 clearly shows the impact of the monsoon development on the retrieved soil moisture. In the beginning of May, low soil moisture values are retrieved over almost the complete study domain. In several parts of the study domain, however, already elevated soil moisture levels can be noted. The moisture content retrieved in these areas increase rapidly to values larger than 0.30 $m^3 m^{-3}$ and remains quite stable for the following months, which is typical for the dynamics in a wetland.

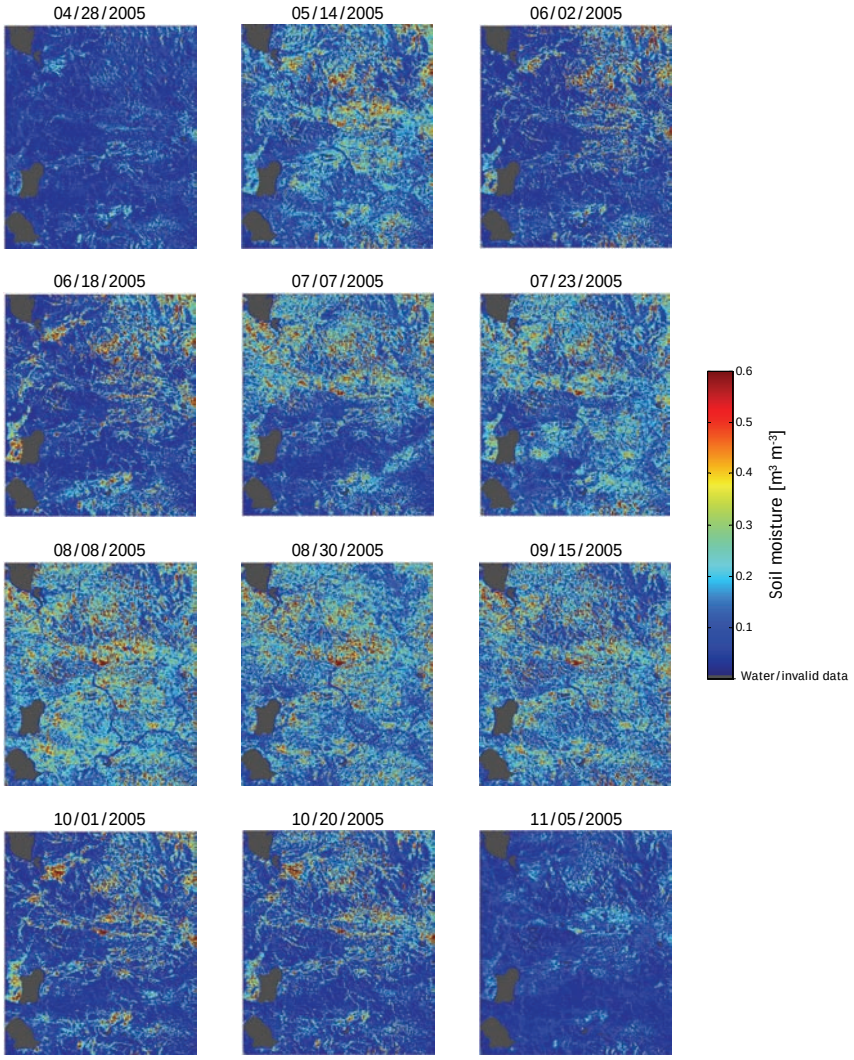

Figure 8-6 Series of soil moisture maps retrieved from ASAR acquisitions during the 2005 Monsoon.

A soil moisture increase in areas other than the wetlands is evidence for the first intensive rain event of the monsoon season. In 2005 such moisture increase is noted on May 14th, while it occurs on June 6th for 2006. It should, however, be noted that the soil moisture maps are snapshots and land surface conditions between SAR acquisitions is, thus, unknown. After this first rain, soil moisture increments are observed around the drainage patterns and, of course, in the wetlands. However, the large-scale soil moisture increase characteristic for the peak of the monsoon stays off till July

for both 2005 and 2006, except in case of some scattered rain events.

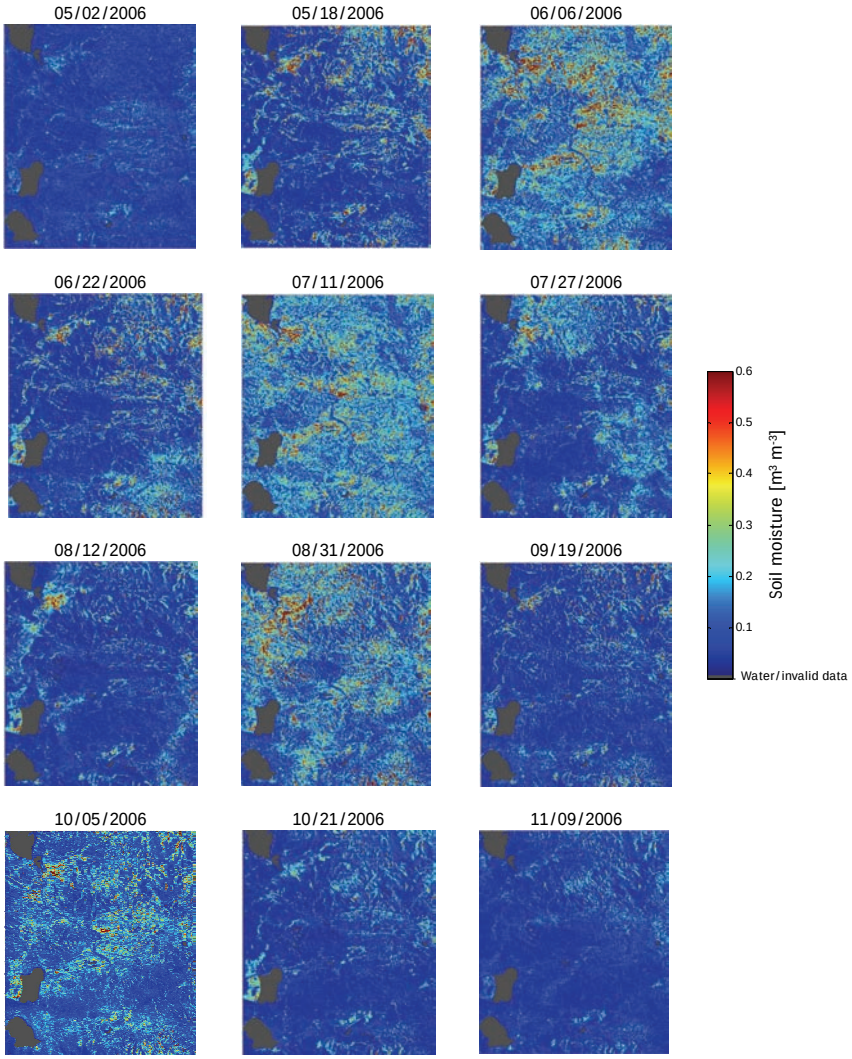

Figure 8-7 Series of soil moisture maps retrieved from ASAR acquisitions during the 2006 Monsoon.

In 2006, this large-scale soil moisture increase is observed on July 11, while in July 2005 the southern part of the study domain still includes a large dry region. The retrieved soil moisture from the images acquired in August (and September) 2005 shows, however, high values across the entire study domain. In these soil moisture maps lower soil moisture values are retrieved over wetlands. As described before, this is explained by the flooded soil surface in the

wetlands, which results in lower σ^o measurements due to specular reflectance. Conversely, significantly lower soil moisture values are retrieved at the end of July and the start of August in 2006. Only, the August 31 map shows comparable soil moisture levels as in 2005. These differences between the 2005 and 2006 dynamics were also noted in analyzing the time series of soil moisture retrievals. The gradual decline in soil moisture in October indicates the end of the monsoon in 2005 and 2006. During this dry-down, the moisture in the wetlands is most persistent.

8.5 Conclusions and discussion

Soil moisture is retrieved from a time series of σ^o images acquired by the ASAR in the WS mode over the central part of the Tibetan Plateau. The employed retrieval algorithm is based on the AIEM, whereby the angular σ^o response is explicitly modelled instead of normalizing for the view angle. Within this retrieval procedure the effects of vegetation on the ASAR σ^o measurements are, thus, assumed to be negligible, which is justified based on the results presented in Chapter 7.

The surface roughness parameterization needed for AIEM simulations is inverted from a sequence of three σ^o measurements collected at different view angles and assumed dry conditions. As the dielectric properties of frozen soils are equivalent to the ones of dry soil, this assumption will be valid during the cold and dry Tibetan winters. As such, a set of three images collected in February 2006 and in January 2007 has been used to invert the surface roughness for the ascending and descending passes, respectively. This inversion resulted for more than 90% of the parameterizations in an absolute difference between the ASAR and simulated σ^o of less than 0.5 dB for the ascending as well as descending orbits. These roughness parameters have been used as input for the retrieval of soil moisture from the ASAR σ^o through inversion of the AIEM model.

An analysis of soil moisture retrievals and measurements collected at a wetland site and three grassland sites shows that on a seasonal time scale the retrievals are in agreement with the measurements. The soil moisture retrieved over the wetland site displays a sharp increase in spring and sharp decrease at the end of the monsoon, and remains, in general, fairly stable near saturation throughout the monsoon. Only, in case of extreme dry and wet episodes the retrieved soil moisture is lower. This might seem somewhat contradictory because the σ^o over wet soils is higher than for dry soils. However, under wet conditions the soil surfaces in the wetland can be flooded and as a water surface behaves as a specular reflector the ASAR σ^o and the retrieved soil moisture are lower. Similarly, the soil moisture retrieved over the grassland sites

increases, on average, in spring and decreases at the end of the monsoon. However, due to the high evaporative demand and the lack of a water supply from upstream areas, both the retrieved and measured soil moisture from the grassland sites have a much larger temporal variability as compared to the wetland.

A direct comparison of the measured with retrieved soil moisture resulted in RMSD's of 0.060 and 0.032 $m^3\ m^{-3}$ for the wetland site and the three grassland sites, respectively. These error levels are comparable to the results of previous SAR based soil moisture retrieval studies. It should, however, be noted that the large RMSD obtained for the wetland site is, somewhat misleading because of the large difference in the measured soil moisture ranges at the wetland and grassland sites. When the RMSD is divided by the soil moisture range the uncertainties levels obtained for the wetland and grassland sites are quite similar; 16.9 and 17.3%, respectively.

In conclusion, the application of a retrieval algorithm based only on a surface scattering model has resulted in retrieval accuracy comparable to previous SAR based soil moisture retrieval studies. With a surface roughness parameterization derived from the time series of σ^o measurements the applied algorithm requires no fitting. Various SAR based retrieval applications (e.g. Baup et al. 2007b, Löw et al. 2006) adopt fitted regression functions as view angle normalization and need an *a priori* specification of the σ^o change due to soil moisture (e.g. Pathe et al. 2009). Within the presented algorithms, these two components of the soil moisture retrieval process are modelled by AIEM.

Of course, the applicability of this algorithm is not unlimited. The effects of vegetation are, for example, assumed to be negligible and the surface roughness parameterization is inverted assuming dry soil moisture conditions. The validity of the algorithm is, therefore, restricted to areas with limited vegetation growth and the series of σ^o images should at least include three images collected during a dry (or frozen) period. This being said the algorithm is suited for monitoring soil moisture over areas with sparse vegetation and a well defined period with subzero temperatures. Requirement for this monitoring capability is, however, a consistent temporal resolution of SAR observations comparable to or better than the ASAR WS.

9 Evaluation of the Noah soil water flow scheme

This chapter is based on:

Van der Velde, R., Su, Z., Rodell, M., Ek, M.B., Bosveld, F.C., "Evaluation of the Noah land model soil water flow scheme", in revision for *Journal of Hydrometeorology*.

9.1 Introduction

Characteristic for most LSM's is the comprehensive description of 'above-ground' processes, while the approaches for simulating the soil processes have primarily been selected for numerical efficiency. For example, the number of soil layers is limited and extends down to a few meters (e.g. De Rosnay et al. 2000); the presence of ground water reservoirs is often ignored (e.g. Gulden et al. 2007); and the vertical soil heterogeneity is neglected (e.g. Yang et al. 2005, Van der Velde et al. 2009). Further, the diffusivity form of Richards' equation is employed by most LSM's, which permits the simulation of the soil water flow using soil moisture as the only prognostic variable; otherwise also soil water potentials would be required (e.g. Van Dam and Feddes 2000). Moreover, the soil hydraulic functions (SHF's) are computed using the Campbell (1974) soil hydraulic model (SHM), while Van Genuchten's (1980) SHM is more accepted in hydrology and soil physics.

In this chapter, two specific aspects of the Noah soil water flow scheme are discussed. Firstly, the choice of the scheme used for integrating the water fluxes computed by the highly non-linear Richards' equation is addressed. Noah employs the diffusivity form of Richards' equation, which simulates the soil water flow through a convective and diffusive component. Gravity is the force driving convective flow and diffusive flow is driven by the soil moisture gradient. Thus, convective flow transports soil water always deeper into the profile, while depending on the soil moisture gradient diffusive flow can transport water downwards or upwards.

The diffusive component enables transportation of soil water from deeper soil layers towards the surface, which is also known as capillary rise. An adequate representation of this mechanism is indispensable for the simulation of water limiting evaporative conditions (e.g. Walker et al. 2001); especially during droughts. Moreover, the underestimation of capillary rise can lead to a hydraulic decoupling of the root zone and the deeper soil layers causing slow soil moisture spin ups particularly in dry regions, such as deserts

(e.g. Rodell et al. 2005). Especially, for models with a limited number of soil layers the selection of an appropriate vertical interpolation scheme is of importance to ensure a proper simulation of water fluxes, which will also be influenced by the number of soil layers.

Secondly, a comparison of Noah simulations with SHF's computed by the Campbell and Van Genuchten SHM's is presented. The SHF's used in soil water flow scheme are based on a soil texture dependent parameterization and the SHM. The parameterization is typically derived from soil textural information through application of a pedotransfer function (PTF). National and international databases of measured SHF's have been utilized for the development of PTF's (i.e. Cosby et al. 1984, Carsel and Parrish 1988, Schaap and Leij 1998, Wösten et al. 2001). Previously, Soet and Stricker (2003) and Gutmann and Small (2005) investigated the land surface modeling uncertainties related to the usage of those PTF's.

The SHM basically shapes the the SHF's. LSM's often use the Campbell (1974) SHM. Campbell describes the relationships from the air-entry soil water potential (ψ_s) and contains, thus, a sharp discontinuity near saturation. A more complete solution is provided by Van Genuchten (1980), which fits the measured SHF's better. It should, however, be noted that differences between these two SHM's not only influences the shape of the SHF, but also lead to discrepancies among the parameterizations.

Previously, Cuenca et al. (1996) and Braun and Schädler (2005) investigated the impact of the SHM differences on the boundary layer development. Cuenca et al. evaluate the SHM's for the entire range of initial soil moisture conditions and found a substantial variability among the SHM's; depending on the initial soil moisture content up to 300 and 200 W m^{-2} for the λE and H, respectively. For a dry soil, Braun and Schädler reported on differences varying -10 to 10 W m^{-2} for H and -30 to 10 W m^{-2} for λE. These results show that the SHM employed within ACM's should be selected with care. It should, however, also be noted that both studies employed standard PTF's developed for a specific SHM and ignore, thus, the differences between parameterizations.

Shao and Irannejad (1999) found for the Atmospheric and Land Surface Interaction Scheme (ALSIS) LSM that resolving the parameter discrepancies eliminates a considerable portion of the disagreement between the SHM's. They, however, constrained the simulation of root wate uptake reduction by fixed soil moisture levels instead of the soil water potential (ψ). As such, an important effect of differently shaped retention curves is disregarded in their evaluation. Moreover, the model structure of Noah and ALSIS are significantly different. Most notably, ALSIS uses a Kirchoff transformed Richards' equation to simulate the soil water transport, while Noah employs the

diffusivity form. We, therefore, argue that the conclusions drawn by Shao and Irannejad may not be transferable to other LSM's and the use of a specific SHM should be evaluated for each LSM independently.

In this chapter, the influence of the vertical interpolation scheme and the employed SHM on the surface energy and water budget is evaluated using offline Noah simulations. Meteorological measurements collected at the Cabauw station have been used to force the model over the period from 1 January to 5 September 2003. This includes the 2003 European heat wave and will, thus, result in a simulated range from wet to dry conditions.

Two types of simulations have been performed. Firstly, the default SHF's have been utilized in combination with initial soil moisture conditions set to saturation for simulating a hypothetical dry down with three different schemes for vertically integrating soil water fluxes and different numbers of soil layers (3-20 layers). Secondly, also for saturated initial soil moisture conditions, Noah has been run for five soil texture classes of the Dutch PTF (Wösten et al. 2001); the Staring Series. Similar to Shao and Irannejad (1999), Van Genuchten parameterizations provided by the Staring Series are utilized to derive consistent Campbell parameter sets, for which two approaches are adopted.

9.2 Vertical integration of soil water flow

As described in Chapter 3, the Noah soil column is by default 2 m deep divided over four layers of 0.1, 0.3, 0.6 and 1.0 m increasing in thickness towards the bottom. At present, the scheme employed for vertical integration of soil water flow is based on calculation of the hydraulic conductivity, K, and soil water diffusivity, D, using the soil moisture content of the upper soil layer; hereafter referred to as '*method **A'*** and is illustrated in Figure 9-1 (left side).

This scheme can be questioned for two reasons. Firstly, the coefficient D is underestimated when the upper soil layer is drier than the bottom one because it decreases strongly and non-linearly with the soil moisture content. This reduces the simulated amount of diffusive flow (or capillary rise). Secondly, the simulated soil moisture contents are defined at the midpoint of the layers. Part of the soil water flows, therefore, through the upper and a part flows through the bottom layer. Hence, some sort of averaging of the coefficients K and D across two soil layers would seem appropriate.

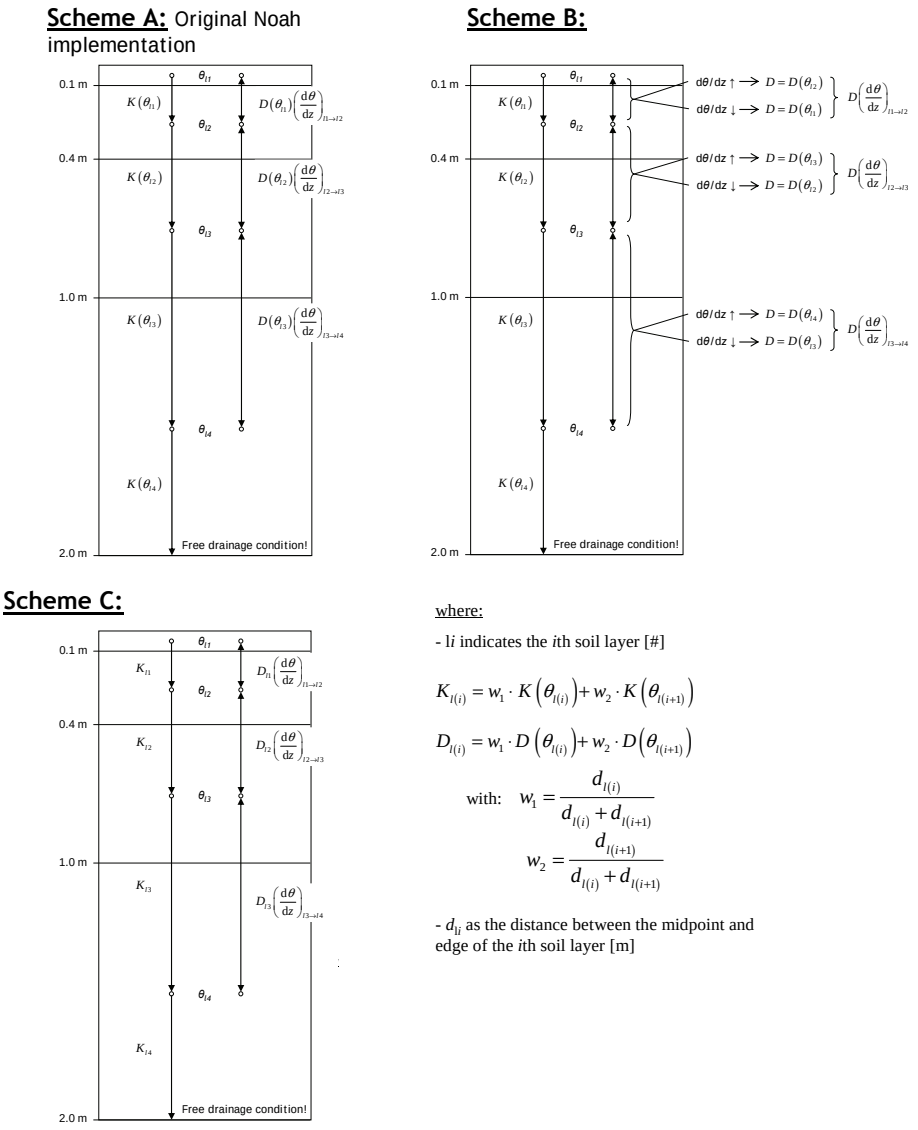

Figure 9-1 Schematization of numerical schemes applied for simulation of vertical integration of the soil moisture flow, At present, method A **is implemented in Noah; Methods** B **and** C **are the alternatives.**

In this thesis, two alternative schemes for vertically integrating soil water flow are evaluated. For the first approach, the coefficient D is computed using the soil moisture of the upper layer when $d\theta/dz$ is pointing downwards and the soil moisture content of the lower layer when $d\theta/dz$ is pointing upwards. This scheme is referred to as

'*method* **B'** and has much similarity with the scheme developed for the Noah's predecessor the OSU LSM (Mahrt and Pan 1984). The difference is, however, that they apply method **B** to both coefficients (*K* and *D*). For the other scheme, referred to as '*method* **C**', weighted averages of coefficients *K* and *D* are calculated between the two soil layers. A similar approach is used in the Simple Biosphere (SiB, Sellers et al. 1986) Model, which uses the soil water potential (ψ) form of Richards' equation (Eq. 3-1). Because the vertical integration of soil water flow may also be influenced by the number of soil layers, 10 discretizations are considered with 3 to 20 layers as listed in Table 9-1.

Table 9-1 Selected vertical soil layer discretizations.

# layers	layer configuration [m]
3 layers	0.4 m; 0.6 m; 1.0 m
4 layers	0.1 m; 0.3 m; 0.6 m; 1.0 m
6 layers	2 x 0.05 m; 2 x 0.15 m; 0.6 m; 1.0 m
8 layers	2 x 0.05 m; 2 x 0.15 m; 2 x 0.3 m; 2 x 0.5 m
10 layer	2 x 0.05 m; 3 x 0.10 m; 3 x 0.2 m; 2 x 0.5 m
12 layers	2 x 0.05 m; 3 x 0.10 m; 3 x 0.2 m; 4 x 0.25 m
14 layers	4 x 0.05 m; 4 x 0.10 m; 2 x 0.2 m; 4 x 0.25 m
16 layers	4 x 0.05 m; 8 x 0.10 m; 4 x 0.25 m
18 layers	8 x 0.05 m; 6 x 0.10 m; 4 x 0.25 m
20 layers	10 x 0.05 m; 5 x 0.10 m; 5 x 0.20 m

9.3 Soil hydraulic functions

Models

The general form of the SHM often employed within LSM's describes the ψ-θ relationship (or retention curve) using a power curve,

$$\Theta = \left(\frac{\psi}{\psi_s} \right)^b \qquad \text{with} \qquad \Theta = \left(\frac{\theta - \theta_r}{\theta_s - \theta_r} \right) \tag{9.1}$$

where, ψ_s is the soil water potential at which air enters the soil matrix [m], θ_s is the saturated soil moisture content [$m^3\ m^{-3}$], θ_r is the residual soil moisture content [$m^3\ m^{-3}$] and the parameter *b* is an empirical fitting parameter related to the pore size distribution [-]. A non-zero value for θ_r is considered in the formulation of Brooks and Corey (1964), while others assume θ_r to be zero (e.g. Campbell 1974, Clapp and Hornberger 1978).

Application of Eq. 9.1 implies a sharp discontinuity at ψ_s. Clapp and Hornberger proposed, therefore, a two-step function of which one part describes the ψ-θ relation up to inflection point and the other part is representative for lower ψ values. Van Genuchten provides, however, a more flexible solution by describing the ψ-θ

relationship over the complete ψ range using a single expression for the soil water retention curve,

$$\Theta = \left[\frac{1}{1+(\alpha\psi)^n} \right]^m \tag{9.2}$$

where, a [m^{-1}] and m [-] are empirical parameters, and n equals $1/(m\text{-}1)$. The parameter a is often considered to be equivalent to the inverse of ψ_s, and m is related to the pore size distribution and, thus, to the Campbell b parameter.

The K - θ and D - θ relationships derived for the Campbell SHM are obtained through application of Burdine's (1953) theory for the hydraulic conductivity and can be written as,

$$K(\theta) = K_s \left(\frac{\theta}{\theta_s} \right)^{2b+3} \tag{9.3}$$

$$D(\theta) = D_s \left(\frac{\theta}{\theta_s} \right)^{b+2} \tag{9.4}$$

where, K_s is the saturated hydraulic conductivity [m s^{-1}] and D_s is saturated soil water diffusivity [m^2 s^{-1}] expressed by,

$$D_s = b \cdot K_s \left(\frac{\psi_s}{\theta_s} \right) \tag{9.5}$$

Van Genuchten's retention function is often applied in combination with Mualem's (1976) theory for the conductivity. Resulting in $K - \theta$ and $D - \theta$ functions that read,

$$K(\theta) = K_s \Theta^{1/2} \left[1 - \left(1 - \Theta^{1/m} \right)^m \right]^2 \tag{9.6}$$

$$D(\theta) = D_s \Theta^{1/2 - 1/m} \left[\left(1 - \Theta^{1/m} \right)^{-m} + \left(1 - \Theta^{1/m} \right)^m - 2 \right] \tag{9.7}$$

with the saturated soil water diffusivity as,

$$D_s = \frac{(1-m) K_s}{\alpha m (\theta_s - \theta_r)} \tag{9.8}$$

Table 9-2 Soil textural properties of the five selected soil classes from the Dutch pedotransfer function (after Wösten et al. 2001).

Description	Class*	Clay [%]	Silt [%]	Organic [%]	M50** [µm]	Density [kg m^{-3}]
Coarse sand	O05	-	-	0 - 2	220-400	1.5 – 1.7
Sandy clay	O10	18 - 22	-	0 - 3	-	1.3 - 1.5
Clay	O13	50 - 77	-	0 - 3	-	1.0 – 1.4
Loam	O15	-	85 - 92	1 - 3	-	1.1 – 1.6
Peat	O17	-	-	60 - 80	-	0.1 – 0.6

* Soil type assigned in the Staring Series;
** M50 ~ median of the particle size of the sand faction.

Parameterizations

The Soil Hydraulic Parameters (SHP's) for the comparison of the Campbell and Van Genuchten SHM's are adopted from the Dutch PTF; also referred to as the Staring Series (Wösten et al. 2001). Five soil classes of this database are used, which cover a range of textures from the finest to coarsest class and include an organic (peat) soil. The soil textural properties and Van Genuchten SHP's of the selected classes are given in Tables 9-2 and 9-3, respectively. The Staring Series provides only the parameters for the Van Genuchten SHM; thus, the Campbell parameterization should be derived.

Table 9-3 Van Genuchten soil hydraulic parameters reported in Wösten et al. (2001) for the soil texture classes presented in Table 9-2.

Description	Class	θ_r [$m^3\ m^{-3}$]	θ_s [$m^3\ m^{-3}$]	K_s [$m\ d^{-1}$]	α [m^{-1}]	n [-]
Coarse sand	O05	0.01	0.32	$2.500 \cdot 10^{-1}$	5.21	2.374
Sandy clay	O10	0.01	0.48	$2.120 \cdot 10^{-2}$	0.97	1.257
Clay	O13	0.01	0.57	$4.370 \cdot 10^{-2}$	1.94	1.089
Loam	O15	0.01	0.41	$3.700 \cdot 10^{-2}$	0.71	1.298
Peat	O17	0.01	0.86	$2.930 \cdot 10^{-2}$	1.23	1.276

One of the differences between the two SHM's is that within Campbell the θ_r is assumed to be equal to 0.00 $m^3\ m^{-3}$. However, as can be observed in Table 9-3, the θ_r values are close to 0.00 $m^3\ m^{-3}$ and do not vary a lot among the selected soil classes (0.00 – 0.01 $m^3\ m^{-3}$). For convenience, the Van Genuchten θ_r is, therefore, also set to 0.00 $m^3\ m^{-3}$. Moreover, the Campbell SHM utilizes the ψ_s and b as shape parameters, while for Van Genuchten the α and m need to be specified. Despite the differences between the Campbell and Van Genuchten shape parameters, Rawls et al. (1993) as well as Van Genuchten (1980) pointed to the their analytical similarity between the parameters and showed that,

$$\psi_s = \frac{1}{\alpha} \qquad \text{and} \qquad b = \frac{1}{(n-1)} \tag{9.9}$$

These relationships follow directly from the similarity in the retention curves of the SHM's. This, however, does not necessarily lead to a good agreement between the K- and D-curves because the Campbell SHM defines the parameters K_s and θ_s at ψ_s. Moreover, differences in the slope of the retention curve near the inflection point may affect the magnitude of the $D(\theta)$. For these reasons, two sets Campbell SHP's are derived focused on agreement of:

1) Retention curves, referred to as Campbell **A**;
2) K- and D-curves, referred to as Campbell **B**.

The Campbell **A** parameters are obtained through application of Eq. 9.9. Parameters for Campbell **B** are derived using a least squares

minimization algorithm to match the K-θ and D-θ relationships, whereby the parameters K_s, ψ_s and b are adjusted and θ_s is kept at its original value. The resulting Campbell **A** and **B** parameters are given in Tables 9-4 and 9-5, respectively, and the ψ-θ, K-θ and D-θ relationships are presented in Figure 9-2. As is expected, Figure 9-2 demonstrates that through application of Campbell **A** a good agreement is obtained with Van Genuchten's retention curve, while substantial differences are noted among the K-θ and D-θ relationships; and vice versa when the Campbell **B** parameterization is applied.

Table 9-4 Campbell soil hydraulic parameters derived from the Van Genuchten parameters through application of Eq. 9.9 (Campbell A).

Description	Class	θ_s [$m^3\ m^{-3}$]	K_s [$m\ d^{-1}$]	ψ_s [m^{-1}]	b [-]
Coarse sand	O05	0.32	$2.500 \cdot 10^{-1}$	0.168	0.94
Sandy clay	O10	0.48	$2.120 \cdot 10^{-2}$	0.935	3.57
Clay	O13	0.57	$4.370 \cdot 10^{-2}$	0.515	11.23
Loam	O15	0.41	$3.700 \cdot 10^{-2}$	1.408	3.36
Peat	O17	0.86	$2.930 \cdot 10^{-2}$	0.813	3.62

Table 9-5 Campbell soil hydraulic parameters obtained by matching to the Van Genuchten relationships (Campbell B).

Description	Class	θ_s [$m^3\ m^{-3}$]	K_s [$m\ d^{-1}$]	ψ_s [m^{-1}]	b [-]
Coarse sand	O05	0.32	$1.290 \cdot 10^{-1}$	0.43	0.60
Sandy clay	O10	0.48	$1.577 \cdot 10^{-3}$	1.08	3.77
Clay	O13	0.57	$4.514 \cdot 10^{-4}$	0.51	11.24
Loam	O15	0.41	$2.531 \cdot 10^{-3}$	2.00	3.17
Peat	O17	0.86	$1.791 \cdot 10^{-3}$	1.14	3.44

A comparison of the exact parameter values shows the largest deviations among the K_s values, which is one order of magnitude smaller for Campbell **B** than for Campbell **A**. This can be argued for because the K_s by Campbell is defined at ψ_s, while the $K(\theta)$ at ψ_s by Van Genuchten is lower than K_s. Thus, to fit the Van Genuchten K- and D-curves requires a lower Campbell K_s. Further, differences are also observed among the shape parameters (ψ_s and b), which induces discrepancies between the retention curves. For smooth retention curves (typical for fine-textured soils) these differences are smaller than for curves with a well-defined 'S' shape (for example: coarse sand, loam and peat).

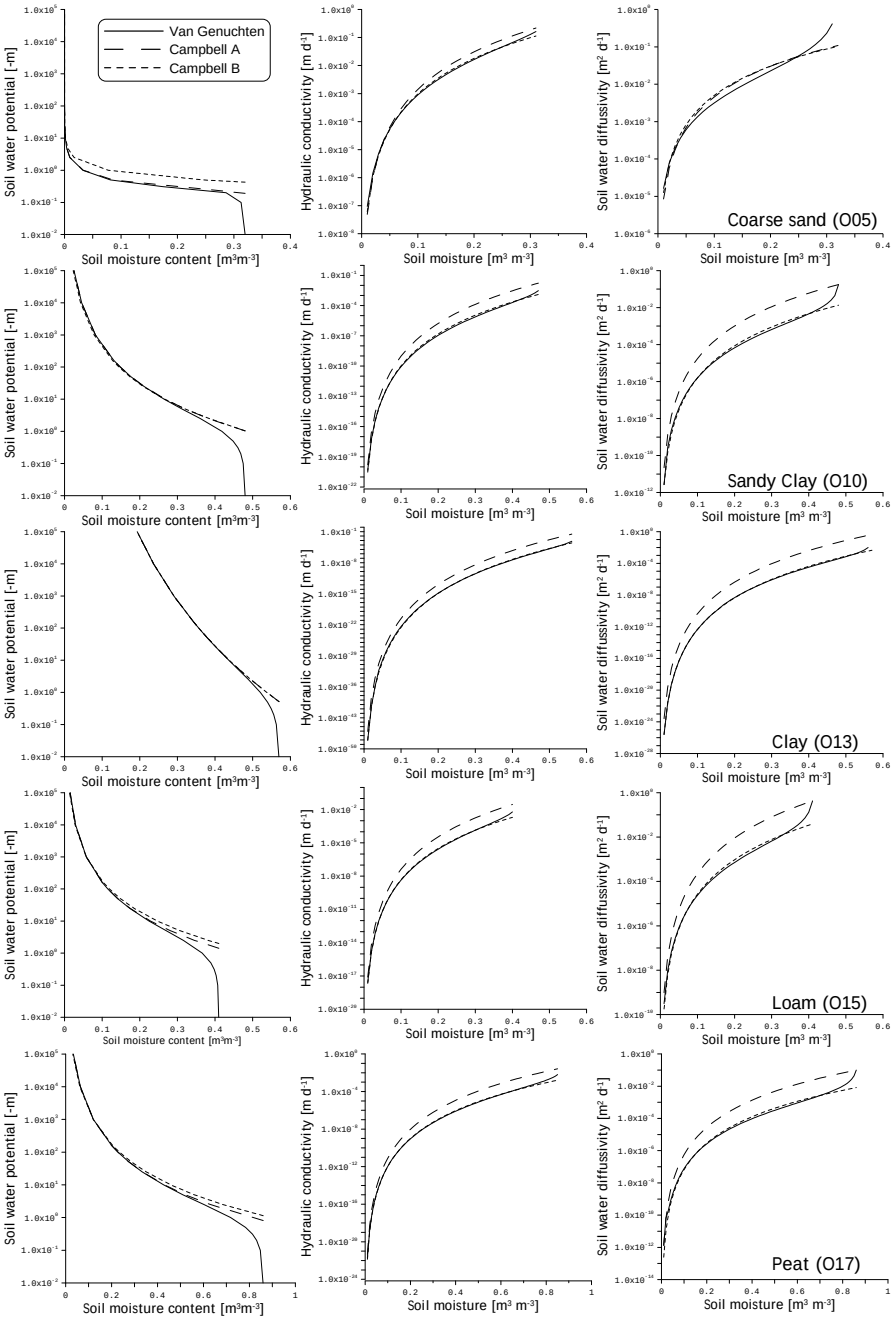

Figure 9-2 Soil hydraulic functions derived using the Van Genuchten and Campbell SHM for five soil classes of the Dutch PTF. Campbell A **is obtained through application of Eq. 9.9 and Campbell** B **is obtained by fitting the *K-θ* and *D-θ* curves.**

9.4 Noah simulations with different vertical integration schemes for the soil water flow

In this section, Noah simulated soil moisture profiles are presented using different schemes for vertical integration of the soil water flow, which include the soil layer discretizations presented in Table 9-1 and vertical integration schemes **A**, **B** and **C**. For these simulations, Noah has been run using atmospheric forcings measured at Cabauw over the period 1 June to 5 September 2003, which are described in Section 4.2. The 'light clay' soil hydraulic and 'cultivations' vegetation parameter sets have been adopted from the standard table utilized for large scale Noah applications. Those parameterizations are given Tables 3-1 and 3-2. The initial soil moisture contents have been set to the θ_s over the complete profile, which is much wetter than expected given the dry conditions of the 2003 summer.

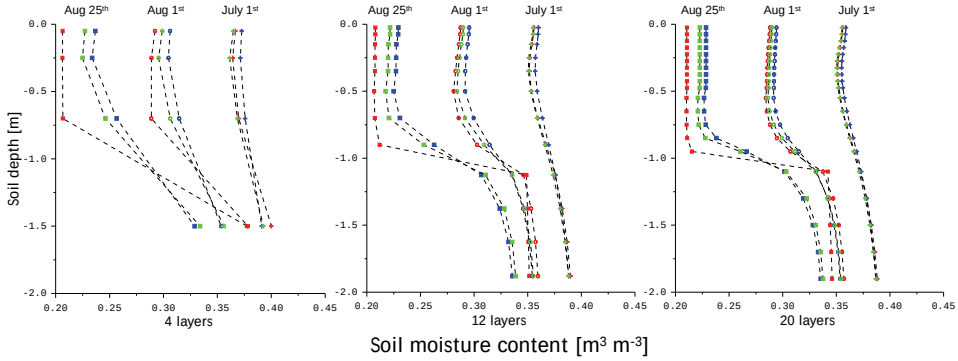

Figure 9-3 Soil moisture profiles simulated by Noah with 4, 12 and 20 soil layers, and scheme A (red), B (blue) and C (green) for 1 July (+), 1 August (o) and 25 August (□).

The simulated soil moisture profiles of 1 July, 1 August and 25 August are presented in Figure 9-3 for Noah configurations with schemes **A**, **B**, and **C**, and 4, 12, and 20 soil layers. Because of the high evaporative demand and the selected initial soil moisture conditions, a dry down cycle is simulated. This is manifested in the development of the profiles shown in Figure 9-3. The root zone (top 1 m) dries out and a transition zone from dry to wet is created between root zone and the deeper soil layer(s). This transition in soil wetness is gradual for method **B** and **C**. However, a sharp contrast between the soil moisture in the root zone and deeper soil layer(s) is simulated using method **A**. Apparently, the implementation of scheme **A** does not (sufficiently) take the capillary rise mechanism into account to simulate a gradual transition from wet to dry conditions.

After 1 August, the soil moisture content is essentially unchanged below 1 m for method **A**, while soil moisture in the root zone decreases further towards residual moisture conditions. For methods **B** and **C**, however, the soil moisture below 1 m does dry out after 1 August. On the other hand, the root zone is 0.044-0.022 and 0.033-0.015 [m^3 m^{-3}] wetter for method **B** and **C**, respectively, depending on the number of layers. These systematic differences in the root zone soil moisture and deep soil moisture indicate that the diffusive soil water flow is underestimated by method **A**. This explains the hydraulic decoupling of the root zone and the deeper soil layer(s) observed for method **A**.

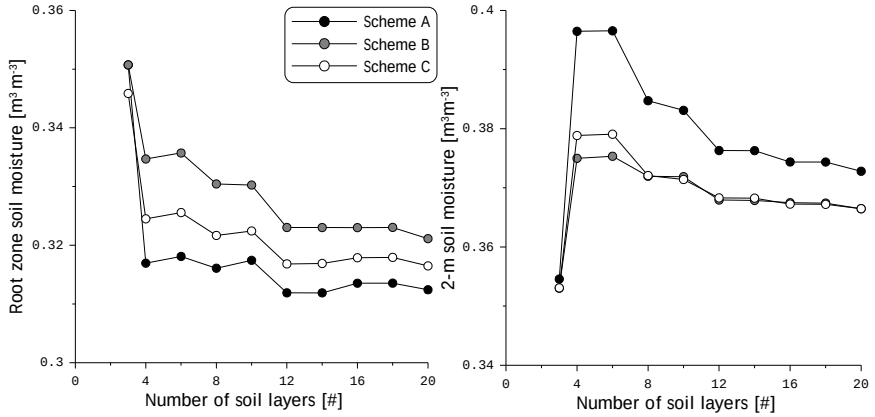

Figure 9-4 Averages of the Noah simulated root zone soil moisture (left panel) and 2 m soil moisture (right panel) calculated over the simulation period and plotted against the number of soil layer.

For further investigation of the relationship between the number of soil layers and the scheme used for vertical integration of the soil water flow, the root zone soil moisture and soil moisture in the second meter of the profile (2 m soil moisture) are averaged over the simulation period. In Figure 9-4, these averages are plotted against the number of soil layers. As expected based on Figure 9-3, the root zone soil moisture simulated by method **A** is systematically lower than that of methods **B** and **C**. Further, higher soil moisture contents of the deeper soil layers are observed for method **A**.

The wettest root zone soil moisture conditions are simulated by method **B**, which is on average 0.010 – 0.005 m^3 m^{-3} wetter than method **C** and 0.018 – 0.009 m^3 m^{-3} wetter than method **A**. The lower soil moisture contents for method **C** are explained by the averaging of the *K* and *D* over two layers. Therefore, the amounts of both diffusive and the gravity induced convective soil water flow increase and soil water is transported faster through the soil column particularly when the deeper soil layer(s) are wetter than the surface. Because the

capillary rise mechanism is underestimated by method **A**, the 2 m soil moisture remains unchanged even under dry conditions. As a result, the scheme **A** simulated 2 m soil moisture is 0.021 – 0.006 m^3 m^{-3} larger than for scheme **B** and 0.018 – 0.006 m^3 m^{-3} larger than for scheme **C**.

The differences in the simulated soil moisture between the schemes are largest for the 4 layer model configuration and decrease as the number of soil layers is increased. A finer discretization of the soil profile results in smaller soil moisture gradients between the layers. Therefore, the differences in the calculation of the coefficients K and D between the schemes are reduced as the number of soil layers is increased. However, consistently for all three schemes, little change was observed in the averaged root zone soil moisture and 2 m soil moisture for an increase in the number of soil layer from 12 to 20 layers. The 12 layer model configuration could, therefore, be considered a good compromise between the numerical efficiency and the physical representation of the soil water flow.

9.5 Noah simulations using the Campbell and Van Genuchten SHM's for five soil classes

For evaluating the influence of the differences in the SHF's presented in Figure 9-2, the five selected soil classes of the Staring series have been used for Noah simulations. Again, the initial soil moisture conditions are artificially set to saturation and atmospheric measurements, collected from 1 January through 5 September 2003 at Cabauw, are used as forcings. These simulations are performed using Method **B** for vertically integrating the soil water flow and the soil column is divided into 12-layers. The soil moisture of 1st (root zone) and 2nd meter (2 m) resulting from these simulations are calculated and plotted in Figure 9-5 and Figure 9-6, respectively. Also the Van Genuchten computed θ_c and θ_w are provided in the root zone soil moisture plots to indicate the conditions under which evaporation is restricted by soil moisture stress.

Differences in the simulated soil moisture among the three SHF's are negligible for the O05 soil class. For this sandy soil, a rapid decay of both the root zone and 2 m soil moisture is noted, while the dry-down for the other soils is less severe. This specific hydraulic behavior of the O05 class is a result of the large K_s value, which generates a faster transport of water through the soil column and, thus, enhances the drying process. The Noah O05 simulations reach, however, the θ_c in about the same period as for the other soils because this critical value is much lower with respect to the θ_s. Also, the range, over which soil moisture reduces the root uptake, is smaller than for the other soils. Due to this limited soil moisture feedback, the root zone soil moisture for the sandy soil decreases

rapidly to θ_w and remains near or at θ_w in the dry period, while the root uptake reduction simulated for the other soils delays the drying.

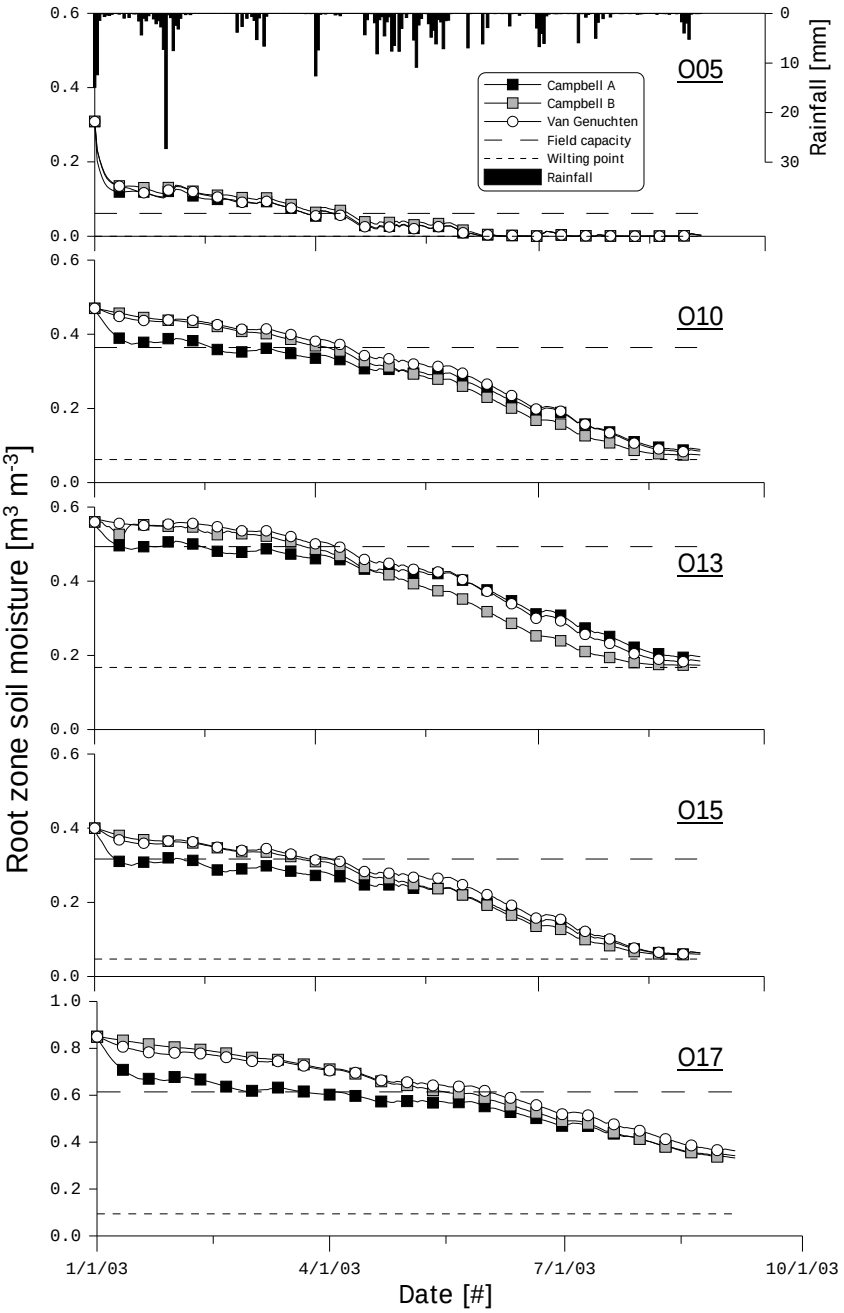

Figure 9-5 The Noah simulated root zone soil moisture using three types of SHF's for five soil classes plotted against time.

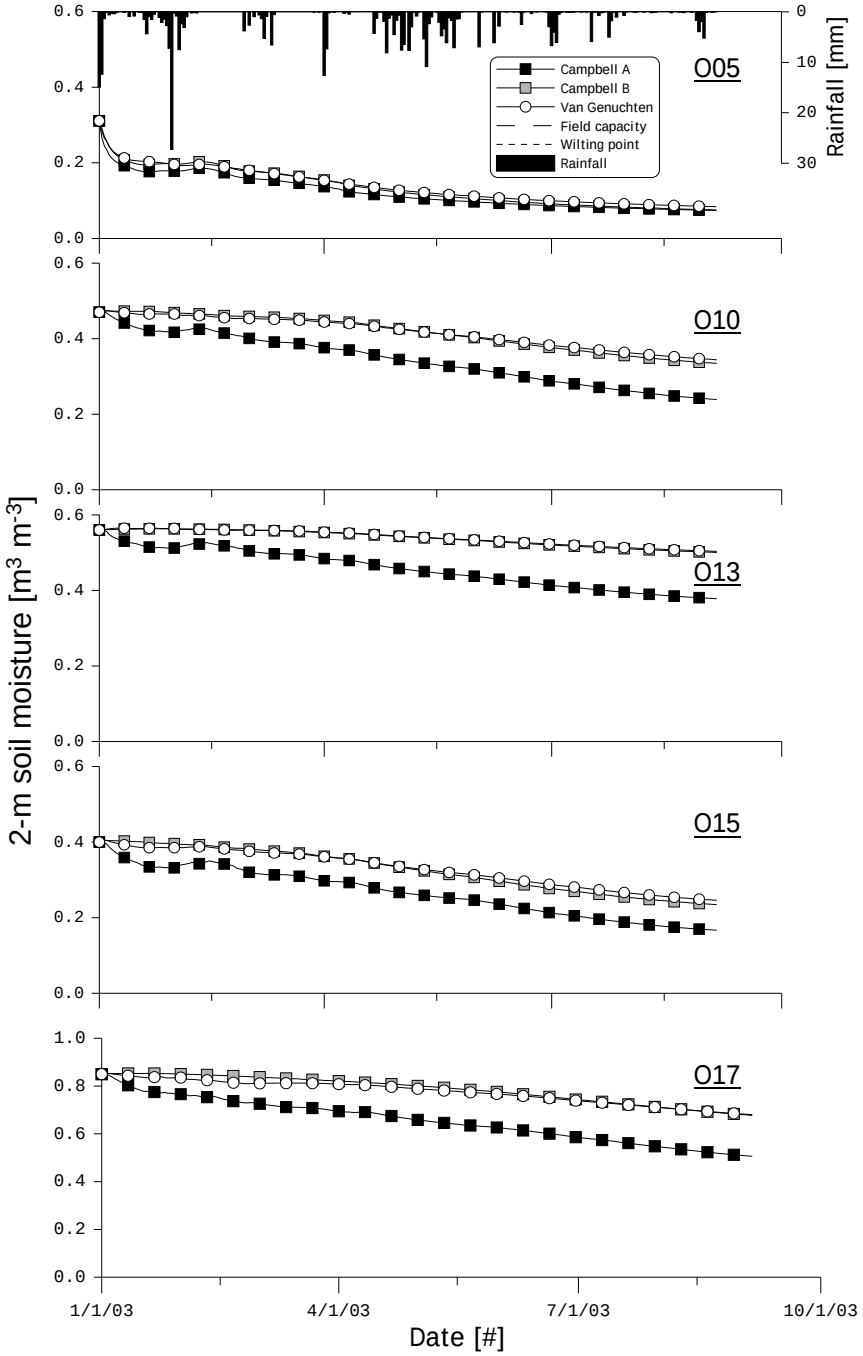

Figure 9-6 The Noah simulated 2 m soil moisture using three types of SHF's for five soil classes plotted against time.

Systematic differences in the simulated soil moisture are, however, observed among the three SHF's of the fine textured and peat soil(s). Using the Campbell **A** SHF's, Noah simulates a rapid decay of the root zone soil moisture for these soils because the $K(\theta)$ is larger, which results in more drainage to the deep layers. After the θ_c has been reached, the root uptake reduction constrains the drying of the root zone. Further, the dry down is also delayed by the upward transport of water from the deep layers because of the larger $D(\theta)$. As a result, the Campbell **A** root zone soil moisture converges towards the Van Genuchten simulations near the end of the simulation period, while the Campbell **A** 2 m soil moisture becomes significantly lower.

The opposite behavior is found when Noah is run with the Campbell **B** SHF's. At the beginning of the simulation, the Campbell **B** root zone soil moisture is comparable to Van Genuchten due to the similarity between the K-θ and D-θ relationships. During the summer, however, the root zone soil moisture reaches θ_w earlier. The Campbell **B** SHF's are derived by matching the K-θ and D-θ relationships, for which most notably a K_s decrease is needed. In Noah, the K_s affects the infiltration capacity positively. The lower K_s reduces, thus, the infiltration capacity and less rain can enter the soil column, which enhances the drying process.

Figure 9-7 presents for each run the drainage, surface runoff and total evaporation accumulated over the simulation period. Characteristic in the plots are the large amount of drainage for Campbell **A** and the large amount of surface runoff for Campbell **B**, which both support the development of the root zone and 2 m soil moisture as discussed above. The high $K(\theta)$ of Campbell **A** in the mid and dry soil moisture range produces the large amount of drainage, and the small infiltration capacity for Campbell **B** induces the large production of surface runoff. Conversely, the simulated drainage and surface runoff are lowest for Campbell **B** and Campbell **A**, respectively.

Because of the large amount of surface runoff simulated using Campbell **B**, the root zone soil moisture is dryer and 6.8 – 13.6% less evaporation is generated for the fine textured mineral soils as compared to Van Genuchten. The differences in evaporation between Van Genuchten and Campbell **B** are smaller for the peat soil (O17) because the conditions are less restrictive. Surprisingly, the Campbell **B** evaporation is larger than Van Genuchten for the sandy soil (O05). This is explained by the smaller amount of surface runoff induced by the larger K_s for this soil class and soil moisture deficit; more soil water is, therefore, available for evaporation. The large downward water flux simulated with the Campbell **A** SHF's is compensated by the upward transport of soil water induced by the larger $D(\theta)$. As a

result, the Campbell **A** evaporation is less 3.4% than Van Genuchten. The Campbell **A** evaporation is even larger for the clay soil (O13) because differences in the K-θ relationships are smaller than for the other soil classes, while the D-θ differences are similar. Therefore, the simulated drainage is lower than for the other soils in the wet episodes, while upward soil water flux is maintained under dry conditions.

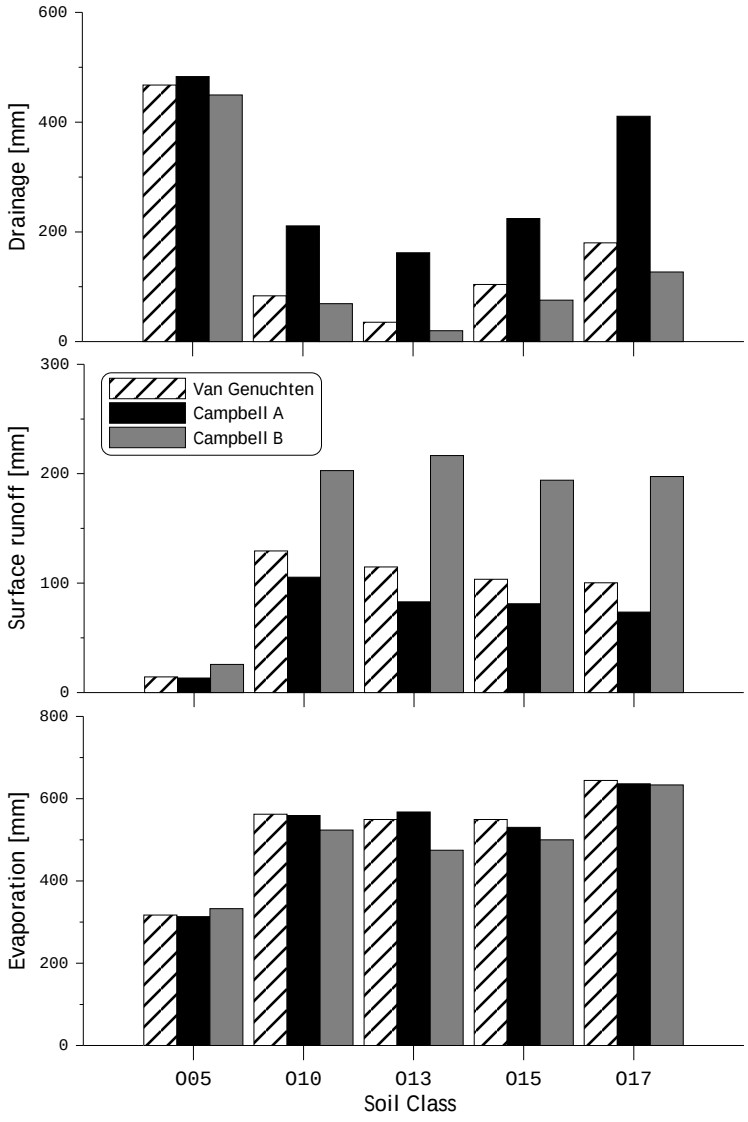

Figure 9-7 Accumulated drainage, surface runoff and total evaporation simulated using three types of SHF's for five soil classes.

9.6 Conclusions and discussion

In this chapter, the scheme for vertically integrating the soil water flow in Noah and the model for calculating the soil hydraulic functions (SHF) are discussed.

Three methods for vertically integrating the soil water flow are compared, which are:

- A scheme based on the calculation of the K and D using the soil moisture (θ) in the upper layer (currently used by Noah); referred to as method **A**.
- A scheme that utilizes the simulated soil moisture of the upper layer for D calculation when $d\theta/dz$ is downwards and simulated soil moisture of lower layer when $d\theta/dz$ is upwards; referred to as method **B**.
- A scheme based on the calculation of weighted averages for K and D of two consecutive soil layers; referred to as method **C**.

The three schemes have been implemented in Noah and have been applied in combination with ten vertical discretizations with 3 to 20 soil layers. Atmospheric boundary layer variables measured between 1 January and 5 September (2003) at the Cabauw meteorological site (The Netherlands) have been used to force Noah. During this period the 2003 European heat wave occured.

Those atmospheric forcings have been used to perform synthetic Noah simulations using the initial soil moisture set to saturation and parameterizations adopted from tables used for large-scale applications. These simulations demonstrate that the method currently used by Noah for vertically integrating the soil water flow systematically underestimates the upward transport of soil water due to capillary rise. Hence, the simulated 2 m soil moisture remains stable even under dry conditions and a high evaporative demand. This is an explanation for the slow spin up of Noah found in previous studies (e.g. Cosgrove et al. 2003 and Rodell et al. 2005). The capillary rise mechanism is accommodated within Noah via the two alternative schemes (**B** and **C**). Further, it is found that the differences between the schemes decrease for an increasing number of layers and a 12 layer configuration forms a good comprise between numerical efficiency and the physical representation of the soil water flow.

Also, the SHF controls the simulation of soil water flow. In Noah, as in most other LSM's, the SHM by Campbell (1974) is employed to describe these functions, while it is commonly understood that the Van Genuchten SHM represents the measured SHF's better. Surface water budgets simulated by Noah using these two SHM's are compared. To cope with the parameter differences, the Van Genuchten SHP's provided by the Dutch pedotransfer function are

utilized to derive the Campbell parameterizations. For this derivation, two different approaches have been adopted:

- The theoretical similarity between the retention curves is used to determine the shape parameters (ψ_s and b), while the other parameters (θ_s and K_s) are kept constant; referred to as Campbell **A**.
- The Campbell parameters, K_s, ψ_s and b are adjusted to fit the Van Genuchten K-θ and D-θ relationships; referred to as Campbell **B**.

Campbell **A** and Campbell **B** parameterizations have been derived for five soil classes of the Staring Series. With respect to Van Genuchten, the most notable difference is the larger Campbell **A** $K(\theta)$ and $D(\theta)$ in the mid and dry soil moisture range, and the lower Campbell **B** $K(\theta)$ and $D(\theta)$ near saturation due to a smaller K_s. Further, the deviations between the retention curves are largest for Campbell **B**.

Using the Van Genuchten, Campbell **A** and Campbell **B** SHF's, atmospheric forcings measured at the Cabauw meteorological station have been used to run Noah from 1 January through 5 September 2003. Again, for these simulations the initial soil moisture (θ_i) has been artificially set to saturation. Moreover, method **B** is used for vertically integrating the soil water flow and the soil column is divided into 12 layers.

Characteristic for these Campbell **A** simulations is a faster transport of water induced by the larger $K(\theta)$ and $D(\theta)$ values. This results in the production of more drainage under wet conditions and more evaporation under dry conditions due to the larger amount of upward soil moisture flux. Using Campbell **B**, Noah generates more surface runoff because its smaller K_s negatively affects the infiltration capacity. Less rain can, therefore, infiltrate which leads to lower root zone soil moisture and less evaporation under dry conditions.

The results from this Chapter demonstrates that significantly different surface water and energy budgets are simulated by Noah when adopting different schemes for vertically integrating soil water flow and using either the Van Genuchten or Campbell SHM. Because at the Cabauw site the groundwater table is maintained at a fixed level throughout seasons, a meaningfull comparison against *in-situ* measurements is not possible to evaluate these results. As Van Genuchten is known to describe measured SHF best, a more physical representation of the soil water flow simulation within Noah can be obtained when the Van Genuchten SHM is used. Incorporation of Van Genuchten and scheme **B** or **C** for vertically integrating soil water flow into Noah would lead to smaller soil water losses (e.g. evaporation, drainage and surface runoff) and would reduce the drought stress simulated under extreme dry situations when also the deep soil layers are exhausted.

10 Adaptation of the Noah land model to Tibetan conditions

This chapter is based on:

Van der Velde, R., Su, Z., Ek, M., Rodell, M., Ma, Y., 2009, "Influence of thermodynamic soil and vegetation parameterizations on the simulation of soil temperature states and surface flux by the Noah LSm over a Tibetan Plateau site", *Hydrology and Earth System Sciences*, **13**, pp. 759-777.

10.1 Introduction

Land models, such as Noah, describe the land-atmosphere interactions within operational ACM's. Because ACM are computationally demanding, numerical efficiency of the LSM is required. A simplified implementation of the physical processes is, therefore, inevitable. For example, the impact of a physically based formulation of roughness lengths for momentum and heat transport on the calculation of the surface fluxes has been stressed (i.e. Chen et al. 1997, Zeng and Dickinson 1998, Su et al. 2001, Liu et al. 2007, Ma et al. 2008) and the influence of a more detailed description of the land surface hydrology has been discussed (see Chapter 9, Gutmann and Small 2007, Gulden et al. 2007). Moreover, the number of soil and vegetation parameterizations accommodated within global modeling systems is limited (e.g. Ek et al 2003).

The impact of those (and other) uncertainties in the simulation of land processes on the output of an ACM was evaluated by Dickinson et al. (2006). They found significant differences between measured and simulated air temperatures and precipitation amounts for selected extreme environments, such as the Sahara desert, the semi-arid Sahel, Amazonian rain forest and Tibetan Plateau. These findings are supported by the results presented in Hogue et al. (2005), which showed that thorough optimization of a comprehensive set of model parameters, can reduce differences between the measured and simulated heat fluxes for the semi-arid Walnut Gulch watershed (Arizona, USA) by as much as 20-40 W m^{-2}. The investigation by Dickinson et al. demonstrates the existence of inconsistencies in the simulations of land surface processes at a global scale, while Hogue et al. (2005) show that adjusting parameterizations improves the model's performance significantly. This suggests that even for extreme environment the implemented LSM physics is flexible enough to represent the land surface processes adequately given the appropriate parameterization.

Within the framework of the Model Parameter Estimation Experiment (MOPEX) the development of area specific land surface parameterization has been accommodated (Schaake et al. 2006). The focus of this initiative has been on the development of parameter estimation methodologies and the calibration of parameters that affect primarily the rainfall-runoff relationships (Duan et al. 2006). As a result, the influence of model parameters on simulating the surface energy balance has received little attention. One of the few investigations addressing the impact of parameter uncertainties on the energy balance simulations has been reported by Kahan et al. (2006). They showed for the Simplified Simple Biosphere (SSiB, Xue et al. 1991) model that adjustment in the Leaf Area Index (LAI), stomatal resistance and saturated hydraulic conductivity (K_s) are required to decrease systematic differences between simulated and measured sensible and latent heat fluxes for a Sahelian study area in Niger. Moreover, the importance of a proper description of the thermal diffusivity is emphasized for reducing biases in the simulated diurnal surface temperature evolution. In a MOPEX-related study, Yang et al. (2005) show for the Tibetan Plateau that also the vertical soil heterogeneity may have a significant impact on the partitioning of radiation.

These previous investigations demonstrate that adjustments in soil and vegetation parameterizations can yield significant improvements in the simulation of the surface energy balance. They also emphasize the need to analyze parameter uncertainties of different LSM's in more detail. In this context, Noah is employed to simulate the land surface processes at a Tibetan Plateau site. For these simulations, the Noah model is forced with the atmospheric measurements collected at Naqu station over a 7-day dry period during the Asian Monsoon from 3 September to 10 September 2005. The objective of this study is to identify the adjustments in soil and vegetation parameterizations needed to reconstruct the temperature states in the soil profile and the measured surface energy fluxes over this short period. This chapter consists of two parts; First, Noah results obtained by using standard parameterizations described in Chapter 3 are presented. Then, the soil and vegetation parameters adjustments required to optimize the model performance are discussed.

10.2 Noah simulations using default parameter sets

In this section, the Noah model runs performed with the input of standard parameterizations given in Tables 3-1 and 3-2 are presented. Based on the available soil texture information, the 'loamy sand' soil parameters are adopted. However, a single vegetation parameterization valid for the extreme Tibetan conditions

is difficult to define. Noah simulations have, therefore, been performed using three vegetation parameter sets considered to be equally representative for the Tibetan Plateau, which are the *tundra*, *bare soil* and *glacial* parameterizations. For these simulations, the model is forced and initialized by measurements collected at Naqu station. Temperatures measured in the soil profile and heat fluxes reconstructed using the Bowen Ratio method are availed to assess Noah's performance. A description of these measurements and the processing of the heat fluxes are documented in Section 4.3.

Figure 10-1 presents the plots with measured and simulated heat fluxes (H, λE and G_0) obtained using the three vegetation parameter sets against time. Similarly, plots with the time series of the measured and simulated soil temperatures at the surface, soil depths of 5-cm and 25-cm are presented in Figure 10-2. In addition, the RMSD's and the biases calculated between the measurements and simulations are presented in Tables 10-1 and 10-2 for the surface energy balance components and the soil temperature states, respectively.

In general, the comparison indicates that the partitioning between the H and λE is not properly simulated. Noah overestimates the measured H resulting in biases of 41.25 – 52.69 W m^{-2} and underestimates the λE by 18.36- 39.53 W m^{-2} depending on the adopted vegetation parameterization. As a result of the biases obtained for H and λE, also the obtained RMSD's are somewhat large as compared to optimized modeling results presented in previous studies (e.g. Sridhar et al. 2002, Yang et al. 2005 and Gutmann and Small 2007).

Table 10-1 RMSD calculated between the measured soil temperature states and surface fluxes, and the Noah simulations.

Land cover	H	λE [W m^{-2}]	G_0	T_{skin}	T_{5cm} [^oC]	T_{25cm}
Tundra	53.50	32.40	34.12	1.48	1.08	1.19
Bare soil	57.85	42.54	33.34	1.84	1.80	1.77
Glacial	47.41	33.20	34.23	1.45	1.28	1.33

Table 10-2 Biases calculated between the measured soil temperatures and surface fluxes, and the Noah simulations.

Land cover	H	λE [W m^{-2}]	G_0	T_{skin}	T_{5cm} [^oC]	T_{25cm}
Tundra	-48.91	18.36	3.80	1.13	0.59	0.69
Bare soil	-52.69	39.35	2.08	0.17	-0.24	0.28
Glacial	-41.25	20.91	2.81	0.56	0.10	0.45

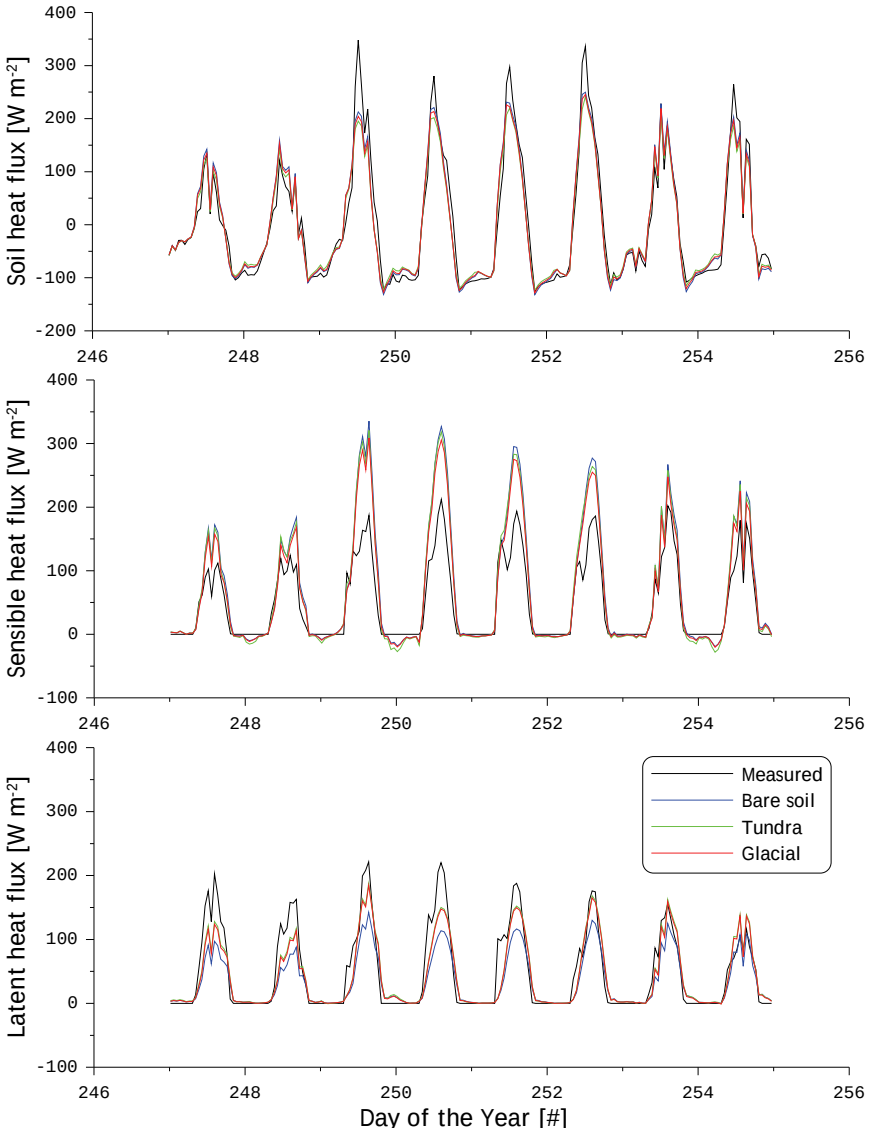

Figure 10-1 Comparison of the measured heat fluxes and the Noah simulations obtained using three standard vegetation parameterizations.

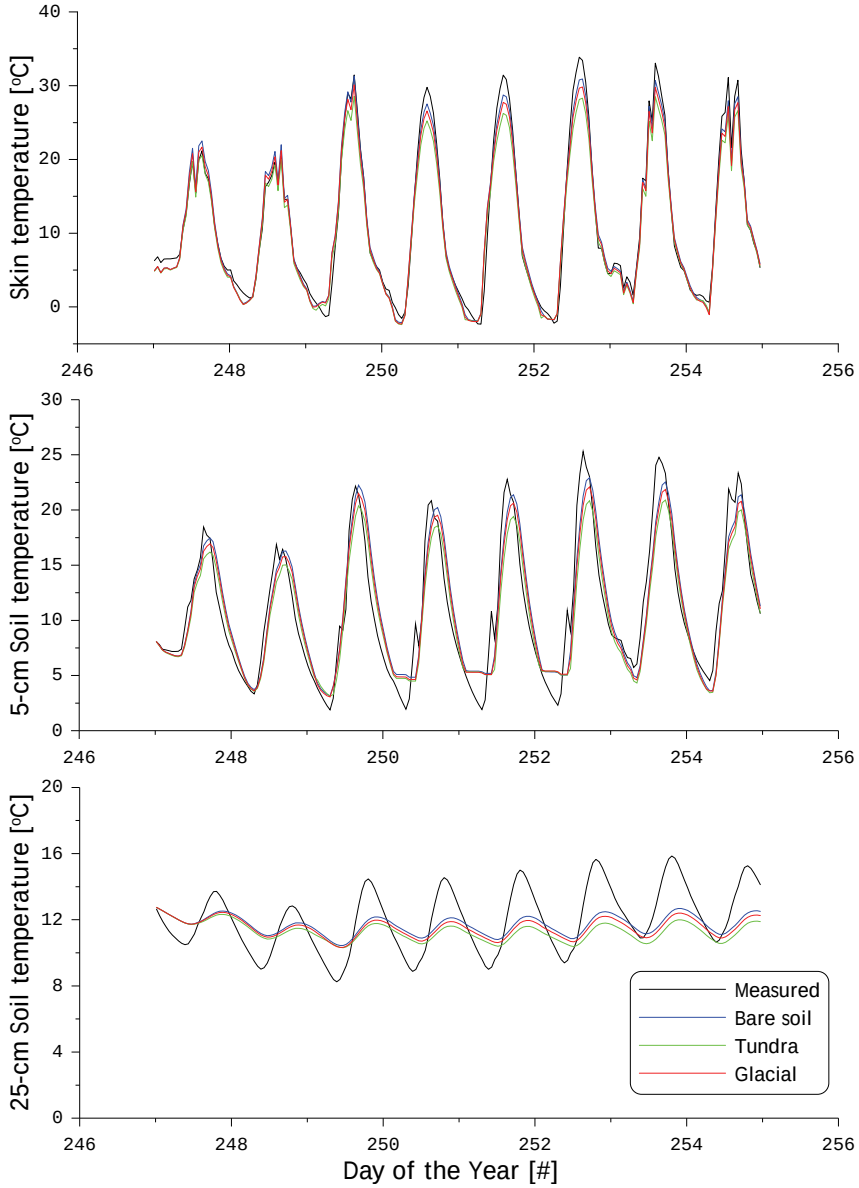

Figure 10-2 Comparison of the measured soil temperature at surface level and soil depths of 5 cm and 25 cm against Noah simulations obtained through application of three standard vegetation parameterizations.

It should be noted that the magnitude of the *H* overestimation is 13.34 – 30.55 W m^{-2} larger than the underestimation of the λE. From an energy balance perspective, this difference should be compensated by other energy components, but only a small

systematic difference can be noted in the G_0. The explanation for this discrepancy is found through the analysis of the measured and simulated temperatures of the soil profile. Although the measured dynamic temperature range is not entirely captured by the simulations, the modeled surface temperature (T_{skin}) and 5-cm soil temperature compare reasonably well with the measurements and results in RMSD's of 1.45-1.84 and 1.08-1.80 ^{o}C, respectively. On the other hand, the 25-cm soil temperature (T_{25cm}) simulations strongly underestimate the measured diurnal temperature variation, which indicates that the heat required for the simulation of temperature variations deeper in the soil profile is not transferred into soil column. Since a relatively small amount of energy is used for heating the deeper soil profile, more energy is available for heating the atmosphere. Hence, the Noah overestimates the H.

Comparable results on the bias in partitioning the H and λE have previously been reported by Kahan et al. (2006). They have reported on over- and underestimation of H and λE measured using SSiB at a Sahelian study site in Niger by as much as 31.2 and 41.8 W m^{-2}, respectively. By reducing the model's stomatal resistance (among other parameters) by more than one order of magnitude, the λE is increased and, because of the energy conservation principle, a reduction in H is enforced. The differences between the modeling results obtained with the three vegetation parameterizations should be viewed in this context. The smallest H overestimation is observed for the glacial vegetation parameterization. This parameterization includes a low value for minimum stomatal resistance ($R_{c,min}$) and the lowest values for the roughness length for momentum transport (z_0), which reduces the mechanically generated atmospheric turbulent fluxes. Therefore, Noah modeling results obtained through application of the *glacial* vegetation parameterization are considered to represent the Tibetan measurements best.

Also, the inconsistency of LSM's in the simulation of the soil heat transfer has been previously recognized. Yang et al. (2005) extensively discussed the impact of the vertical heterogeneity in the soil profile for the simulation of the H and λE, and concluded that accounting for the vertical soil heterogeneity is indispensable for a proper characterization of the soil heat transfer. In the default parameterization, vertical heterogeneous soils are not accommodated in Noah, which could be the explanation for the inconsistencies between the simulated and measured temperature at a soil depth 25 cm. This is supported by the investigation of Yang et al. who concluded that over the Tibetan prairie grasslands the roots significantly alter the soil thermal properties (STP) of the top soil.

10.3 Optimized Noah simulations

The analysis of the Noah results obtained using standard parameterizations has shown that the transfer of heat through the soil column and the partitioning between H and λE are not properly simulated. In this section, the simulation of these two land surface processes is optimized by adjusting soil and vegetation parameterizations. These adjustments consist of evaluating different numerical discretizations of the soil layers and calibration of soil and vegetation parameters.

Calibration of the soil and vegetation parameters is performed using the Parameter Estimation (PEST, Doherty 2003) tool, which is based on minimizing the sum of squared differences (SSD) between measurements and simulations using the Gauss-Levenberg Marquardt algorithm.

PEST allows users to assign weights to specific observations and different numerical schemes for the minimization of the SSD. For a complete mathematical description of PEST, readers are referred to Gallagher and Doherty (2007) and Doherty (2003). Here, PEST is applied using its default configuration. To assure convergence, the optimization process has been performed for a wide range of initial parameter values and during each optimization run only a single parameter is calibrated. A SSD based on the measured and simulated G_0 (SSD_{G0}) is adopted for calibration of the soil parameters and a SSD based on the measured and simulated λE ($SSD_{\lambda E}$) is utilized to calibrate the vegetation parameters, independently. In this section, first, the influence of the soil parameterizations on the simulation of temperature states and surface energy balance is discussed and, then, the impact of the vegetation parameters is addressed.

Table 10-3 Calibrated *qtz* parameters using seven soil layer discretizations within the Noah model.

Number of soil layers [#]	Top layer thickness [cm]	Quartz content [-]
4 layers	10.0	0.82
5 layers	0.1	1.50
	0.5	1.58
	1.0	1.63
	2.0	1.66
	3.0	1.67
	4.0	1.68

Soil heat transfer

Because of the large number of roots and the higher organic matter content, the thermal properties of the topsoil are expected to be different from the subsoil. Noah is, therefore, adapted to

accommodate different soil thermal layers (STL's). In terms of STL's, a 0.10 m topsoil layer and 1.90 m subsoil layer has been selected for this investigation. For the subsoil the default parameterization for the thermal conductivity (κ_h) and heat capacitiy (C) have been assigned, while for the top soil a C_{soil} value of $1.0 \cdot 10^6$ J m^{-3} K^{-1} is taken and the *qtz* parameter in the κ_h parameterization is optimized by minimizing the Φ_{G0}. Within this calibration procedure, the upper and lower limits of the quartz content are set to 0.01 and 2.0 beyond values that are physically possible in order to maintain maximum flexibility in the modeling system. In addition, different discretizations of the soil profile are evaluated, for which the default 4-soil layer and six alternate 5-soil layer models are used. Within the 5-layer model setups, thicknesses for the top soil layers of 0.1, 0.5, 1.0, 2.0, 3.0 and 4.0 cm have been selected, while maintaining the thickness of the top two layers 0.10 m in total.

The *qtz* parameter is calibrated for all seven soil profile discretizations and the optimized values are presented in Table 10-3. The *glacial* vegetation parameterization has been used for these simulations. The modeled and measured surface fluxes are presented in Figure 10-3. Similar plots are presented in Figure 10-4 for the temperatures at the surface and soil depths of 5 and 25 cm. The RMSD's and biases between modeling results and measurements of the heat fluxes and soil temperatures are given in Tables 10-4 and 10-5, respectively. It should be noted that the Noah simulations using the 5-layer model setup with thicknesses of the top soil of 2.0, 3.0 and 4.0 cm are not shown in Figures 10-3 and 10-4.

The results demonstrate that differentiation between the STP of the top- and subsoil alone improves the simulation of the soil temperatures only slightly and even increases the differences between the simulated and measured surface fluxes. The simulation of the soil heat transfer only improves when a thin soil layer is added to soil model discretization. For all six thicknesses of the top layer, the largest improvements are noted in the simulation of T_{25cm}. The RMSD for the T_{25cm} ($RMSD_{T25cm}$) decreases from 1.33 °C obtained with the *glacial* vegetation parameterization and the default discretization to values varying between 0.71 and 0.66 °C depending on the thickness of the top soil layer, which is a reduction of 46.6-50.3 %. Also, the RMSD's for simulated T_{skin} and T_{5cm} obtained with the 5-layer model setups decrease as compared to the model results obtained with the default 4-layer configuration. The T_{skin} RMSD ($RMSD_{Tskin}$) decreases from 1.45 °C to values of 1.15-1.35 °C and for the T_{5cm} RMSD ($RMSD_{T5cm}$) a decrease of 1.28 °C to 1.02-1.11 °C is observed. Both the $RMSD_{Tskin}$ as well as $RMSD_{T5cm}$ depend on the thickness of the top layer; the lowest $RMSD_{Tskin}$ and $RMSD_{T5cm}$ for a

0.1 cm top layer, while the lowest $RMSD_{T25cm}$ is obtained for a 1.0 cm top layer.

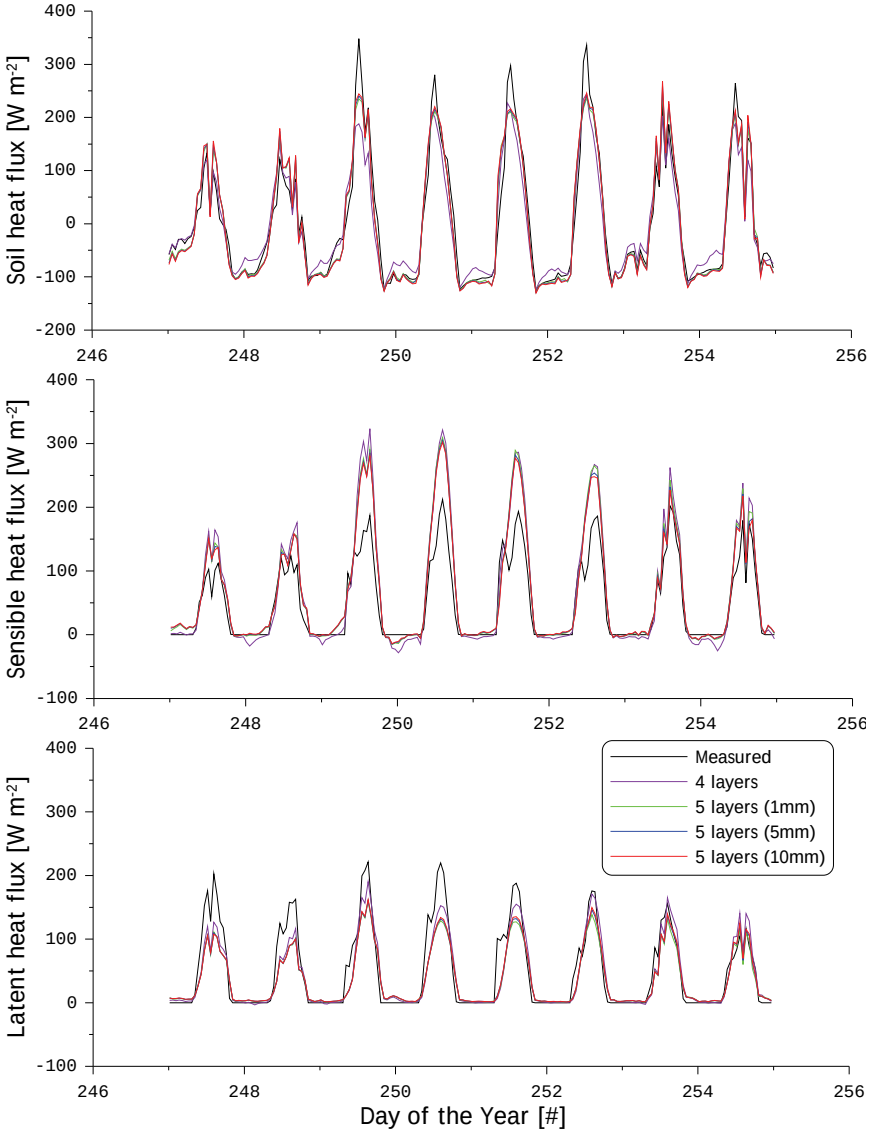

Figure 10-3 Comparison of the heat fluxes measured and simulated using Noah with two soil thermal layers and different numerical discretizations of the soil profile. For reference also modeling results obtained with the default parameterizations are shown.

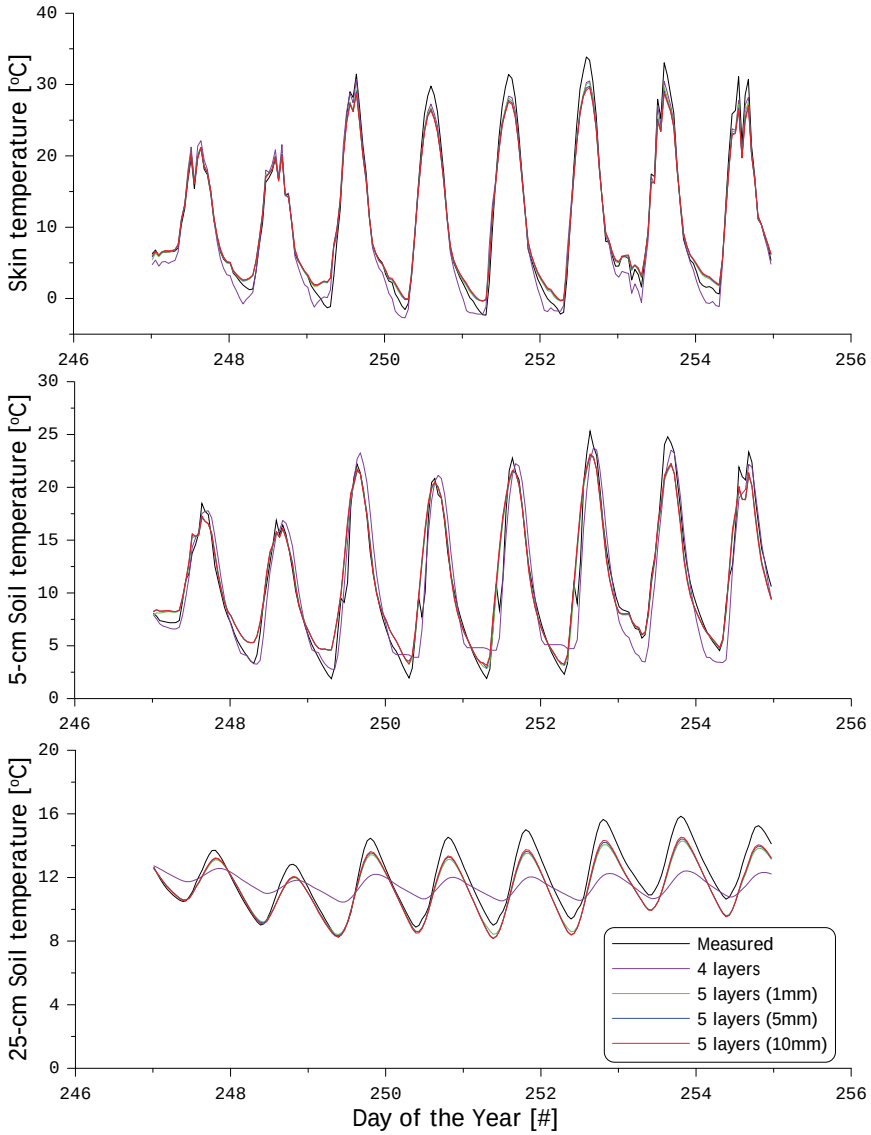

Figure 10-4 Same as Figure 10-3, except that the measured and simulated soil temperatures are shown for the surface level and soil depths of 5 and 25 cm.

The impact of the adjustments in soil parameterization on the simulation of the surface energy balance is primarily manifested in the H and G_0. Its influence on the simulation of the λE is limited and resulting RMSD ($RMSD_{\lambda E}$) values vary only between 33.17 and 37.04 W m^{-2}. This is explained by the direct relationship between the soil temperature and the calculation of the H and G_0, which is absent for

the λE. Computations of H and G_0 are both based on a temperature gradient either between the surface and the air temperature (for the H) or between the surface and the mid-point of the first soil layer (for the G_0). For the G_0, the lowest RMSD ($RMSD_{G0}$) is obtained using the 5-layer model with a 0.1 mm top layer (33.17 W m^{-2}) because using the configuration diurnal temperature variations at the surface and at a 5-cm soil depth are simulated best. However, the change in the simulated surface temperature modifies also the temperature gradient between the skin and air. As a result, an increase of RMSD for H ($RMSD_H$) is observed as the $RMSD_{G0}$ decreases, and vice versa. The lowest $RMSD_H$ is obtained for the 5-layer model configuration using 4.0-cm top layer, which is 35.87 W m^{-2}. The decrease in $RMSD_H$ observed for thicker top layer in 5-layer model configuration is coupled with a decrease in the obtained bias, which range from 40.42 to 22.90 W m^{-2} for top soil layer thicknesses of 0.1 – 4.0 cm. This indicates an improvement in the simulation of the heat flux partitioning, while even the lowest bias obtained for the H as well as λE remain quite significant, 22.90 and 26.04 W m^{-2}, respectively.

Table 10-4 RMSD's calculated between the measured and simulated soil temperature and surface fluxes. The modelling results are obtained with Noah configured to accommodate different STP for the top- and subsoil and different discretizations of the soil profile.

layers	Top soil thickness	H	λE	G_0	T_{skin}	T_{5cm}	T_{25cm}
[#]	[cm]	[W m^{-2}]				[^oC]	
4 layers	10.0	52.72	33.17	41.28	1.40	1.49	1.32
5 layers	0.1	46.92	37.04	33.17	1.15	1.02	0.71
	0.5	44.34	36.21	34.73	1.25	1.05	0.68
	1.0	43.30	36.13	36.83	1.32	1.07	0.66
	2.0	43.24	36.06	39.34	1.36	1.09	0.66
	3.0	43.51	35.97	40.47	1.35	1.11	0.67
	4.0	35.87	35.89	40.68	1.35	1.03	0.67

Table 10-5 Same as Table 10-4, except the biases are presented.

layers	Top soil thickness	H	λE	G_0	T_{skin}	T_{5cm}	T_{25cm}
[#]	[cm]	[W m^{-2}]				[^oC]	
4 layers	10.0	-46.40	18.70	17.33	0.84	0.30	0.44
5 layers	0.1	-40.42	31.07	2.31	0.05	-0.21	0.67
	0.5	-37.69	29.12	3.92	0.06	-0.28	0.65
	1.0	-35.91	28.19	5.35	0.06	-0.30	0.63
	2.0	-34.86	27.08	5.64	0.08	-0.29	0.64
	3.0	-34.62	26.45	5.33	0.10	-0.28	0.64
	4.0	-22.90	26.04	5.30	0.11	-0.25	0.65

In general, from these modeling results it may be concluded that differentiation between top- and subsoil and including a thin top soil layer improve the soil heat transfer simulation. However, these adjustments in the soil parameterization do not improve the simulation of the surface fluxes. The G_0 simulation using 0.1 cm top layer represents the measurements best, while difference between the measured and simulated H is smallest using a 4.0 cm top soil layer. The overestimation of the H with 0.1 cm top soil layer might suggest that the simulated solar radiation available for heating of the air and soil is too large; meaning that the simulated solar radiation consumed by the cooling of surface through evaporation and transpiration is too low. Further, it should be noted that the optimized values for the quartz content for the all 5-layer model configurations exceed its physical limits varying between 1.50 and 1.68. An explanation for these unrealistic values will be provided in the discussion.

Vegetation parameterization

Amelioration of inconsistencies in simulating the partitioning between H and λE can be obtained by adopting an aerodynamic approach through reconsideration of kB^{-1} parameterization (e.g. Yang et al. 2008). However, Kahan et al. (2006) demonstrated that the simulation of the heat flux partitioning can also be improved by calibrating the vegetation parameters and showed that most notably an adjustment in stomatal resistance is needed to increase model performance. Similarly, the $R_{c,min}$ of the Noah vegetation parameterization is used, here, to improve the simulated heat flux partitioning. In addition, the optimum temperature for transpiration (T_{opt}), currently fixed at a value of 24.85 ^{o}C, may need to be tuned to represent the Tibetan conditions.

Ideally, the $R_{c,min}$ and T_{opt} would be obtained from long term data sets as has been done by Gilmanov et al. (2007). This reaches, however, beyond the scope of this study. The parameters $R_{c,min}$ and T_{opt} are, therefore, calibrated by minimizing the cost function between the measured and simulated λE. For this minimization, the 5-layer Noah model configuration is used with a 0.5 cm top soil layer and a *qtz* value of 1.58. The calibration of the $R_{c,min}$ and T_{opt} yields values of 49.88 s m^{-1} and 7.21 ^{o}C, respectively. Thus, the $R_{c,min}$ is reduced by 100.12 s m^{-1} and T_{opt} by 17.61 ^{o}C in comparison to the default parameterization. For the Tibetan conditions, the decrease in the $R_{c,min}$ and T_{opt} within Noah results in an λE increase. Lowering the $R_{c,min}$ reduces the resistance for transpiration and 7.21 ^{o}C is closer to the averaged air temperature at the study site, which is 6.27 ^{o}C for the selected period.

Both changes to the two plant physiological parameters can be argued for. Growing seasons on the plateau are short and, in this short period, vegetation should be productive in order to be able to survive the harsh Tibetan environment. Further, temperatures on the plateau are, generally, lower than at sea level; a lower temperature at which plants transpire optimally is, therefore, required. At the same time, the validity of the default T_{opt} can be questioned for all environments that substantially differ from the humid climate for the original parameterization (Dickinson, 1984). A climate dependent parameterization could be considered for global Noah applications.

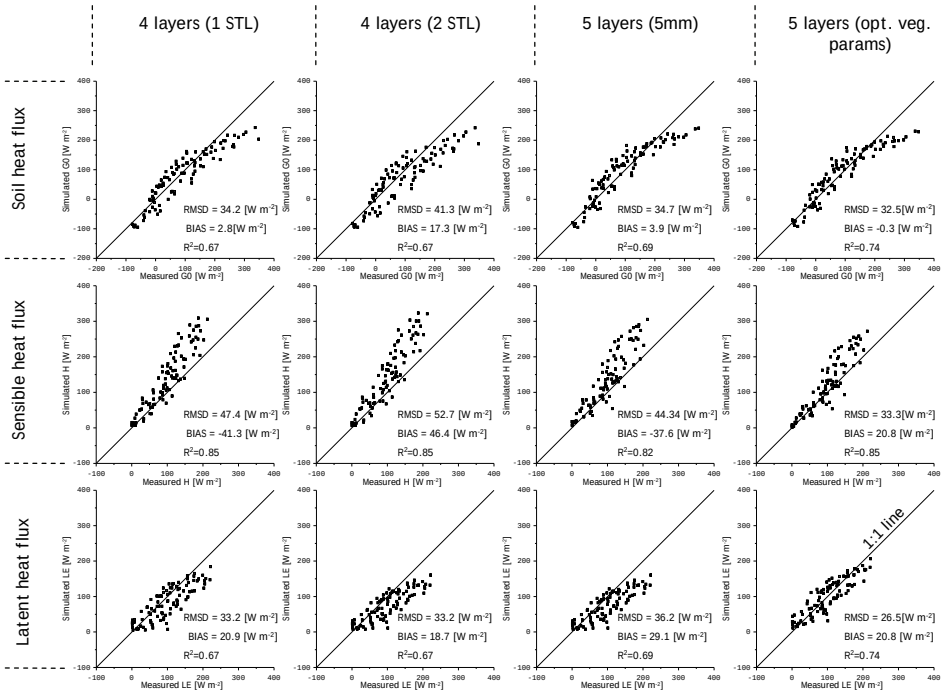

Figure 10-5 Scatter plots of surface fluxes (G_0, H, λE) measured and simulated using Noah in its 1) default configuration; 2) default numerical discretizations of the soil profile and 2 STL's; 3) 5-layer model setup, 2 STL's and top layer of 0.5 cm; 4) same as 3) except the vegetation parameters are calibrated.

The modeling results of Noah simulations with the optimized vegetation parameters are plotted against measurements, which are presented in Figures 10-5 and 10-6 for the heat fluxes and soil temperatures, respectively. For comparison purposes, a selection of the Noah simulations discussed previously is also presented in these

figures, which are: 1) the default 4-layer model with the *glacial* vegetation parameters; 2) the 4-layer model with two STL's and *glacial* vegetation parameters; and 3) the 5-layer model with two STL's, 0.5-cm top layer and *glacial* vegetation parameters. The basic statistics, such as R^2, RMSD and bias, are presented in the plots.

Comparison of the plots in Figure 10-5 and 10-6 shows that the adjustments in the parameterization of STP improves the simulation of the soil temperature states, but does not result in a reduction in the differences between the simulated and measured surface fluxes. By using the calibrated $R_{c,min}$ and T_{opt}, the simulated partitioning between H and λE represents the measured surface energy budget better. The RMSD's obtained for the H and λE are reduced from 47.4 and 33.2 W m^{-2} for the default simulations to 33.3 and 26.5 W m^{-2} for simulations obtained with calibrated parameters, respectively. Kahan et al. (2006) have reported similar results. They showed for an application of the SSiB LSM to a Sahelian study area that lowering the model constraints for the transpiration, not only increases simulated λE, but also reduces the overestimation in the H.

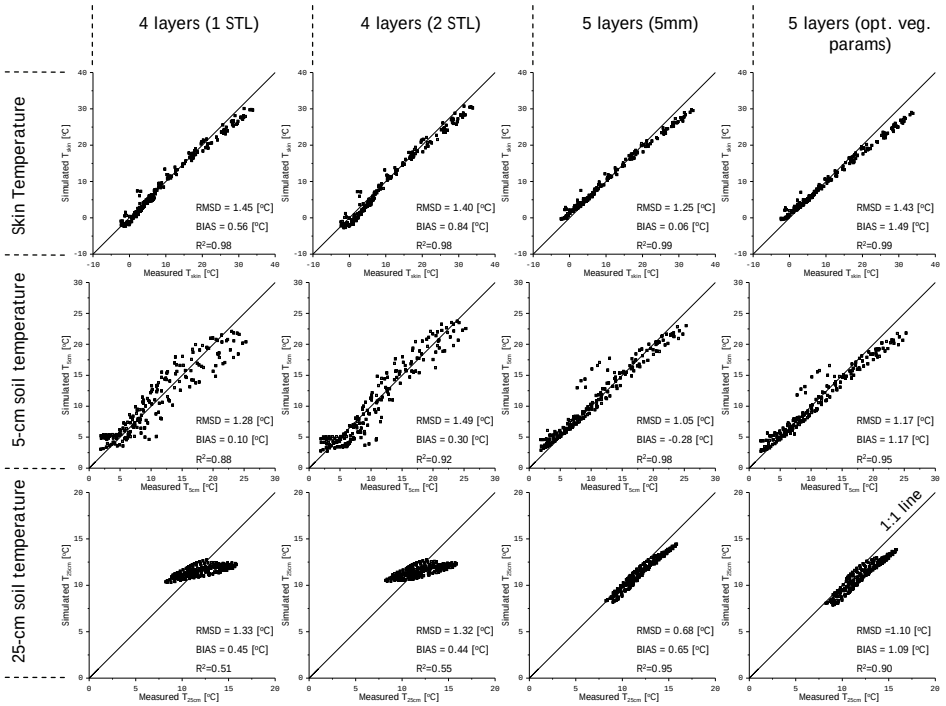

Figure 10-6 Same as Figure 10-5 except that the soil temperature (T_{skin}, T_{5cm} and T_{25cm}) are shown here.

10.4 Discussion

The adjustments in the parameterization of the STP and calibration of the vegetation parameters, $R_{c,min}$ and T_{opt}, have ameliorated the simulation of the soil heat transfer and reduced uncertainties in the simulated H and λE to levels comparable to those reported in previous investigations (e.g., Sridhar et al. 2002, Gutmann and Small 2007 and Pauwels et al. 2008). Despite the optimized Noah simulations are able to represent the soil temperature and surface energy balance measurements better, still some inconsistencies in the modeling results can be observed when radiative forcings become large. For example, Noah systematically overestimates the measured H at values larger than approximately 150 W m^{-2}, which coincides with an underestimation of the G_0 and T_{skin} when the measured values are larger than approximately 150 W m^{-2} and 20 ^{o}C, respectively. Apparently, under large radiative forcings Noah is not able to simulate T_{skin} increase measured on the Tibetan Plateau. Therefore, the simulated temperature gradients between the surface and atmosphere, and between surface and the mid-point of the first soil layer become too large and too small, respectively. As a result, an over- and underestimation of the measured H and G_0 are observed. The explanation of this discrepancy in the simulated T_{skin} is twofold.

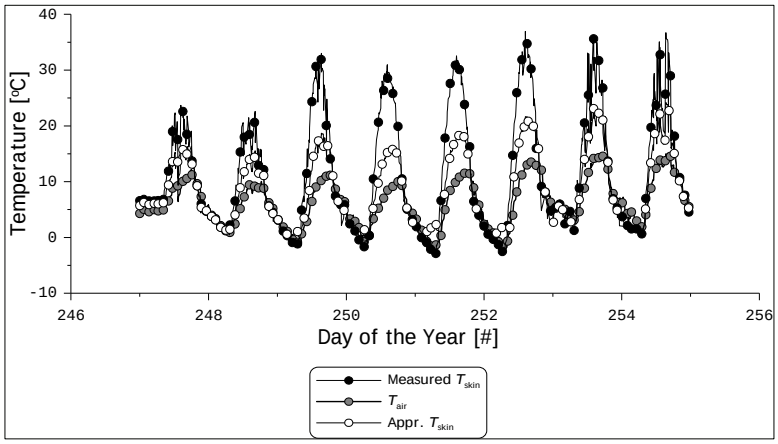

Figure 10-7 Measurements of the air and surface temperature, and the surface temperature approximated using Eq. 3.21 plotted as a time series for the analyzed period of meteorological forcing collected at a Tibetan Plateau site.

First, the surface exchange coefficient for heat (C_h) may not be properly parameterized for the Tibetan conditions. Noah uses the Reynolds number dependent method proposed by Zilintinkevich (1995) to determine the kB^{-1}. However, Yang et al. (2008) showed

for bare soil surfaces that Reynolds number dependent kB^{-1} methods, in general, tend to underestimate the strong diurnal kB^{-1} variations observed over the Tibetan Plateau (e.g. Ma et al. 2005 and Yang et al. 2003). A kB^{-1} underestimation during daytime results in more efficient heat transfer between the soil surface and the atmosphere, which causes an H overestimation and explains also the discrepancy between the measured and simulated T_{skin}. Other kB^{-1} methods (e.g. Su et al. 2001 and Yang et al. 2002) that are able to capture this diurnal kB^{-1} variation would further improve Noah's overall performance over the Tibetan Plateau. For evaluations of the available kB^{-1} methods readers are referred to Liu et al. (2007) and Yang et al. (2008).

Second, the linearization of the surface energy balance, Eq. 3.21, utilized to compute the T_{skin} contributes to explaining the differences between the simulated and measured T_{skin}. This approximation is exact when T_{air} is equal to T_{skin} and loses its validity as the difference between T_{air} and T_{skin} increases. For our Tibetan study site, differences between the T_{air} and T_{skin} can be expected to be significantly larger than at sea level because the air pressure is much lower and fewer air molecules are available to transport energy from the surface towards the air. To demonstrate the impact of the applied approximation for our Tibetan site, the measured T_{skin} and T_{air}, the T_{skin} calculated by using Eq. 3.21 are plotted in Figure 10-7. This plot shows that the applied approximation holds rather well during nighttime. After sunrise, however, differences between measured T_{air} and T_{skin} increase resulting in a discrepancy between the measured and approximated T_{skin} of more than 10 ^{o}C at midday. Obviously, this leads to an underestimation of T_{skin} even when the parameterization of the soil-vegetation-atmosphere system is in agreement with the local conditions.

Within the uncertainties embedded in the C_h calculation and in the linearization applied for the T_{skin} simulation lies also the explanation for the unrealistically high values of the calibrated *qtz* parameter. With the increase of the *qtz* parameter, the thermal heat conductance is raised to increase the transport of heat into soil and to compensate for the lower simulated temperature gradient between surface and the mid point of the first soil layer. When the *qtz* parameter is not used to compensate for the T_{skin} underestimation, biases arise in the simulation of the soil temperature profile as occurs in Noah applications in the default configuration.

10.5 Conclusions

In this chapter, adjustments in the soil and vegetation parameterizations required to be able to reproduce the soil temperatures and surface fluxes using the Noah LSM are investigated

for a 7-day period of *in-situ* measurements collected at the Tibetan Naqu station. Analysis of the simulations obtained through application of the default parameterization has shown that,

1) Heat transfer through the soil column is not represented adequately;
2) Partitioning between the sensible (H) and latent heat (λE) flux is biased.

Amelioration of the parameterization of these land surface processes is achieved through adjustment of soil and vegetation parameterizations. By differentiating between the soil thermal properties of a top- and subsoil, and including a thin top soil layer, uncertainties in the simulation of the soil heat transfer are reduced and RMSD's between the measured and simulated T_{skin}, T_{5cm} and T_{25cm} are obtained of 1.25 ^{o}C, 1.05 ^{o}C and 0.68 ^{o}C by using a 0.5 cm thick top soil layer. It is found that adding a thin top soil layer has stronger effect than differentiating between the soil thermal properties of a top- and subsoil. A decrease in the vegetation parameters, $R_{c,min}$ and T_{opt}, constraining the transpiration reduces the RMSD for the λE from 33.2 W m^{-2} obtained using the default Noah configuration to 26.5 W m^{-2} using the optimized parameterization. In addition, the improvement in the λE simulation also influences the H simulation and decreases the RMSD from 47.41 to 33.3 W m^{-2}, while the differences between the measured and simulated G_0 do not change significantly.

Although the adjustments in the parameterization of the STP and calibration of vegetation parameters improved Noah's capability of representing the soil temperature states and the surface energy balance components measured on the Tibetan Plateau, under conditions of the high radiative forcings an underestimation is observed of measured T_{skin}. This underestimation of the T_{skin} results in an overestimation of the H and underestimation G_0. The explanation for the discrepancy in the T_{skin} simulation is twofold. First, the surface exchange coefficient for heat may not be properly parameterized. Second, the approximation, adopted for linearization of the surface energy balance for the T_{skin} calculation, introduces some uncertainties when differences between the measured T_{skin} and T_{air} are large, which are typical midday conditions on the Tibetan Plateau.

11 How may high resolution soil moisture retrievals improve large-scale modeling?

This chapter is based on:

Van der Velde, R., Salama, Mhd. S., Van Helvoirt, M.D., Su, Z., "Source of difference between SAR based retrievals and low resolution MM5-Noah soil moisture simulations", to be submitted to Journal of Hydrometeorology.

11.1 Introduction

The first part of this thesis dealt with the retrieval of soil moisture from active microwave measurements and Noah LSM simulations were evaluated in the second part. The results presented in Chapters 5 to 8 show that soil moisture can be retrieved from both SAR and scatterometer measurements with a reasonable accuracy. The soil moisture retrieved from remote sensing observations provides, however, only information on an instantaneous basis, while for monitoring purposes the soil moisture products should be available at shorter and regular time intervals. Moreover, one is often not only interested in soil moisture monitoring alone, but also in the quantification of processes, such as evaporation and runoff. For these reasons, integrating the remote sensing observations into a LSM is considered as an elegant method for a quantitative use of remotely sensed soil moisture products.

The research on integrating remote sensing measurements into LSM simulations has had over the past decade a strong focus on data assimilation; readers are referred to McLaughlin (2002) and Reichle (2008) for reviews. In data assimilation, the simulated state(s) are updated by a weighted average of the originally simulated and the measured state(s) when available. A fundamental assumption in applying such data assimilation methods is that both model and measurements uncertainties are unbiased. This assumption is, however, hardly ever valid for both simulations and measurements when they are based on retrievals from remote sensing observations (Ni-Meister et al. 2005).

For example, Chapters 5 and 6 show how changes in surface roughness and vegetation affect the retrieval of soil moisture. Further, the results from Chapter 9 and Walker et al. (2001) indicate that differences in the model structure of soil water flow schemes may severely affect the simulated soil moisture. The Noah simulations for the Tibetan Plateau site (in Chapter 10) have shown that the parameterizations used for large-scale applications has only a limited validity locally. Other sources of uncertainty affecting the

land surface modeling results are related to the reliability of the atmospheric forcings (Berg et al. 2003, Sheffield et al. 2006) and the selection of the initial and boundary conditions.

Various authors (e.g. Reichle and Koster 2004, De Lannoy et al. 2007) advocate, therefore, for a removal of this bias prior to data assimilation. This method can be effective in eliminating the bias between simulations and measurements. Such approach can, however, not change the fact that some physical processes are not adequately simulated by the LSM. Yang et al. (2007) addresses this issue with the so-called dual pass variational data assimilation method. Within the first pass, model parameters are estimated using months of satellite measurements and in the second pass states are updated daily. In this way, the long term effects of parametric uncertainties and short term atmospheric forcing errors can be reduced. Via the calibration of model parameters on a long term basis the effects of the uncertainties due to the model structure are also taken into account, while the deficiencies in the model structure yet remain.

Initially, the setup of this research was to assimilate the soil moisture retrieved from the ASAR data over the Tibetan Plateau into the Noah LSM. The data record of atmospheric forcings and heat flux measurements are, however, only available for a limited number of days and a single station on Tibetan Plateau. The Noah LSM simulations would have to be performed with atmospheric forcings obtained from ACM simulations. However, atmospheric forcings simulated by ACMs are uncertain particularly over extreme environments, such as the Tibetan Plateau, and the validation of the heat fluxes would be limited to measurements collected at a single location.

This chapter is, therefore, not based on the assimilation of soil moisture retrieved from ASAR measurements. Instead the SAR based retrievals presented in Chapter 8 are compared to 10 km resolution soil moisture simulations by the Noah LSM coupled to the fifth generation Pennsylvania State University - National Center for Atmospheric Research (PSU/NCAR) Mesoscale Model (MM5) regional climate model. The advantage of using the Noah LSM coupled to MM5 is that the regional atmospheric circulation is included in these simulations, whereas the spatial and temporal scale of ACMs is typically too coarse to take this into account.

The MM5 Noah simulations provide soil moisture at 10 km spatial resolution whereas the ASAR soil moisture is retrieved at a 100 m resolution. A comparison of the two yields, thus, deviations that are related to 1) the inherent bias due to differences in the climatology of the simulated and retrieved soil moisture, 2) uncertainties associated with the simulations as well as retrievals, and 3) the differences in

the spatial representation. An understanding of the contribution of these sources of difference is needed to fully appreciate the value of integrating satellite soil moisture with models operating at a lower spatial resolution. This chapter presents a method for the quantification of the above-mentioned sources of difference between the two soil moisture data sets.

11.2 MM5 simulations

The PSU/NCAR MM5 modelling system is a limited area non-hydrostatic model for predicting the regional atmospheric circulation that uses a terrain-following vertical coordinate systems. The core of MM5 system is described in Dudhia (1993) and Grell et al. (1994). It has two-way nesting capabilities and allows users to select different physics options. Here, the MM5 simulations were performed using the simple ice explicit moisture scheme (Dudhia 1989), the Medium-Range Forecast planetary boundary layer scheme (Hong and Pan 1996), the Rapid Radiative Transfer Model radiation scheme (Mlawer et al. 1997) and the Grell cumulus scheme (Grell et al. 1994). The default version of the Noah LSM has been coupled to MM5 to parameterize the exchange of water and energy between the land surface and atmosphere (Chen and Dudhia 2001).

For this study, the MM5 modelling domain has been centred on Naqu station (31^{o}N and 91^{o}E) and is based on 43 x 43 grid cells in the horizontal plane with 10-km resolution. Boundary conditions for this simulation have been obtained from the NCEP-NCAR reanalysis project. In this configuration MM5 has been run from September 2003 till September 2007. The simulation starts, thus, 20 months prior to the first ASAR acquisitions, which can be considered as model spinup, and covers the entire ASAR WS data set.

11.3 Separating the sources of difference

In developing the method for separating the sources contributing to the differences between the simulated and retrieved soil moisture we start with defining,

$$\theta_{\mathrm{MM5}} = \theta'_{\mathrm{MM5}} + b_{\mathrm{clim}} \tag{11.1}$$

$$\bar{\theta}_{\mathrm{ASAR}} = \frac{1}{n-1}\sum \theta^{i}_{ASAR} \tag{11.2}$$

where, θ_{MM5} and θ_{ASAR} are the MM5 Noah and ASAR soil moisture content [m^3 m^{-3}], b_{clim} is the inherent bias between the climatology of the simulated and retrieved soil moisture [m^3 m^{-3}], n is the number of pixels [#], superscript i is i^{th} ASAR pixel within the model grid.

Via a linearization based on Taylor series expansion, it can be shown that the total mean of squared differences (σ_t^2) can be approximated as the sum of individual contributions as follows,

$$\sigma_t^2 = \sigma_b^2 + \sigma_u^2 + \sigma_s^2 \quad (11.3)$$

where, σ_b^2 is the contribution related to the inherent bias due to difference in the climatology of the simulated and retrieved soil moisture, σ_u^2 follows from uncertainties embedded with both the simulations and the retrievals, and σ_s^2 is the discrepancy between the two products arising from their difference in spatial resolution.

For unbiased differences between the simulated and retrieved soil moisture Eq. 11.3 reduces to,

$$\sigma_{t'}^2 = \sigma_u^2 + \sigma_s^2 \quad (11.4)$$

When the uncertainty in the ASAR soil moisture product is assumed to be unbiased at the scale of the MM5 model grid, σ_t^2 can be defined as,

$$\sigma_t^2 = \frac{1}{n-1}\sum_{i=1}^{n}\left(\theta_{\mathrm{MM5}} - \theta_{\mathrm{ASAR}}^i\right)^2 \quad (11.5)$$

and when the bias, b, is removed the $\sigma_{t'}^2$ can be defined as,

$$\sigma_{t'}^2 = \frac{1}{n-1}\sum_{i=1}^{n}\left(\theta'_{\mathrm{MM5}} - \theta_{\mathrm{ASAR}}^i\right)^2 \quad (11.6)$$

Substitution of Eq. 11.4 into Eq. 11.3 yields,

$$\sigma_b^2 = \sigma_t^2 - \sigma_{t'}^2 \quad (11.7)$$

Then assuming retrieval uncertainty are normally distributed, the σ_s^2 can be determined by,

$$\sigma_s^2 = \frac{1}{n-1}\sum_{i=1}^{n}\left(\overline{\theta}_{\mathrm{ASAR}} - \theta_{ASAR}^i\right)^2 \quad (11.8)$$

Substitution of Eq. 11.8 into Eq. 11.4 gives,

$$\sigma_u^2 = \sigma_{t'}^2 - \sigma_s^2 \quad (11.9)$$

11.4 Bias reduction

From the above section follows that for separating σ_b^2, σ_s^2 and σ_u^2 the bias due to difference in the soil moisture climatology should be understood and corrected for. Such systematic deviations are inherent to the comparison of two independent data sources. Simulations are, for example, biased because its dynamics and absolute range are constrained by model parameterizations. Also, the temporal characteristics of the retrieved soil moisture are strongly determined by the retrieval method. Because both process and observational models are non-linear systems, a bias correction based on merely regression is often found too crude.

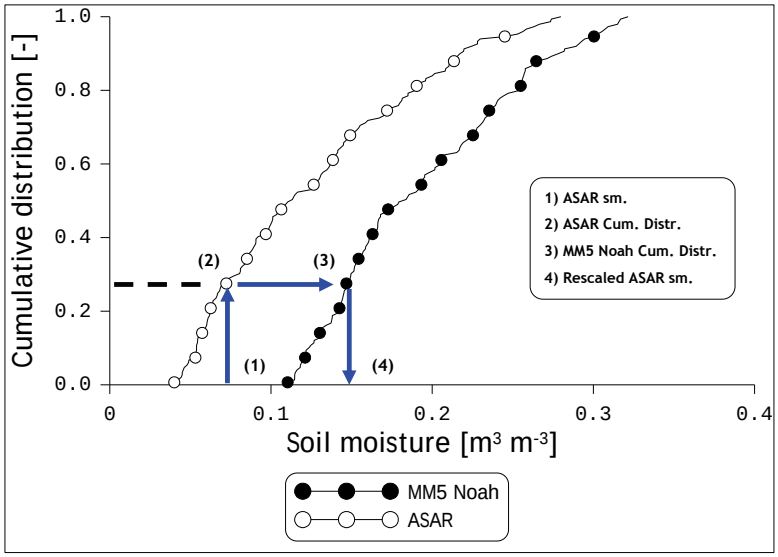

Figure 11-1 Illustration of the cdf matching technique applied for removing the bias between the MM5 Noah simulated and retrieved soil moisture.

Methods for transforming the retrieved into the simulated soil moisture climatology focus on obtaining a match in the first and second statistical moments. Crow et al. (2005) propose, for example, to evaluate the standardized anomalies of the simulated and retrieved soil moisture for unbiased comparisons. This approach requires, however, a long record of simulations and retrievals to accurately determine the mean and standard deviation. Alternatively, Reichle and Koster (2004) present a bias removal technique based on matching the cumulative distribution functions (cdf's) of the simulated and retrieved soil moisture. This approach is adopted here and is illustrated in Figure 11-1.

Table 11-1 Root Mean squared difference computed between the MM5 Noah and ASAR soil moisture.

	Original		**CDF matched**	
	RMSD $m^3\ m^{-3}$	*Bias* $m^3\ m^{-3}$	*RMSD* $m^3\ m^{-3}$	*Bias* $m^3\ m^{-3}$
Daily	0.085	0.067	0.051	0.008
Monthly	0.075	0.067	0.035	0.008

In our application, the cumulative distribution of the θ_{MM5} and the θ_{ASAR} is estimated for each MM5 grid cell seperately, whereby the θ_{MM5} is only considered for the cdf when also the θ_{ASAR} is available. The obtained cdf's of the θ_{MM5} and the θ_{ASAR} are, thus, based on a total of 150 soil moisture values. As such, the estimated cdf's provide a statistical link between the MM5 Noah soil moisture climatology and the retrievals, from which the θ_{ASAR} can be easily rescaled to the θ_{MM5} and vice versa. Because in data assimilation studies retrievals are used to reduce uncertainties in the simulated states, the θ_{MM5} is considered as the baseline and the θ_{ASAR} is transformed.

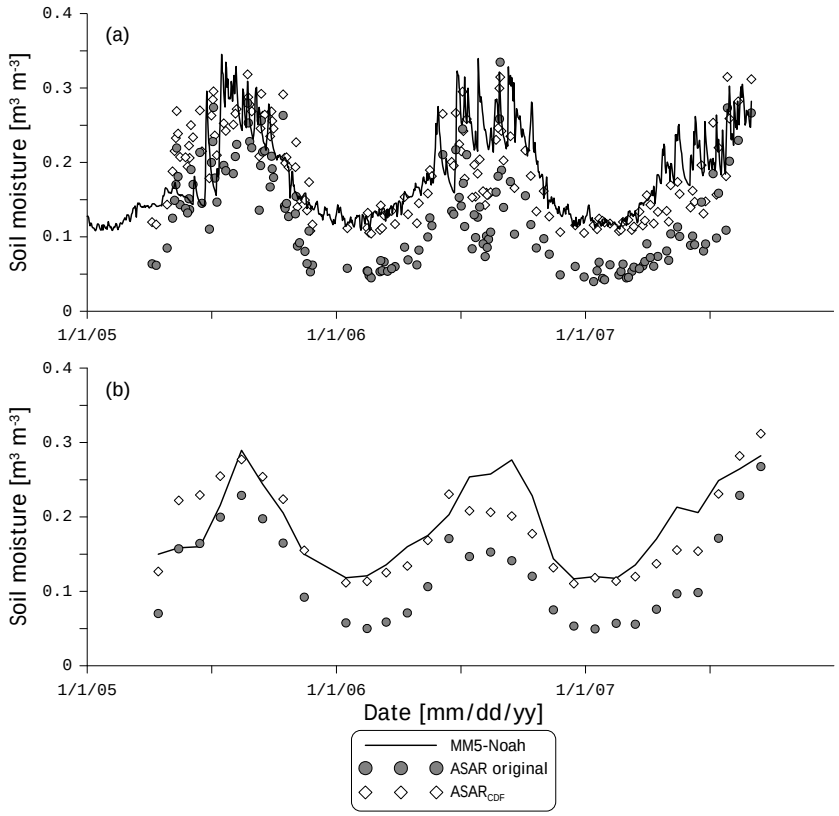

Figure 11-2 Time series of MM5-Noah simulated and retrieved soil moisture averaged over the entire study domain; a) presents the results on a daily basis and b) shows monthly averages.

The result of this rescaling is presented in Figure 11-2. The upper panel shows on a daily basis the θ_{MM5} and θ_{ASAR} averaged over the entire study domain, while the lower panel presents its monthly averages. Table 11-1 gives the RMSD's and biases computed between the θ_{MM5} and the θ_{ASAR} with and without the bias removal.

The figure shows that the temporal evolution of the θ_{MM5} and the θ_{ASAR} are similar. The minimum simulated and retrieved values occur in the winters and the peak soil moisture is observed during the monsoon season. As expected, however, there is clear bias between the θ_{MM5} and the uncorrected θ_{ASAR}. The simulated minimum soil moisture is around 0.11 m^3 m^{-3}, while the minimum of the retrievals is at 0.03 m^3 m^{-3}. After applying the cdf matching, this bias is reduced from 0.067 m^3 m^{-3} to 0.008 m^3 m^{-3}. As a result, also a reduction in the RMSD is observed, from 0.085 m^3 m^{-3} to 0.051 m^3 m^{-3} on a daily basis. These differences are similar to the error levels noted between *in-situ* and retrieved soil moisture presented in Chapter 8.

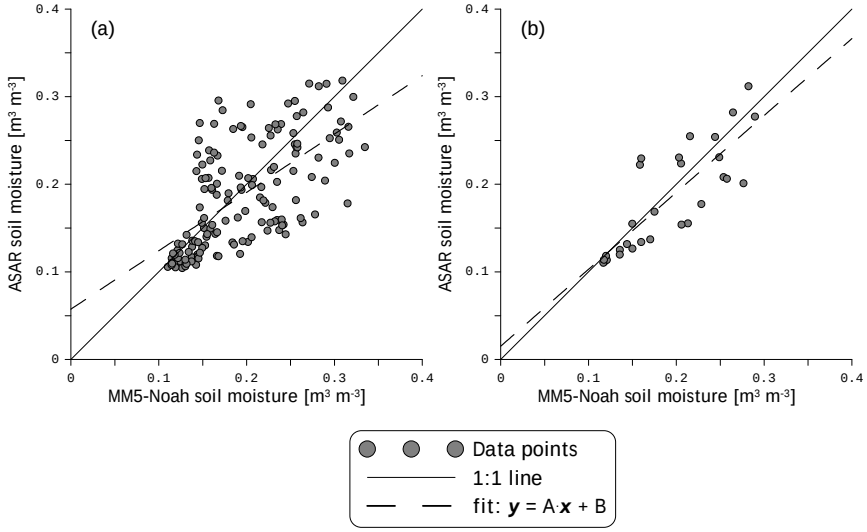

Figure 11-3 MM5 Noah soil moisture plotted against the ASAR retrieved soil moisture a) on a daily basis and b) for monthly averages.

Although the general patterns of the θ_{MM5} and the θ_{ASAR} are comparable, considerable differences can be noted at a shorted time scale. The deviations between the θ_{MM5} and θ_{ASAR} are largest on a daily basis (see Figure 11-2a). However, discrepancies between two data sets are also present on a monthly basis. At the beginning of the 2005 monsoon, for example, the θ_{ASAR} is on average about 0.08 m^3 m^{-3} wetter than the θ_{MM5}. Conversely, the 2006 summer and during the 2007 spring the θ_{ASAR} is drier than the simulated soil moisture.

In order to quantify the temporal correlations on a daily and monthly time scale, Figure 11-3 presents scatter plots between the θ_{MM5} and the bias corrected θ_{ASAR}. Statistics related to the linear regression fitted through the data points are given in Table 11-2. In general, the data points in both plots follow the 1:1 line. However,

the scatter between the θ_{MM5} and the θ_{ASAR} is considerably larger on a daily basis. This mismatch between the simulated and retrieved soil moisture can be argued for. The simulated soil moisture depends strongly upon rainfall input and the exact timing of precipitation events is often wrong in general circulation models (Reichle et al. 2004). Moreover, soil moisture retrievals are also subject to uncertainties. Within the monthly means, these stochastic sources of uncertainty are averaged out resulting in a R^2 increase from 0.413 to 0.683. As Reichle and Koster (2005) indicate that even with an anomaly correlation coefficient of 0.32 assimilating soil moisture retrievals leads to improvements, the θ_{ASAR} on a daily as well as a monthly basis can be considered as meaningful.

Table 11-2 Statistics of linear regressions fitted through the data points in Figure 11-3.

	A	B	R^2
Daily	0.666	0.057	0.413
Monthly	0.877	0.015	0.683

11.5 Results and discussion

The previous analysis shows that after application of the cdf matching technique, the bias due to differences in the soil moisture climatology has been largely reduced. Figure 11-4 presents for each month a histogram of the remaining differences between the θ_{MM5} and the bias corrected θ_{ASAR} at the MM5 spatial resolution. The histograms illustrate that the differences between the θ_{MM5} and the θ_{ASAR} are fairly small during the winter months, while they increase towards the peak of the monsoon. In winters, the temporal and spatial soil moisture variability in the simulated and retrieved data sets are small. Therefore, mismatches between the two soil moisture products following from the model and retrieval uncertainties as well as differences in the spatial resolution are limited.

Although the mean values of the differences between the θ_{MM5} and the θ_{ASAR} are closely centered on 0.0 m^3 m^{-3} during the monsoon, its range covers differences from +0.15 to -0.15 m^3 m^{-3}. Given these large differences between the model and retrievals, it is valid to question if assimilation of the retrieved soil moisture into a large scale model would lead to an improvement. It should, however, be noted that soil moisture is much more variable in both space and time due to the intensive rain events occuring during the monsoon. Larger uncertainties in the simulated and retrieved soil moisture can, thus, be expected. On the other hand, the deviations between the θ_{MM5} and the θ_{ASAR} may also arise from the differences in the spatial resolution. Storms during the monsoon are strong convective systems that can produce large amounts of rain locally, while nearby

areas remain dry. Separation of the different sources contributing to the deviations between the θ_{MM5} and the θ_{ASAR} could indicate the value of the high resolution ASAR soil moisture retrievals for improving modeling of land surface processes at a large scale.

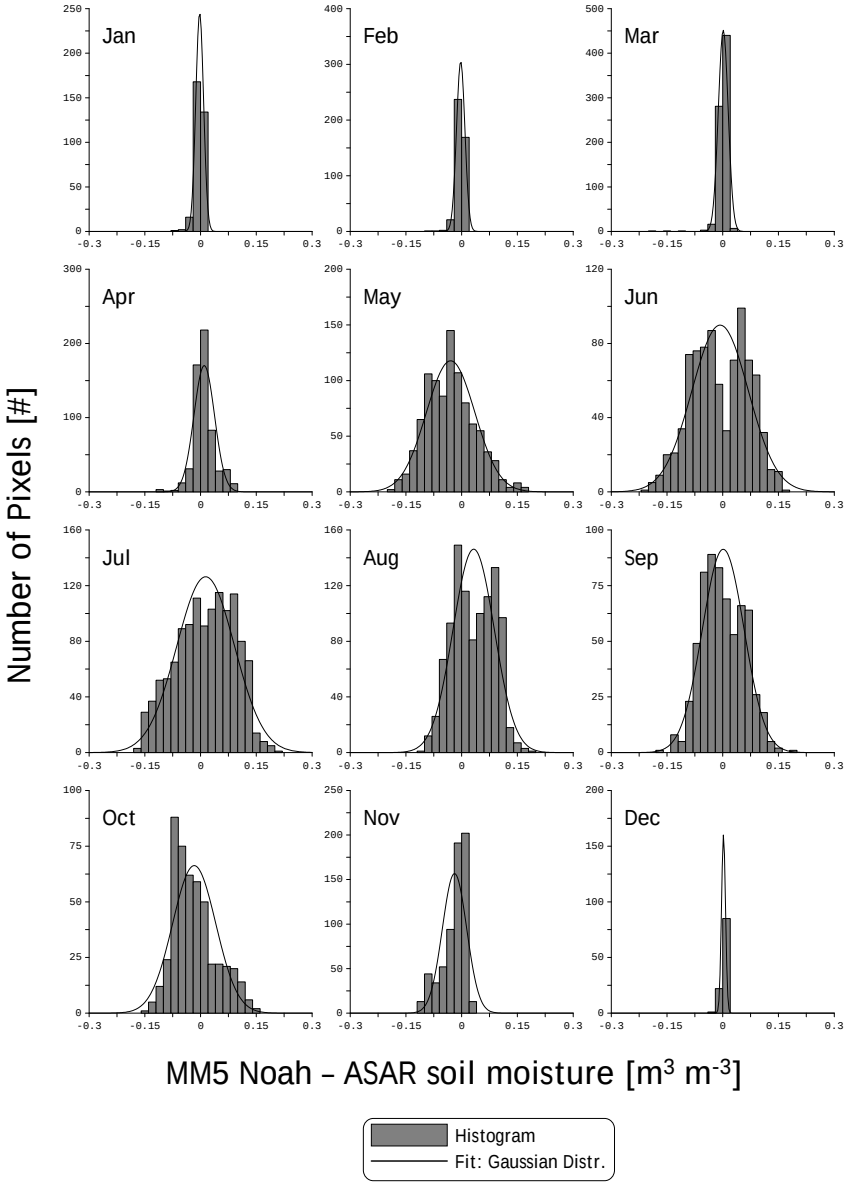

Figure 11-4 Histograms of differences between the MM5 Noah and ASAR soil moisture averaged for MM5 grid cell for each month.

Here, the differentiation between σ_b^2, σ_s^2 and σ_u^2 is based on the application of Eqs. 11.7, 11.8 and 11.9, respectively. As the magnitude of the individual contributions varies with time and space, the following normalization is applied,

$$\sigma_{x\_n}^2 = \frac{\sigma_x^2}{\sigma_t^2} \tag{11.10}$$

where, subscript x represents either the subscripts b, s or u and the σ_{xn}^2 is the relative contribution of x the total difference observed between the θ_{MM5} and the θ_{ASAR}.

Figure 11-5 presents the relative contribution of the three sources in the form of a cdf for each month. These cdf's are based on the σ_{bn}^2, σ_{sn}^2 and σ_{un}^2 computed for each MM5 grid cell. Monthly averages of the relative contributions are given in Figure 11-6. Both Figures 11-5 and 11-6 illustrate the importance of the spatial soil moisture variations in explaining the deviations between the θ_{MM5} and the θ_{ASAR}. The σ_{sn}^2 contribution is larger than the other factors during each months.

Even though σ_{sn}^2 is larger than σ_{bn}^2, it is observed that during winters the relative contribution of the bias is comparable to the spatial variability, on average 40% and 53%, respectively. With an averaged contribution of about 7 %, the differences induced by model and retrieval uncertainties have the smallest impact during the winter season. This is somewhat expected based on the results shown in Figure 11-4 because deviations between the θ_{MM5} and the bias corrected θ_{ASAR} are fairly small during the winter months. As the inherent bias due to different soil moisture climatologies is less subject to temporal variations, its relative contribution to the observed differences is larger during the winter months.

Towards the peak of the monsoon, a descreasing bias contribution is observed, and the contributions of the uncertainties and spatial variability increase. Figure 11-4 shows for those months also an increase in the difference between the θ_{MM5} and the biased corrected θ_{ASAR}. As such, the decrease of the relative bias contribution can be explained. For the months affected by the monsoon (May-October), the relative contributions of the bias and uncertainty are comparable, on average 16% and 13 %, respectively. However, the majority of the deviations (71%) can be attributed to the spatial soil moisture variability as is retrieved from the ASAR measurements.

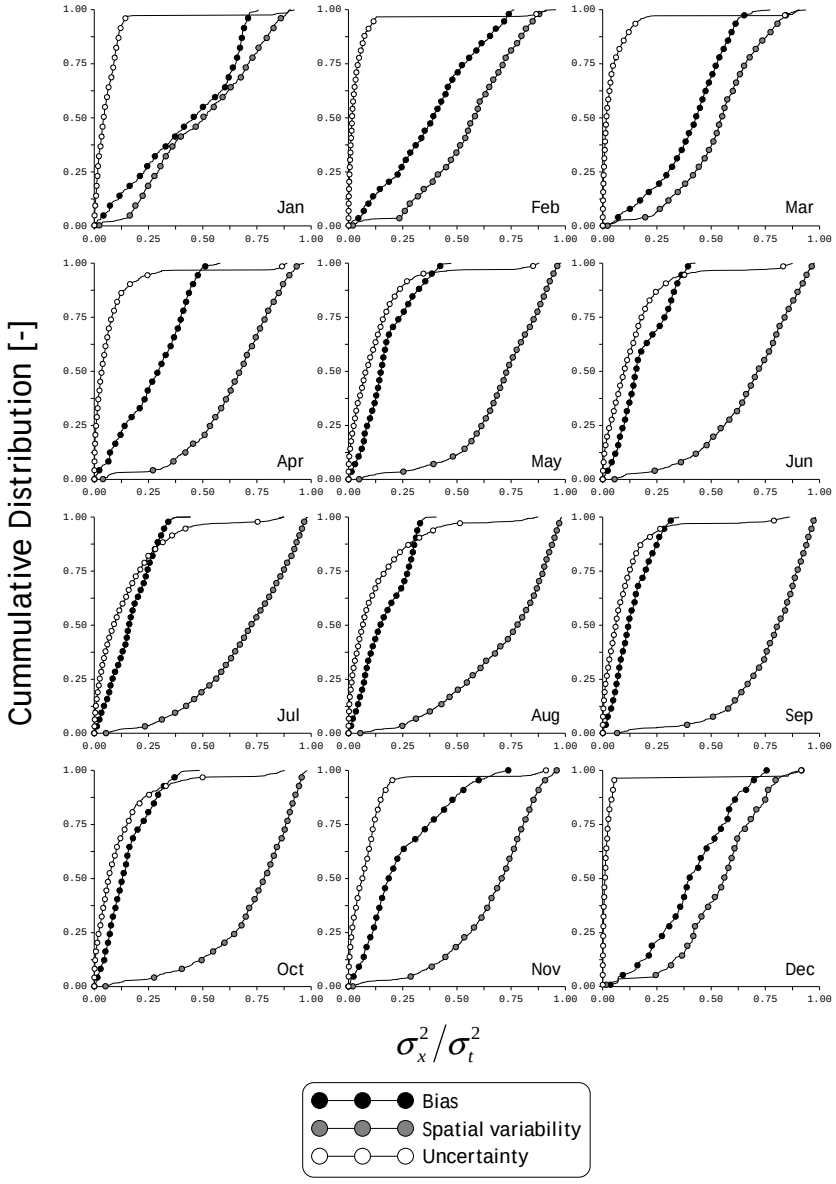

Figure 11-5 Cumulative distribution functions derived from the σ_{bn}^2, σ_{sn}^2 and σ_{un}^2 computed for each MM5 grid cell for each month.

This result has important implications for our perspective on how to improve the simulation of large-scale land surface processes using high resolution soil moisture products. So far data assimilation/integration studies are strongly biased towards

accommodating the global products from coarse resolution microwave radiometers and scatterometers. The use of high resolution soil moisture products for such purposes has been given less attention because of alleged problems with its accuracies. The agreement between the bias corrected θ_{ASAR} and the θ_{MM5} demonstrates, however, that skill of the ASAR soil moisture product is no less than the ones of available global products (e.g. Reichle et al. 2004). Moreover, the decomposition of the θ_{MM5} and the θ_{ASAR} differences into different components shows that the ASAR soil moisture variations is the largest contributor to those deviations. As such, perhaps the true value of integrating high resolution soil moisture products with large-scale modeling systems lies in improving the spatial representation rather than data assimilation.

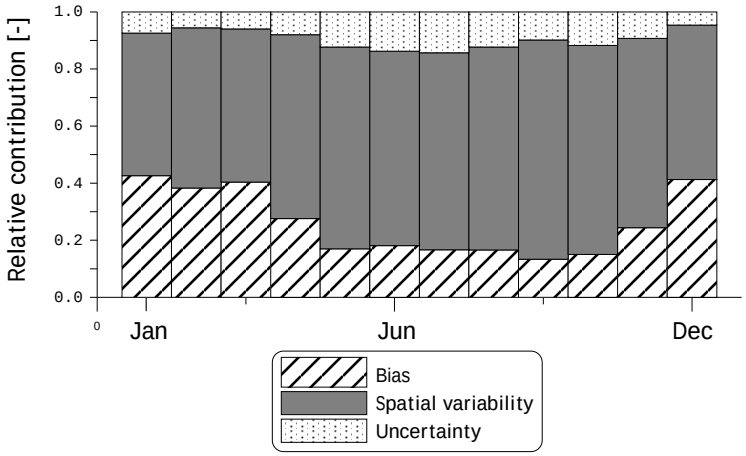

Figure 11-6 Monthly averages of the σ_{bn}^2, σ_{sn}^2 and σ_{un}^2.

11.6 Summary and conclusions

This chapter deals with the comparison of the soil moisture simulations and retrievals. The soil moisture is simulated at 10 km horizontal resolution by Noah LSM coupled to MM5 regional climate model. The 100 m resolution SAR based soil moisture products presented in Chapter 8 are adopted, here, as the retrievals. Given the difference in the spatial resolution, the comparison is considered to yield deviations related to 1) a bias caused by the difference in their soil moisture climatologies, 2) uncertainties embedded within simulations as well as retrievals, and 3) differences in the spatial representation. A method for quantifying these three sources of difference has been presented.

Matching the cumulative distribution functions (cdf's) of the θ_{ASAR} and the θ_{MM5} is used for reducing the bias caused by their different

soil moisture climatologies, which results in a bias corrected θ_{ASAR}. The comparison of the θ_{MM5} and the bias corrected θ_{ASAR} shows that bias between the two products has been largely reduced and yield RMSD of 0.051 m^3 m^{-3} on a daily basis. This error level is comparable to the differences between the retrievals and *in-situ* measurements presented in Chapter 8. Moreover, the resulting R^2's are similar to the values obtained between models and readily available global soil moisture products.

The standard deviation of the θ_{ASAR} within a MM5 Noah grid cell is assumed to represent deviations between the θ_{MM5} and θ_{ASAR} caused by their different spatial resolutions. Then, from the standard deviations between the θ_{MM5} and the θ_{ASAR}, and between the θ_{MM5} and the bias corrected θ_{ASAR}, the three sources of difference are determined. Analysis of the relative contributions on a monthly basis shows that the largest part of the deviations between the θ_{MM5} and the θ_{ASAR} is explained by the spatial soil moisture variability retrieved from ASAR observations. During winter months, the spatial variability contributes for about 50% to the differences between the two products, while this contribution increases to more than 70% in the monsoon affected period.

The observed agreement between the θ_{ASAR} and the θ_{MM5} demonstrates that the potential of the high resolution soil moisture products for improving the simulation of large-scale land processes is no less than that of soil moisture products from coarse resolution microwave sensors. One should, however, also consider that the differences between the θ_{ASAR} and the θ_{MM5} are largely caused by the spatial soil moisture variability. Integrating high resolution soil moisture products with large-scale models should, therefore, not only focus on data assimilation, but also on improving the spatial representation of soil moisture at the subgrid level.

However, the development of an operational high resolution global soil moisture product is currently hindered by the temporal availability of SAR observations. This issue will be resolved with the launch (expected in 2011) of the Sentinel-1 mission, which is a part of ESA's contribution to the GMES program.

12 Summary and Conclusions

Soil moisture has an important effect on the partitioning of solar radiation and influences, thus, the development of weather systems. It is, therefore, expected that an improved representation of the soil moisture dynamics in atmospheric circulation models (ACM's) will enhance their predictive skills. There are different methods to achieve this. For example, the reliability of simulated soil moisture can be improved by using more realistic model structures. Increasingly popular with the availability of more remote sensing observations is, however, to reduce the uncertainties of simulations through integration with measurements (or satellite retrievals).

This thesis contributes to both aspects. **Chapters 5 to 8** deal with the retrieval of soil moisture from active microwaves, whereas **Chapter 9** and **10** discuss land surface model simulations performed by the Noah model. In **Chapter 11**, the soil moisture retrievals are compared to simulations by the Noah model coupled to the MM5 regional climate model. These parts are summarized below.

12.1 Soil moisture retrieval from active microwaves

A ground-based C- and L-band scatterometer data set collected throughout the corn growth cycle and a set including 2.5 years of ASAR (C-band and VV polarization) acquisitions over the central part of the Tibetan Plateau have been used for studying the soil moisture retrieval. The ground-based scatterometer data set benefits from a comprehensive set of *in-situ* measurement, specifically vegetation biomass and soil moisture. Unique about the ASAR data set over the data scarce Tibetan Plateau is that the high resolution microwave measurements are acquired at a fairly high temporal and over a substantial period of time. The ground-based scatterometer data has been utilized for evaluating the vegetation and surface roughness effects on backscatter (σ^o) measurements. Over a larger temporal and spatial scale, the impact of different land surface conditions (e.g. soil moisture, sparse vegetation, freeze/thaw) on the σ^o has been investigated and the retrieval of soil moisture has been performed using the ASAR data set.

Chapter 5 discusses the effect of vegetation on fully polarimetric (HH, HV, VV) C- and L-band σ^o measured at incidence angles of 15, 35, and 55 degrees for the corn growth cycle. The analysis shows that depending on the antenna configuration and growth stage, the σ^o measurements can be dominated either by attenuated surface scattering or by scattering from vegetation. The first mechanism is strongest within C-band σ^o measurements collected at 15 degrees during the early growth stage. The latter is more notable among the

σ^o measured at peak biomass and incidence angles of 35 and 55 degrees. Somewhat surprising is, however, that even at peak biomass the measured σ^o response to soil moisture is still considerable enabling the retrieval of soil moisture. This σ^o sensitivity to soil moisture is ascribed to scattering along the soil-vegetation pathways.

Based on these observations an alternate method is proposed to correct σ^o measurements for vegetation and obtain more reliable soil moisture retrievals. The method is based on the concept that the ratio of the surface scattering contribution over the observed σ^o is affected by vegetation and can be described as a function of the vegetation water content (W). Experimentally determined relationships between this ratio and W have been used to reconstruct the surface scattering component from the σ^o measurements and retrieve soil moisture. Validation of the retrievals obtained with this method against the measured soil moisture yields errors varying from 0.033 to 0.063 $m^3\ m^{-3}$ depending on the antenna configuration. This accuracy is quite good specifically given the dense vegetation coverage with at peak biomass with a W of 5.1 kg m^{-2}. Additional studies are, however, needed to establish the validity of the proposed method for other crop types.

Also, the roughness of the soil surface influences the observed σ^o and has to be considered when retrieving soil moisture. The (Advanced) Integral Equation Method ((A)IEM, Fung et al. 1992, Chen et al. 2003) is the most widely applicable surface scattering model and is often used to simulate the σ^o from bare soil surfaces. This model represents the complex geometry of the soil surface as a single-scale stationary process, which allows adopting a parameterization based on 1-D surface height profile consisting of the root mean square height (s), correlation length (l) and autocorrelation length function (ACF). However, over large spatial domains typically insufficient information is available to determine this parameterization reliably. For retrieving soil moisture, therefore, a reduced number of parameters has to be used and the surface roughness is often assumed to be temporally stable.

Chapter 6 discusses the impact of these simplifications on the accuracy of the retrieved soil moisture using the vegetation corrected σ^o measurements. The surface roughness parameters have been inverted for four parameterization types by assuming an 'Exponential' and 'Gaussian' ACF's, and by using fixed (measured) or variable l. An evaluation of the retrieval accuracies shows that the most significant differences are noted when using different ACF's, while the l has only a minor impact. However, differences in the retrieval accuracy are smaller than 0.01 $m^3\ m^{-3}$. This suggests that regardless of the

employed parameterization type, an effective value for the *s* can be found without having a large impact on the retrieval accuracy.

Additional analyses on the temporal stability of the roughness indicates that over the entire growth cycle surface roughness changes have only a limited impact on the retrieved soil moisture (<0.01 m^3 m^{-3}). On a daily basis, however, the largest differences between the measured and retrieved soil moisture occur specifically after rain events. This increase in the retrieval error is strongest at HH polarization, L-band, and large incidence angles, which is in agreement with previous reports on σ^o sensitivities to surface roughness (e.g. Holah et al. 2005, Beaudoin et al. 1990, Zribi et al 1997). In contradiction to previous reports (e.g. Ulaby and Batlivala 1976, Ulaby et al. 1996, Shi et al. 1997, Macelloni et al. 1999) the soil moisture retrieved throughout the corn growth cycle is, therefore, more accurate for the VV polarization.

Chapter 7 discusses the influence of land surface states on the ASAR σ^o at longer temporal and different spatial scales over the Tibetan Plateau. The σ^o signatures from 1x1 km^2 areas covering a grassland and a wetland have been studied to identify its sensitivity to the changing land surface states. The lowest σ^o values from the grassland and wetland areas are obtained throughout the winter seasons because soil water is predominantly frozen resulting in dielectric properties comparable to dry soil conditions. Towards the summer, the wetland σ^o increases steadily and reaches its maximum as the monsoon is at peak intensity, while the grassland σ^o in the summer is characterized by large temporal variations. This contrast between the grassland and wetland σ^o dynamics is attributed to the highly variable soil moisture in the grassland caused by a large evaporative demand, while soil moisture conditions in wetlands are temporally stable.

The differences between the grassland and wetland σ^o dynamics has consequences for the spatial σ^o variability observed at different spatial scales (e.g. 1x1 km^2, 5x5 km^2 and 30x30 km^2). The comparison of the mean σ^o with its standard deviation (stdev) results in a specific triangular data points distribution, whereby the peak located near the mid range of σ^o values. When these σ^o dynamics are considered to be representative for the soil moisture conditions, these results suggest that the relationship between mean soil moisture and the spatial variability is not always uniquely defined. This implicates that relationships between the mean soil moisture and stdev, used for downscaling coarse resolution soil moisture products, cannot be assumed to be time-invariant, but should be obtained from additional near real-time data sources, such as SAR data.

Another important observation is the discrepancy between the annual cycles of the NDVI and the wetland σ^o. The NDVI increase

starts later than for the wetland σ^o and its decrease is observed earlier. This, supported by the small portion of σ^o variations explained by the NDVI for both the grassland and wetland suggests that the vegetation effects on the ASAR σ^o observed over the Tibetan Plateau is fairly small.

Therefore, the algorithm employed in **Chapter 8** for retrieving soil moisture is solely based on the AIEM surface scattering model and assumes that the effects of vegetation are negligible. The roughness parameters needed for AIEM simulations is obtained through the inversion of a sequence of three σ^o measurements collected at different view angles under assumed dry conditions. As the dielectric properties of frozen soil are equivalent to the ones of dry soil, ASAR images collected in February and January have been utilized for the roughness inversion. The derived roughness parameterizations are used as input for retrieving soil moisture from the time series of ASAR σ^o.

The resulting soil moisture retrievals represent the monsoon sequence quite well with their maximum values registered in the months July to September. Spatially, the retrieved soil moisture dynamics is also in accordance with the expectations; with the soil moisture retrieved over grasslands being highly variable, and wet and fairly stable conditions observed over the wetlands. A comparison of the retrieved against the soil moisture measured at a wetland site and three grassland sites yields Root Mean Squared Differences (RMSD's) of 0.060 and 0.032 $m^3\ m^{-3}$ for the wetland site and the three grassland sites, respectively. Normalized for their different dynamic soil moisture ranges the uncertainty levels obtained for the wetland and grassland are, however, quite similar, 16.9 and 17.3 % respectively. These error levels are comparable to the results of previous SAR based soil moisture retrieval studies.

12.2 Simulation of land processes

At present, the Noah land model is coupled to the National Centers for Environmental Prediction (NCEP) operational weather and climate prediction model for quantifying the soil moisture impact on land-atmosphere interactions. Crucial for its performance is a proper simulation of water movement through the soil column. **Chapter 9** evaluates different numerical schemes for vertically integrating the soil water flow and analyses the impact of the soil hydraulic model (SHM) employed for calculating the transport coefficients.

Noah simulations forced by atmospheric variables measured at the Cabauw meteorological station (The Netherlands) shows that the current method used for vertical integration of the soil water flow systematically underestimates the upward water transport; often referred to as capillary rise. Therefore, a rapid dry-down of the root

zone is observed, while the deep soil layers remain relatively wet even under dry conditions and a high evaporative demand. Two alternative schemes are presented that incorporate the capillary rise mechanism.

The SHM shapes the soil hydraulic functions (SHF's), which determine the magnitude of the transport coefficients and the impact of the soil moisture stress on the heat flux partitioning. Noah (and most other LSMs) uses the SHM by Campbell (1974), while it is commonly understood that the Van Genuchten (1980) SHM represents measured SHF's better. Surface water and energy budgets simulated by Noah using these two SHM's are compared. The difference in the parameterization utilized by the Van Genuchten and Campbell SHM prevents, however, a direct comparison. The SHF's of five soil type provided by the Dutch pedotransfer function (Wösten et al. 2001) have, therefore, been used to derive the Van Genuchten and two type Campbell parameterizations, whereby,

1. The theoretical similarity in the retention curves is used (Campbell **A**);
2. The Campbell parameters are fitted to the relationships between the transport coefficient and soil moisture content (Campbell **B**).

Compared to Van Genuchten, typical for Campbell **A** are the larger transport coefficients in the mid and dry soil moisture range, while for Campbell **B** these coefficients are lower near saturation due to the necessity of smaller saturated conductivity. A consequence of these differences is that Noah with Campbell **A** transports water faster through the soil column, while with Campbell **B** it generates more surface runoff. Noah simulates, thus, larger soil water losses (e.g. evaporation, drainage and surface runoff) using both forms of Campbell SHF's. This as well as the underestimation of the capillary rise mechanism could be one of the explanations for the prediction of too warm and too dry summers by ACM's.

Apart from issues related to the model physics, various investigations have also shown that the performance of land models can be improved by adjusting its parameterizations, specifically in the extreme environment, such as the Tibetan Plateau. **Chapter 10** discusses the adjustment in Noah's soil and vegetation parameters needed to reproduce the soil temperature states and surface fluxes measured at a site on the Tibetan Plateau. An analysis of the Noah simulations obtained using the standard parameterizations shows that,

1. The transfer of heat through the soil column underestimates the diurnal temperature cycle of the deeper layers;
2. The partitioning of solar radiation results in an overestimation of the sensible heat flux.

By using different soil thermal properties for the top- and subsoil, and including an additional thin top soil layer, the diurnal cycle of the temperature in deep soil layer is enlarged. This also improves the temperature simulation in the shallow soil layer. Further, a decrease in the vegetation parameters constraining transpiration was found to be necessary for reducing the sensible heat flux overestimation from 41 W m^{-2} to 20 W m^{-2}. This illustrates once again that parameterizations utilized for global simulations can introduce large uncertainties locally, specifically over extreme environments, such as the Tibetan Plateau. Encouraging is, however, that model structures of land models, in this case Noah, are flexible enough to reproduce the measured land surface process with some minor adjustments.

12.3 Integration of satellite retrievals with land models

Some uncertainties within Noah related to its model structure and the utilized parameterizations were discussed in Chapters 9 and 10. Nowadays, a reduction in model uncertainties is also being pursued by integrating simulated with modeled land surface states, for which often data assimilation techniques are used. A fundamental assumption in the application of data assimilation techniques is that the modeled and retrieved soil moisture climatologies are unbiased. This is hardly ever the case. Moreover, the spatial resolution of LSM's is at least several kilometers, while ASAR observes soil moisture at a 100 m resolution. A comparison of Noah simulations at a 10 km resolution against ASAR soil moisture retrievals from Chapter 8 yields, thus, deviations that are related to 1) the inherent bias due to differences in the climatology of the simulated and retrieved soil moisture, 2) the differences in the spatial representation, and 3) the uncertainties associated with the simulations as well as retrievals. An understanding of the contribution of these sources of difference is needed to fully appreciate the value of integrating satellite soil moisture with models operating at a lower spatial resolution.

Chapter 11 presents a method for quantification of these sources of differences. The decomposition of the sources of difference shows that during winters the spatial variability contributes for about 50% to the differences between the two products. This contribution increases to more than 70% for the monsoon affected period. In spite of the differences, however, the comparison of the two unbiased soil moisture products yields a RMSD of 0.051 m^3 m^{-3} on a daily basis. This agreement between the simulated and ASAR retrieved soil moisture is no less than that for soil moisture products from coarse resolution microwave sensors.

As such, the integration of SAR based soil moisture products with large-scale simulations deserves more attention than it has obtained so far. One should, however, be aware that soil moisture differences between the large-scale simulation and high-resolution retrievals are largely caused by different spatial resolutions. Perhaps, the true value of using high resolution soil moisture products for large-scale modeling lies in improving the spatial soil moisture representation at the sub-grid level. Unfortunately, the temporal availability of SAR observations still hinders the development of operational high resolution soil moisture products.

Pfff ...

Bibliography

Altese, E., Bolognani, O., Mancinin, M., Troch, P.A., 1996, "Retrieving soil moisture over bare soil from ERS 1 synthetic aperture radar data: Sensitivity analysis based on a theoretical surface scattering model and field data", *Water Resources Research*, **32**, pp. 653-661.

Alvarez-Mozos, J., Casali, J., Gonzalez-Audicana, M., Verhoest, N.E.C., 2006, "Assesment of the Operational Applicability of RadarSat-1 data for surface soil moisture estimation", *IEEE Transactions on Geoscience and Remote Sensing*, **44**, pp. 913-924.

Alvarez-Mozos, J., Verhoest, N.E.C., Larranaga, A., Casali, J., Gonzalez-Audicana, M., 2006, "Influence of surface roughness spatial variability and temporal dynamics on the retrieval of soil moisture from SAR observations", *Sensors*, **9**, pp. 463-489.

Attema, E.P.W., and Ulaby, F.T., 1978, "Vegetation modeled as a water Cloud", *Radio Science*, **13**, pp. 357-364.

Baghdadi, N., King, C., Bourguignon, A., Remond, A., 2002a, "Potential of ERS and Radarsat data for surface roughness monitoring over bare agricultural fields: application to catchments in Nothern France", *International Journal of Remote Sensing*, **23**, pp. 3427-3442.

Baghdadi, N., King, C., Chanzy, A., Wigneron, J.P., 2002b, "An empirical calibration of the integral equation model based on SAR data, soil moisture and surface roughness measurements over bare soils", *International Journal of Remote Sensing*, **23**, pp. 4325-4340.

Baghdadi, N., Gherboudj, I., Zribi, M., Sahebi, M., King, C., Bonn, F., 2004, "Semi-empirical calibration of the IEM backscattering model using radar images and moisture and roughness field measurements", *International Journal of Remote Sensing*, **25**, pp. 3593-3623.

Badhdadi, N., Holah, N., Zribi, M., 2006, "Soil moisture estimation using multi-incidence and multi-polarization ASAR data", *International Journal of Remote Sensing*, **27**, pp. 1907-1920.

Bartalis, Z., Wagner, W., Naeimi, V., Hasenauer, S., Scipal, K., Bonekamp, H., Figa, J., Anderson, C., 2007, "Initial soil moisture retrieval from Metop-A Advanced Scatterometer", *Geophysical Research Letters*, **34**, DOI:10.1029/2007GL031088.

Baup, F., Mougin, E., Hiernaux, P., Lopes, A., De Rosnay, P., Chenerie, I., 2007a, "Radar signature of Sahelian surfaces in Mali using ENVISAT-ASAR data", *IEEE Transactions on Geoscience and Remote Sensing*, **45**, pp. 2354-2363.

Baup, F., Mougin, E., de Rosnay, P., Timouk, F., Chenerie, I., 2007b, "Surface soil moisture estimation over the AMMA Sahelian site in Mali using ENVISAT/ASAR data", *Remote Sensing of Environment*, **109**, pp. 473-481.

Beaudion, A., Le Toan, T., Gwyn, Q.H.J., 1990, "SAR observations and modeling of the C-band backscatter variability due to multiscale geometry and soil moisture", *IEEE Transactions on Geoscience and Remote Sensing*, **28**, pp. 886-895.

Beckmann, P., and Spizzichino, A., 1963, "Scattering of electromagnetic waves from rough surfaces", MacMillan, New York.

Beljaars, A.C.M., and Bosveld, F.C., 1997, "Cabauw data for the validation of land surface parameterization schemes", *Journal of Climate*, **10**, pp. 1172-1193.

Beljaars, A.C.M., Schotanus, P., Nieuwstadt, F.T.M., 1983, "Surface layer similarity under nonuniform fetch conditions", *Journal of Climate and Applied Meteorology*, **22**, pp. 1800-1810.

Beljaars, A.C.M., and Holtslag, A.A.M., 1991, "Flux parameterization over land surface for atmospheric models", *Journal of Applied Meteorology*, **30**, pp. 327-341.

Berg, A.A., Famiglietti, J.S., Walker, J.P., Houser, P.R., 2003, "Impact of bias correction to reanalysis products on simulations of North American soil moisture and hydrological fluxes", *Journal of Geophysical Research*, **108**, DOI:10.1029/2002/JD003334.

Bindlish, R., and Barros, A.P., 2000, "Multi-frequency soil moisture inversion from SAR measurements using IEM", *Remote Sensing of Environment*, **71**, pp. 67-88.

Bindlish, R., and Barros, A.P., 2001, "Parameterization of vegetation backscatter in radar-based soil moisture estimation", *Remote Sensing of Environment*, **76**, pp. 130-137.

Bindlish, R., Jackson, T.J., Wood, E., Gao, H., Starks, P., Bosch, D., Lakshmi, V., 2003, "Soil moisture estimates from TRMM Microwave Imager observations over the Southern United States", *Remote Sensing of Environment*, **47,** pp. 132-141.

Bosilovich, M.G., and Sun, W.Y., 1999, "Numerical simulation of the 1993 Midwestern flood: land-atmosphere interactions", *Journal of Climate*, **12**, pp. 1490-1504.

Braun, F.J., and Schädler, G., 2005, "Comparison of soil hydraulic parameterizations for meteorological models", *Journal of Applied Meteorology*, **44**, pp. 1116-1132.

Brown, S.C.M., Quegan, S., Morrison, K., Bennett, J.C., Cookmartin, G., 2003, "High-resolution measurements of scattering in wheat canopies-implication for crop parameter retrieval", *IEEE Transaction of Geoscience and Remote Sensing*, **41**, pp. 1602-1610.

Bryant, R., Moran, M.S., Thoma, D.P., Holifield-Collins, C.D., Skirvin, S., Rahman, M., Slocum, K., Starks, P., Bosch, D., Gonzalez Dugo, M.P., 2007, "Measuring surface roughness height to parameterize radar backscatter models for retrieval of surface soil moisture", *IEEE Geoscience and Remote Sensing Letters*, **4**, pp. 137-141.

Buck, C.H., Suchail, J.L., Torres, R., Zink, M., 2000, "ASAR instrument calibration", In: Proceedings of ERS-ENVISAT Symposium, 16-20 October 2000, Gothenburg, available at: http://envisat.esa.int/m-s/envisat_mission_2001/CalVal/3ASAR.html

Burdine, N.T., 1953, "Relative permeability calculation from size distribution data", *Transactions of the American Institute of Mining Engineering*, **198**, pp. 71-78.

Callens, M., Verhoest, N.E.C., Davidson, M.W.J., 2006, "Parameterization of tillage-induced single scale soil roughness from 4-m profile", *IEEE Transactions on Geoscience and Remote Sensing*, **44**, pp. 878-888.

Campbell, G.S., 1974, "A simple method for determining unsaturated conductivity from moisture retention data", *Soil Science*, **117**, pp. 311-314

Carsel, R.G., and Parrish, R.S., 1988, "Developing joint probability distributions of soil water retention characteristics", *Water Resources Research*, **24**, pp. 755-769.

Cashion, J., Lakshmi, V., Bosch, D., Jackson, T.J., 2005, "Microwave remote sensing of soil moisture: evaluation of the TRMM microwave imager (TMI) satellite for the little River Watershed Tifton, Georgia", *Journal of Hydrology*, **307***,* pp. 242-253.

Ceccato, P., Flasse, S., Tarantola, S., Jacquemond, S., Gregoire, J.M., 2001, "Detecting vegetation leaf water content using reflectance in the optical domain", *Remote Sensing of Environment*, **77**, pp. 22-33.

Champion, I., and Faivre, R., 1996, "The field row direction relative to the radar azimuth considered as an apparent surface roughness for smooth bare soils", *International Journal of Remote Sensing*, **17**, pp. 3305-331.

Chauhan, N.S., and Lang, R.H., 1999, "Radar backscattering from alfalfa canopy: a clump modeling approach", *International Journal of Remote Sensing*, **20**, pp. 2203-2220.

Chauhan, N., Lang, R.H, Ranson, K.J., 1991, "Radar modeling of a boreal forest", *IEEE Transactions on Geoscience and Remote Sensing*, **29**, pp. 627-638.

Chauhan, N.S., Le Vine, D.M., Lang, R.H., 1994, "Discrete scatter model for microwave radar and radiometer to corn: comparison of the theory and data", *IEEE Transactions on Geoscience and Remote Sensing*, **32**, pp. 416-426.

Chen, F., and Dudhia, J., 2001, "Coupling an advanced land surface hydrology model with the Penn State-NCAR MM5 modeling system. Part I: Model implementation and sensitivity", *Monthly Weather Review*, **129**, pp. 569-585.

Chen, F., Mitchell, K., Schaake, J., Xue, Y., Pan, H.-L., Koren, V., Duan, Q.Y., Ek, M., Betts, A., 1996, "Modeling of land surface evaporation by four schemes and comparison with FIFE observations", *Journal of Geophysical Research*, **101**, pp. 7251-7268.

Chen, F., Janjic, Z., Mitchell, K., 1997, "Impact of atmospheric surface-layer parameterizations in the new land-surface scheme of the NCEP mesoscale ETA model", *Boundary-layer Meteorology*, **85**, pp. 391-421.

Chen, K.S., Wu, T.D., Tsang, L., Li, Q., Shi, J., Fung, A.K., 2003, "Emission of rough surfaces calculated by the integral equation method with comparison to three dimensional moment method simulations", *IEEE Transactions on Geoscience and Remote Sensing*, **41**., pp. 90-101.

Chen, D., Huang, J., Jackson, T.J., 2005, "Vegetation water content estimation for corn and soybean using spectral indices derived from MODIS near- and short-wave infrared bands", *Remote Sensing of Environment*, **98**, pp. 225-236.

Chiu, T., and Sarabandi, K., 2000, "Electromagnetic scattering from short branching vegetation", *IEEE Transactions on Geoscience and Remote Sensing*, **38**, pp. 911-925.

Clapp, R.B., and Hornberger, G.M., 1978, "Empirical equation for some soil hydraulic properties", *Water Resources Research*, **14**, pp. 601-604.

Cookmartin, G., Saich, P., Quegan, S., Cordey, R., Burgess-Allen, P., Sowter, A., 2000, "Modeling microwave interaction with crops and comparison with ERS-2 SAR observations", *IEEE Transactions on Geoscience and Remote Sensing*, **38**, pp. 658-670.

Cosby, B.J., Hornberger, C.M., Clapp, R.B., Ginn, T.R., 1984, "A statistical exploration of the relationships of soil moisture characteristic to the physical properties of soil", *Water Resources Research*, **20**, pp. 682-690.

Cosgrove, B.A., Lohmann, D., Mitchell, K.E., Houser, P.R., Wood, E.F., Schaake, J.C., Robock, A., Sheffield, J., Duan, Q., Luo, L., Higgins, R., Pinker, R.T., Tarpley, J.D., 2003, "Land surface model spin-up behaviour in the North American Land Data Assimilation System (NLDAS)", *Journal of Geophysical Research*, **108**, DOI: 10.1029/2002JD003316.

Cosh, M.H., Jackson, T.J., Bindlish, R., Prueger, J.H., 2004, "Watershed scale temporal and spatial variability of soil moisture and its role in validating satellite estimates", *Remote Sensing of Environment*, **92**, pp. 427-435.

Crow, W.T., Koster, R.D., Reichle, R.H., Sharif, H.O., 2005, "Relevance of time-varying and time-invariant retrieval error sources on the utility of spaceborne soil moisture products", *Geophysical Research Letter*, **32**, DOI: 10.1029/2005GL024889.

Cuenca, R.H., Ek, M., Mahrt, L., 1996, "Impact of soil water properties parameterization on atmospheric boundary layer simulation", *Journal of Geophysical Research*, **101**, pp. 7269-7277.

Dai, Y., Zeng, X., Dickinson, R.E., Baker, I., Bonan, G.B., Bosilovich, M.G., Denning, A., Scott, Dirmeyer, S., Houser, P.A., Niu, P.R., Guoyue, O., Schlosser, K.W., Adam, C., Zong-Liang, Y., 2003, "The Common Land Model", *Bulletin of the American Meteorological Society*, **84**, pp. 1013-1023.

Davidson, M.W.J., Le Toan, T., Mattia, F., Satalino, G., Manninen, T., Borgeaud, M., 2000, "On the characterization of agricultural soil roughness for radar remote sensing studies", *IEEE Transactions on Geoscience and Remote Sensing*, **38**, pp. 630-639.

De Lannoy, G.J.M., Reichle, R.H., Houser, P.R., Pauwels, V.R.N., Verhoest, N.E.C., 2007, "Correcting for forecast bias in soil moisture assimilation with the ensemble Kalman filter", *Water Resources Research*, **43**, DOI: 10.1029/2006ER005449.

De Roo, R.D., Du, Y., Ulaby, F.T., Dobson, M.C., 2001, "A semi-empirical bakcscattering model at L-band and C-band for a sybean canopy with soil moisture inversion", *IEEE Transactions on Geoscience and Remote Sensing*, **39**, pp. 864-872.

De Rosnay, P., Bruen, M., Polcher, J., 2000, "Sensitivity of surface fluxes to the number of layers in the soil model used in GCMs", *Geophysical Research Letters,* **27**, pp. 3329-3332.

De Vries, D.A., 1963, "Thermal properties of soils. Physics of Plant Environments", W.R. van Wijk (Ed.), Noord-Holland, pp. 210-235.

Della Vecchia, A., Ferrazzoli, P., Guerriero, L., Blaes, X., Defourny, P., Dente, L., Mattia, F., Satalino, G., Strozzi, T., Wegmuller, U., 2006, "Influence of geometrical factors on crop backscattering at C-band", *IEEE Transactions on Geoscience and Remote Sensing*, pp. 778-790.

Della Vecchia, A., Ferrazzoli, P., Guerriero, L., Ninivaggi, L., Strozzi, T., Wegmuller, U., 2008, "Observing and modelling multifrequency scattering of maize during the whole growth cycle", *IEEE Transactions on Geoscience and Remote Sensing*, **46**, pp. 3709-3718.

Dente, L., Satelino, G., Mattia, F., Rinaldi, M., 2008, "Assimilation of leaf area index derived from ASAR and MERIS data into CERES-Wheat model to map wheat yield", *Remote sensing of Environment*, **112**, pp.1395-1407.

Dickinson, R., Henderson-Sellers, A., Kennedy, P., 1993, "Biosphere-atmosphere transfer scheme (BATS) version 1e as coupled to the NCAR community climate model", Technical Report NCAR/TN-387 + STR, NCAR Boulder, Colorado.

Dickinson, R.E., Oleson, K.W., Bonan, G., Hoffman, F., Thornton, P., Vertenstein, M., Yang, Z.L., Zeng, X., 2006, "The community land model and its climate statistics as a component of the community climate system model", *Journal of Climate*, **19**, pp. 2302-2324.

Dickinson, R.E., 1984, "Modeling evapotranspiration for three-dimensional global climate models", In: Hanson, J.E., and Takahashi, (Eds.) Climate processes and climate sensitivity, American Geophysical Union, *Geophys. Monogr.*, **29**, pp. 58-72.

Dobson, M.C., Ulaby, F.T., Hallikainen, M.T., El-Rayes, M.A., 1985, "Microwave dielectic behavior of wet soil – Part II: Dielectric mixing models", *IEEE Transactions on Geoscience and Remote Sensing*, **GE-23**, pp. 35- 46.

Doherty, J., 2003. "Manual for the PEST Surface Water Modelling Utilities", Watermark Numerical Computing Australia. Available at http://www.sspa.com/pest (Last verified on April 2010).

Duan, Q., Schaake, J., Andreassian, V., Franks, S., Goteti, G., Gupta, H.V., Gusev, Y.M., Habets, F., Hall, A., Hay, L., Hogue, T., Huang, M., Leavesley, G., Liang, X., Nasonova, O.N., Noilhan, J., Oudin, L., Sorooshian, S., Wagener, T., Wood, E.F., 2006. "Model parameter estimation experiment (MOPEX): An overview of science strategy and major results from the second and third workshops", *Journal of Hydrology*, **320**, pp. 3-17.

Dubois, P.C., Van Zyl, J., Engman, T., 1995, "Measuring soil moisture with imaging radars", *IEEE Transactions on Geoscience and Remote Sensing*, **33**, pp. 915-926.

Dudhia, J., 1989, "Numerical study of convection observed during the winter monsoon experiment using a mesoscale two-dimensional model", *Journal of Atmospheric Science*, **46**, pp. 3077-3107.

Dudhia, J., 1993, "A nonhydrostatic version of the Penn State-NCAR Mesoscale Model: Validation tests and simulation of an Atlantic cyclone and cold front", *Monthly Weather Review*, **121**, pp. 1493-1513.

Durden, S.L., Morrissey, L.A., Livington, G.P., 1995, "Microwave backscatter and attenuation dependence on leaf area index for flooded rice fields", *IEEE Transactions on Geoscience and Remote Sensing*, **33**, pp. 807-810.

Ek, M.B., and Holtslag, A.A.M., 2004, "Influence of soil moisture on boundary layer cloud development", *Journal of Hydrometeorology*, **5**, pp. 86-99.

Ek, M.B., and Holtslag, A.A.M., 2005, "Evaluation of a land-surface scheme at Cabauw", *Theoretical and Applied Climatology*, **80**, pp. 213-227.

Ek, M.B., Mitchell, K.E., Lin, Y., Rogers, E., Grunmann, P., Koren, V., Gayno, G., Tarpley, J.D, 2003, "Implementation of Noah land surface model advances in the National Centers for Environmental Prediction operational mesoscale Eta model", *Journal of Geophysical Research*, **108**, DOI: 10.1029/2002JD003296.

El-Rayes, M.A., and Ulaby, F.T., 1987, "Microwave dielectric spectrum of vegetation-part I: experimental observations", *IEEE Transactions on Geoscience and Remote Sensing*, **GE-25**, pp. 541-549.

Entekhabi, D., Njoku, E.G., Houser, P.R., Spencer, M., Doiron, T., Kim, Y., Smith, J., Girard, R., Belair, S., Crow, W., Jackson, T.J., Kerr, Y.H., Kimball, J.S., Koster, R., McDonald, K.C., O'Neill, P.E., Pultz, T., Running, S.W., Shi, J., Wood, E., Van Zyl, J., 2004, "The Hydrosphere State (Hydros) mission: An Earth system pathfinder for global mapping of soil moisture and land freeze/thaw", *IEEE Transactions on Geoscience and Remote Sensing,* **42**, pp. 2184-2195.

Eom, H., and Fung, A., 1984, "Backscattering coefficient of a perturbed sinusoidal surface", *IEEE Transaction on Antennas and Propagation*, **32**, pp. 291-295.

Evensen, G., "Data Assimilation: The Ensemble Kalman Filter", Springer, 2006

Famiglietti, J.S., Devereaux, J.A., Laymon, C.A., Tsegaye, T., Houser, P.R., Jackson, T.J., Graham, S.T., Rodell, M., Van Oevelen, P.J., 1999, "Ground-based investigation of soil moisture variability within remote sensing footprints during the Southern Great Plains 1997 (SPG97) Hydrology Experiment", *Water Resources Research,* **35**, pp. 1839-1851.

Ferranti, L., and Viterbo, P., 2006, "The European summer of 2003: Sensitivity to soil water initial conditions", *Journal of Climate*, **19**, pp. 3659-3680.

Ferrazzoli, P., and Guerriero, L., 1996, "Passive microwave remote sensing of forests: a model investigation", *IEEE Transactions on Geoscience and Remote Sensing*, **34**, pp. 433-443.

Fung, A. K., 1994 "Microwave Scattering and Emission Models and Their Applications", Artech House.

Fung, A.K., and Pan, G.W., 1987 "A scattering model for perfectly conducting random surfaces I. Model development", *International Journal of Remote Sensing*, **8**, pp. 1579-1593.

Fung, A.K., Li, Z., Chen, K.S., 1992, "Backscattering from a randomly rough dielectric surface", *IEEE Transactions on Geoscience and Remote Sensing*, **30**, pp. 356-369.

Fung, A.K., Liu, W.Y., Chen, K.S., Tsay, M.K., 2002, "An improved IEM model for bistatic scattering from rough surfaces", *Journal of Electromagnetic Waves and Application*, **16**, pp. 689-702.

Gallagher, M., and Doherty, J., 2007, "Parameter estimation and uncertainty analysis for a watershed model", *Environmental modelling & Software*, **22**, pp. 1000-1020.

Garratt, J.R., 1993, "Sensitivity of climate simulations to land-surface and atmospheric boundary-layer treatments – A review", *Journal of Climate*, **6**, pp. 419-448.

Gilmanov, T.G., Soussana, J.F., Aires, L., and co-authors, 2007, "Partitioning European grassland net ecosystem CO_2 exchange into gross primary

productivity and ecosystem respiration using light response function analysis", *Agriculture Ecosystems and Environment*, **121**, pp. 93-120.

Grell, G.A., Dudhia, J., Stauffer, D., 1994, "A description of the fifth-generation Penn State/NCAR mesoscale model (MM5)", NCAR Techn. Note NCAR/TN-398+STR, 117 pp.

Gulden, L.E., Rosero, E., Yang, Z., Rodell, M., Jackson, C.S., Niu, G., Yeh, P.J.F., Famiglietti, J., 2007, "Improving land-surface model hydrology: Is an explicit aquifer model better than a deeper soil profile?", *Geophysical Research Letters*, **34**, DOI:10.1029/2007GL029804.

Gutmann, E.D., and E.E. Small, 2005, "The effect of soil hydraulic properties vs. soil texture in land surface models", *Geophysical Research Letters*, **32**, DOI:10.1029/2004GL021843.

Gutmann, E.D., and Small, E.E., 2007, "A comparison of land surface model soil hydraulic properties estimated by inverse modeling and pedotransfer functions", *Water Resources Research*, **43**, DOI: 10.1029/2006WR005135.

Hecht, E., 1998, "Optics", Addison-Wesley, Third edition, 694 pp.

Henderson-Sellers, A., McGuffie, K., Pitman, A., 1996, "The project for intercomparison of land-surface schemes: 1992 to 1995", *Climate Dynamics*, **12**, pp. 849-859.

Hillel, D., 1998, "Environmental soil physics", Academic Press, 771 pp.

Hoeben, R., and Troch, P.A., 2000, "Assimilation of active microwave observations data for soil moisture profile estimation", *Water Resources Research*, **36**, pp. 2805-2819.

Hoekman, D.H., 1991, "Speckle ensemble statistics of logarithmically scaled data", *IEEE Transactions on Geoscience and Remote Sensing*, **29**, pp.180-182.

Hogue, T.S., Bastidas, L., Gupta, H., Sorooshian, S., Mitchell, K., Emmerich, W., 2005, "Evaluation and transferability of the Noah land surface model in semiarid environments", *Journal of Hydrometeorology*, **6**, pp. 68-83.

Holah, N., Baghdadi, N., Zribi, M., Bruand, A., King, C., 2005, "Potential of ASAR/ENVISAT for the characterization of soil surface parameters over bare agricultural fields", *Remote Sensing of Environment*, **96**, pp.78-86.

Hong, S.Y., and Pan, H.L., 1996, "Nonlocal boundary layer vertical diffusion in a medium range forecast model", *Monthly Weather Review*, **124**, pp. 2322-2339.

Hsieh, C., and Fung, A., 1999, "Application of an extended IEM to multiple surface scattering and backscatter enhancement", *Journal of Electromagnetic Waves and Application*, **13**, pp. 121-135.

Hsieh, C.Y., Fung, A.K., Nesti, G., Sieber, A.J., Coppo, P., 1997, "A further study of the IEM surface scattering model", *IEEE Transactions on Geoscience and Remote Sensing*, **35**, pp. 901-909.

Inoue, Y., Kurosu, T., Maeno, H., Uratsuka, S., Kozu, T., Dabromska-Zielinska, K., Qi, J., 2002, "Season-long daily measurements of multifrequency (Ka, Ku, X, C, and L) and full-polarization backscatter signatures over paddy rice fields and their relationship with biological variables", *Remote Sensing of Environment*, **81**, pp. 194-204.

Jackson, T.J., 1993, "Measuring surface soil moisture using passive microwave remote sensing", *Hydrological Processes*, **7**, pp. 139-152.

Jackson, T.J., McHairn, H., Weltz, M.A., Brisco, B., Brown, R., 1997, "First order surface roughness correction of active microwave observations for estimating soil moisture", *IEEE Transactions on Geoscience and Remote Sensing*, **35**, pp. 1065-1069.

Jackson, T.J., Le Vine, D.M., Hsu, A.Y., Oldak, A., Starks, P.J., Swift, C.T., Isham, J.D., Haken, M., 1999, "Soil moisture mapping at regional scales using microwave radiometry: the Southern Great Plains hydrology experiment", *IEEE Transactions on Geoscience and Remote Sensing*, **37**, pp. 2136-2151.

Jackson, T.J., Chen, D., Cosh, M., Li, F., Anderson, M., Walthall, C., Doriaswamy, P., Hunt, E.R., 2004, "Vegetation water content mapping using Landsat data derived normalized difference water index for corn and soybeans", *Remote Sensing of Environment*, **92**, pp. 475-482.

Jacquemin, B., and Noilhan, J., 1990, "Sensitivity study and validation of a land surface parameterization using the HAPEX-MOBILHY data set", *Boundary-Layer Meteorology*, **52**, pp. 93-134.

Jager, C.J., Nakken, T.C., Palland, C.L., 1976, "Bodemkundig onderzoek van twee graslandpercelen nabij Cabauw", (in Dutch), N.V. Heidemaatschappij Beheer, 9 pp.

Jarvis, P.G., 1976, "The interpretation of the variations in leaf water potential and stomatal conductance found in canopies in the field", *Philosophical Transactions of the Royal Society of London. Series B, Biological Sciences*, **273**, pp. 593-610.

Johansen, O., 1975, "Thermal conductivity of soils", Ph.D thesis, University of Trondheim, 236 pp.

Joseph, A.T., van der Velde, R., O'Neill, P.E., Lang, R.H., Gish, T., 2008, "Soil moisture retrieval during a corn growth cycle using L-band (1.6 GHz) radar observations", *IEEE Transactions on Geoscience and Remote Sensing*, **46**, pp. 2365-2374.

Kahan, D.S., Xue, Y., Allen, S.J., 2006, "The impact of vegetation and soil parameters in simulations of surface energy and water balance in the semi-arid sahel: A case study using SEBX and HAPEX-Sahel data", *Journal of Hydrology*, **320**, pp. 238-259.

Kalnay, E., and Kanamitsu, M., 1988, "Time schemes for strongly nonlinear damping equations", *Monthly Weather Review*, **116**, pp. 1945-1958.

Karam, M.A., Fung, A.K., Lang, R.H., Chauhan, N.S., 1992, "A microwave scattering model for layered vegetation", *IEEE Transactions on Geoscience and Remote Sensing*, **30**, pp. 767-784.

Karam, M.A., 1997, "A physical model for microwave radiometry of vegetation", *IEEE Transactions on Geoscience and Remote Sensing*, **35**, pp. 1045-1058.

Kato, H., Rodell, M., Beyrich, F., Cleugh, H., van Gorsel, E., Liu, H., Meyers, T.P., 2007, "Sensitivity of land surface simulations to model physics, land characteristics, and forcings, at four CEOP Sites", *Journal of the Meteorological Society of Japan*, **87A**, pp. 187-204.

Kerr, Y.H., Waldteufel, P., Wigneron, J-P., Martinuzzi, J-M., Font, J., Berger, M., 2001, "Soil moisture retrieval from space: The soil moisture and Ocean Salinity (SMOS) mission", *IEEE Transactions on Geoscience and Remote Sensing*, **39**, pp.1729-1735.

Kersten, M.S., 1949, "Thermal properties of soils", *University of Minnesota Engineering Experiment Station Bulletin*, **28**, 227 pp. (Available from

University of Minnesota Agricultural Experiment Station, St. Paul, MN 55108).

Koorevaar, P., Menelik, G., Dirkson, C., 1983, "Elements of soil physics", Elsevier Science.

Koskinen, J.T., Pulliainen, J.T., Hallikainen, M.T., 2007, "The use of ERS-1 SAR data in snow melt monitoring", *IEEE Transactions on Geoscience and Remote Sensing*, **35**, pp. 601-610.

Koster, R., and Suarez, M., 1992, "Modeling the land surface boundary in climate models as a composite of independent vegetation stands", *Journal of Geophysical Research*, **97**, pp. 2697-2715.

Koster, R.D., Suarez, M.J., Ducharne, A., Stieglitz, M., Kumar, P., 2000, "A catchment-based approach to modeling land surface processes in a GCM, Part 1, Model Structure", *Journal of Geophysical Research*, **105**, pp. 24809-24822.

Koster, R.D., Dirmeyer, P.A., Guo, Z., and co-authors, 2004, "Regions of strong coupling between soil moisture and precipitation", *Science*, **305**, pp. 1138-1140.

Lang, R.H., and Sidhu, J.S., 1983, "Electromagnetic backscattering from a layer of vegetation: a discrete approach", *IEEE Transactions on Geoscience and Remote Sensing*, **GE-21**, pp. 62-71.

Lawford, R.G., Roads, J., Lettenmaier, D.P., Arkin, P., 2007, "GEWEX Contributions to Large-Scale Hydrometeorology", *Journal of Hydrometeorology*, **8**, Iss. 4, pp. 629–641.

Laymon, C.A., Crosson, W.L., Soman, V.V., Belisle, W.R., Coleman, T.L., Fahsi, A., Manu, A., Senwo, Z.N., Tsegaye, T.D., O'Neill, P.E., Jackson, T.J., 1999, "Huntsville'96: an experiment in ground-based microwave remote sensing of soil moisture", *International Journal of Remote Sensing*, **20**, pp.823-828.

Le Hegarat-Mascle, S., Zribi, M., Alem, F., Weisse, A., Loumagne, C., 2002, "Soil moisture estimation from ERS/SAR data: toward an operational methodology", *IEEE Transactions on Geoscience and Remote Sensing*, **40**, pp. 2647-2658.

LeVine, D.M., Meneghini, R., Lang, R.H., Seker, S.S., 1983, "Scattering from arbitrarily oriented dielectric disks in the physical optics regime", *Journal of the Optical Society of America*, **73**, pp. 1255-1262.

Le Toan, T., Quegan, S., Woodward, I., Lomas, M., Delbart, N., Picard, G., 2004, "Relating Rradar remote sensing of biomass to modeling of forest carbon budgets", *Climate Change*, **67,** pp. 379-402.

Liang, X., Lettenmaier, D.P., Wood, E.F., Burges, S.J., 1994, "A simple hydrologically based model of land surface water and energy fluxes for GSMs", *Journal of Geophysical Research*, **99**, pp. 14415-1,428

Liu, S., Lu, L., Mao, D., Jia, L., 2007, "Evaluating parameterizations of aerodynamic resistance to heat transfer using field measurements", *Hydrology and Earth System Science*, **11**, pp. 769-783.

Löw, A., Ludwig, R., Mauser, W., 2006, "Derivation of surface soil moisture from ENVISAT ASAR Wide Swath and Image Mode data in agricultural areas", *IEEE Transactions on Geoscience and Remote Sensing*, **44**, pp. 889-899.

Ma, Y., Fan, S., Ishikawa, H., Tsukamoto, O., Yao, T., Koike, T., Zuo, H., Hu, H., Su, Z., 2005, "Diurnal and inter-monthly variation of land surface

heat fluxes over the central Tibetan Plateau area", *Theoretical and Applied Climatology*, **80**, pp. 259-273.

Ma, Y., Tian, H., Wang, J., Ishikawa, H., Menenti, M., Koike, T., 2006, "Determination of regional distribution and seasonal variation of land surface heat fluxes from Landsat-7 Enhanced Thematic Mapper data over the central Tibetan Plateau area", *Journal of Geophysical Research*, **111**, DOI:10.1029/2005JD006742.

Ma, Y., Menenti, M., Feddes, R., Wang, J., 2008, "Analysis of the land surface heterogeneity and its impact on atmospheric variables and the aerodynamic and thermodynamic roughness lengths", *Journal of Geophysical Research*, **113**, DOI:10.1029/2007JD009124.

Macelloni, G., Paloscia, S., Pampaloni, P., Sigismondi, S., De Matthaeis, P., Ferrazzoli, P., Schiavon, G., Solimini, D., 1999, "The SIR-C/X-SAR experiment on the Montespertoli: sensitivity to hydrological parameters", *International Journal of Remote Sensing*, **20**, pp. 2597-2612.

Macelloni, G., Nesti, G., Pampaloni, P., Sigismondi, S., Tarchi, D., Lolli,S., 2000, "Experimental validation of surface scattering and emission models", *IEEE Transactions on Geoscience and Remote Sensing*, **38**, pp. 459-469.

Macelloni, G., Paloscia, S., Pampaloni, P., Marliani, F., Gai, M., 2001, "The relationship between the backscattering coefficient and the biomass of narrow and broad leaf crops", *IEEE Transactions on Geoscience and Remote Sensing*, **39**, pp. 873-884.

Mahfouf, J.F., and Noilhan, J., 1991, "Comparative study of various formulation of evaporation from bare soil using in situ data", *Journal of Applied Meteorology*, **30**, pp. 1354- 1365.

Mahrt, L., and Ek, M., 1984, "The influence of atmospheric stability on potential evaporation", *Journal of Climate and Applied Meteorology*, **23**, pp. 222-234.

Marht, L., and Pan, H.L., 1984, "A two-layer model of soil hydrology", *Boundary-Layer Meteorology*, **29**, pp. 1-20.

Maity, S., Patnaik, C., Chakraborty, M., Panigraphy, S., 2004, "Analysis of temporal backscattering of cotton crops using a semi-empirical model", *IEEE Transactions on Geoscience and Remote Sensing*, **42**, pp. 577-587.

Manabe, S., 1969, "Climate and the ocean circulation: 1. The atmospheric circulation and the hydrology of the earth's surface", *Monthly Weather Review,* **97**, pp. 739–805.

Mancini, M., Hoeben, R., Troch, P.A., 1999, "Multifrequency radar observations of bare surface soil moisture content: A laboratory experiment", *Water Resources Research*, **35**, pp. 1827-1838.

Manninen, T., Stenberg, P., Rautiainen, M., Voipio, P., Smolander, H., 2005, "Leaf Area Index estimation of boreal forest using ENVISAT ASAR", *IEEE Transactions on Geoscience and Remote Sensing*, **43**, pp. 2627-2635.

Mattia, F., Le Toan, T., Picard, G., Posa, F.I., D'Alessio, A., Notarnicola, C., Gatti, A.M., Rinaldi, M., Satalino, G., Pasquariello, G., 2003a, "Multitemporal C-band radar measurements on wheat fields", *IEEE Transactions on Geoscience and Remote Sensing*, **41**, pp. 1551-1560.

Mattia, F., Davidson, M.W.J., Le Toan, T., D'Haese, C.M.F., Verhoest, N.E.C., Gatti, A.M., Borgeaud, M., 2003b "A comparison between soil roughness statistics used in surface scattering models derived from mechnanical and laser profilers", *IEEE Transactions on Geoscience and Remote Sensing*, **41**, pp. 1659-1671.

Mattia, F., Satalino, G., Dente, L., Pasquariello, G., 2006, "Using *A Priori* information to improve soil moisture retrieval from ENVISAT ASAR AP data in semi-arid regions", *IEEE Transactions on Geoscience and Remote Sensing*, **44**, pp. 900-912.

Mätzler, C., 1994, "Microwave (1-100 GHz) dielectric model of leaves", *IEEE Transactions on Geoscience and Remote Sensing*, **32**, pp. 947-949.

McCumber, M.C., and Pielke, R.A., 1981, "Simulation of the effects of surface fluxes of heat and moisture in a mesoscale numerical model, 1. soil layer", *Journal of Geophysical Research*, **86**, pp. 9929-9938.

McLaughlin, D., 2002, "An integrated approach to hydrologic data assimilation: interpolation, smoothing and filtering", *Advances in Water Resources*, **25**, pp. 1275-1286.

Miller, J.D., Gaskin, G.J., Anderson, H.A., 1997, "From drought to flood: Catchment responses revealed using novel soil water probes", *Hydrological Processes*, **11**, pp. 533-541.

Mlawer, E.J., Taubman, S.J., Brown, P.D., Iacono, M.J., Clough, S.A., 1997, "Radiative transfer for inhomogeneous atmosphere: RRTM, a validated correlated-k model for the longwave", *Journal of Geophysical Research*, **102**, pp. 16 663-16 682.

Monakov, A.A., Vivekanandan, J., Stjernman, A.S., Nystrom, A.K., 1994, "Spatial and frequency averaging techniques for a polarimetric scatterometer system", *IEEE Transactions on Geoscience and Remote Sensing*, **32**, pp. 187-196.

Moran, S.M., Hymer, D.C., Qi, J., Kerr, Y., 2002, "Comparison of ERS-2 SAR and Landsat TM imagery for monitoring agricultural crop and soil conditions", *Remote Sensing of Environment*, **79**, pp. 243-252.

Mualem, Y., 1976, "A new model for predicting the hydraulic conductivity of unsaturated porous media", *Water Resources Research*, **12**, pp. 513-521.

Narayan, U., Lakshmi, V., Jackson, T.J., 2006, "High-resolution change estimation of soil moisture using L-band radiometer and radar observations made during the SMEX02 experiments", *IEEE Transactions on Geoscience and Remote Sensing*, **44**, pp. 1545-1554.

Nesti, G., and Hohmann, M., 1990, "An efficiënt calibration procedure for polarimetric radar systems", *Geoscience and Remote Sensing Symposium 1990 (IGARSS '90)*, pp. 1099-1103.

Ni-Meister, W., Walker, J.P., Houser, P.R., 2005, "Soil moisture initialization for climate prediction: Characterization of model and observation errors", *Journal of Geophysical*, **110**, DOI: 10.1029/2004JD005746.

Njoku, E.G., Wilson, W.J., Yueh, S.H., Dinardo, S.J., Li, F.K., Jackson, T.J., Lakshmi, V., Bolten, J., 2002, "Observation of soil moisture using a passive and active low-frequency microwave airborne sensor during SGP99", *IEEE Transactions on Geoscience and Remote Sensing*, **40**, pp. 2659-2673.

Noilhan, J., and Planton, S., 1989, "A simple parameterization of land surface processes for meteorological models", *Monthly Weather Review*, **117,** pp. 536-549.

O'Neill, P.E., and Chauhan, N., 1992, "Truck mounted radar system", Chapter XII: Washita'92 data report, available at http://www.ars.usda.gov/SP2UserFiles/ad_hoc/12650600SoilMoistureProgram/chap12.pdf (Last verified on December 2009).

O'Neill, P.E., Chauhan, N.S., Jackson, T.J., 1996, "Use of active and passive microwave remote sensing for soil moisture estimation through corn", *International Journal of Remote Sensing*, **17**, pp. 1851-1865.

Oh, Y., and Kay, Y.C., 1998, "Condition for precise measurement of soil surface roughness", *IEEE Transactions on Geoscience and Remote Sensing*, **36**, pp. 691-695.

Oh, Y., Sarabandi, K., Ulaby, F.T., 1992, "An empirical model and an inversion technique for radar scattering from bare soil surfaces", *IEEE Transactions on Geoscience and Remote Sensing*, **30**, pp. 370-381.

Oldak, A., Jackson, T.J., Starks, P., Elliot, R., 2003, "Mapping near-surface soil moisture on regional scale using ERS-2 SAR data", *International Journal of Remote Sensing*, **24**, no. 22, pp. 4579-4598.

Owe, M., De Jeu, R.A.M., Walker, J.P., 2001, "A methodology for surface soil moisture and vegetation optical depth retrieval using the microwave polarization difference index", *IEEE Transactions on Geoscience and Remote Sensing*, **39**, pp. 1643-1654.

Pan, G.W., and Fung, A.K., 1987, "A scattering model for perfectly conducting random surfaces II. Rang of validity", *International Journal of Remote Sensing*, **8**, pp. 1595-1605.

Pan, H.L., and Marht, L., 1987, "Interaction between soil hydrology and boundary-layer development", *Boundary-Layer Meteorology*, **38**, pp. 185-202.

Pathe, C., Wagner, W., Sabel, D., Doubkova, M., Basara, J.B., 2009, "Using ENVISAR ASAR Global model data for surface soil moisture retrieval over Oklahoma, USA", *IEEE Transactions on Geoscience and Remote Sensing*, **27**, pp. 468-480.

Pauwels, V.R.N., and Samson, R., 2006, "Comparison of different methods to measure and model actual evapotranspiration rate for a wet sloping grassland", *Agricultural Water Management*, **82**, pp. 1-24.

Pauwels, V.R.N., Timmermans, W., Loew, A., 2008, "Comparison of the estimated water and energy budgets of a large winter wheat field during AgriSAR 2006 by multiple sensors and models", *Journal of Hydrology*, **349**, pp. 425-440.

Perez, P.J., Castellvi, F., Ibanez, M., Rosell, J.I., 1999, "Assessment of reliability of Bowen ratio method for partitioning fluxes", *Agricultural and Forest Meteorology*, **97**, pp. 141-150.

Peters-Lidard, C.D., Blackburn, E., Liang, X., Wood, E.F., 1998, "The effect of soil thermal conductivity parameterization on surface energy fluxes and temperatures", *Journal of Atmospheric Sciences*, **55**, pp. 1209-1224.

Prevot, L., Champion, I., Gayot, G., 1993, "Estimating surface soil moisture and leaf area index of a wheat canopy using a dual frequency (C- and X Bands) Scatterometer", *Remote Sensing of Environment*, **46**, pp. 331- 339.

Quesney, A., Le Hegarat-Mascle, S., Taconet, O., Vidal-Madjar, D., Wigneron, J.P., Loumagne, C., Normand, M., 2000, "Estimation of watershed soil moisture index from ERS/SAR data", *Remote Sensing of Environment*, **72**, pp. 290-303.

Rahman, M.M., Moran, M.S., Thoma, D.P., Bryant, R., Sano, E.E., Holifield-Collins, C.D., Skirvin, S., Kershner, C., Orr, B.J., 2007, "A derivation of roughness correlation length for parameterizating radar backscatter models", *International Journal of Remote Sensing*, **28**, pp. 3995-4012.

Rahman, M.M., Moran, M.S., Thoma, D.P., Bryant, R., Holifield-Collins, C.D., Jackson, T., Orr, B.J., Tischler, M., 2008, "Mapping surface roughness and soil moisture using multi-angle radar imagery without ancillary data", *Remote Sensing of Environment*, **112**, pp. 391-402.

Rawls, W.J., Ahuja, J.R., Brakensiek, D.L., Shirmohammadi, A., 1993, "Infiltration and soil water movement", In: Handbook of Hydrology, D.R. Maidment (Ed.), McGraw-Hill, Chapter 5.

Reichle, R.H., 2008, "Data assimilation methods in the Earth sciences", *Advances in Water Resources*, **31**, pp.1411-1418.

Reichle R.H., and Koster, R.D., 2004, "Bias reduction in short record of satellite soil moisture", *Geophysical Research Letters*, **31**, DOI: 10.1029/2004GL020938.

Reichle, R.H., and Koster, R.D., 2005, "Global assimilation of satellite surface soil moisture retrievals into the NASA Catchment land surface model", *Geophysical Research Letters*, **32**, DOI:10.1029/2004GL021700.

Reichle, R.H., Koster, R.D., Dong, J., Berg, A.A., 2004, "Global soil moisture from satellite observations, land surface models and ground data: Implication for data assimilation", *Journal of Hydrometeorology*, **5**, pp. 430-442.

Reynolds, C.A., Jackson, T.J., Rawls, W.J., 2000, "Estimating soil water-holding capacities by linking the food and agriculture organization soil map of the world with global pedon databases and continuous pedotransfer functions", *Water Resources Research*, **36**, pp. 2653-3662.

Rice, S.O., 1957, "Reflection of electromagnetic waves from slightly rough surface", *Communications in Pure and Applied mathematics*, **4**, pp. 361-378.

Rignot, E., Way, J.B., McDonald, K., Viereck, L., Williams, C., Adams, P., Payne, C., Wood, W., 1994, "Monitoring of environmental conditions in taiga forests using ERS-1 SAR", *Remote Sensing of Environment*, **49**, pp. 145-154.

Rignot, E., and Way, J.B., 1994, "Monitoring freeze-thaw cycles along north-south Alaskan transects using ERS-1 SAR", *Remote Sensing of Environment*, **49**, pp. 131-137.

Rodell, M., Houser, P.R., Berg, A.A., Famiglietti, J.S., 2005, "Evaluation of 10 methods for initializing a land surface model", *Journal of Hydrometeorology*, **6**, pp. 146-155.

Saatchi, S., Soares, J.V., Alves, D.S., 1997, "Mapping deforestation and land cover in Amazon rainforest using SIR-C imagery", *Remote Sensing of Environment*, **59**, pp. 191-202.

Schaake, J.C., Koren, V.I., Duan, Q-Y., Mitchell, K., and Chen, F., 1996, "Simple water balance model for estimating runoff at different spatial

and temporal scales", *Journal of Geophysical Research*, **101**, pp. 7461-7575.

Schaake, J., Duan, Q., Andreassian, V., Franks, S., Hall, A., and Leavesley, G., 2006, "The model parameter estimation experiment MOPEX", *Journal of Hydrology*, **349**, pp. 425-440.

Schaap, M.P., and Leij, F.J., 1998, "Database-related accuracy and uncertainty of pedotransfer functions", *Soil Science*, **163**, pp. 765-779

Seker, S.S., Schneider, A., 1988, "Electromagnetic scattering from a dielectric cylinder of finite length", *IEEE Antennas and Propagation*, **36**, pp. 303-307.

Sellers, P.J., Mintz, Y., Sud, Y.C., Dalcher, A., 1986, "A Simple Biosphere Model (SIB) for use within general circulation models", *Journal of the Atmospheric Sciences*, **43**, pp. 505-531.

Schaake, J.C., Koren, V.I., Duan, Q.Y., Mitchell, K., Chen, F., 1996, "Simple water balance model for estimating runoff at different spatial and temporal scales", *Journal of Geophysical Research*, **101**, pp. 7461-7475.

Shao, Y., and Irannejad, P., 1999, "On the choice of soil hydraulic models in land-surface schemes", *Boundary-Layer Meteorology*, **90**, pp. 83-115.

Sheffield, J., Goteti, G., Wood, E. F., 2006, "Development of a 50-yr high-resolution global dataset of meteorological forcings for land surface modeling", *Journal of Climate*, **19**, pp. 3088-3111.

Shi, J., Wang, J., Hsu, A., O'Neill, P.E., Engman, E.T., 1997, "Estimation of bare surface soil moisture and surface roughness parameter using L-band SAR image data", *IEEE Transactions on Geoscience and Remote Sensing*, **35**, pp. 1254-1266.

Shukla, J., and Mintz, Y., 1982, "Influence of land surface evapotranspiration on the Earth's Climate", *Science*, **215**, pp. 1498-1501.

Soet, M., and Stricker, J.N.M., 2003, "Functional behaviour of pedotransfer function in soil water flow simulation", *Hydrological Processes*, **17**, pp. 1659-1970.

Sridhar, V., Elliott, R.L., Chen, F., Brotzge, J.A., 2002, "Validation of the Noah-OSU land surface model using surface flux measurements in Oklahoma", *Journal of Geophysical Research*, DOI: 10.1029/2001JD001306.

Stiles, J.M., and Sarabandi, K., 2000, "Electromagnetic scattering from grassland. I. A fully phase-coherent scattering model", *IEEE Transactions on Geoscience and Remote Sensing*, **38**, pp. 339-348.

Stiles, J.M., Sarabandi, K., Ulaby, F.T., 2000, "Electromagnetic scattering from grassland. II. Measurement and modeling results", *IEEE Transactions on Geoscience and Remote Sensing*, **38**, pp. 349-356.

Su, Z., Troch, P.A., De Troch, F.P., 1997, "Remote sensing of bare surface soil moisture using EMAC/ESAR data", *International Journal of Remote Sensing*, **18**, pp. 2105-2124.

Su, Z., Schmugge, T., Kustas, W.P., Massman, W.J., 2001, "An evaluation of two models for estimation of the roughness length for heat transfer between the land surface and the atmosphere", *Journal of Applied Meteorology*, **40**, pp. 1933-1951.

Taconet, O., Benallegue, M., Vidal-Madjar, D., Prevot, L., Dechambre, M., Normand, M., 1994, "Estimation of soil and crop parameters for wheat

from airborne radar scattering data in C and X bands", *Remote Sensing of Environment*, **50**, pp. 287-294.

Thoma, D.P., Moran, M.S., Bryant, R., Rahman, M., Holifield-Collins, C.D., Skirvin, S., Sano, E.E., Slocum, K., 2006 "Comparison of four models to determine surface soil moisture from C-band radar imagery in a sparsely vegetated semiarid landscape", *Water Resources Research*, **42**, W01418.

Thoma, D.P., Moran, M.S., Bryant, R., Rahman, M.M., Holifield Collins, C.D., Keefer, T.O., Noriega, R., Osman, I., Skrivin, S.M., Tischler, M.A., Bosch, D.D., Starks, P.J., Peters-Lidard, C.D., 2008, "Appropriate scale of soil moisture retrieval from high resolution radar imagery for bare and minimally vegetated soils", *Remote Sensing of Environment*, **112**, pp. 403-414.

Topp, G.C., Davis, J.L., Annan, A.P., 1980, "Electromagnetic Determination of Soil Water Content: Measurements in Coaxial Transmission Lines", *Water Resource Research*, **16**(3), pp. 574–582.

Uitdewilligen, D.C.A., Kustas, W.P., Van Oevelen, P.J., 2003, "Estimating surface soil moisture with the scanning low frequency microwave radiometer (SLFMR) during the Southern Great Plains 1997 (SGP97) hydrology experiment", *Physics and Chemistry of the Earth*, **28**, pp. 41-51.

Ulaby, F.T., Allen, C.T., Eger, G., Kanemasu, E., 1984, "Relating the microwave backscattering coefficient to leaf area index", *Remote Sensing of Environment*, **14**, pp. 113-133.

Ulaby, F.T., and Batlivala, P.P., 1976, "Optimum radar parameters for mapping soil moisture", *IEEE Transactions on Geoscience Electronics*, **GE-14**, pp. 81-93.

Ulaby, F.T., Fung, A.K., Moore, R.K., 1981, "Microwave remote sensing: active and passive: Vol.I microwave remote sensing fundamentals", Reading, MA: Addison-Wesley.

Ulaby, F.T., Fung, A.K., Moore, R.K., 1982, "Microwave Remote Sensing: Active and Passive, vol II. Vol. II radar remote sensing and surface scattering and emission theory", Reading, MA: Addison-Wesley.

Ulaby, F.T., Moore, R.K., Fung, A.K., 1986, "Microwave remote sensing: active and passive. Vol. III From theory to application", Reading, MA: Artech House.

Ulaby, F., Allen, C., Eger, G., Kanemasu, E., 1984, "Relating microwave backscattering coefficient to leaf area index", *Remote Sensing of Environment*, **14**, pp. 113-133.

Ulaby, F.T., Sarabandi, K., McDonald, K., Whitt, M., Dobson, M.C., 1990, "Michigan microwave canopy scattering model", *International Journal of Remote Sensing*, **11**, pp. 1223-1253.

Ulaby, F.T., Dubois, P.C., van Zyl, J., 1996, "Radar mapping of surface soil moisture", *Journal of Hydrology*, **184**, pp. 57-84.

Van der Velde, R., Su, Z., Ma, Y., 2008, "Impact of soil moisture dynamics on ASAR σ^o signatures and its spatial variability observed over the Tibetan Plateau", *Sensors*, **8**, pp. 5479-5491.

Van der Velde, R., Su, Z., Ek, M., Rodell, M., Ma, Y., 2009, "Influence of thermodynamic soil and vegetation parameterizations on the simulation of soil temperature states and surface flux by the Noah LSm

over a Tibetan Plateau site", *Hydrology and Earth System Sciences*, **13**, pp. 759-777.

Van Genuchten, M. Th., 1980, "A closed-form equation for predicting the hydraulic conductivity of unsaturated soils", *Soil Science Society of America*, **44**, pp. 892-898.

Van Oevelen, P.J., 2000, "Estimation of areal soil water content through microwave remote sensing", Ph.D thesis, Wageningen University.

van Oevelen, P.J., and Hoekman, D.H., 1999, "Radar backscatter inversion techniques for estimation of surface soil moisture: EFEDA-Spain and HAPEX-Sahel case studies", *IEEE Transactions on Geoscience and Remote Sensing*, **37**, pp. 113-123.

Van Ulden, A.P., and Wieringa, J., 1996, "Atmospheric boundary layer research at Cabauw", *Boundary-Layer Meteorology*, **78**, pp. 39-69.

Verhoest, N.E.C., Lievens, H., Wagner, W., Alvarez-Mozos, J., Moran, M.S., Mattia, F., 2008, "On the soil roughness parameterization problem in soil moisture retrieval of bare surfaces from Synthetic Aperture Radar", *Sensors*, **8**, pp. 4213-4248.

Verhoest N.E.C., Troch P.A., Paniconi C., De Troch F.P., 1998, "Mapping basin scale variable source areas from multitemporal remotely sensed observations of soil moisture behavior", *Water Resources Research*, **34**, pp. 3235-3244.

Vinnikov, K.Y., Robock, A., Speranskaya, N.A., Schlosser, C.A., 1996, "Scales of temporal and spatial variability of midlatitude soil moisture", *Journal of Geophysical Research*, **101**, pp. 7163-7174.

Wagner, W., and Scipal, K., 2000, "Large-scale soil moisture mapping in western Africa using the ERS scatterometers", *IEEE Transactions on Geoscience and Remote Sensing*, **38**, pp. 1777-1782.

Walker, J.P., and Houser, P.R., 2004, "Requirements of a global near-surface soil moisture satellite mission: accuracy, repeat time and spatial resolution", *Advances in Water Resources*, **27**, pp. 785-801.

Walker, J.P., Willgoose, G.R., Kalma, J.D., 2001, "One-dimensional soil moisture profile retrieval by assimilation of near-surface measurements: A simplified soil moisture model and field application", *Journal of Hydrometeorology*, **2**, pp. 356-373.

Wang, J.R., and Schmugge, T.J., 1980, "An empirical model for the complex dielectric permittivity of soils as a function of water content", *IEEE Transactions on Geoscience and Remote Sensing*, **GE-18**, pp. 288-295.

Way, J.B., Zimmermann, R., Rignot, E., McDonald, K., Oren, R., 1997, "Winter and spring thaw as observed with imaging radar at BOREAS", *Journal of Geophysical Research*, **102**, pp. 29673-29685.

Wegmüller, U., 1990, "The effect of freezing and thawing on the microwave signatures of bare soil", *Remote Sensing of Environment*, **33**, pp. 125-135.

Wen, J., and Su, Z., 2003a, "The estimation of soil moisture from ERS wind scatterometer data over the Tibetan plateau", *Physics and Chemistry of the Earth*, **28**, pp .53-61.

Wen, J., and Su, Z., 2003b, "A Method for Estimating Relative Soil Moisture with ESA Wind Scatterometer Data", *Geophysical Research Letters*, **30**, DOI:10.1029/ 2002GL016557.

Wen, J., Su, Z., Ma, Y., 2003, "Determination of land surface temperature and soil moisture from Tropical Rainfall Measuring Mission/Microwave Imager remote sensing data", *Journal of Geophysical Research*, **108**, DOI:10.1029/2002JD002176.

Wismann V., 2000, "Monitoring of seasonal thawing in Siberia with ERS Scatterometer data.", *IEEE Transactions on Geoscience and Remote Sensing*, **38**, pp. 1804-1809.

Wood, E.F., Lettenmaier, D.P., Liang, X., and co-authors, 1998, "The Project for Intercomparison of Land-surface Parameterization Schemes (PILPS) Phase 2(c) Red–Arkansas River basin experiment: 1. Experiment description and summary intercomparisons", *Global and Planetary Change*, **19**, pp. 115-135.

Woodhouse, I.H., 2006, "Introduction to microwave remote sensing", CRC Press.

Woodhouse, I.H., and Hoekman, D.H., 2000, "Determining land-surface parameters from the ERS wind scatterometer", *IEEE Transactions on Geoscience and Remote Sensing*, **38**, pp. 126-140.

Wösten, J.H.M., Veerman, G.J., de Groot, W.J.M., Stolte, J., 2001, "Waterretentie- en doorlatendheidskarakteristieken van boven- en ondergronden in Nederland: de Staringreeks, Vernieuwde uitgave 2001", Wageningen, Alterra, Research Institute voor de Groene Ruimte, Alterra-rapport 153, 86 pp [in Dutch, available at: http://library.wur.nl/WebQuery/wurpubs/lang/313559]

Yang, Y., Koike, T., Yang, D., 2003, "Surface flux parameterization in the Tibetan Plateau", *Boundary-Layer Meteorology*, **116**, pp. 245-262.

Yang, K., Koike, T., Ye, B., Bastidas, L., 2005, "Inverse analysis of the role of soil vertical heterogeneity in controlling surface soil state and energy partition", *Journal of Geophysical Research*, **110**, DOI: 10.1029/2004/JD005500.

Yang, K., Watanabe, T., Koike, T., Li, X., Fujii, H., Tamagawa, K., Ma, Y., Ishikawa, H., 2007, "Auto-calibration system developed to assimilate AMSR-E data into land surface model for estimating soil moisture and the surface energy budget", *Journal of the Meteorological Society of Japan*, **85**, pp. 229-242.

Yang, K., Koike, T., Ishikawa, H., Kim, J., Li, X., Liu, H., Liu, S., Ma, Y., Wang, J., 2008, "Turbulent flux transfer over bare-soil surfaces: Characteristics and Parameterizations", *Journal of Applied Meteorology and Climatology*, **47**, pp. 276-290.

Yilmaz, M.T., Hunt, E.R, Jackson, T.J., 2008, "Remote sensing of vegetation water content from equivalent water thickness using satellite imagery", *Remote Sensing of Environment*, **112**, pp. 2514-2522.

Zeng, X., and Dickinson, R.E., 1998, "Effect of surface sublayer on surface skin temperature and flux", *Journal of Climate*, **11**, pp. 537-550.

Zilitinkevich, S. S., 1995, "Non-local turbulent transport: Pollution dispersion aspects of coherent structure of convective flow", in H. Power, N. Moussiopoulos, and C. A. Brebbia (eds.), Air Pollution, Vol. 1, Air Pollution Theory and Simulation, Computational Mechanics Publication, Southampton, pp. 53–60.

Zink, M., Torres, R., Buck, C.H., Rosich, B., Closa, J., 2002, "Calibration and early results of the ASAR on ENVISAT", *IEEE International Geoscience and Remote Sensing Symposium (IGARSS'02)*, pp. 596-598.

Zobeck, T.M., and Onstad, C.A., 1987, "Tillage and rainfall effects on random roughness: A review", *Soil and Tillage Research*, **9**, pp. 653-661.

Zribi, M., Taconet, O., Le Hegarat-Mascle, S., Vidal-Madjar, D., Emblanch, C., Loumagne, C., Normand, M., 1997, "Backscattering behavior and simulation comparison over bare soils using SIR-C/X-SAR and ERASME 1994 data over Orgeval", *Remote Sensing of Environment*, **59**, pp. 256-266.

Zribi, M., Ciarletti, V., Taconet, O., Paille, J., Boissard, P., 2000, "Characterisation of the soil structure and microwave backscattering based on numerical three-dimensional surface representation: analysis with a fraction brownian model", *Remote Sensing of Environment*, **72**, pp. 159-169.

Zribi, M., and Dechambre, M., 2002, "A new empirical model to retrieve soil moisture and roughness from C-band radar data", *Remote Sensing of Environment*, **84**, pp. 42-52.

Zribi, M., Taconet, O., Ciarletti, V., Vidal-Madjar, D., 2002, "Effect of row structure on radar microwave measurements over soil surface", *International Journal of Remote Sensing*, **23**, pp. 5211-5224.

Zribi, M., Baghdadi, N., Guerin, C., 2006, "Analysis of surface roughness heterogeneity and scattering behavior for radar measurements", *IEEE Transactions on Geoscience and Remote Sensing*, **44**, pp. 2438-2444.

Zribi, M., Saux-Picart, S., Andre, C., Descroix, L., Ottle, C., Kallel, A., 2007, "Soil moisture mapping based on ASAR/ENVISAT radar data over a Sahelian region", *International Journal of Remote Sensing*, **28**, pp. 3547-3565.

Samenvatting

Bodemvocht heeft een belangrijke invloed op de verdeling van zonne-straling en dus ook op de ontwikkeling van weersystemen. Een verbeterde bodemvocht simulatie binnen klimaat modellen zal hun voorspellende vaardigheid kunnen verbeteren. Dit kan met verschillende methoden bereikt worden, bijvoorbeeld door het gebruik maken van realistischer model structuren. Echter, de integratie van modellen met observaties is ook populair door de toenemende beschikbaarheid van satelliet gegevens.

Dit proefschrift draagt bij aan beide aspecten. **Hoofdstukken 5 - 8** gaan over de verbetering van bodemvocht schattingen uit actieve microgolf data, terwijl in **hoofdstukken 9 en 10** simulaties met het Noah model besproken worden. Tot slot, wordt in **hoofdstuk 11** de bodemvocht geschat uit satelliet metingen vergeleken met de simulaties uitgevoerd door het Noah model gekoppeld aan het MM5 regionaal klimaat model. Deze onderdelen zijn hieronder samengevat.

Bodemvocht schattingen door middel van actieve microgolven

Het schatten van bodemvocht uit actieve microgolf metingen is bestudeerd met behulp van een C- en L-band scatterometer data set verzameld over een maïs veld gedurende het groeiseizoen en een 2.5 jaar lange reeks aan ASAR (C-band en VV polarisatie) beelden verkregen over het centrale deel van het Tibetaanse plateau. De interpretatie van scatterometer data is gesteund door een uitgebreide collectie *in-situ* metingen, wat een gedetailleerde analyse mogelijk maakt. Uniek aan de Tibetaanse ASAR data set is dat over een aanzienlijk tijdsbestek de SAR beelden beschikbaar zijn met relatief hoge temporele resolutie. Als zodanig is de scatterometer data set gebruikt om de effecten van vegetation en ruwheid op backscatter (σ^o) metingen te analyseren. Daarnaast is de ASAR data set gebruikt om, op een grotere temporele en ruimtelijke schaal, de invloed van verschillende condities (bodemvocht, vegetatie, vries/dooi) aan het landoppervlak op de σ^o te onderzoeken en bodemvocht te schatten.

Hoofdstuk 5 bespreekt de invloed van maïs gedurende het groeiseizoen op polarimetrische (HH, HV, VV) C- en L-band σ^o gemeten vanuit invalshoeken van 15, 35 en 55 graden. Uit de analyse blijkt dat, afhankelijk van de antenne configuratie en het groeistadium, de σ^o metingen gedomineerd kunnen worden door een uitgedoofde verstrooiing van het land oppervlak of door verstrooiing geproduceerd met tussenkomst van de vegetatie. Het eerste mechanisme is het sterkst bij C-band metingen verzameld vanuit een kijkhoek van 15 graden aan het begin van het groei stadium. De

laatste is dominant in σ^o data gemeten tijdens piek biomassa en vanuit invalshoeken van 35 en 55 graden. Enigszins verrassend is echter dat zelfs ten tijde van piek biomassa de σ^o nog steeds gevoelig is voor bodemvocht. Deze gevoeligheid van de σ^o is toe te schrijven aan de verstrooiing langs de bodem-vegetatie trajecten.

Op basis van deze analyze is een alternatieve methode ontwikkeld om σ^o metingen te corrigeren voor de effecten van vegetatie en betrouwbaardere bodemvocht schattingen te verkrijgen. De methode is gebaseerd op het concept dat de ratio van de oppervlakte verstrooiing over de gemeten σ^o beïnvloed wordt door de vegetatie en beschreven kan worden als functie van het watergehalte van de vegetatie (*W*). Experimenteel bepaalde relaties tussen deze ratio en *W* zijn gebruikt om de oppervlakte verstrooiing te reconstrueren vanuit de gemeten σ^o en bodemvocht te schatten. Validatie van de verkregen bodemvocht waarden tegen de in-situ metingen resulteert in gemiddelde fouten variërend van 0.033 tot 0.063 m^3 m^{-3} afhankelijk van de antenne configuratie. Een dergelijke nauwkeurigheid is behoorlijk goed zeker als ook de dichte begroeiing gedurende het groeiseizoen in beschouwing wordt genomen. Aanvullende studies zijn echter nodig om de geldigheid van de voorgestelde methode voor andere gewassen te bepalen.

Ook de ruwheid van het bodemoppervlak is van invloed op de waargenomen σ^o en is nodig voor het schatten van bodemvocht. De (Advanced) Integral Equation Method ((A)IEM, Fung et al. 1992, Chen et al. 2003), toepasbaar voor oppervlakken met verschillende ruwheden, wordt vaak gebruikt om de σ^o van kale grond te simuleren. Dit model representeert de complexe geometrie van het oppervlak als een ‘single-scale’ stationair process. Door deze aanname kan de geometrie van het oppervlak gekarakteriseerd worden door drie statische variabelen te bepalen uit 1-dimensionale hoogte profielen, bestaande uit root mean square height (*s*), autocorrelatie lengte (*l*) and autocorrelatie functie (ACF). Echter, over grote ruimtelijke domeinen is meestal onvoldoende informatie beschikbaar om deze parameters betrouwbaar te kunnen bepalen. Voor het schatten van bodemvocht uit σ^o is het daardoor noodzakelijk om het aantal ruwheidsparameters te reduceren en deze parameterisatie als constant in tijd te beschouwen.

Hoofdstuk 6 behandelt de invloed van deze aannames op de nauwkeurigheid van bodemvocht bepalingen vanuit de voor vegetatie gecorrigeerde σ^o metingen. Vier typen ruwheidsparameterisaties zijn gecalibreerd, zijnde met Gaussische of Exponentïele ACF, en met de vaste (gemeten) of een gecalibreerde *l*. Uit de analyse van de nauwkeurigheid van de bodemvochtbepalingen blijkt dat de meest significant verschillen zich voordoen tussen de Gaussische en

Exponentïele ACF, en dat de *l* slechts een geringe invloed heeft. Echter, de meeste verschillen tussen de vier typen parameterizaties zijn kleiner dan 0.01 m^3 m^{-3}. Dit laat zien dat ongeacht het type parameterisatie een effectieve waarde voor de *s* kan worden gevonden zonder dat het de nauwkeurigheid van bodemvocht schattingen significant aantast.

De bestudering van de temporele stabiliteit van de ruwheid suggereert dat gemiddeld over het gehele groeiseizoen ruwheidsveranderingen een beperkte invloed (<0.01 m^3 m^{-3}) hebben op de nauwkeurigheid van bodemvocht bepalingen. Op een dagelijkse basis treden echter de grote verschillen op specificek na periodes met regen. De verhoogde discrepantie tussen de metingen en schattingen is het grootst voor HH polarisatie, L-band and grote invalshoeken. Dit is consistent met eerdere studies die de gevoeligheid van σ^o voor de ruwheid bediscusseerden (bijv. Holah et al. 2005, Beaudoin et al. 1990, Zribi et al. 1997). Hierdoor is in tegenstelling tot voorgaande studies (bijv. Ulaby en Batlivala 1979, Ulaby et al. 1996, Shi et al. 1997, Macelloni et al. 1999) de bodemvocht geschat tijdens groei seizoen nauwkeuriger voor de VV polarisatie.

Hoofdstuk 7 bespreekt de invloed van de toestand van het landoppervlak op de ASAR σ^o over een langere tijdsschaal en voor verschillende ruimtelijke schaalniveau's op het Tibetaans Plateau. Reeksen aan σ^o metingen verzameld over een 1x1 km^2 grasland en een 1x1 km^2 moerasgebeid zijn bestudeerd om de gevoeligheid voor veranderingen in de toestand van het landoppervlak te indentificeren. De laagste σ^o waarden over zowel het grasland als het moerasgebeid zijn verkregen tijdens de winters, omdat in deze periode van het jaar het water in de bodem voornamelijk bevroren is wat resulteert in diëlektrische eigenschappen die vergelijkbaar zijn met die van een droge bodem. Richting het zomer seizoen stijgt de σ^o waargenomen over het moerasgebeid gestaag en bereikt het maximum als de moesson intensiteit op zijn hoogst is. De σ^o waargenomen over het grasland wordt echter gekenmerkt door grote fluctuaties in tijd, voornamelijk tijdens de zomers. Dit contrast in de σ^o dynamiek over het grasland en het moerasgebied kan toegeschreven worden aan enerzijds de sterk variabele bodemvocht in het grasland door de grote verdampingsvraag en anderzijds de temporeel stabiele omstandigheden in het moerasgebied.

Het duidelijke verschil tussen de σ^o dynamieken van het grasland en het moerasgebied heeft gevolgen voor de ruimtelijke σ^o variabiliteit waargenomen op verschillende ruimtelijke schalen (bijv. 1x1 km^2, 5x5 km^2 en 30x30 km^2). Met als gevolg dat de vergelijking van de gemiddelde σ^o voor een bepaalde domein met de standaarddeviatie (stdev) resulteert in een driehoekige verdeling van de data punten waarbij de piek in het ongeveer midden van het totale

σ^o bereik ligt. Wanneer de σ^o beschouwd wordt als representant van de bodemvocht condities laten deze resultaten zien dat de relatie tussen het ruimtelijk gemiddelde en variabiliteit niet altijd eenduidig is gedefinieerd. Dit betekent dat voor downscaling van lage resolutie bodemvocht producten de relatie tussen het gemiddelde en de stdev niet onafhankelijk van tijd kan worden genomen, maar verkregen dient te worden uit andere data bronnen, zoals SAR data.

Een andere belangrijke observatie is het verschil tussen de jaarlijkse NDVI cyclus en de σ^o van het moerasgebied. De NDVI stijging tijdens het seizoen begint later dan de toename in de σ^o en de daling wordt eerder waargenomen. Dit suggereert dat het effect van vegetatie op de σ^o waargenomen door ASAR over het Tibetaans Plateau beperkt is.

Het algoritme gebruikt in **Hoofdstuk 8** voor het schatten van bodemvocht is daarom enkel gebasseerd op het AIEM model en verwaarloost dus de invloed van vegetatie op σ^o. De ruwheidsparameters benodigd voor het AIEM model zijn bepaald door middel van calibratie met als input drie σ^o metingen verzameld vanuit verschillende kijkhoeken en onder droge omstandigheden. Aangezien de diëlektrische eigenschappen van een diep bevroren bodem gelijk zijn aan die van een droge bodem zijn ASAR beelden verzameld in februari en januari gebruikt voor de bepaling van de ruwheid. De verkregen ruwheidsparameters zijn gebruikt als input voor de bodemvocht bepaling uit de reeks ASAR metingen.

Binnen de tijdreeks aan bodemvocht bepalingen is het karakteristieke moesson patroon goed vertegenwoordigd met de maximale waarden verkregen van juli tot en met september. Ook de ruimtelijke dynamiek is zoals verwacht; met een zeer variabele bodemvocht in de graslanden, en natte maar stabiele omstandigheden waargenomen in de moerasgebieden. De vergelijking tussen de satelliet bepaalde en het gemeten bodemvocht in drie grasland en een moeras locaties resulteert in Root Mean Squared Differences (RMSD's) van 0.032 en 0.060 m^3 m^{-3} respectievelijk. Genormaliseerd voor de verschillende dynamieken van graslanden en moerasgebieden zijn de onzekerheden verkregen voor de twee landbedekkingstypen vergelijkbaar. Dergelijke onzekerheden zijn in overeenstemming met de resultaten uit eerdere studies.

Simulatie van land processen

Het Noah land model is momenteel gekoppeld aan de National Centers for Environmental Prediction (NCEP) operationele weer en klimaat voorspellingsmodel om onder andere de invloed van bodemvocht op land-atmosfeer interacties te beschrijven. Cruciaal voor de kwaliteit van de voorspellingen is een correcte representatie

van de stroming van water door de bodem. **Hoofdstuk 9** evalueert verschillende numerieke schema's voor de verticale integratie van het bodemvocht transport en bespreekt de invloed van het gebruikte bodemfysische model op de gesimuleerde waterbalans en warmte-uitwisselingen.

Uit de Noah simulaties blijkt dat de huidige methode om het bodemvocht transport vertical te integreren het opwaartse transport door capillaire stijging systematisch onderschat. Hierdoor droogt de wortelzone snel uit, terwijl de diepere bodemlagen relatief nat blijven zelfs onder droge omstandigheden met een hoge verdampings vraag. Twee alternatieve methoden zijn gepresenteerd die wel het capillaire stijgingsmechanisme mee nemen.

Het bodemfysisch model (BFM) vormt de bodemfysische functies (BFF) die op hun beurt de grote van de transportcoëfficiënten en het effect van vochttekort op de verdamping bepalen. Noah (en de meeste andere land modellen) gebruikt het BFM ontwikkeld door Campbell (1974), terwijl het algemeen bekend is dat het BFM van Van Genuchten (1980) beter de gemeten BFF schat. De water- en energiebalans gesimuleerd door middel van Noah met deze twee BFM's zijn vergeleken met elkaar. Het verschil in de parameterisatie benodigd voor de Van Genuchten en Campbell BFM'en hindert echter een direkte vergelijking. De BFF's van vijf bodemtypen gedefinieerd binnen de Nederlandse pedotransfer functie (Wösten et al. 2001) zijn daarom gebruikt om de parameterisaties te bepalen. Twee typen Campbell parameters zijn afgeleid, waarbij,

1. De theoretische gelijkenis in de retentie curven in tact wordt gehouden (Campbell **A**);
2. De parameters gefit om de relaties tussen de transport-coëfficiënten en bodemvocht zo goed mogelijk te beschrijven (Campbell **B**).

In vergelijking met Van Genuchten zijn grotere transport-coëfficiënten onder gemiddelde en lage bodemvocht condities karakteristiek voor Campbell **A**. Aan de andere kant, typisch voor de Campell **B** parameterisatie zijn de lagere coëfficiënten bij saturatie, terwijl in het overige bodemvocht traject een goede match met Van Genuchten is verkregen. Het gevolg van deze verschillen is dat Noah met Campbell **A** het water snel door de bodemkolom transpoteert, terwijl met Campbell **B** meer surface runoff wordt gegenereerd. Noah simuleert dus grotere bodemvocht verliezen (verdamping, drainage, surface runoff) met beide typen Campbell parameterisaties. Dit in combinatie met de onderschatting van het opwaarts vochttransport zou een van de verklaringen kunnen zijn voor de voorspelling te warme en te droge zomers door de klimaatmodellen.

Naast de structurele veranderingen in de modelfysica, hebben verschillende onderzoeken ook aangetoond dat de prestaties van land

modellen sterk verbeterd kunnen worden door het aanpassen van de modelparameters, vooral in extreme gebieden zoals het Tibetaans Plateau. **Hoofdstuk 10** bespreekt de benodigde veranderingen aan de bodem en vegetatie parameterisaties om de bodemtemperaturen en verdamping gemeten bij een station op het Tibetaans Plateau te kunnen reproduceren. Uit een analyse van Noah simulaties verkregen met behulp van standard parameterisaties blijkt dat:

1. De gesimuleerde warmteoverdracht in het bodemprofiel de dagelijke temperatuur cyclus in de diepere lagen onderschat;
2. De voelbare warmtestroom overschat wordt en dus de verdamping onderschat.

Door het toekennen van verschillende thermische eigenschappen aan de bodem- en ondergrond, en het opnemen van een extra dunne bodemlaag in de modelstructuur is de dagelijkse gang in dieper bodemlagen vergroot. Dit verbetert ook de simulatie van de temperaturen in de ondiepere lagen. Daarnaast blijkt een reductie in de vegetation parameters, die de transpiratie beperken, nodig te zijn om de overschatting van de voelbare warmte stroom te verkleinen van 41 W m^{-2} naar 20 W m^{-2}. Dit illustreert eens te meer dat parameterisaties gebruikt voor simulatie op continentale schaal, lokaal grote onzekerheden kunnen veroorzaken. Het is echter bemoedigend dat de modelstructuren van land modellen, in dit geval Noah, flexible genoeg zijn om met een kleine aanpassing de land-atmosfeer processen met een redelijke nauwkeurigheid kunnen reproduceren, zelfs voor een extreem gebied als het Tibetaans Plateau.

Integratie van satellite observaties met land modellen

Bepaalde onzekerheden binnen Noah simulaties ten aanzien van de modelstructuur en de parameterisatie zijn besproken in Hoofdstukken 9 en 10. Vandaag de dag wordt een reductie van dergelijke onderzekerheden ook wel nagestreefd door de integratie van de gesimuleerde met geobserveerde toestanden. Een veel gebruikte methode is data assimilatie. Een cruciale aanname in de toepassing van veel data assimilatie technieken is echter dat de gemodelleerde en geobserveerde bodemvocht niet systematisch van elkaar afwijken. Dit is vrijwel nooit het geval. Bovendien is de ruimtelijke resolutie van land modellen op zijn minst enkele kilometers, terwijl satellite beelden een resolutie kunnen hebben van tientallen meters. Een vergelijk tussen 10-km resolutie Noah simulaties en de 100-m resolutie ASAR bodemvocht van Hoofstuk 8 zal dus leiden tot verschillen die veroorzaakt zijn door 1) het inherente verschil tussen de klimatologie van de gesimuleerde en geobserveerde bodemvocht, 2) de verschillen in de ruimtelijke

representatie, en 3) de individuele onzekerheden als gevolg van de simulaties en observaties zelf. Een inzicht in deze verschilbronnen is nodig om de waarde van de integratie van bodemvocht uit satelliet beelden met modellen, die operationeel zijn op een lagere ruimtelijke resolutie, daadwerkelijk te kunnen appreciëren.

Hoofdstuk 11 presenteert een methode voor het kwantificeren van deze verschilbronnen. Uit de decompositie blijkt dat gedurende de winters de ruimtelijke variabiliteit bijdraagt aan ongeveer 50% van de verschillen tussen de twee producten. Deze bedrage stijgt tot meer dan 70% voor de periode tijdens de moesson. Ondanks deze verschillen resulteert de vergelijking van de twee (voor de systematische afwijking gecorrigeerde) producten tot een RMSD van 0.051 m^3 m^{-3} op een dagelijkse basis. Deze overeenkomst tussen de gesimuleerde en ASAR geobserveerde bodemvocht is niet slechter dan de resultaten verkregen met bodemvocht producten uit microgolf observaties met een grove resolutie.

Op basis van deze resultaten kan worden gezegd dat de integratie van bodemvocht producten uit SAR meer aandacht verdient dan het tot nu toe heeft gekregen. Men moet echter wel beseffen dat een groot deel van de verschillen tussen lage-resolutie simulaties en hoge-resolutie SAR bodemvocht veroorzaakt wordt door de verschillende ruimtelijke resoluties. Misschien ligt de werkelijke waarde van hoge resolutie bodemvocht producten wel in verbetering van de ruimtelijke representativiteit binnen modellen. Helaas vormt de beschikbaarheid beelden op een hoge temporele resolutie nog een belemmering voor de ontwikkeling van een bodemvocht product gebaseerd op SAR data.

Pfff ...

ITC Dissertation List

http://www.itc.nl/research/phd/phd_graduates.aspx